Temperature and pressure retrievals and mitigation of the impact of dust for a high-resolution Fourier transform spectrometer mission to Mars

by

Kevin Sutherland Olsen

A thesis submitted in conformity with the requirements
for the degree of Doctor of Philosophy
Graduate Department of Physics
University of Toronto

Abstract

Temperature and pressure retrievals and mitigation of the impact of dust for a high-resolution Fourier transform spectrometer mission to Mars

Kevin Sutherland Olsen
Doctor of Philosophy
Graduate Department of Physics
University of Toronto
2016

On the path to sending a Fourier transform spectrometer (FTS) to Mars to measure the trace gas composition of the atmosphere, several critical elements of the analysis routine need to be adapted from Earth to Mars observation. I have developed new algorithms and software for retrieving vertical profiles of temperature and pressure from infrared spectra, and created interferograms simulating observations at Mars in the presence of dust. The temperature and pressure retrieval algorithm exploits the temperature dependence of absorption lines in CO_2 vibration rotation bands. It was applied to terrestrial spectra from the Atmospheric Chemistry Experiment (ACE) FTS, a solar occultation instrument in orbit since 2003, and the basis for the instrument selected for a Mars mission. ACE-FTS makes multiple spectral measurements during an occultation, separated in altitude by 1.5-5 km, and ten CO_2 bands are analyzed at each altitude, each with a different usable altitude range. I present an inter-comparison of temperature profiles retrieved from ACE-FTS using my algorithm and that of the ACE Science Team, and from the Constellation Observing System for Meteorology, Ionosphere, and Climate (COSMIC, coincident within 1.5 hours and 150 km). Compared to the ACE-FTS standard product, my retrievals exhibit mean differences between -5 and +2 K and compared to COSMIC, mean differences are between -4 and +1 K. A solar occultation FTS vertically scans the limb of the atmosphere continuously, and so the optical path for a Mars observation will move through layers of varying dust levels during a single interferogram acquisition, resulting in source intensity variations (SIVs), negatively impacting trace

gas retrievals. I have simulated SIV using synthetic spectra for the Martian atmosphere, and investigated high-pass filters in the wavenumber domain, and smoothing methods in the optical path difference (OPD) domain. The use of a convolution operator in the OPD domain can isolate the SIV and be used to correct for it. Comparing the original synthetic spectra to SIV-corrected spectra, I obtain spectral residuals of less than 0.25% in simulations for both high- and low-dust conditions, and VMR vertical profile differences on the order of 0.5-3% for several trace gases known to be present in the Martian atmosphere. The work presented in this thesis directly addresses some of the problems faced at Mars: detectability and sources of methane, determining the temperature and pressure of the atmosphere, and estimating the impact of dust on high-resolution solar occultation spectra.

Dedication

For Susan Elizabeth Olsen
September 13, 1955 – June 4, 2014

Ah, they said. Qué bueno. And after and for a long time to come he'd have reason to evoke the recollection of those smiles and to reflect upon the good will which provoked them for it had power to protect and to confer honor and to strengthen resolve and it had power to heal men and to bring them to safety long after all other resources were exhausted.

— Cormac McCarthy,
All the Pretty Horses

Acknowledgements

Completing my PhD was no easy task, and I couldn't have done it without the support of my family, my partner, and my friends, old and new. Heather, you were an integral part of my life in Toronto and Edmonton. No one knows what I've gone through personally or professionally as well as you. Thank you for your support in all my activities, getting me started here, supporting my hobbies, my lifestyle and my academics, always. Mom, you were the greatest, I have had such a great life because of you, I hope you are honoured by my PhD completion. Dad, thank you for your encouragement, patience, and support throughout my academics. I'll get the shells and bait next time we go hunting or fishing together. To my siblings, thank you for putting up with me for so long, I missed skiing with you and spending time at the lake while I was in Toronto.

This couldn't have happened without my committee. Kim, you've been great, providing guidance, support, feedback and structure alongside freedom and opportunity. I've been able to be involved in so many projects, visit many great institutes, and meet many important people. My committee members, Sabine and Kaley, have been a great help throughout, challenging me and keeping me on track. Thank you to my examiners and exam chairs, Dylan, Kristen, Young-June, Roman. Thank you to my external appraiser, Gabi, who came all the way from Germany to make sure I had the right stuff. Thank you to those who proof read my work and kept all the the typos away, Kim, Heather, Ellen. Thank you, Ana, for all your service.

I have had many collaborators during my studies who I've learned a great deal from. In MMM, Ed and all your students in Winnipeg, Lyle, Diana, and Roland at McGill, Roman and Ala at MPB, Alex and Claire at Carleton. From TCCON, Joseph, Paul, and Debra, I had so much help with GGG and spectroscopy and Subversion from you. Thank you, Chris, Sean and Stephen at Waterloo, for your help with ACE-FTS data and retrievals. Patrick, I bumped so many ideas off you, thanks for all your help and input. Geoff, you had so many ideas and knowledge for me, thank you for your time reading my work, answering emails, checking problems out, and meeting with me over the years. My visits to JPL were a highlight of my studies.

The MMM analogue mission to Jeffrey Mine was funded by the CSA and operated through MPB. Thanks to my collaborators for providing the Picarro data and to everyone who participated in both MMM field deployments. They were terrific fun! Funding for by MATMOS investigations was provided by the CSA and NSERC. A big thank you to the ACE Science Team for providing all levels of data and their support files, and for helping me understand them, and for their help and input throughput the project. Thanks to the LMD-GCM team for making their model accessible for researchers, thanks

to the COSMIC collaboration for providing their data for comparisons, thanks to NCEP for providing model data, and thanks to JPL for access to GGG source code, *a priori* data, and the Mars model.

A major part of life in Toronto was sailing. Thank you, C. S., for inviting me to the club as soon as I arrived. Thank you, Gripper, for my first ride on the harbour (and thank you, Plaid, for becoming a CFA and leaving Grip skipper-less). Thank you, Lakota, for the first season of racing. Thank you, Haywire, for all your advice, and for proposing me as a member of RCYC. Thank you, Corn Pants, for taking me under your wing, making me feel welcome, showing me the ways of *big* campaigns and the IPYC, and ensuring I enjoyed the parties and that they ended well. Thank you, Selena, for encouraging me to join up, and to Maeve for bringing me in. Here's to MetalOnMetal! The Gorge was a hell of a time! Thank you to my team/match racing team, Ethan, Seth, Dirk, Will, Tony, Selena, Adam, Isaac, Lando. The Jackson Cup was a blast. Thanks for the advice, Marco, Lumber, Chucky, and Cheddar, for the fun, Samurai, Grambo, and Cuz, and for the coaching, Cunningham. Thank you to the rest of fleet for bringing me in, Marco, Randy, Dirty, Jen, Pink, Clean, Norm, Struthers, Fredo, Keating, Snapper, Coat Hanger, Billy, John. And thank you to all the other sailors I met along the way, for the camaraderie, opportunites, and fun.

To my friends at the university, thank you for all the good times and fond memories, all the Friday nights, and for putting up with me after all the Saturday nights I refused. My office mates, Ellen, Erik, Paul, and Ilya, it was great having you. To the other group members past and present, Patrick, Joseph, Zen, Camille, Felicia, Aubyn, Jenny, Marie-Eve, Ashley K., Ashley J., Dan, honourary Keven [sic], Cyndi, Rodica, Boris, Conan, Xiaoyi, Diane, Anthony, Tony, Orfeo, Stephanie, Alex Geddes, and Ralf. To those outside of the group, it was a pleasure knowing you, Alex Tev, Phil, Garrin, Joe, Angela, Sophie, and Mel. To those from Edmonton, I'm glad we stuck together and supported each other here, Molly and Eve. To all the others I haven't named, but know, I hope our time together was good, I know it helped me. A special thank you to all those I travelled with, and those I met along the way. Thank you to all my Edmonton friends who visited, Josh, Liz, Denis, Kelly, Scott, Brett, Chris, Mike, Ian and Maura, and to all those who put me up when I visited, Charles, Fraser, John, and Allison. Patrick, thanks for all the chess and deep chats.

I wouldn't be where I am today without all the support, connection, advice, friendship, mentorship, and love from my colleagues, acquaintances, friends, competitors, crews, and family members. Thank you all!

Contents

List of Figures

List of Tables

List of Symbols

ACE ..... Atmospheric Chemistry Experiment
ACE-FTS .... Atmospheric Chemistry Experiment Fourier Transform Spectrometer
ADC ..... Analog-to-digital converter
AIRS ..... Advanced InfraRed Sounder
APXS ..... Alpha Particle X-ray Spectrometer
ATMOS ..... Atmospheric Trace Molecule Spectroscopy
ATOVS ..... Advanced TIROS Operational Vertical Sounder
A.U. ..... Arbitrary units
Caltech ..... California Institute of Technology
CHAMP ..... CHAllenging Minisatellite Payload for geoscientific research
CheMin ..... Chemistry and Mineralogy
COSMIC Constellation Observing System for Meteorology, Ionosphere, and Climate
CMC ..... Canadian Meteorological Centre
CRISM ..... Compact Reconnaissance Imaging Spectrometer for Mars
CSA ..... Canadian Space Agency
EDM ..... Entry, Descent and landing demonstrator Module
EDU ..... Engineering Demonstration Unit
EMCS ..... ExoMars Climate Sounder
EMIS ..... ElectroMagnetic Induction Sounder
ESA ..... The European Space Agency
FFT ..... Fast Fourier transform
FTIR ..... Fourier transform infrared spectrometer
FTS ..... Fourier transform spectrometer
GCM ..... General circulation model
GFDL ..... Geophysical Fluid Dynamics Laboratory
GEM ..... Global Environmental Multiscale model
GFIT ..... Spectral fitting software
GGG ..... Software suite containing GFIT

GOSAT ..... Greenhouse Gases Observing Satellite
GPS ..... Global Positioning System
GRACE-A ..... Gravity Recovery and Climate Experiment
GRS ..... Gamma Ray Spectrometer
HALOE ..... Halogen Occultation Experiment
HIRDLS ..... High Resolution Dynamics Limb Sounder
HiRISE ..... High Resolution Imaging Science Experiment
HITRAN ..... HIgh Resolution TRANsmission
$I(x)$ ..... Interferogram in the OPD domain
$I(\tilde{\nu})$ ..... Spectrum in the wavenumber domain
$\hat{I}(\tilde{\nu})$ ..... Fourier transform of $I(x)$
$I_{corr}(x)$ ..... Interferogram corrected for SIV
$I_{SIV}(x)$ ..... Interferogram perturbed with SIV
$I_{smooth}(x)$ ..... Smoothed interferogram
IASI ..... Infrared Atmospheric Sounding Interferometer
JPL ..... NASA's Jet Propulsion Laboratory
LIDAR ..... Light detection and ranging
LMD-GCM ... Oxford-Laboratoire de Météorologie Dynamique-General Circulation Model
M3 ..... Mars Methane Analogue Mission
MAESTRO ..... Measurement of Aerosol Extinction in the Stratosphere and Troposphere Retrieved by Occultation
MATMOS ..... Mars Atmospheric Trace Molecule Occultation Spectrometer
MARCI ..... Mars Color Imager
MARSIS ..... Mars Advanced Radar for Subsurface and Ionosphere Sounding
MarsWRF ..... Mars Weather Research and Forecasting
MAVEN ..... Mars Atmosphere and Volatile EvolutioN
MCD ..... Mars Climate Database
MCS ..... Mars Climate Sounder
MCT ..... Mercury cadmium telluride or HgCdTe
MER ..... Mars Exploration Rover
MET ..... Meteorological Station
MEX ..... Mars Express
MGS ..... Mars Global Surveyor
Mini-TES ..... Miniature Thermal Emission Spectrometer
MIPAS ..... Michelson Interferometer for Passive Atmospheric Sounding

MIRS ..... Microwave Integrated Retrieval System
MLS ..... Microwave Limb Sounder
MM5 ..... Mesoscale Model Version 5
MMM ..... Mars Methane Analogue Mission
MRAMS ..... Mars Regional Atmospheric Modeling System
MRO ..... Mars Reconnaissance Orbiter
MSIS ..... Mass Spectrometer and Incoherent Scatter
MSL ..... Mars Science Laboratory Curiosity
NASA ..... National Aeronautics and Space Administration
NCEP ..... National Centers for Environmental Prediction
NOMAD ..... Nadir and Occultation for MArs Discovery
NRL ..... US Naval Research Laboratory
NSERC ..... Natural Sciences and Engineering Research Council of Canada
NSPO ..... Taiwan's National Space Organization
OMEGA ..... Observatoire pour la Minéralogie, l'Eau, les Glaces, et l'Activité
OPD ..... Optical path difference
OSIRIS ..... Optical Spectrograph and InfraRed Imaging System
P ..... Pressure
P_a ..... Pressure level from which the vertical profile of T is integrated to obtain a vertical profile of P
PARIS ..... Portable Atmospheric Research Interferometric Spectrometer
PFS ..... Planetary Fourier Spectrometer
Q ..... Methane source strength
$Q_R(T)$ ..... Rotational partition function
$Q_V(T)$ ..... Vibrational partition function
QMS ..... Quadrupole Mass Spectrometer
SABER ..... Sounding of the Atmosphere using Broadband Emission Radiometry
SAM ..... Sample Analysis at Mars suite
SBF ..... Source brightness fluctuations
SHARAD ..... Shallow Subsurface Radar
SIV ..... Source intensity variations
SNR ..... Signal-to-noise ratio
SOFIE ..... Solar Occultation For Ice Experiment
SOIR ..... Solar Occultation at Infrared
SPICAM ..... Spectroscopy for Investigation of Characteristics of the Atmosphere of Mars

SPICAV ..... Spectroscopy for Investigation of Characteristics of the Atmosphere of Venus

SPIRALE SPectromètre Infra Rouge pour l'étude de l'Atmosphère par diodes Laser Embarquées

T ..... Temperature

TANSO ..... Thermal And Near infrared Sensor for carbon Observation

TES ..... Thermal Emission Spectrometer

THEMIS ..... THermal EMission Imaging System

TIROS ..... Television InfraRed Observation Satellite

TIRVIM ..... Thermal InfraRed V-shape Interferometer Mounting

TCCON ..... Total Carbon Column Observing Network

TGO ..... Trace Gas Orbiter

TLS ..... Tunable Laser Spectrometer

UCAR ..... University Corporation for Atmospheric Research

$V(x)$ ..... Raw signal from an FTS, generally voltage as a function of OPD

VEX ..... Venus Express

VMR ..... Volume mixing ratio (χ)

VSF ..... VMR scaling factor

ZPD ..... Zero optical path difference

Chapter 1

Introduction

This work was motivated by the selection of the Mars Atmospheric Trace Molecule Occultation Spectrometer (MATMOS) to fly on the ExoMars Trace Gas Orbiter (TGO), to be launched in 2016. MATMOS was jointly led by the Canadian Space Agency (CSA) and the National Aeronautics and Space Administration's (NASA's) Jet Propulsion Laboratory (JPL), but has since been withdrawn[1] from the mission. The MATMOS instrument would have been a high-resolution Fourier transform spectrometer (FTS) operating in solar occultation mode. It was based on the CSA's Atmospheric Chemistry Experiment FTS (ACE-FTS), in Earth orbit since 2003.

In solar occultation spectroscopy, an instrument makes measurements of solar radiation passing through the limb of the atmosphere. With highly inclined orbits, MATMOS would make, and ACE-FTS makes, two sets of measurements per orbit, one as the satellite enters the shadow of the planet, and another as it exits, referred to as sunset and sunrise occultations. A series of measurements are made at tangent altitudes spaced a few kilometres apart, covering an altitude range from the troposphere to the thermosphere. Each measured spectrum is compared to un-occulted observations of the Sun and deep space to determine the amount of incident solar radiation absorbed by gases in the instrument's wavenumber range at each altitude. Solar occultation geometry is shown in Figure 1.1. Because a solar occultation instrument may only make two observations at the terminator per orbit, its main limitation is in spatial and temporal coverage.

The advantages of a solar occultation FTS make it ideally suited for exploring the

[1]In the fiscal years 2013 and 2014, NASA's priorities underwent heavy restructuring to focus on the future of human spaceflight, job creation, and supporting private enterprise. NASA's budgets in fiscal years 2013 and 2014 featured reductions in the Mars Exploration program of 51% (from $587M actual in 2012 to $288M actual in 2014) (*NASA*, 2013, 2015) and NASA terminated its participation in the ExoMars mission. With the departure of JPL from the MATMOS investigation, the MATMOS mission was withdrawn from ExoMars. A summary of NASA's responsibilities within the ExoMars program is found in Section 3.2.

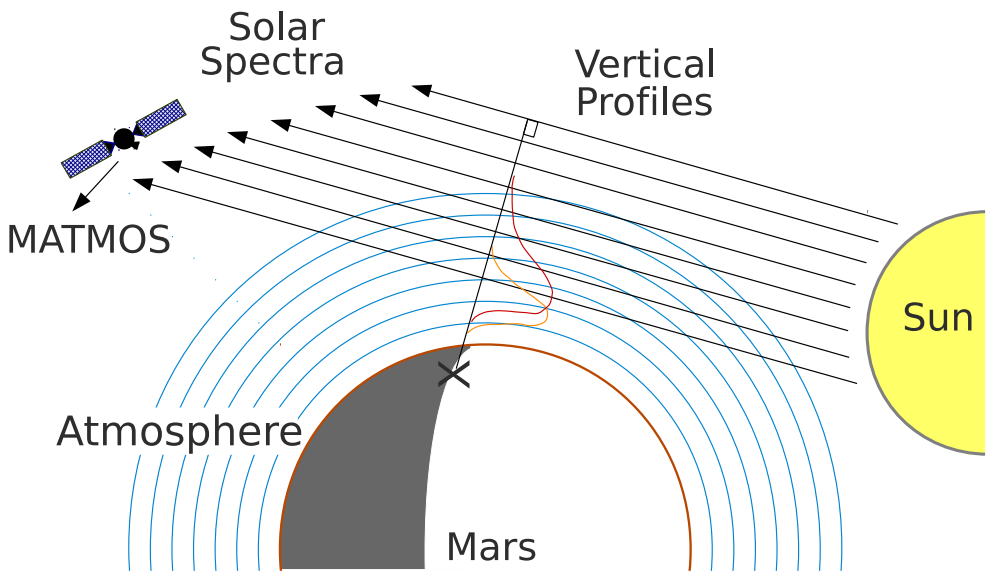

Figure 1.1: Solar occultation geometry. SCISAT and ExoMars orbit at a high orbital inclination (not a requirement for solar occultation) and make a series of solar observations when the satellite comes out of, or enters, the shadow of the planet. The line-of-sight will be occulted by the atmosphere and the amount of solar light absorbed by trace gases at each wavenumber can be inferred by comparing occulted observations with observations made while the satellite orbits between the planet and the Sun. The red and orange curves illustrate retrieved volume mixing ratio vertical profiles for arbitrary trace gases at the location of the terminator.

Martian atmosphere, where many trace gases hypothesized by chemical models have not been detected, or observations have not been confirmed. The optical path provided by solar occultation is very long, allowing for more absorption to be observed than for a nadir-viewing instrument. Using the Sun as a radiation source provides a strong signal, leading to high signal-to-noise ratios (SNRs). The instrument makes observations throughout the vertical extent of the atmosphere, yielding valuable insights into the vertical distribution of target gases. An FTS can have a wide wavenumber range, improving its sensitivity to multiple trace gases active in that region. An FTS can also be made to have a spectral resolution suitably high enough to resolve individual spectral lines, to the extent that isotopologues of a gas can be distinguished.

NASA's 2003 Decadal Survey on Planetary Science (*United States National Research Council*, 2003) had the four following key themes: The First Billion Years of Solar System History; Volatiles and Organics: The Stuff of Life; The Origin and Evolution of Habitable Worlds; Processes: How Planetary Systems Work. Key questions that can be answered at Mars are:

- What global mechanisms affect the evolution of volatiles on planetary bodies?
- What planetary processes are responsible for generating and sustaining habitable worlds?
- Does (or did) life exist beyond Earth?
- Why have the terrestrial planets differed so dramatically in their evolutions?
- How do the processes that shape the contemporary character of planetary bodies operate and interact?

The survey authors recommended distinct Mars missions to study the upper atmosphere and the surface, and to return surface samples to Earth. Among them were the Mars Science Laboratory (MSL) Curiosity rover, which landed in August 2012, and the Mars Atmosphere and Volatile EvolutioN (MAVEN), which arrived in orbit in September 2014. A sample return mission has yet to be realized.

In 2001, the European Space Agency (ESA) launched its Aurora Exploration Programme (*Bonnet and Swings*, 2004) to create a roadmap for the exploration of Mars, the first implementation of which was the ExoMars mission. In 2005, ESA released its Cosmic Vision: Space Science for Europe 2015-2025 plan (*Bignami et al.*, 2005). The Cosmic Vision plan outlines four themes within which to develop science missions: What are the conditions for planet formation and the emergence of life; How does the Solar System work; What are the fundamental physical laws of the Universe; and How did the Universe originate and what is it made of? Within the first theme, ESA plans to pursue the following topics:

- From gas and dust to stars and planets,
- From exo-planets to biomarkers,
- Life and habitability in the Solar System.

ESA established the ExoMars program to investigate whether life ever existed on Mars, which ESA views as one of the outstanding scientific questions of our time.

To address complementary scientific goals and reduce mission costs, NASA and ESA began to jointly develop the ExoMars mission. JPL and the California Institute of Technology proposed contributing an FTS to the ExoMars TGO, and entered into a partnership with the CSA, which has expertise from ACE and has contributed to ExoMars development from its conception. MATMOS would directly address the key goal

of the ExoMars TGO, to deliver a detailed characterization of the Martian atmosphere's composition (*Wennberg and Hipkin*, 2010):

- to detect a broad suite of atmospheric trace gases and isotopologues,
- to map the distribution of trace gases and isotopic ratios geographically and seasonally,
- to characterize the state of the atmosphere by monitoring temperatures, aerosols, water vapour, and ozone.

Data from a successful mission would provide insights about water reservoirs, atmospheric escape, trace gas sources and sinks, and atmospheric circulation.

1.1 Objectives

The objective of the work presented in this thesis is to further our understanding of the chemical processes in the atmosphere of Mars by performing simulation and model studies that address some of the primary topics of interest and to prepare for a future mission that will detect and quantify trace gases in the Martian atmosphere.

Sending an ACE-FTS-like instrument to Mars is an exciting prospect, but faces serious challenges in data analysis. The retrieval problem for Mars is considerably more difficult than for Earth due to its atmospheric conditions and dearth of input parameters. We lack the meteorological infrastructure to provide temperature and pressure, and the spacecraft lacks communication infrastructure to determine its location and the locations of its measurements (*e.g.*, no global navigation satellite system or ground station tracking and communication). The atmosphere is much colder, making it more sensitive to errors in temperature, and some parameters are less well known at these temperatures (e.g. CO_2 natural broadening). The thin atmosphere means absorption will be less strong at all altitudes, and reduces pressure broadening. Seasonal CO_2 cycles are of such a magnitude relative to the total atmosphere that they affect the surface pressure. There can be high levels of dust suspended in the atmosphere, dust storms can be global in scale and can last as long as MATMOS's proposed mission duration (*Cantor et al.*, 2010). Dust attenuates input solar radiation, has broad spectral features at all wavelengths, and its opacity will vary during the acquisition of a single spectrum, distorting the shape of spectral lines.

This thesis addresses these challenges by developing software to retrieve temperature and pressure, and by simulating the effects that varying dust quantity would have on spectrum acquisition. The scientific objectives of this work are as follows:

1. Participate in Mars Methane Analogue Mission field deployments to study local sources of methane.
2. Apply GGG to ACE-FTS solar occultation spectra, implement improvements, and produce production-ready software.
3. Develop a method for retrieving temperature and pressure from solar occultation spectra.
4. Generate synthetic Mars-observing spectra and perform retrievals using GGG.
5. Identify, quantify and correct for the effects that solar intensity variations caused by dust have on spectra and retrievals.

These are described in the following sections.

1.1.1 Participate in Mars Methane Analogue Mission field deployments to study local sources of methane

Through MATMOS collaborators, I also became involved in the CSA's Mars Methane Analogue Mission (MMM), which deployed a micro-rover to Mars analogue sites in Québec. My objective during my involvement with MMM was to study and quantify the ability of a point-source instrument on Mars' surface to detect methane. While we prepared for ExoMars, Curiosity was *en route* to Mars with instruments for measuring the composition of the atmosphere, and these studies were completed prior to its arrival. I accompanied the MMM micro-rover on two field deployments as an atmospheric science specialist, and embarked on a third excursion to collect water and gas samples for laboratory analysis. On the two MMM field deployments, I collected gas samples and operated a cavity ring-down spectrometer in the field to measure the isotopic abundance of CO_2 and methane, and the isotope ratio of carbon. During the first field campaign, we were able to detect and measure the isotopic composition of methane seeping from boreholes in a serpentine mine in Québec. Results were highly localized and methane enhancement was found to fall off rapidly outside of the boreholes. The CSA requested that we provide modelling and analysis of the expected behaviour of a methane source on Mars, to understand whether it would behave in a similar manner to the methane seeps observed in Québec, given the different atmospheric composition and physical properties. A specific answer could not be found in the scientific literature and general circulation models (GCMs) have resolution on the order of kilometres, so a very simple metre-scale dispersion model was written. The aim was to determine spatial limits for detecting

a point source of methane above the terrestrial background concentration of methane using gradient transport models. On the second campaign we released bottled methane of abiotic and biotic origin with known isotopic signatures to test the model. Because of winds, rapid dispersion and mixing with ambient air, samples taken had widely different methane abundances and isotopic signatures. The same gradient transport models were applied to the Mars surface environment to determine whether an instrument on a rover would be capable of detecting a methane point source when not directly downwind of it. Results from this study are presented in Chapter 2.

1.1.2 Apply GGG to ACE-FTS solar occultation spectra, implement improvements, and produce production-ready software

GGG[2] is a spectral fitting software suite maintained at JPL and was selected for use on the MATMOS mission. In this work, the most recent version of GGG was prepared for analyzing solar-occultation spectra from an orbital platform, such as ACE-FTS and MATMOS. The main components of GGG were developed for solar observation by a balloon platform for the MkIV FTS by Dr. Geoff Toon. I created new input files for ACE-FTS, built routines to generate them, incorporated additional GGG functions, and prepared post-processing scripts. Input files provide occultation location and time, *a priori* temperature and pressure, and the viewing geometry. A key portion of this work was the inclusion of a method to retrieve tangent altitude using the volume mixing ratio (VMR) scaling factors (VSF) of CO_2. At low altitudes or in cloud, the CO_2 VSF may become unreliable, so I created a smoothing algorithm to improve the retrieved tangent altitude vertical profiles, and is shown in Section 4.2.1. These changes were uploaded to the GGG version control repository and became part of the main GGG suite.

1.1.3 Develop a method for retrieving temperature and pressure from solar occultation spectra

Performing accurate gas retrievals requires accurate temperature and pressure knowledge at the tangent altitudes of each observation, since the magnitude of vibration-rotation absorption lines depends on temperature and pressure. A primary objective of my thesis work was to determine a new way to determine temperature and pressure from FTS measurements, to produce retrieval software, and to test it with ACE-FTS spectra. Tem-

[2]GGG is not an acronym.

perature is estimated by examining the difference between the computed and measured spectra for vibration-rotation bands of CO_2, which makes up 95% of the Martian atmosphere. This method was originally proposed and used during the Atmospheric Trace Molecule Spectroscopy (ATMOS) Space Shuttle missions by *Stiller et al.* (1995), but was followed up with a different technique for ACE-FTS that fixed the VMR of CO_2 and varied temperature when performing spectral fitting. ACE was able to do this by partitioning the atmosphere into two regions and computing the CO_2 VMR and pressure profiles from a combination of empirical formulae and model results (*Boone et al.*, 2005). For Mars, however, we lack highly reliable model outputs and *a priori* information, and some of the assumptions and formulae may not be valid.

After fitting a CO_2 absorption line, the calculated absorption feature is approximately equal to the true absorption feature (*Stiller et al.*, 1995) and an expression can be derived from the Beer-Lambert law relating VSFs to the *a priori* and true temperatures and pressures (see Equation 4.5). Around 40 CO_2 lines are fitted in a vibration-rotation band and the true T and P are estimated using least squares regression. This is done for ten CO_2 bands and their results are averaged to get the best estimate for T.

Obtaining a temperature profile this way is quite straight-forward. Pressure results are inhibited by two problems: pressure varies exponentially with altitude, so small errors in altitude lead to large errors in the retrieved pressure; it is assumed that each air mass is in hydrostatic equilibrium, so varying both temperature and pressure at a fixed altitude is unphysical. Pressure is constrained by determining the altitude at which the best estimate for pressure was made, based on a combination of minimal standard deviation and regression uncertainties. The vertical profile of temperature is integrated from the best pressure level to all other observation altitudes and the equation of hydrostatic equilibrium is used to compute pressure at all altitudes.

The temperature and pressure retrieval algorithms are applied to spectra of the Earth's atmosphere recorded by ACE-FTS and compared to the ACE-FTS data product and that of the Constellation Observing System for Meteorology, Ionosphere, and Climate (COSMIC). COSMIC is a joint mission by Taiwan's National Space Organization (NSPO) and the University Corporation for Atmospheric Research (UCAR) in the US. It is a constellation of six small satellites that observe GPS (Global Positioning System) radio signals occulted by the lower atmosphere. Using accurate and precise GPS timing and phase changes between the emitted and received radio signal, the amount of bending in the light path from refraction can be estimated. From the refraction data they retrieve temperature, pressure and water vapour. Their data are very precise, have very high vertical resolution (0.1 to 1 km), and extend from the surface to 40 km.

Temperature and pressure retrievals and comparisons to ACE-FTS and COSMIC are discussed in Chapter 4.

1.1.4 Generate synthetic Mars-observing spectra and perform retrievals using GGG

GGG can create synthetic spectra by computing a spectrum for a given wavenumber range and outputting it, rather than performing spectral fitting. These spectra will be used to evaluate corrections for solar intensity variations (SIVs), as well as for simulating SIVs and their effects. Suitable *a priori* profiles to generate synthetic spectra for a Mars-like environment came from empirical data from JPL, and outputs of the Oxford-Laboratoire de Météorologie Dynamique-GCM (LMD-GCM) (*Forget et al.*, 1999). Synthetic spectra have been generated for a variety of dust conditions for both HgCdTe and InSb detectors and are discussed in Section 5.2.

1.1.5 Identify, quantify and correct for the effects that solar intensity variations caused by dust have on spectra and retrievals

A primary problem that a MATMOS-like instrument will face at Mars is that the rate of change of dust abundance with altitude can be very high. The gradient at mid-altitudes is large enough that dust content can change significantly over only a few kilometres. When an interferogram is acquired by MATMOS, the satellite tracks the Sun through the atmosphere continuously and the field of view crosses an altitude range of around 4 km. Over the course of acquisition, the amount of light absorbed by dust varies from start to finish, causing SIVs. My objective was to investigate what effects SIVs have on spectra and whether those effects can be minimized.

Work has been done by the Total Carbon Column Observing Network (TCCON) collaboration to correct for SIVs due to clouds and water vapour (*Keppel-Aleks et al.*, 2007). In their method, they filter a DC interferogram to isolate the SIV signal and divide the DC interferogram with it, obtaining a corrected AC interferogram. This technique works very well for SIVs caused by a grey source, which is not wavenumber-dependent. Dust, however, causes non-uniform attenuation across the MATMOS spectral range. The method still improves the results for analyzing interferograms affected by non-grey sources, but may not be adequate for the requirements of a MATMOS-like mission. Using synthetic spectra, inverse Fourier transformed into synthetic interferograms, a simulation

of the effects of varying dust loading was applied to spectra, and then mitigation was attempted. These simulations are discussed in Chapter 5.

1.2 The atmosphere of Mars

The atmosphere of Mars is 95% CO_2 with temperatures and pressures sufficient to force a condensation cycle. The poles support ice caps that vary in size seasonally, but to such a high extent that they affect surface pressure by up to 25%. Due to Mars' orbital eccentricity, the south polar CO_2 ice cap persists through southern summer, while the north polar CO_2 ice cap sublimates nearly completely, exposing a water ice cap beneath (e.g., *Rafkin et al.*, 2013). Other major chemical species present in the Martian atmosphere are argon and nitrogen (1.9% each) and oxygen (0.15%).

The surface pressure on Mars is around 600 Pa, compared to 1013 hPa on Earth. The atmosphere of Mars is also generally colder than that of Earth at all altitudes, and can have diurnal variations as high as 80 K. Like Earth, the atmospheric temperature decreases with height in the troposphere, which can extend up to 50 or 60 km. A weak ozone layer leads to some warming near 60–70 km, and the exosphere is reached above 120 km. Figure 1.2 compares the temperature vertical profiles on Earth and Mars.

Asymmetric seasonal heating drives meridional circulation, while diurnal thermal tides drive strong surface winds. Dust is frequently lifted from the surface and can build into storms with global extent. A trace amount of water is present and supports an active hydrological cycle. Ice clouds can form from both CO_2 and water and precipitate, while CO_2 and water ices on the surfaces sublimate. Objectives of past Mars exploration have been to determine its atmospheric composition; to monitor temperature, pressure, dust levels, cloud cover, and major constituents; to understand the hydrological cycle, climate, and circulation; to understand the past climate, and history of water on the surface; and to determine whether Mars hosts, or ever hosted, an environment suitable for life. Temperature and pressure have been continuously monitored by instruments on orbiting spacecraft since 1999, as have been the properties and effects of aerosols. The composition of the Martian atmosphere was measured by the Viking missions and Curiosity rover. Other trace gases have been sought from Earth and spacecraft, but few have been discovered or confirmed, and the vertical structure of even fewer is known.

Methane has recently been confirmed in the atmosphere of Mars by Curiosity's Tunable Laser Spectrometer (TLS) on the Sample Analysis at Mars suite (SAM) (*Webster et al.*, 2015). Thought to have a lifetime of only hundreds of years (*Summers et al.*, 2002; *Wong et al.*, 2003), this result suggests that Mars is either geologically or bio-

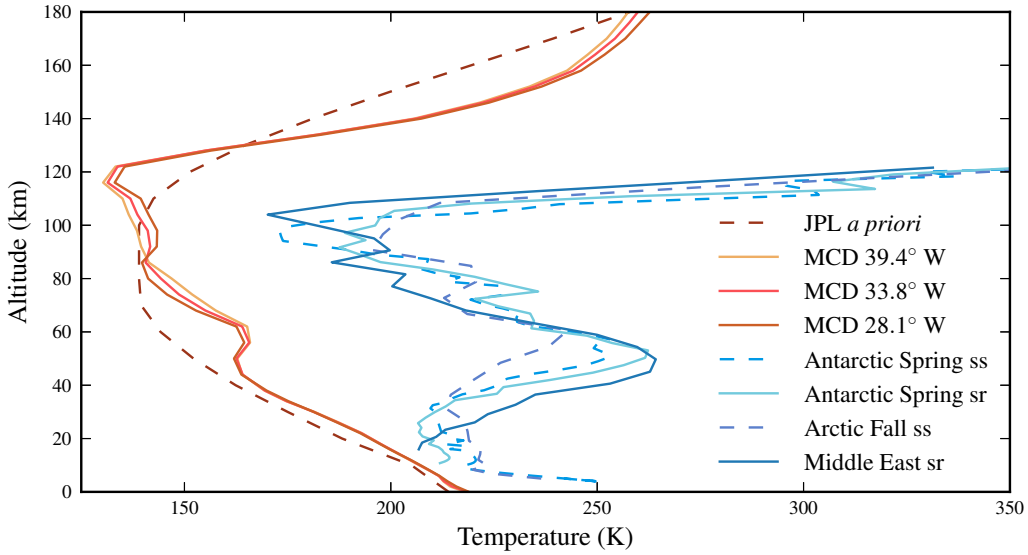

Figure 1.2: Example vertical profiles of temperature for Earth and Mars. The blue lines are for Earth and the red lines are for Mars. The profiles for Earth have been retrieved by ACE-FTS for a variety of conditions. The dashed blue lines were measured at sunset (ss) and the solid blue lines were measured at sunrise (sr). The seasons and locations of the profiles for Earth include over the Antarctic during northern spring, over the Arctic during fall, and over the Middle East in the fall. The dashed red line is the *a priori* Mars temperature profile provided by JPL for a latitude of $-72°$. The solid red lines have been provided by the Mars Climate Database (MCD) (*Forget et al.*, 1999) and show slight variations with changing longitude. Their latitude is 26°.

genically active, hosting a production mechanism for methane. Understanding such a process will impart insight into whether Mars is currently, or has been, habitable. On Earth, methane is mainly produced biologically (*Atreya et al.*, 2007), but on Mars several geologic and exogenic sources have been suggested (e.g., *Webster et al.*, 2015, and references therein). The discovery of methane was originally published over a decade ago by three independent groups: *Formisano et al.* (2004); *Krasnopolsky et al.* (2004) and *Mumma et al.* (2009). The results of all three groups were met with skepticism and criticism (*Lefèvre and Forget*, 2009; *Zahnle et al.*, 2011) and followed by both searches without positive results (*Krasnopolsky*, 2012; *Webster et al.*, 2013a), and bolstered with supporting evidence (*Fonti and Marzo*, 2010; *Geminale et al.*, 2011).

To date, observations of trace gases in the Martian atmosphere have only been made by orbiting instruments with limited capability, *in situ* landers, and Earth-based observatories, largely limiting results to a detection or confirmation. To understand any active processes on Mars, we need to further characterize atmospheric methane and other trace gases. We require definitive detection of trace gases; long-term global measurements to understand temporal and spatial variability, and to quantify their lifetimes; sensitivity to isotopic ratios to estimate sources; and vertical profiles to probe transport. There are currently five operational satellites orbiting Mars and two rovers exploring its surface, but none are capable of accomplishing these tasks.

Vertical profiles of gas abundances have only been measured for CO_2 (*Fedorova et al.*, 2009), O_3 (*Lebonnois et al.*, 2006), and H_2O (*Maltagliati et al.*, 2011, 2013). The Herschel Space Observatory has been used to attempt to measure vertical profiles of O_2 and CO (*Hartogh et al.*, 2010a,b), but to date only spectra and vertical profiles of temperature have been published, which have both been inferred from airglow measurements made on Earth (*Krasnopolsky*, 2007). CO has been studied using spacecraft data (e.g., *Smith et al.*, 2009a; *Sindoni et al.*, 2011), while O_2 airglow has recently been confirmed from observations by Mars Express (MEX) and the Mars Reconnaissance Orbiter (MRO) (*Bertaux et al.*, 2012; *Clancy et al.*, 2012). NO has also been inferred from airglow measurements from MEX measurements (*Bertaux et al.*, 2005a; *Gagné et al.*, 2013). The existence of O_2 and NO in the upper atmosphere imply complex photochemistry (e.g., *Atreya et al.*, 2007; *Barth et al.*, 1992), but several predicted molecules, including N_2O, NO_2, and HO_2, have not been observed (*Villanueva et al.*, 2013, and references therein).

Conversely, H_2O_2 has been discovered, originally from Earth (*Clancy et al.*, 2004; *Encrenaz et al.*, 2012), but recently confirmed by MEX data (*Aoki et al.*, 2015a). H_2 has been observed from Earth (*Krasnopolsky and Feldman*, 2001), which suggests that the radical OH should also be present, which was also recently confirmed by MRO ob-

servations (*Clancy et al.*, 2013). Searches are ongoing, without a detection, for sulphur species, such as SO_2 (*Encrenaz et al.*, 2011; *Krasnopolsky*, 2012), indicative of volcanic activity, and chlorine species, such as HCl (*Villanueva et al.*, 2013), which is suggested by the discovery of perchlorates on the surface (*Hecht et al.*, 2009; *Glavin et al.*, 2013).

A MATMOS-like instrument would be capable of setting detection limits of N_2O, NO_2, HO_2, HCl, SO_2, OCS, and other organic molecules between 1 and 50 ppt (*Wennberg and Hipkin*, 2010; *Wennberg et al.*, 2011). In dust-free conditions, the sensitivity of MATMOS would be < 10 ppt for most infrared-active target gases. The following sections give a historical overview of remote and *in situ* observations related to the Mars atmosphere.

1.2.1 Early missions

The first detailed measurements of the Martian atmosphere were made by NASA's Viking program, consisting of two landers and two orbiters, launched in 1975. Atmospheric measurements were performed with mass spectrometers mounted on the landers (observing the surface) (*Nier and McElroy*, 1976) and their aeroshells (observing above 100 km) (*Owen et al.*, 1977). They determined the composition of the atmosphere to be 95.3% CO_2, 2.7% nitrogen, 1.6% argon, 0.13% oxygen, 0.07% CO, 0.03% water vapour, and with trace amounts of krypton, xenon and ozone. These measurements were not updated until the arrival of MSL in 2012. The two landers survived for more than three and six years, making their record of atmospheric temperature, pressure, and wind speed at the surface the longest to date.

1.2.2 Mars Global Surveyor

Mars was not successfully revisited until 1997 when NASA's Mars Global Surveyor (MGS) entered orbit and the Mars Pathfinder rover landed. The Pathfinder measured surface temperature, pressure and wind speed, and photographed the horizon (*Schofield et al.*, 1997). It observed water ice clouds and haze, and was able to estimate the size of aerosols (*Smith et al.*, 1997). MGS operated until 2007 and carried the Thermal Emission Spectrometer (TES), which produced two dimensional false-colour images of the infrared radiation emitted from the surface (nadir viewing) and atmosphere of Mars (limb viewing) (*Clancy et al.*, 2000). TES was a low-resolution (10 or 20 cm^{-1}) infrared FTS with a range of 200-1650 cm^{-1}, with a radiance sensor and a solar reflectance sensor. TES was sensitive to aerosols and was able to measure dust opacity and constrain dust particle characteristics, such as optical depth, mean particle size and single scattering albedo (*Smith et al.*, 2000; *Clancy et al.*, 2003; *Wolff and Clancy*, 2003). TES was also able to

detect water ice clouds in the atmosphere and distinguish them from dust layers (*Clancy et al.*, 2000; *Tamppari et al.*, 2008), and to measure water vapour and track its variability over time (*Smith*, 2002). The ten-year life span of MGS allowed the first detailed study of the spatial, seasonal, and annual variability of the Martian climate (e.g., *Smith*, 2004; *Pankine et al.*, 2009).

1.2.3 2001 Mars Odyssey

The oldest operational Mars orbiter is NASA's 2001 Mars Odyssey, which arrived in 2001 and is still collecting data with its three instruments: Thermal Emission Imaging System (THEMIS), Gamma Ray Spectrometer (GRS), and Mars Radiation Environment Experiment. THEMIS follows the TES mission with over ten times increased spatial resolution (near-nadir viewing) and made major contributions to finding evidence for past and present water activity. It made the first observations of exposed water ice (*Titus et al.*, 2003), observed gullies forming from melting snow (*Christensen*, 2003), and found evidence for lakes and precipitation in Mars' past (e.g., *Mangold et al.*, 2004; *Glotch and Christensen*, 2005). Like TES, THEMIS is also sensitive to water ice clouds and atmospheric dust (*Smith et al.*, 2003; *Smith*, 2009). The GRS measured the abundance and distribution of elements in the Martian soil at the surface. Contributions relevant to the atmosphere include monitoring the distribution of surface water ice (*Tokar et al.*, 2002) and CO_2 ice (*Kelly et al.*, 2006), monitoring the abundance of ^{40}Ar (*Sprague et al.*, 2004), and making the first map of chlorine abundance (*Keller et al.*, 2006) (first discovered by Viking 1 lander (*Clark et al.*, 1976)).

1.2.4 Mars Express

ESA's Mars Express (MEX) entered Martian orbit in 2004 carrying a robust instrument suite aimed at determining whether Mars was once suitable for life. Its Visible and Infrared Mineralogical Mapping Spectrometer (OMEGA, limb and nadir viewing) observed instances of hydrated sulfates, such as gypsum (*Langevin et al.*, 2005; *Gendrin et al.*, 2005), and phyllosilicates (*Poulet et al.*, 2005), which are formed in the presence of liquid water. OMEGA also made the first direct measurements of CO_2 ice clouds (*Montmessin et al.*, 2007). MEX's Mars Advanced Radar for Subsurface and Ionosphere Sounding (MARSIS, nadir viewing) is able to penetrate several kilometres under the surface and detected sub-surface polar ice caps of pure water (*Plaut et al.*, 2007). Later analysis of MARSIS data was able to produce a dielectric map of the surface and suggested that an ocean once covered the northern plains (*Mouginot et al.*, 2012). The

Analyser of Space Plasmas and Energetic Atoms was able to detect accelerated ions in the upper atmosphere and verify the depth at which interaction with the solar wind can cause atmospheric loss (*Lundin et al.*, 2004).

MEX carried two instruments that were able to directly measure the composition of the Martian atmosphere: the Planetary Fourier Spectrometer (PFS, nadir viewing) and the Spectroscopy for Investigation of Characteristics of the Atmosphere of Mars (SPICAM, nadir and limb viewing). SPICAM is a dual grating spectrometer with an ultraviolet imaging channel and an infrared channel utilizing an acousto-optic tunable filter. The infrared channel operates in the range 5882-10000 cm^{-1} with a resolution of 3-7 cm^{-1}. The PFS is an FTS operating in the range of 220-8190 cm^{-1} with a resolution of 1.3 cm^{-1}. SPICAM was mainly aimed at measuring the abundance of water vapour, but has also measured the abundances of CO_2 and ozone (*Fedorova et al.*, 2006; *Lebonnois et al.*, 2006). SPICAM has been able to detect dust and clouds and determine their properties (*Rannou et al.*, 2006) and their impact on retrievals in the ultraviolet (*Montmessin et al.*, 2006). The ultraviolet channel is sensitive to the upper atmosphere and has been able to probe the density and temperature between 60 and 130 km (*Forget et al.*, 2009), and measure airglow (*Bertaux et al.*, 2005a). One of SPICAM's most striking discoveries was its observation of aurora at the Martian poles (*Bertaux et al.*, 2005b). PFS has been responsible for measuring water vapour abundances (*Fouchet et al.*, 2007; *Tschimmel et al.*, 2008) and dust properties (*Määttänen et al.*, 2009a; *Zasova et al.*, 2005) in the lower atmosphere (below 50 km). The PFS reported the detection of methane in the Martian atmosphere (*Formisano et al.*, 2004; *Geminale et al.*, 2011), which has been controversial, but also set off a search to verify the signal, which included MATMOS. Spectra showing the PFS discoveries of methane and H_2O_2 (*Aoki et al.*, 2015a) are shown in Figure 1.3.

1.2.5 Mars Exploration Rovers

The next missions to Mars were the Mars Exploration Rovers (MERs), which arrived in 2004. MER-A, Spirit, operated until 2010, and MER-B, Opportunity, is still conducting science operations. On the ground, the MERs found ample evidence for past liquid water flowing on the surface (e.g., *Squyres et al.*, 2004; *Grotzinger et al.*, 2005; *Squyres et al.*, 2008), including the presence of gypsum (*Squyres et al.*, 2012), jarosite (*Klingelhöfer et al.*, 2004), and phyllosilicates (*Arvidson et al.*, 2014). Their Alpha Particle X-ray Spectrometers (APXS) were used to monitor seasonal variability of argon isotopes (*Sprague et al.*, 2012), but they carried out dedicated studies of the atmosphere with a

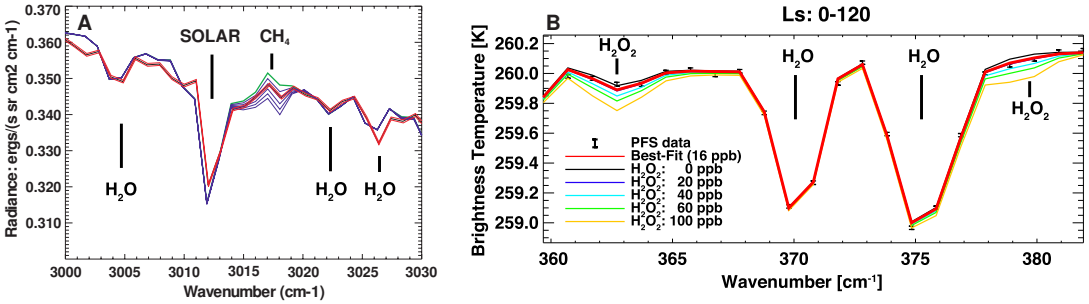

Figure 1.3: Averaged PFS spectra showing the detected absorption features of methane (**A**) and H_2O_2 (**B**). In panel **A**, the red line is the data, and the blue and green lines are best-fit synthetic spectra featuring different methane VMRs. In panel **B**, the black markers are the data, the red line is the best-fit synthetic spectrum, and the coloured lines are the fit line with varying H_2O_2 VMRs. Adapted from *Formisano et al.* (2004) and *Aoki et al.* (2015a).

suite of cameras and the Miniature Thermal Emission Spectrometer (Mini-TES), a low-resolution (10 cm^{-1}) infrared FTS with a range of 339 to 1997 cm^{-1}. Mini-TES monitors dust optical depth and water abundance through the atmospheric column along the vertical line-of-sight, and atmospheric temperature up to 2 km (*Smith et al.*, 2006). Mini-TES worked in conjunction to the MER cameras, which make observations of clouds, haze, and atmospheric dynamics. Observations of wind were made directly, such as when dust devils could be seen (*Greeley et al.*, 2006a), and by studying surface features created by aeolian processes (*Sullivan et al.*, 2005; *Greeley et al.*, 2006b). They were able to measure dust optical depth and cross section, and estimate its vertical distribution and the scale height (*Lemmon et al.*, 2004). Working with MGS TES, they produced the first vertical profiles of temperature from the ground, measured by Mini-TES (*Smith et al.*, 2004, 2006) and to 40-60 km, measured by MGS TES (*Hinson et al.*, 2004; *NASA/JPL/Goddard/ASU/Cornell*, 2004). Co-located MGS TES and Mini-TES observations allowed the measurement of dust indices of refraction in the infrared, leading to accurate retrieval of dust optical depth, dust size, and vertical profiles of dust mixing (*Wolff et al.*, 2006). Spirit and Opportunity have been able to characterize the atmospheric dust loading at Mars and its effects on energy balance and water ice clouds with their multi-year record at two sites (*Lemmon et al.*, 2015).

1.2.6 Mars Reconnaissance Orbiter

The Mars Reconnaissance Orbiter (MRO) entered Martian orbit in 2006 and still operates. Larger than its predecessors, it carries a telemetry and engineering package, Shallow

Subsurface Radar (SHARAD), two spectrometers, and three cameras, of which the High Resolution Imaging Science Experiment (HiRISE) is the largest and most powerful camera to leave Earth orbit. HiRISE was able to observe the effects of winds on the surface in sand movement and dune formation (*Bridges et al.*, 2007), and even observed avalanches of sand mixed with snow and ices made of water or CO_2 in the northern springtime (*Russell et al.*, 2008; *Hansen et al.*, 2011). In the warmer southern hemisphere, HiRISE found evidence for seasonal flows of liquid brine (*McEwen et al.*, 2011). Daily images from the Mars Color Imager (MARCI) on MRO and Mars Orbiter Camera on MGS tracked the extent of cloud cover, atmospheric dust and dust storms, and the size of the north polar cap and its dust cover (*Cantor et al.*, 2010). The depth of the north polar ice cap was studied by SHARAD (*Phillips et al.*, 2008) and was able to estimate the total volume of stored water (*Putzig et al.*, 2009). SHARAD also discovered buried glaciers at lower latitudes (*Holt et al.*, 2008).

MRO carried the Compact Reconnaissance Imaging Spectrometer for Mars (CRISM, nadir and limb viewing) and continues to find evidence of ample liquid water in the past by identifying mineralogy that forms in aqueous environments in the form of clays, phyllosilicates and sulfates (*Murchie et al.*, 2009). CRISM identified jarosite (*Farrand et al.*, 2009), serpentine (*Ehlmann et al.*, 2009, 2010), and kaolin (*Mustard et al.*, 2008). CRISM and MEX OMEGA have together made enough observations to build a global map of aqueous minerals (*Carter et al.*, 2013) on Mars' surface. By combining CRISM and HiRISE observations, *Ehlmann et al.* (2008) directly associated clay deposits with lakebeds and fluvial deltas. HiRISE images were also combined with spectral data from TES and THEMIS and found globally-distributed deposits of chlorides, indicating there was widespread availability of near-surface water in Mars' past. CRISM observations of the seasonal brine flows detected by HiRISE found hydrated salts associated will all flow instances, suggesting that the observed flows are the source of hydration (*Ojha et al.*, 2015), a sign of contemporary water activity on Mars.

CRISM also makes direct observations of the atmosphere, monitoring CO and H_2O column abundances (*Smith et al.*, 2009a), and measuring properties of suspended dust particles, such as single scattering albedo (*Wolff et al.*, 2009) and mean particle size (*Guzewich et al.*, 2014). These properties, and refractive indices, have also been measured by MARCI (*Wolff et al.*, 2010). Using CRISM data, *Clancy et al.* (2012) measured atomic oxygen and O_2, and *Clancy et al.* (2013) reported the first detection of the hydroxyl radical.

Temperature, pressure, dust and water ice aerosols were extensively investigated with MRO's second spectrometer, the Mars Climate Sounder (MCS), a nine-channel filter ra-

diometer (*Kleinböhl et al.*, 2009) in limb viewing geometry. MCS studied the seasonal and vertical distribution of dust, and made the first identification of high-altitude detached dust layers (*McCleese et al.*, 2010; *Heavens et al.*, 2011), which do not conform with standard assumptions about vertical mixing (*Conrath*, 1975), and which have been intensely investigated (*Heavens et al.*, 2014; *Navarro et al.*, 2014), and confirmed by TES (*Guzewich et al.*, 2013a) and CRISM (*Smith et al.*, 2013). MCS dust measurements have been compared with and validated against TES (*Shirley et al.*, 2015), and combined with TES, MiniTES and THEMIS to produce an extensive climatological record (*Montabone et al.*, 2015). Seasonal variations in temperature and water ice have been observed with MCS (*McCleese et al.*, 2010), and ice clouds have been found to form thinner layers and at higher altitudes than previous models suggested (*Heavens et al.*, 2010). MCS is capable of identifying CO_2 clouds and CO_2 snowfall in thermal limb observations (*Hayne et al.*, 2012) and has estimated the extent to which snowfall accounts for replenishing the polar caps (*Hayne et al.*, 2014). The long record of temperature observations has allowed MCS data to identify large-scale dynamic processes such as diurnal thermal tides (*Lee et al.*, 2009) and planetary waves (*Guzewich et al.*, 2012).

1.2.7 Phoenix

Phoenix was a static lander that landed in the north polar region of Mars in 2008 to study the history of water in the geologic record, and past habitability of Mars. It carried a Meteorological Station (MET) to observe winds (*Holstein-Rathlou et al.*, 2010), pressure (*Taylor et al.*, 2010) and local atmospheric dynamics (*Moores et al.*, 2010). A comprehensive campaign of coordinated measurements between instruments on Phoenix and MRO was undertaken throughout the Phoenix mission of one Mars summer (*Tamppari et al.*, 2010). Phoenix carried cameras and photographed dust devils (*Ellehoj et al.*, 2010), water ice clouds, and snowfall (*Whiteway et al.*, 2009). In the ground below it, Phoenix found calcium carbonate, suggesting a water-rich past (*Boynton et al.*, 2009), and soluble sulfates with compositions and concentrations that would have formed habitable conditions in a warm and wet past (*Kounaves et al.*, 2010). Phoenix also discovered perchlorate, which may allow water to be liquid at a lower temperature, and suggests chlorine could be found in the atmosphere (*Hecht et al.*, 2009). The site also hosted water ice close to the surface (*Smith et al.*, 2009b). A LIDAR (light detection and ranging) instrument was able to measure the vertical distribution of dust (*Komguem et al.*, 2013) and the height and thickness of clouds (*Dickinson et al.*, 2010) within the planetary boundary layer. Phoenix also made high-precision measurements of oxygen and carbon

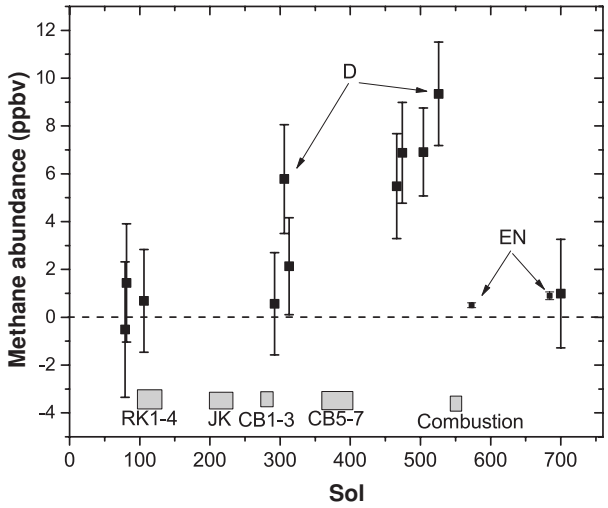

Figure 1.4: Local methane VMRs measured by the SAM TLS on MSL Curiosity over the course of one Mars year. The first six measurements were originally published by *Webster et al.* (2013a) and were found be consistent with zero. Upon reanalysis, *Webster et al.* (2015) found consistently positive values, reduced uncertainty, and increased methane abundance after sol 400. The values denoted "D" were ingested during the day, all others were ingested at night. Those denoted "EN" were ingested during methane enrichment runs. The shaded boxes show the time and duration for evolved gas analysis runs derived from various rock samples. Adapted from *Webster et al.* (2015).

isotopes, and their ratios, in CO_2 (*Niles et al.*, 2010).

1.2.8 Mars Science Laboratory

Measurements of CO_2 and argon isotopic fractions were made by SAM on MSL Curiosity (*Mahaffy et al.*, 2013). MSL landed in 2012 and carried a comprehensive suite of instruments including a radiation sensor, many cameras (17!), the Rover Environmental Monitoring Station (REMS), SAM, and a robotic arm. The arm included a rock drill, an α particle spectrometer, a camera, and a sample collection unit. Collected samples can be delivered to either SAM, which has three instruments, including TLS and Chemistry and Mineralogy (CheMin), an X-ray diffraction instrument. The VMRs and isotopic compositions of the major constituents of the Martian atmosphere were measured at the surface with the SAM TLS and the SAM Quadrupole Mass Spectrometer (QMS) (*Mahaffy et al.*, 2013; *Webster et al.*, 2013b; *Franz et al.*, 2015). Initially, analysis of atmospheric samples returned a null result for methane (*Webster et al.*, 2013a), but reanalysis of existing spectra and new measurements later found variable methane abundances between 1 and 10 ppbv in 13 measurements made over a Mars year (*Webster et al.*, 2015). TLS CH_4

measurements are shown in Figure 1.4. Analysis of argon isotopic ratios in the air with QMS (*Atreya et al.*, 2013) and of deuterium-to-hydrogen ratios in soil and air (*Mahaffy et al.*, 2015) imply substantial loss of atmosphere in Mars' past. Soil analysis detected perchlorates, suggesting widespread abundance (*Glavin et al.*, 2013), and pressure and temperature data from REMS predict that liquid brines may form in the soil at MSL's landing site. REMS monitors relative humidity (*Harri et al.*, 2014) of the air, and temperature (*Hamilton et al.*, 2014) and pressure (*Haberle et al.*, 2014) of the surface and the air just above the surface.

Curiosity continued to build evidence for liquid surface water in Mars' past, but also made several novel discoveries due to its ability to drill into rock faces. It found pebbles and evidence for weathering from a stream bed, suggesting sustained flowing liquid water of substantial depth and speed (*Williams et al.*, 2013). Shortly after landing, Curiosity drove into an area that was determined to be a lakebed made of sedimentary rocks, clays, and smectites (*Vaniman et al.*, 2014). The past lake would be characterized by low salinity, neutral pH, and hosting biogenic elements. The MSL team determined that the site was potentially a habitable environment (*Grotzinger et al.*, 2014). Samples drilled from rocks in the area revealed organic compounds (*Ming et al.*, 2014).

1.2.9 MAVEN and Mangalyaan

In 2014, two spacecraft with complementary objectives reached Mars orbit: NASA's MAVEN and the Indian Space Research Organisation's Mangalyaan. Their objectives were to study the upper atmosphere of Mars, its interactions with the solar wind, and the escape rates of neutral gases and ions. Initial results from MAVEN show the extent of atomic carbon (*University of Colorado and NASA*, 2014a), oxygen (*University of Colorado and NASA*, 2014b), and hydrogen (*University of Colorado and NASA*, 2014c) in the upper exosphere and beyond (1–3 Mars radii). MAVEN has also reported previously unseen, and currently unconfirmed thin detached dust layers at orbital altitudes (*University of Colorado, Laboratory for Atmospheric and Space Physics*, 2014)[3]. At the time of writing, Mangalyaan has yet to report scientific results.

1.3 Summary of work done

Manuscripts have been prepared related to each of the objectives in this thesis and they have been published or submitted to peer-reviewed journals. The dispersion modelling

[3]MAVEN press release material preceding peer-reviewed publications.

presented in Chapter 2 was published in *Geophysical Research Letters* (*Olsen et al.*, 2012), the temperature and pressure analysis in Chapter 4 is currently under open peer review in *Atmospheric Measurement Techniques Discussions* (*Olsen et al.*, 2015a), and the SIV simulations in Chapter 5 have been submitted to a special issue on atmospheric spectroscopy in the *Journal of Molecular Spectroscopy* (*Olsen et al.*, 2015b). For all three manuscripts, all text and figures were prepared by me.

For MMM, the Kapvik rover was developed at Carleton University with MPB Technologies, and the field campaigns were run by Prof. Ed Cloutis from University of Winnipeg. The spectrometer taken on field campaigns was from the lab of Prof. Lyle Whyte at McGill University and its operation was shared by students Roland Wilhelm (first field deployment) and Diana Popa (second field deployment). For the second field deployment, spectrometer results were analyzed and figures were generated automatically by software written by me. The modelling presented in *Olsen et al.* (2012) was done by me. Gas and water samples collected on the third field outing were analyzed by Trevor Brisco (student) in the lab of Prof. Barbara Sherwood Lollar at the University of Toronto.

Temperature and pressure retrievals and SIV simulation made heavy use of the GGG software, primarily developed by Dr. Geoff Toon at JPL, who provided guidance and feedback throughout my research. The temperature and pressure retrieval software integrated into GGG was written by me. The ACE Science Team provided Level 0 (interferograms) and Level 1 data (spectra) and Dr. Chris Boone provided input on their analysis and Level 0 to Level 1 conversion. Scripts were used to generate GGG input files for ACE-FTS spectra, which were written by Dr. Debra Wunch at Caltech. Synthetic Mars spectra were created by me with GGG using input files provided by Dr. Geoff Toon initially, and later using input files created by me. To convert synthetic spectra into interferograms, I used instrument functions created at JPL, and to convert interferograms into spectra, I used the phase correction algorithm used by slice-ipp, software developed at JPL for performing Fourier transforms of infrared spectra. All other software and analysis were written and performed by me.

Chapter 2

Mars Methane Mission micro-rover field deployments

The CSA initiated four analogue rover missions in 2010. Each mission was operated by a different Canadian university, paired with an industrial partner, and had a unique learning objective (*Hipkin et al.*, 2013). Upon completion, the rovers used by, or developed for, the missions were delivered to the CSA's John H. Chapman Space Centre where they are used by the CSA for research at their Analogue Testing Terrain facility. Through MATMOS collaborator Prof. Ed Cloutis, University of Winnipeg, I became involved in the Mars Methane Analogue Mission (MMM or M3) as their atmospheric science specialist and operated instruments on two deployments to analogue sites in Québec.

With MMM, I participated in two field deployments with rovers, and operated an *in situ* instrument which analyzed gas samples to measure the VMR of methane and the ratio of its isotopologues. Interpretation of measurements made in the field led to the development of a small-scale dispersion model to quantify the spread of methane from a seep and to probe the detectability of a methane plume on Mars from a point-source detector, such as TLS on Curiosity. As a follow up to MMM, I returned to the site of the first field deployment to collect a larger set of water and gas samples for more rigorous characterization, but that work was left incomplete due to the departure of key personal and the accidental destruction of several samples. Section 2.1 provides an overview of Mars atmospheric modelling studies, Section 2.2 gives an overview of MMM, Section 2.3 describes the process of serpentinization and why it is important for Mars, Section 2.4 describes the surface conditions on Mars that will be used in the dispersion model, Section 2.5 presents my estimation of the strength of methane sources on Earth and Mars, Section 2.6 describes the gradient transport model used, and Sections 2.7 and 2.8 present the results of gradient transport modelling.

2.1 Modelling of the Martian atmosphere

Previous modelling studies of the Martian atmosphere have used GCMs adapted for Mars. The first such Mars GCM was developed at the University of California by *Leovy and Mintz* (1969) and was used to interpret observations made by the Mariner and Viking missions. This model eventually became maintained at NASA Ames Research Center and is now known as the NASA/Ames GCM (*Haberle et al.*, 1999; *Kahre et al.*, 2006). It features a 7.5° by 9.0° latitude-longitude grid and 30 vertical levels. Other well-developed GCMs include GEM-Mars (*Neary and Daerden*, 2014), the LMD-GCM (*Forget et al.*, 1999), the Mars Weather Research and Forecasting Model (MarsWRF) (*Richardson et al.*, 2007; *Mischna et al.*, 2011), and the Geophysical Fluid Dynamics Laboratory (GFDL) Mars GCM (*Basu et al.*, 2004). Each of these models can simulate the weather, circulation and climate on Mars over the whole planet. However, they also each have spatial resolutions on the order of 1°–5° in latitude and longitude, which means each grid square covers thousands of square kilometres. We want to understand the behaviour of methane between a source and a detector on the scale of 0–100 m, rendering GCMs inappropriate. Smaller scale models have been developed to predict local effects, such as dust lifting. The NCAR Mesoscale Model Version 5 (MM5) can be run over a limited domain at resolutions of 0.1–10 km (*Toigo and Richardson*, 2002). The Mars Regional Atmospheric Modelling System (MRAMS) is another mesoscale model that featured a grid resolution of 60 km (*Rafkin et al.*, 2001).

2.2 The Mars Methane Analogue Mission

The CSA laid out six sub-categories for analogue rover missions for Martian and lunar exploration. MMM was developed for the search for methane, discriminating abiotic from biotic origin. The mission deployed a small rover in an environment with similar visual characteristics to Mars. A systematic observation program was produced, where images and data were collected, transmitted via satellite or cellular network to CSA headquarters and mission control, which returned commands to the rover based on its observations. The mission objectives covered operational and technical aspects, testing the abilities of the rover, communications, and the ability to run a rover campaign in the field (*Qadi et al.*, 2015):

- Develop mission planning and operational methodologies to accomplish science remotely from a micro-rover platform based on simulated Mars-like communications links and data capacities.

- Acquire mission operational experience for remote operations in realistic simulated conditions.
- Select and validate the instrumentation required to detect the presence of methane in support of planetary geological and astrobiological investigations.
- Study the correlation between methane emissions and the local geology – especially the presence of serpentine deposits and hydrated minerals, emission pathways, and associated microbiological activity.
- Provide recommendations on the scientific, operational and technical advancement required to support future micro-rover-based Mars missions.

MMM deployed a Pioneer micro-rover at the Jeffrey Mine, Québec, in June 2011 (*Cloutis et al.*, 2012), and deployed Carleton University's Kapvik rover at the Norbestos Mine, Québec, in June 2012 (*Cloutis et al.*, 2013) (Kapvik was not ready at the time of the first deployment). Both mines are located in the Ordovician Asbestos ophiolite (*Laurent and Hébert*, 1979; *Pinet and Tremblay*, 1995). Norbestos is abandoned and Jeffrey was being prepared to return to active mining (now cancelled) while MMM was deployed. The mines produce chrysotile, a member of the serpentine group of phyllosilicates, which have been detected on the Martian surface and may be a possible source of Martian methane.

The instruments deployed, except for cameras, were not miniaturized, but were standard laboratory and field equipment, and were not carried or controlled by the micro-rovers. The instrument suite included a Picarro G1112-i cavity ring-down spectrometer for analyzing gas samples (*Olsen et al.*, 2012), an electromagnetic induction sounder (EMIS) (*Boivin et al.*, 2013), stereo cameras, an ultraviolet-visible imager, a Raman point spectrometer (B&W Tek), a field hyperspectral point spectrometer (ASD Inc.), an ultraviolet fluorescence spectrometer, and a visible hyperspectral imager. Images from the rover-mounted stereo cameras and ultraviolet-visible imager were transmitted to mission control and used by operators to select sites of interest without input from the field team. Air samples were taken at given sites, followed by geological spectrometer readings (taken by the field team) if methane was detected.

The background methane volume mixing ratio, $\mathrm{VMR}_{\mathrm{CH}_4}$, at Jeffrey Mine was measured to be 1.6 ppmv, with a standard deviation, σ_{SD}, of 0.5 ppmv. Separate measurements of methane emanating from a borehole in the Jeffrey Mine wall found methane levels of 137.5 ± 0.3 ppmv and 200 ± 2 ppmv, while a measurement from a second borehole found 13.2 ± 0.2 ppmv. Measurements from near (< 1 m) the boreholes showed

a very rapid return to background methane mixing ratios. *In situ* measurements made by instruments on a rover, which may be unable to get sufficiently close to the methane source, would not be able to detect these enhancements, so the spatial range of detectable enhancement due to a source is of interest. No naturally occurring methane was found at the Norbestos mine.

On the second deployment, methane with known δ^{13}C ratios was released from gas bottles near the rover site. Due to mixing with ambient air, the measured δ^{13}C did not match that of the gas contained in the bottle. Dispersion and winds also caused the measured VMR to vary strongly. We were asked by the CSA what the behaviour of gas dispersion would be on Mars and whether a Mars rover near a methane point source would face similar challenges as MMM. Therefore, I created metre-scale dispersion models to quantify this behaviour. I located the point source at the site of the Curiosity's landing, and estimated emission source strengths from modelling studies of Mars methane observations, and the findings at Jeffrey Mine.

Another MATMOS collaborator, Prof. Barbara Sherwood-Lollar, University of Toronto, expressed interest in our methane measurements at Jeffrey Mine. A return trip to Jeffrey Mine was made in 2013 to carry out a detailed investigation of subsurface gas and water as part of a study to characterize abiogenic and biogenic methane sources (e.g., *Telling et al.*, 2013), criteria essential for inferring exobiology from gases and liquids sampled on another planet. We used portable H_2 and CH_4 sensors to determine targets and attempted to collect water and gas samples for future analysis. Gas pressure in the boreholes was too low to collect useful gas samples, so we planned to measure dissolved gases in water samples. Samples were taken from four boreholes, and surface runoff. Measurements included cations, anions, conductivity, pH, and total and dissolved inorganic/organic carbon (TIC/TOC and DIC/DOC). Results suggest that water samples gathered from boreholes were likely surface water flowing through the rock, rather than from subsurface origin. Unfortunately, several water samples were destroyed when they froze while being stored in a refrigerator. Prof. Barbara Sherwood-Lollar's graduate student undertaking the research left the program as well.

2.3 Serpentinization

The serpentine group contains three polymorphs, antigorite, chrysotile and lizardite, with the chemical formula $(Mg,Fe)_3Si_2O_5(OH)_4$. Serpentine minerals are classified as phyllosilicates due to their 2:5 ratio of Si to O and their sheet-like structure. Phyllosilicates also encompass the clay minerals group, (including kaolinite), the mica group, and the chlorite

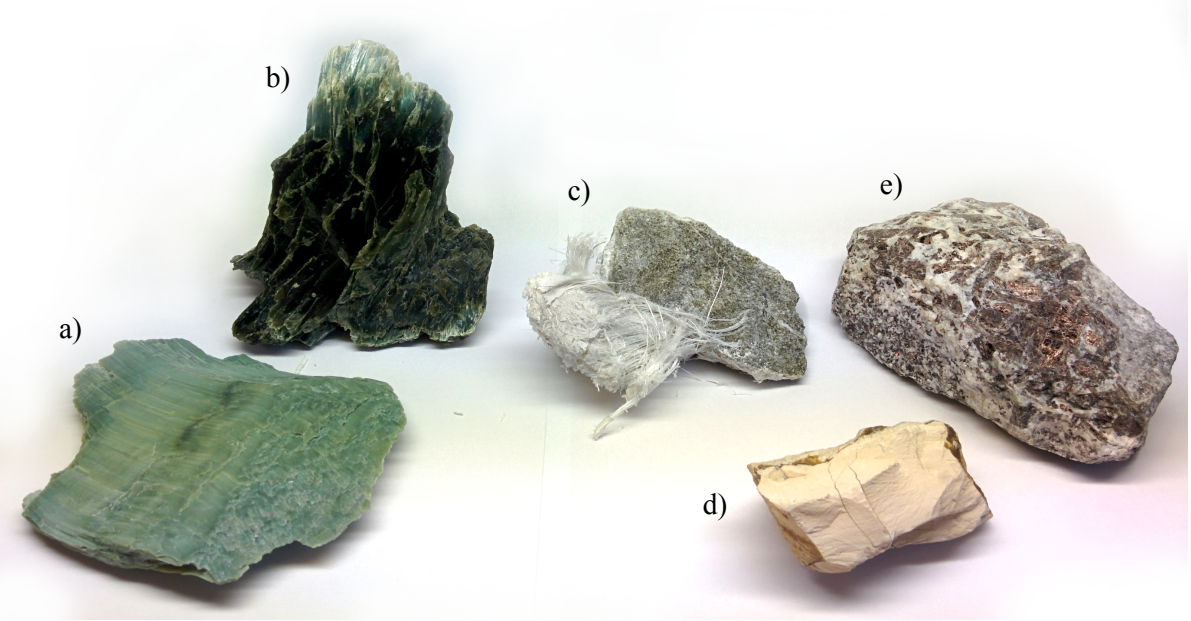

Figure 2.1: A collection of phyllosilicate samples found at Jeffrey Mine during the MMM field deployment. They have been tentatively identified (i.e. without spectroscopic analysis) as: a) antigorite, b) lizardite, c) chrysotile, d) kaolinite, and e) mica.

group. Figure 2.1 shows phyllosilicate mineral samples found in the Jeffrey Mine. While several different types of phyllosilicate have been detected on Mars, all phyllosilicates are hydrated and form in the presence of water.

The process by which serpentine minerals are formed is serpentinization and is actively observed on Earth (e.g., *Abrajano et al.*, 1988; *Kelley et al.*, 2005; *Etiope et al.*, 2011), and an example is shown in Figure 2.2. The requirements are heat, water, and mafic or ultramafic rocks (silica-bearing iron and magnesium oxides). A reaction between olivine minerals and water can produce atomic hydrogen ions or H_2, which can react in the CO_2-rich atmosphere of Mars (*Sleep et al.*, 2004; *Oze and Sharma*, 2005). If the reaction takes place in the presence of CO_2, methane can be formed directly. The process has been observed under laboratory settings (*Horita and Berndt*, 1999; *Neubeck et al.*, 2011) and has been found to occur at temperatures as low as 50°C (*Neubeck et al.*, 2011; *Etiope et al.*, 2013).

On Mars, olivine was detected by MGS TES (*Christensen et al.*, 2000), and confirmed by MER Opportunity (*Christensen et al.*, 2004). Phyllosilicates were identified by MEX OMEGA (*Poulet et al.*, 2005), while serpentinite was resolved by MRO CRISM (*Ehlmann et al.*, 2009). OMEGA and CRISM results are shown in Figure 2.2. Widespread observations of hydrated minerals hint at an abundance of surface water in Mars' past, but also at

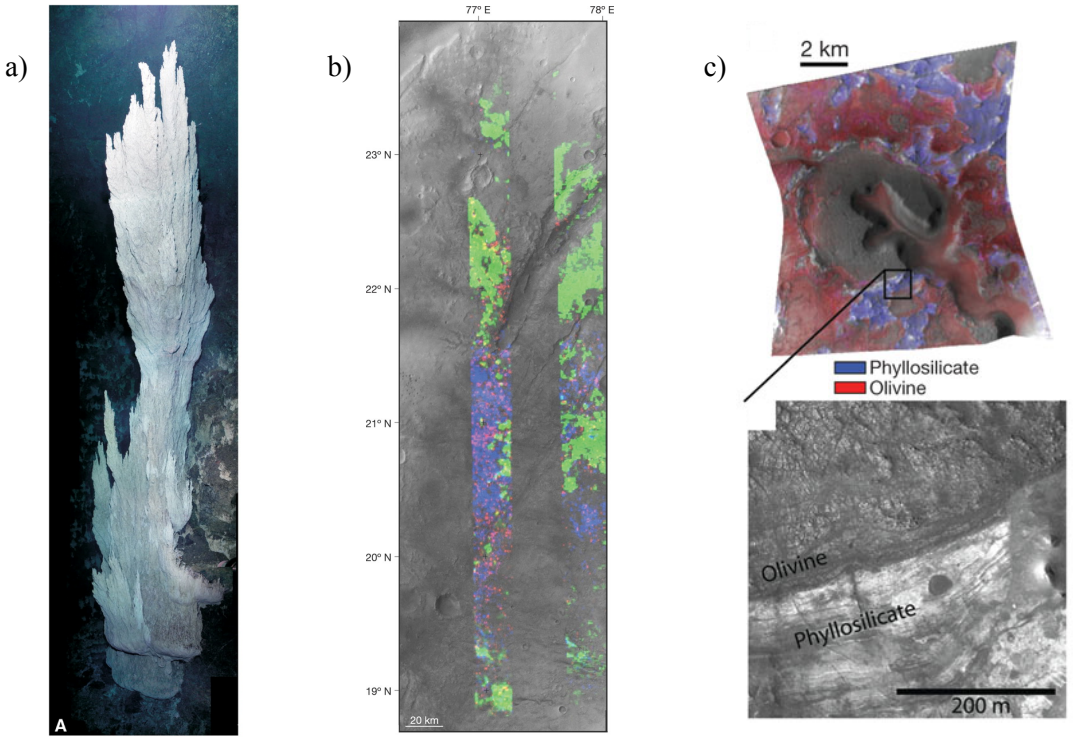

Figure 2.2: Evidence for serpentinization on Earth and Mars. a) An underwater hydrothermal vent expelling gases produced by active serpentinization at the Lost City, near the mid-Atlantic Ridge (*Kelley et al.*, 2005). b) Multi-spectral images recorded by the MEX OMEGA spectrometer that show signatures of phyllosilicates (*Poulet et al.*, 2005). Olivine is shown in green and hydrated minerals are purple. c) Multi-spectral images recorded by the MRO CRISM spectrometer, with olivine and phyllosilicates indicated (*Mustard et al.*, 2008).

a loss mechanism. The serpentinization process stores water during alteration, requiring six water molecules to release a single H_2, which may then escape the atmosphere. Even if the hydrogen is stored as methane, the methane will photolyze, freeing the hydrogen for future escape. *Chassefière and Leblanc* (2011) estimated that serpentinization may have stored as much as a ∼500 m global equivalent layer of surface water. Modelling studies by *Quesnel et al.* (2009) suggest that serpentinization may be responsible for Mars' north-south topographic dichotomy and southern magnetic field anomalies.

Intense interest in the characteristics of a methane source on Mars has been spurred by recent observations of a plume structure. Co-located observations of serpentine and methane on Mars (*Mumma et al.*, 2009) suggested a causal link supporting the hypothesis of a serpentinization source (*Oze and Sharma*, 2005). Future landers and orbiters will be tasked with understanding the sources of methane, which will require accurately

measuring the isotopic fractionation of C and H in methane, and other gases in the methane chemical cycle, such as CO_2 and water (e.g., *Summers et al.*, 2002; *Webster and Mahaffy*, 2011). Terrestrial research in support of interpreting results from Mars has been undertaken at several methane-emitting sites to build an observation database to provide context for measured isotopic ratios (*Ueno et al.*, 2006; *Chassefière et al.*, 2013; *Etiope and Sherwood Lollar*, 2013).

Isotopic ratios, such as $^{13}C/^{12}C$, are often expressed as a permil difference relative to a standard. Carbon isotopic ratios are denoted $\delta^{13}C$ and expressed relative to the Vienna Pee Dee Belemnite sample:

$$\delta^{13}C = \left(\frac{\left(\frac{^{13}C}{^{12}C}\right)_{sample}}{\left(\frac{^{13}C}{^{12}C}\right)_{standard}} - 1 \right) \times 1000‰. \tag{2.1}$$

The relative isotopic ratio of deuterium to hydrogen is denoted δ^2H or δD. The source of methane can be established by calculating $\delta^{13}C$ in CO_2 and methane, and δ^2H in water and methane, and contextualizing the methane observations by placing them in two-dimensional isotopic diagrams, e.g. Figure 2.3. If only methane is measured, its δ^2H can be compared to its $\delta^{13}C$, however this is insufficient. If CO_2 is also measured, then the methane source can be restricted by comparing the CO_2 $\delta^{13}C$ to the CH_4 $\delta^{13}C$ (*Ueno et al.*, 2006; *Etiope and Sherwood Lollar*, 2013). The Picarro spectrometer directly measures $\delta^{13}C$ for methane and CO_2 .

2.4 Mars surface conditions

The northwest corner of Gale Crater, 5.4° S and 137.8° E, was the chosen landing site of MSL. Its floor lies at an elevation of -4.4 km and can be considered smooth for convection purposes, allowing us to disregard effects from surface roughness. The LMD-GCM model resolution is too coarse (5° × 5°) to provide accurate simulations within the crater, but there are four grid points surrounding the crater rim that we can use to infer surface conditions inside the crater. I use climatological averages of pressure and temperature, with standard deviations, from midday (12:00) near the autumn equinox to avoid temperature highs and lows (solar longitude 180°-210°). Each of the four grid points are at different altitudes, determined from *Smith et al.* (1999), above and below a reference altitude, $z_\circ$. The model's climatological average surface pressures are used to determine $P_\circ$ at $z_\circ$ for each point, using the barometric law, $P(z) = P_\circ e^{(-z/H)}$, and a scale height of 11.1 km. The average from the four points was $P_\circ = 533$ Pa, and the average of the

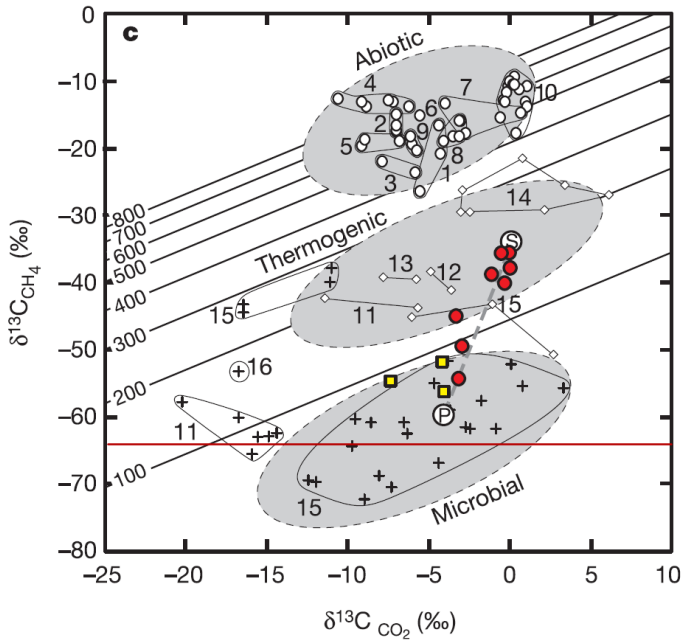

Figure 2.3: Separation of methane sources based on the δ^{13}C ratios for CO_2 and CH_4. The value of the gas sampled from a Jeffrey Mine borehole is indicated in red. Adapted from *Ueno et al.* (2006).

model's climatological standard deviations was 17 Pa. Similarly, the temperature at $z_\circ$ was found to be 208 K, using an adiabatic lapse rate of −4.9 K/km (*Lindal et al.*, 1979). Pressure at the crater floor is 792 ± 27 Pa, and the temperature at the crater floor is 229 K. The model's climatological standard deviations for temperature are small, ∼1 K, while the diurnal temperature variation on Mars can be around 60 K. The diffusion coefficient depends on temperature as $T^{3/2}$ and its accuracy is dominated by the temperature variation (Equation 2.2 below). Temperature and pressure are used to determine the atmospheric number density: $n_\circ = A_\nu P/RT$, with Avogadro's number A_ν and the gas constant R. I estimate that in Gale Crater I have $n_\circ = 2.51 \times 10^{23}$ molecules m^{-3}, with a lower limit of 2.14×10^{23} molecules m^{-3} and an upper limit of 3.31×10^{23} molecules m^{-3} (for a temperature range of 259 to 179 K).

2.5 Estimation of source terms

From *Mumma et al.* (2009), I compute the total mass of methane released during a Mars plume event to be 1.86×10^7 kg. *Mumma et al.* (2009) assumed that the emission is from a single source region and that the source strength must be 3.66 kg s^{-1} if active for 60 days (Q_{60}), 1.8 kg s^{-1} if active for 120 days (Q_{120}), or 0.63 kg s^{-1} if active for half a Mars year

Table 2.1: Summary of source strengths and diffusion-only results. The upper section is for sources on Mars, and the lower section is for terrestrial sources.

	Strength (kg s^{-1})	CH_4 mass (kg)	Duration (days)	VMR_{CH_4} limits (m)	
				18 ppbv	0.1 ppbv
Q_{60} [a]	3.66	1.86×10^7	60	1444	1493
Q_{120} [a]	1.8	1.86×10^7	120	2029	2098
Q_{344} [a]	0.63	1.86×10^7	344	3399	3517
Q_{LF} [b]	0.050	2.6×10^5	60	1404	1454
Q_{1k} [c]	1.7×10^{-5}	4.4	3	299	311
Q_{10k} [c]	1.7×10^{-3}	441	3	310	321
Q_{100k} [c]	0.17	4.4×10^4	3	320	331
Q_{Jef}	5.3×10^{-10}	1.4×10^{-4}	3	3.1 ppmv at 35 m	
Q_{COP} [d]	1	2.6×10^5	3	3.1 ppmv at 41 m	

[a] Derived from *Mumma et al.* (2009).
[b] Derived from *Lefèvre and Forget* (2009).
[c] Derived from *Mischna et al.* (2011).
[d] Derived from *Mau et al.* (2007).

(Q_{344}). *Lefèvre and Forget* (2009) used the same release scenario, but with a much smaller mass, and performed their analysis with the LMD-GCM. They estimated the total mass of methane lost annually via photochemical processes, 2.6×10^5 kg, and released it from a single point over 60 days, resulting in a source strength of $Q_{LF} = 0.050$ kg s^{-1}. *Mischna et al.* (2011) used the MarsWRF GCM (*Richardson et al.*, 2007) to try to constrain the source of the observed plume. Their best fit scenario has the entire plume mass released over only a few days, from an area roughly 4.2×10^6 km^2 ($80° \times 15°$). I assume that the release is from discrete points with an average spacing of 1, 10, or 100 km, resulting in source strengths of $Q_{1k} = 1.7 \times 10^{-5}$ kg s^{-1}, $Q_{10k} = 1.7 \times 10^{-3}$ kg s^{-1}, and $Q_{100k} = 0.17$ kg s^{-1}, respectively. From these modelling studies, we thus have a variety of source strengths to examine, extending over several orders of magnitude, summarized in Table 2.1.

In the Jeffrey Mine, we found a source significantly weaker than those considered for Mars. To estimate its strength, I consider the diffusive mass concentration flux through the borehole, $D(\partial C/\partial z)$, and multiply it by the area through which it passes. Using a borehole diameter of 16 cm, ΔC of 200 ppmv, and Δz of 10 cm, we estimate that it is 5.3×10^{-10} kg s^{-1}. *Mumma et al.* (2009) compared their Mars observations to Coal Oil Point in Santa Barbara, which releases methane at a rate of 1.0 kg s^{-1} (*Mau et al.*, 2007),

comparable to those for Mars. I evaluate my models using this strength, as well.

For these source terms, the observed abundance must exceed the natural variability. At Jeffrey Mine the standard deviation of VMR_{CH_4} was 0.5 ppmv, or 32% of the background. For Mars, I examine background levels of 0, 3, 6 and 10 ppbv, and examine the spatial extent of enhancements of 1, 3 and 6 σ_{SD}. When the background is 0 ppbv, the detection sensitivity of the MSL's TLS, 0.1 ppbv (*Webster and Mahaffy*, 2011), becomes the minimum VMR_{CH_4} that I am seeking. The maximum target is 28 ppbv, or six standard deviations above a background of 10 ppbv with a σ_{SD} of 3 ppbv (subsequently referred to as an 18 ppbv enhancement). In general, I restrict our discussion to upper and lower limits for clarity.

2.6 Gradient transport modelling

I use the observations presented by *Mumma et al.* (2009) and their subsequent examination by atmospheric models (*Mumma et al.*, 2009; *Lefèvre and Forget*, 2009; *Mischna et al.*, 2011) to estimate the strength of a local methane source. I locate it on the Martian surface at the landing site of MSL, Gale Crater, and derive atmospheric parameters (temperature, pressure, mean wind velocity) from the LMD-GCM (*Forget et al.*, 1999). I calculate a dispersion coefficient for methane in the Martian atmosphere at the surface and compute the VMR_{CH_4} distribution 1 m above the surface around the source using a gradient transport model (*Hanna et al.*, 1982). I consider a variety of situations and examine the methane source observed at Jeffrey Mine for comparison.

The time evolution of the distribution of methane that has been injected into the atmosphere is governed by several factors: chemical interactions, diffusion, buoyancy, eddy motion and advection. I consider time scales significantly shorter than the lifetime of methane on Mars, estimated to be as much as several hundred years from photochemical analysis (*Wong et al.*, 2003) or on the order of hundreds of days to account for observations (*Lefèvre and Forget*, 2009; *Geminale et al.*, 2011), and assume that the contribution from chemical interactions is negligible. I also assume that the methane plume is at the same temperature as the ambient air and mixes sufficiently rapidly with CO_2 to result in no net buoyancy. In a situation with no wind, thermal motion will move methane molecules away from the source symmetrically. Winds will carry methane downwind from the source, where it will spread outward from its trajectory. Simple first-order methods are used for the model and to calculate the diffusion coefficient since there is large variability and uncertainty in several contributing factors, such as wind speed, pressure, temperature, and source strength.

Interest in chemical diffusion on Mars has been largely devoted to high altitudes and high temperatures (*Catalfamo et al.*, 2009; *Rodrigo et al.*, 1990; *Izakov*, 1978). Interest at the surface has been motivated by diffusion in soils and ice, and subsurface transport (*Hudson et al.*, 2007; *Hudson and Aharonson*, 2008; *Gough et al.*, 2010). Diffusion is a thermal process governed by intermolecular collisions, and depends on pressure, temperature, particle size, and proximity. Chapman-Enskog theory (*Chapman and Cowling*, 1970) gives the coefficient of diffusion, D, for gas B in gas A as:

$$D = \frac{3}{8n_\circ\sigma_{AB}^2}\sqrt{\frac{k_B T}{2\pi}\left(\frac{1}{m_A}+\frac{1}{m_B}\right)}\frac{f_D}{\Omega_{AB}} \tag{2.2}$$

where m_A and m_B are the molecular masses of the two gases in the mixture and k_B is Boltzmann's constant. σ_{AB} is the characteristic length of the mixture, determined by averaging the characteristic Lennard-Jones length of the two gases. f_D is a correction factor between 1.0 to 1.02, which I set to unity. Ω_{AB} is a dimensionless diffusion integral that depends on the characteristic Lennard-Jones energy ϵ and temperature. An analytic expression for Ω_{AB} is given in *Reid et al.* (1987) and values for ϵ and σ are tabulated in *Reid et al.* (1987) for air, CH_4, CO_2, N_2, Ar, and O_2. CH_4 is mixed with Martian air ($Mair$), so I estimate ϵ_{Mair} and σ_{Mair} from assumed gas concentrations (*Owen et al.*, 1977). Using $\epsilon_{Mair}/k_B = 190.1$ K and $\epsilon_{\mathrm{CH_4}}/k_B = 148.6$ K, we find $\Omega_{Mair,CH_4} = 1.25$ at 229 K, and using $\sigma_{Mair} = 3.932$ Å and $\sigma_{\mathrm{CH_4}} = 3.758$ Å, I find $\sigma_{Mair,CH_4} = 3.845$ Å. I therefore calculate that the coefficient of diffusion, D, for methane on the surface of Mars is 13.03 $\mathrm{cm^2 s^{-1}}$. Variations in temperature produce a range of between 8.99 and 15.64 $\mathrm{cm^2 s^{-1}}$. The diffusion coefficient of CH_4 in air on Earth is 0.2175 $\mathrm{cm^2 s^{-1}}$ (*Cowie and Watts*, 1971).

Gradient transport models are solutions to the continuity equation (see *Hanna et al.* (1982)):

$$\frac{\partial C}{\partial t} + u\frac{\partial C}{\partial x} + v\frac{\partial C}{\partial y} + w\frac{\partial C}{\partial z} = S + \frac{\partial}{\partial x}K_x\frac{\partial C}{\partial x} + \frac{\partial}{\partial y}K_y\frac{\partial C}{\partial y} + \frac{\partial}{\partial z}K_z\frac{\partial C}{\partial z} \tag{2.3}$$

where C is concentration; K_x, K_y, and K_z are radial diffusion coefficients; u, v, and w are wind speed in the x, y, and z directions; and S represents internal processes such as chemical reactions. In my models, I assume that $S \approx 0$ and diffusivity is constant in time and not dependent on direction, with $K_x = K_y = K_z = D$. The simplest case is for

no wind, $u = v = w = 0$, which simplifies the equation to:

$$\frac{\partial C}{\partial t} = D\left(\frac{\partial^2 C}{\partial x^2} + \frac{\partial^2 C}{\partial y^2} + \frac{\partial^2 C}{\partial z^2}\right). \tag{2.4}$$

Solutions are given in *Hanna et al.* (1982) for a variety of initial conditions.

2.7 Diffusion-only model with instantaneous release

With $u = v = w = 0$ and an instantaneous source function, I consider a mass, M, of methane diffusing over time, t. The solution of the continuity equation is (*Hanna et al.*, 1982)

$$C = \frac{M}{(4\pi t D)^{3/2}} \exp\left(-\frac{x^2 + y^2 + z^2}{4tD}\right). \tag{2.5}$$

I set $z = 1$, $y = 0$ and determine x for each concentration. Results are summarized in Table 2.1 for Earth and Mars.

For source considered in *Mischna et al.* (2011) is over an area, so the total mass is divided by the number of sites enclosed within the area. For all three release scenarios, I found that the minimum enhancements and above were found within a distance close to 300 m from the source. For the weakest scenario, where methane sources are separated by ∼1 km (total mass is 1.86×10^7 kg from 4.2×10^6 sites), we find that a $\mathrm{VMR_{CH_4}}$ of 0.1 ppbv is found within 311 m of one of the point sources, while an 18 ppbv enhancement occurs at 299 m. For the strongest source scenario, where sources are around 100 km apart, a $\mathrm{VMR_{CH_4}}$ of 0.1 ppbv is found at 331 m, and an 18 ppbv enhancement occurs at 320 m. The scenario from *Mumma et al.* (2009) uses the total mass, 1.86×10^7 kg, and longer time periods, resulting in greater spatial limits. After 60 days we find $\mathrm{VMR_{CH_4}}$ values of 0.1 ppbv at 1493 m and 18 ppbv at 1444 m; after 120 days 0.1 ppbv is found at 2098 m, and 18 ppbv at 2029 m; after 344 days 0.1 ppbv is found at 3517 m, and 18 ppbv at 3517 m. In the *Lefèvre and Forget* (2009) scenario, we have 2.6×10^5 kg released over 60 days and find the minimum $\mathrm{VMR_{CH_4}}$ 1454 m from the source while the 18 ppbv limit is only 50 m closer.

Modelling the Earth scenarios this way is less informative since I am representing a continuous source with an instantaneous plume. If I consider the same short-term scenario as *Mischna et al.* (2011), 3 days, I overestimate the concentration near the source. A $6\sigma_{SD}$ $\mathrm{VMR_{CH_4}}$ enhancement (3.1 ppmv above background) will be seen within 34 m from the Jeffrey Mine source and 41 m from the stronger Coal Oil Point source. At Jeffrey Mine, we did not see any enhancement beyond 10 cm from the borehole, due

to strong advection, and smaller released mass. I can approximate the continuous source by considering the mass released in a very small time interval, such as 1 minute, in which case the range of $6\sigma_{SD}$ $\mathrm{VMR}_{\mathrm{CH_4}}$ enhancement falls to the order of 4 m.

2.8 Model with mean wind

I now consider a more realistic model with wind and a continuous plume source. The average surface wind speed from the LMD-GCM is 14 ± 5 m s^{-1} at the data points around Gale Crater. I consider three wind cases, this average surface wind, light wind (5 m s^{-1}) and calm wind (0.5 m s^{-1}). The solution to the continuity equation (*Hanna et al.*, 1982) is now:

$$C = \frac{Q}{4\pi D x} \exp\left(-\frac{y^2}{4D(x/u)} - \frac{z^2}{4D(x/u)}\right) \tag{2.6}$$

where x is the direction of wind with speed u, y is the distance perpendicular to the plume, z is altitude, and Q is the source strength. There are several limitations associated with this first-order model. It assumes no change in wind direction and can give the spread, in z and y, of the plume for any length x, which ignores large-scale advection and turbulence, therefore, it is only valid on short length scales. The assumption of constant source strength Q does not account for rapid diffusion over small time intervals, resulting in a slower decrease in concentration with y than observed on Earth. The initial conditions also assume that $C \to \infty$ as $x, y, z \to 0$ (*Hanna et al.*, 1982).

This model provides a limit on the radial distance, y, along the x axis within which a methane source is larger than my imposed limit. I run the model over a 30-km downwind range to give an upper limit to diffusion-only spread and present results for the plume shape over the first 1500 m. The largest factor affecting the width of the methane plume over distance is the wind speed. Figure 2.4a shows the model results using the average wind speed near Gale Crater of 14 m s^{-1}. For clarity, I show only the maximum and minimum enhancement limits for the strongest source, $Q_{60} = 3.66$ kg s^{-1}, in blue, and the weakest source, $Q_{1k} = 1.7 \times 10^{-5}$ kg s^{-1}, in red. All cases show a maximum radial spread on the order of only ± 6 m after 1.5 km, which grows to ± 30 m after 30 km. The effects of reducing the wind speed to 5 m s^{-1} are shown in Figure 2.4b, where the width of the plume grows to ± 10 m after 1.5 km, and up to ± 50 m after 30 km. Calm wind conditions provide the most likely scenario for *in situ* plume detection. These are shown in Figure 2.4c and can have plume widths greater than ± 30 m after 1.5 km. I am primarily interested in the behaviour at < 100 m, since it is unlikely that the trajectory would remain stable longer than this.

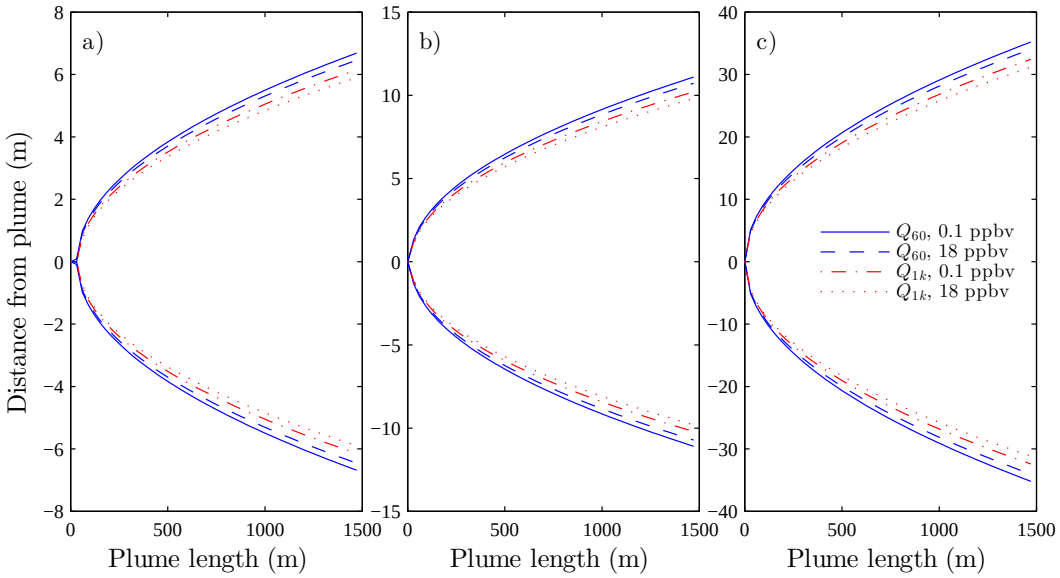

Figure 2.4: Model results, spatial distribution of $\mathrm{VMR}_{\mathrm{CH_4}}$ at $z = 1$ m, for the Mars surface using a wind speed of a) 14 m s^{-1}, b) 5 m s^{-1}, and c) 0.5 m s^{-1}. Two source strengths are plotted, with two detection limits each. Blue shows results for $Q_{60} = 3.66$ kg s^{-1}, with 0.1 ppbv (solid) and 18 ppbv (dashed) limits. Red shows results for $Q_{1k} = 1.7 \times 10^{-5}$ kg s^{-1} with 0.1 ppbv (dash-dot) and 18 ppbv (dotted) limits.

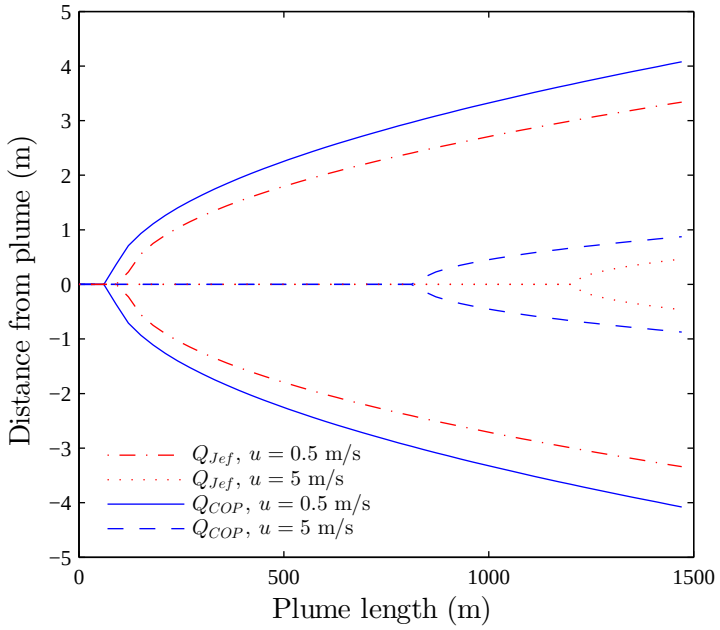

Figure 2.5: Model results, spatial distribution of $\mathrm{VMR}_{\mathrm{CH_4}}$ at $z = 1$ m, for Jeffrey Mine, showing $6\sigma_{SD}$, or 3.1 ppmv, detection limits. Red shows results for $Q_{Jef} = 5.3 \times 10^{-10}$ kg s^{-1} for 5 m s^{-1} winds (dotted) and 0.5 m s^{-1} winds (dash-dot). Blue shows results for $Q_{COP} = 1$ kg s^{-1} for 5 m s^{-1} winds (dashed) and 0.5 m s^{-1} winds (solid).

Applying the model to these two scenarios on Earth, we find that the rate of advection downwind is faster than the rate of diffusion from the plume axis. The estimated source strength in Jeffrey Mine is $Q_{Jef} = 5.3 \times 10^{-10}$ kg s^{-1}. In light wind conditions, 5 m s^{-1} the $6\sigma_{SD} = 3.1$ ppmv limit I consider is not reached until 1.2 km downwind of the source. Calm wind conditions, 0.5 m s^{-1}, decrease the distance at which this enhancement is observed, to around 90 m. The radial range, however, is on the order of only 1-3 m. Figure 2.5 shows the model results for both wind conditions (in red). The stronger Coal Oil Point source (shown in blue), $Q_{COP} = 1$ kg s^{-1}, produces similar results, but at shorter ranges: at 60 m for calm conditions and at 800 m for light wind conditions. This source produces similar results to those found for Mars, with enhancements greater than $1\sigma_{SD}$ $\mathrm{VMR}_{\mathrm{CH_4}}$ found beyond 2 m over much of the 1.5 km range shown.

2.9 Conclusions

This work was motivated by finding weak methane sources at Jeffrey Mine and determining that it is unlikely that a deployed micro-rover could detect an enhancement autonomously. A simple dispersion model was applied to examine small-scale methane distributions originating from a point source on Mars and Earth. These results are most strongly affected by the strength of surface winds and in light wind conditions the possibility of *in situ* measurements detecting a methane enhancement due to a local source is greatly increased.

I estimated a source strength of 5.3×10^{-10} kg s^{-1} at Jeffrey Mine and found that this weak a source cannot produce measurable enhancements of 0.5 to 3.1 ppmv above background levels (1.6 ppmv) within reasonable length scales when wind is present. Under calm wind conditions (0.5 m s^{-1}), the plume would have to travel over 90 m before the plume broadens from its axis enough to produce a $6\sigma_{SD} = 3.1$ ppmv enhancement, and then a measurement would need to be made within metres of the plume axis, so the chance of identifying it remains dubious.

Since these measurements were made as part of a Mars analogue mission, we wanted to place these findings in the context of the Mars surface environment. Using current estimates for Martian source strengths, we show that an *in situ* measurement that is not directly in the plume path would need to be made within ∼5–15 m of the plume axis, depending on wind speed, to see appreciable enhancement above background levels. I estimated the strength of these plumes from three current modelling studies aimed at understanding recent observations (*Mumma et al.*, 2009; *Lefèvre and Forget*, 2009; *Mischna et al.*, 2011). More recent observations have been published (*Fonti and Marzo*,

2010; *Geminale et al.*, 2011; *Krasnopolsky*, 2012) and current modelling work will continue to focus on determining the optimal methane source conditions. A new set of highly sensitive *in situ* measurements were made by Curiosity, which have provided the best constraints on the background methane concentration to date. Initially, they reported no methane beyond their detection limits (*Webster et al.*, 2013a), but later reanalyzed their data, and included new measurements, and detected around 10 ppbv and some temporal variability (*Webster et al.*, 2015). The dispersion calculations I presented here suggest that the temporal variability observed by Curiosity would not be related to a nearby source emitting a methane plume.

Chapter 3

MATMOS and ACE-FTS

3.1 MATMOS scientific objectives

The primary goal of the MATMOS instrument was to determine the sources and sinks of trace gases in the Martian atmosphere that are diagnostic of biology or active geology. To accomplish this, MATMOS had six objectives in three phases: detection, characterization, and localization:

1. Detection: search for atmospheric chemical tracers of geological and biogenic activity.

2. Detection: quantify the lifetimes of diagnostic gases and establish the role of heterogeneous chemistry.

3. Characterization: quantify the exchange of water, CO_2 and their isotopologues with the surface and cloud providing unique insight into atmospheric cycles of CO_2, dust and water.

4. Characterization: understand upper atmosphere coupling toward improving the description of atmospheric escape.

5. Localization: provide essential support to localization campaigns.

6. Localization: solve the mystery of Mars methane.

The MATMOS investigation would measure the vertical distribution of primary atmospheric components, CO_2, CO, H_2O, clouds, dust, temperature and pressure, and identified a set of 21 target trace gases with absorption lines in the infrared. These gases, summarized in Tables 3.1 and 3.2, either have biogenic or geologic sources on Earth, or

can be used as biomarkers (*Wennberg and Hipkin*, 2010; *Wennberg et al.*, 2011; *Hipkin et al.*, 2011).

Oxidizing agents (e.g., H_2O_2 and O_3) and free radicals (e.g., OH and NO) have been detected in the atmosphere of Mars leading to predictions that chemical cycles occur in the Martian atmosphere (e.g., *Wong et al.*, 2003; *Krasnopolsky*, 2010). MATMOS would search for reagents in these cycles to help understand active chemical processes, constrain reaction rates, and identify sources and sinks. Several reviews of the detection limits for such species have recently been published (e.g., *Atreya et al.*, 2007; *Krasnopolsky*, 2011; *Krasnopolsky and Lefèvre*, 2013; *Villanueva et al.*, 2013), mostly set by Earth-based telescopes.

Trace gases targeted by the MATMOS investigation may be directly produced by biogenic or geological activity, or both, or may be part of a chemical cycle indirectly indicative of such activity. Tables 3.1 and 3.2 note possible roles of the MATMOS target gases. Geological sources include volcanism, hydrothermal activity and sub-surface venting. Biogenic sources include trace gases biogenically produced (e.g., methane), and trace gases that act as biomarkers. Some species may have multiple possible sources, but can be constrained by measuring the ratio of their abundance to that of another gas, or detecting gases that are part of a chemical cycle. The source strength of a diagnostic trace gas critically depends on the magnitude and nature of its sinks. MATMOS would be able to detect and characterize chemical species that react with the target gas, or are byproducts of sink reactions. For example, methane photolysis produces the methyl radical, which reduces with water vapour to form methanol (CH_3OH). The detection and characterization of methanol will help constrain methane's photolysis sink. The nature of methane's source can then be deduced from the detection of other diagnostic gases, or co-products. MATMOS would be able to identify isotopologues of CO_2 and methane, and the isotopic ratios of carbon and hydrogen will also be a strong indication of methane's source (e.g., *Ueno et al.*, 2006; *Sherwood Lollar et al.*, 2008).

Biomarkers are trace gases with very short lifetimes (on the order of days) that have mainly biogenic or anthropogenic emission sources on Earth. Their discovery on Mars would indicate active production sources. The discovery of CH_3OH and H_2CO would imply an active volatile organic chemical cycle indicative of biogenic activity. C_2H_6 and CH_4 may be part of such a cycle, but also geologically produced, and CH_4 has a lifetime of several hundred years. The ratio of CH_4 and C_2H_6 abundances or isotopes can help differentiate between a geological of biogenic source (*Sherwood Lollar et al.*, 2008; *Etiope and Sherwood Lollar*, 2013). C_2H_4 and C_2H_2 also have very short lifetimes and may be products of a C_2H_6 sink (*Wong et al.*, 2004).

Table 3.1: List of gases detected in the Martian atmosphere that MATMOS was to monitor and that are important for chemical processes in the atmosphere. Expected detection limits were determined for two dust scenarios defined by different dust extinction optical depths at 1075 cm^{-1}, τ (e.g., *Wolff and Clancy*, 2003). The high-dust scenario is $\tau = 0.6$, and the low-dust scenario is $\tau = 0.1$.

Gases sought	Measured abundance (ppmv)	Expected detection limit (ppt)[a] $\tau = 0.1$	$\tau = 0.6$	Sources, roles
H_2O	10-1000[b]			Photochemistry, biogenic
CO	700[b]			Photochemistry
NO	70[c]	8	45	Radical, nitrogen chemistry
O_3	0.04-0.2[b,d]			Oxidizing agent
H_2O_2	0-50[e]			Oxidizing agent
CH_4	0.69[f]	4	10	Biogenic or geological

[a] From the MATMOS mission proposal *Wennberg and Hipkin* (2010).
[b] *Owen* (1992).
[c] *Encrenaz* (2001).
[d] *Montmessin and Lefèvre* (2013, and references therein).
[e] *Encrenaz et al.* (2012); *Aoki et al.* (2015a, and references therein).
[f] *Webster et al.* (2015).

Table 3.2: List of undetected gases with absorption lines within the spectral range of ACE-FTS and MATMOS that may be diagnostic of geological or biogenic activity.

Gases sought	Measured upper limit (ppbv)	Expected detection limit (ppt)[a] $\tau = 0.1$	$\tau = 0.6$	Sources, roles
HO_2	$< 200^{g}$	12	46	Radical, photochemistry
NO_2	$< 10^{h}$	1	4	Radical, nitrogen chemistry
N_2O	$< 76^{g}$	1	2	Radical, nitrogen chemistry, biogenic, geological
C_2H_2	$< 4^{g,i}$	3	10	Biogenic, volatile organic chemistry
C_2H_4	$< 8^{g}$	8	42	Biogenic, volatile organic chemistry
C_2H_6	$< 0.6^{g,j}$	5	23	Biogenic, volatile organic chemistry, geological
H_2CO	$< 4^{g,i}$	6	42	Biogenic,
CH_3OH	$< 7 - 21^{g}$	6	60	Biogenic, volatile organic chemistry
NH_3	$< 5^{h}$	2	10	Biogenic, geological, nitrogen chemistry
HNO_3		2	5	Biogenic, nitrogen chemistry
CH_3CN		26	107	Biogenic, nitrogen chemistry
HCN	$< 2 - 4.5^{g}$	3	21	Geological, meteoritic or cometary
H_2S	$< 20^{c}$	500	2500	Geological, sulfur chemistry
OCS	$< 70 - 100^{c,k}$	1	3	Geological, sulfur chemistry
SO_2	$< 0.3^{j,l}$	2	5	Geological, sulfur chemistry
HCl	$< 0.3 - 2^{g,i,m}$	4	26	Geological, perchlorates
HF		1	7	Geological
PH_3	$< 100^{h}$	3	74	Geological

[g] *Villanueva et al.* (2013).
[h] *Maguire* (1977).
[i] *Krasnopolsky et al.* (1997).
[j] *Krasnopolsky* (2012).
[k] *Krasnopolsky* (2011).
[l] *Encrenaz et al.* (2011).
[m] *Hartogh et al.* (2010b).

MATMOS would look for the free radicals HO_2, NO and NO_2. HO_2 participates in photochemical pathways involving the primary atmospheric constituents CO_2, CO, O_2, O_3 and H_2O and may lead to production of the oxidant H_2O_2. NO and NO_2 are part of a nitrogen cycle and will help identify the sources and sinks of N_2. N_2O may be part of an atmospheric chemical cycle, or may be produced by abiotic or biogenic reactions with sub-surface nitrogen stores (*Villanueva et al.*, 2013). HNO_3 can be produced by the reaction of NO_2 with H_2O or H_2O_2, linking the photochemical and nitrogen cycles. HCN is not expected to be produced in the Martian atmosphere and may indicate that vented nitrogen has a primordial source (*Mancinelli and Banin*, 2003), while the ratio of HCN abundance to methane abundance will constrain comet or meteor impacts as a methane source (*Bockelée-Morvan et al.*, 2004). NH_3 is indicative of sub-surface venting, but also of the possibility of a sub-surface liquid water environment (*Villanueva et al.*, 2013) as its presence alters the freezing point.

A sulfur chemical cycle is expected if there are active volcanic or hydrothermal processes, and target gases included SO_2, OCS, and H_2S. The detection of perchlorates in Martian soil suggests that chlorine species can be lofted into the atmosphere resulting in a chlorine cycle, so target species include HCl. H_2S and HNO_3 may also be produced by fermentation of organic material.

Of primary interest is methane because on Earth it is produced from the fermentation of organic material, plant growth, microbial activity, and animal digestion. A dominant sink is photolysis and in Mars conditions, a thinner atmosphere and reduced insolation than Earth, the lifetime of atmospheric methane would be relatively short, between 300 and 600 years. The detection of methane, therefore indicates that there must be an active source. Possible sources include an active subsurface biosphere, release of decay products from a past biosphere, the release of stored methane deposits, active volcanism or subsurface magmatism, water-rock interactions such as serpentinization (see Section 2.3), hydrothermal activity, or cometary impacts (e.g., *Wong et al.*, 2004; *Atreya et al.*, 2007; *Etiope and Sherwood Lollar*, 2013). Methane sources and sinks are summarized in Figure 3.1. Observations have been inconsistent, however, and have shown strong, localized signatures that disappear rapidly (*Mumma et al.*, 2009; *Fonti and Marzo*, 2010; *Geminale et al.*, 2011; *Krasnopolsky*, 2012). Photochemical models suggest a source strength that makes volcanic or cometary sources unlikely (*Formisano et al.*, 2004; *Atreya et al.*, 2007), and a sink whose strength cannot yet be explained (*Forget et al.*, 2009).

Following the detection of a diagnostic trace gas, coincident profiles of oxidants, dust, water ice, temperature, and other trace gases that share a chemical cycle will help constrain their lifetimes. Accurately quantifying the vertical distribution of dust in coinci-

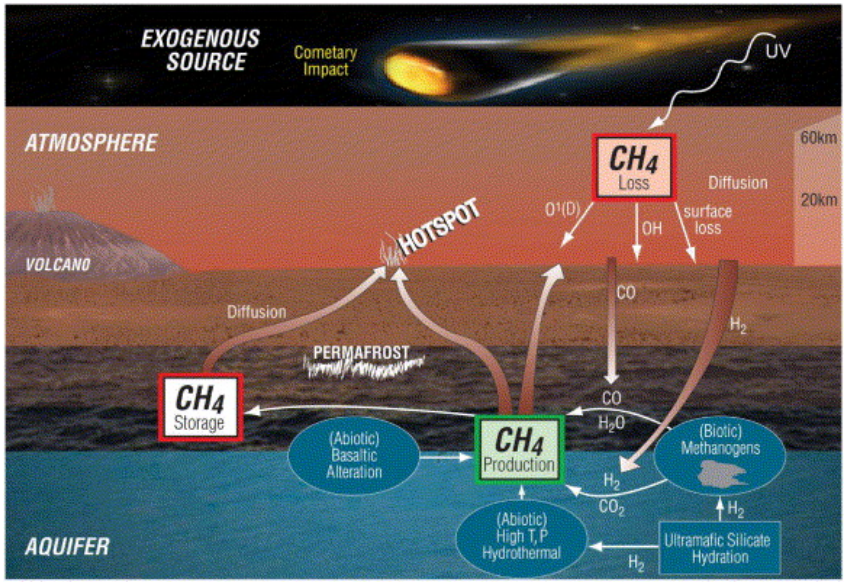

Figure 3.1: A depiction of possible methane sources and sinks in the atmosphere of Mars from *Atreya et al.* (2007). Depicted sources are cometary impacts, volcanism, subsurface methane stores, and subsurface production (biogenic, hydrothermal, and rock alteration). Depicted sinks are photolysis, surface deposition, oxidation, and other chemical reactions.

dence with trace gas measurements is very important because dust plays a role in the water cycle and heterogeneous chemistry, and our ability to include its effects in photochemical models is hampered by the lack of an analog system on Earth. Dust affects the temperature of the atmosphere, in turn affecting water vapour content and reaction rates. Dust acts as a nucleation site for water vapour condensation leading to cloud formation, while water ice clouds restrict the vertical transport of dust. The coupling of the water and dust cycles is not yet understood well enough to incorporate into GCMs (*Rafkin et al.*, 2013). Heterogeneous chemistry on dust particles has been shown to affect hydrocarbon chemistry by facilitating H_2O and CO_2 dissociation, creating free radicals, and increasing the production of H_2O_2 (*Atreya et al.*, 2006), an oxidant and methane sink (*Lefèvre and Forget*, 2009). Ozone, another oxidant, is created from CO_2 dissociation, but destroyed by OH and HO_2 released by water dissociation and photolysis, the rates of which depend on dust loading (e.g., *Lefèvre et al.*, 2008).

Seasonal polar condensation cycles lead to a drastic exchange of CO_2 and H_2O between the atmosphere and the surface. Surface winds lofting dust into the atmosphere may also contribute to to the transport of volatiles to the atmosphere. Reservoirs of subsurface ice, or volatile organics released from rocks and soil may have different isotopic compositions than atmospheric gases, leading to seasonal variation in isotopic ratios, which has been

observed for HDO and H_2O (e.g., *Krasnopolsky*, 2015; *Aoki et al.*, 2015b). MATMOS would be able to measure global and seasonal isotopic ratios of CO_2 and H_2O, volatiles, and aerosols to constrain and quantify this surface exchange.

MATMOS observations would extend from the surface to around 200 km, and may provide insight into the exchange of gases to the upper atmosphere, where they may escape. MATMOS would also be able to generate global maps of trace gases, aiding a localization campaign primarily undertaken by cameras on the TGO.

3.2 The ExoMars mission and MATMOS

The ExoMars mission is now a joint mission between ESA and the Russian Federal Space Agency (Roscosmos). The original structure of the mission was for a launch in 2016 carrying the TGO and a static lander, the Entry, Descent and Landing Demonstrator Module (EDM), followed by a 2018 launch of a pair of micro-rovers, with the capability to store rock samples for later return to Earth. Prior to NASA's withdrawal, the 2018 launch was transformed into a single large rover which would utilize the landing capabilities demonstrated by MSL. NASA's contributions were launch vehicles, the rover landing capabilities, and several TGO instruments, telemetry and communications with Earth. MATMOS was a collaboration between CSA and JPL, and with NASA's withdrawal, the MATMOS investigation was terminated. In the current ESA-Roscosmos configuration, CSA will continue to contribute a solar imager manufactured by ABB Inc., and the rover chassis and suspension manufactured by MacDonald, Dettwiler and Associates.

NASA was originally to supply four instruments to the TGO: MATMOS, ExoMars MCS (EMCS), and two cameras. ESA was to provide the Nadir and Occultation for MArs Discovery spectrometer (NOMAD) (*Drummond et al.*, 2011), which is a dual spectrometer similar to the Solar Occultation at Infrared (SOIR) channel on Venus Express' (VEX's) Spectroscopy for Investigation of Characteristics of the Atmosphere of Venus (SPICAV) instrument (*Bertaux et al.*, 2007), itself similar to SPICAM. The ESA-Roscosmos configuration will have a single camera system provided by ESA, a neutron detector provided by Roscosmos, the original NOMAD instrument, and an infrared spectrometer system provided by Roscosmos. Roscosmos will now also be providing the launch vehicles, rover landing capabilities, and some instruments for the rover. The Roscosmos spectrometer system is the Atmospheric Chemistry Suite (ACS) and contains three distinct infrared spectrometers (*Korablev et al.*, 2014) originally designed for Roscosmos' Fobos-Grunt mission which failed to leave Earth orbit in 2011. It features a near infrared echelle spectrometer with the goal of monitoring water vapour and aerosols,

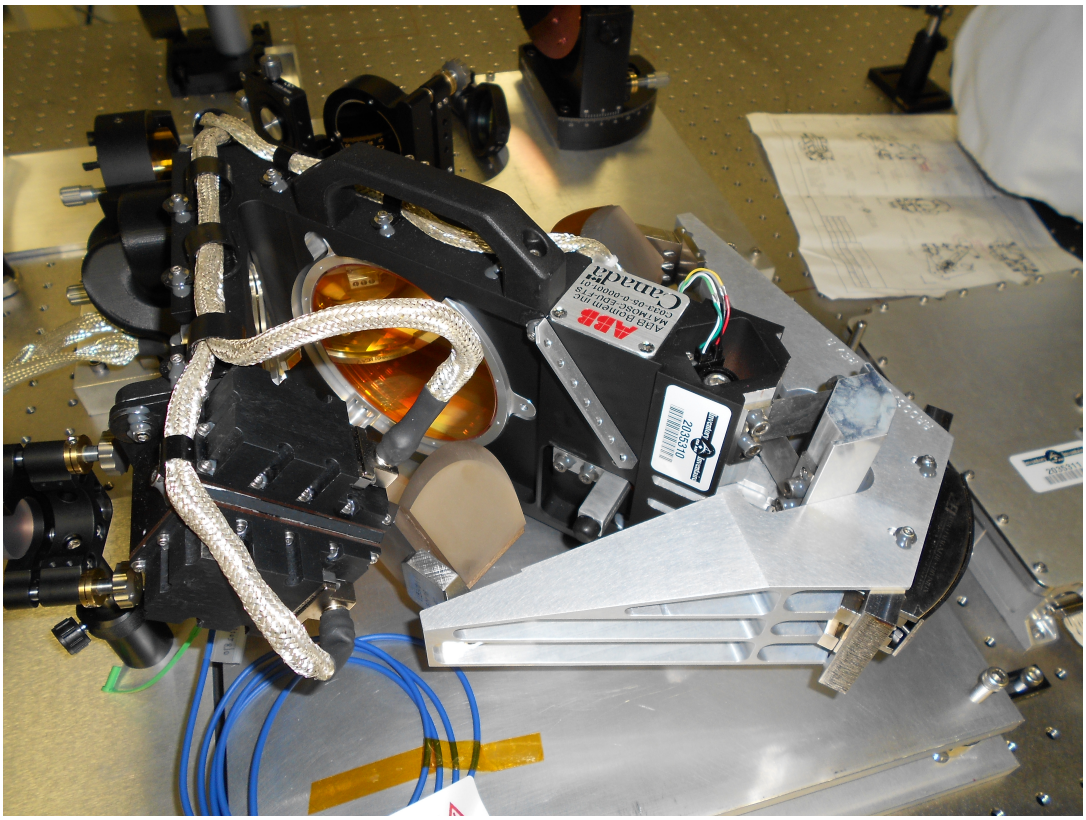

Figure 3.2: The MATMOS Engineering Demonstration Unit (EDU) at JPL. Shown are the corner-cube mirrors on the end of their pendulum arms (right, silver), the beamsplitter (centre, orange), and metrology lasers and end mirror (left).

a mid-infrared echelle spectrometer dedicated to solar occultation geometry with the goal of detecting methane and other trace gases, and a thermal infrared FTS with a resolution of 0.2 to 1.6 cm^{-1} with the goal of monitoring temperature and aerosol states. The mid-infrared and thermal infrared channels are based on VEX SOIR, and the MEX and VEX PFS, respectively.

MATMOS was a double pendulum interferometer with double-passed beam line, and a maximum optical path difference (OPD) of ±25 cm, resulting in a spectral resolution of 0.02 cm^{-1}. By the time of withdrawal, an Engineering Demonstration Unit (EDU) was delivered, and tested at JPL. The EDU is shown in Figure 3.2. The interferometer, metrology sub-system, and solar imager were to be provided by CSA and built by ABB Inc. while the telescope, detector optics, radiative cryo-cooler, analog and digital electronics, thermal sub-systems, and on-board processing computer were to be provided by JPL. The optical layout was similar to that of ACE-FTS. Instrument details are discussed in Section 3.3 and the optical layout is shown in Figure 3.4.

The spectral resolution, extended altitude range, and strong solar signal and SNR of MATMOS were all to be novel contributions to Mars atmospheric remote sensing. MATMOS would have higher resolving power compared to other Mars-observing FTSs such as PFS. A comparison of the spectral resolution of an ACE-FTS-like instrument to a SOIR-type instrument with a resolution of 0.15 cm^{-1} is shown in Figure 3.3. An ACE-FTS-like instrument is able to distinguish H_2O, O_3, CH_4 and its isotopologue CH_3D, while a lower-resolution instrument would not be able to do so.

3.3 ACE-FTS

The CSA's SCISAT-1 was launched into low Earth orbit in 2003 with ACE-FTS and ACE-MAESTRO (Measurements of Aerosol Extinction in the Stratosphere and Troposphere Retrieved by Occultation), which measures in the near-infrared to ultraviolet range. SCISAT-1 has an orbital inclination of 74°, an altitude of around 650 km and a period of just over 90 minutes (*Bernath et al.*, 2005). ACE-FTS and ACE-MAESTRO are still operational as of writing and have recently had their missions extended.

ACE-FTS is a double pendulum interferometer built by ABB Inc. having the same configuration seen in Figure 3.2 of the MATMOS EDU and also has spectral resolution of 0.02 cm^{-1}. The optical layout is shown in Figure 3.4. Incoming solar radiation is focused by an optical telescope and passed through an infrared filter. A suntracker mirror maintains telescope alignment with the centre of the solar disk with the aid of a sun tracker. Light hits a beamsplitter and is passed to two corner-cube mirrors which

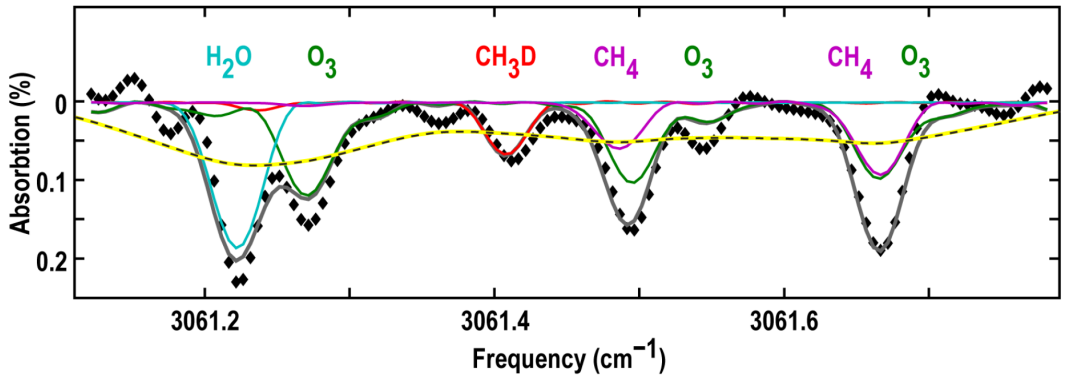

Figure 3.3: Comparison of a mean spectrum recorded by ACE-FTS with 0.02 cm^{-1} resolution and a 0.15 cm^{-1} resolution spectrum representative of current instruments such as ACS and SOIR. The black points are the mean of 189 spectra acquired at ∼50 km in Earth's atmosphere by ACE-FTS, the grey line shows the fitted spectrum, and the cyan, green, red and violet lines show the contributions to the fit for the target gases H_2O, O_3, CH_3D, and CH_4, respectively, showing the capability of a high-resolution instrument to resolve isotopologues of CH_4. The dashed line shows a computed spectrum for a lower-resolution instrument, which cannot distinguish these features. From *Wennberg and Hipkin* (2010).

move on the pendulum arms. The arm movement creates an OPD between the two light paths which are reflected off an end mirror to increase path length and are recombined at the beamsplitter. The recombined photons create an interference pattern measured by two semiconductor detectors which are sensitive to different wavenumber ranges. Digital interferograms are measured with analog-to-digital converters (ADCs) and are sampled using a metrology system that passes a laser beam through the interferometer to provide a real-time measurement of OPD. The signal amplitude at zero OPD (ZPD) is several orders of magnitude larger than elsewhere, so two ADC channels are used with different gains.

An HgCdTe (MCT) detector has a range of around 750-1810 cm^{-1}, while an InSb detector is sensitive within 1810-4400 cm^{-1}. The MCT detector requires a voltage supplied to it which gives the interferogram an offset. Both detectors operate at cryogenic temperatures (80–90 K) and are cooled using a passive radiative cryo-cooler.

Interferograms are Fourier transformed from the OPD domain to the wavenumber domain using a fast Fourier transform (FFT) algorithm (the Fastest Fourier Transform in the West (*Frigo and Johnson*, 2005) is implemented in ACE-FTS processing, MATLAB, Python, and ROOT). During each occultation, calibration measurements are made by observing deep space using the suntracker mirror and by observing the Sun without atmospheric interference while SCISAT-1 is between the Earth and the Sun, closely before

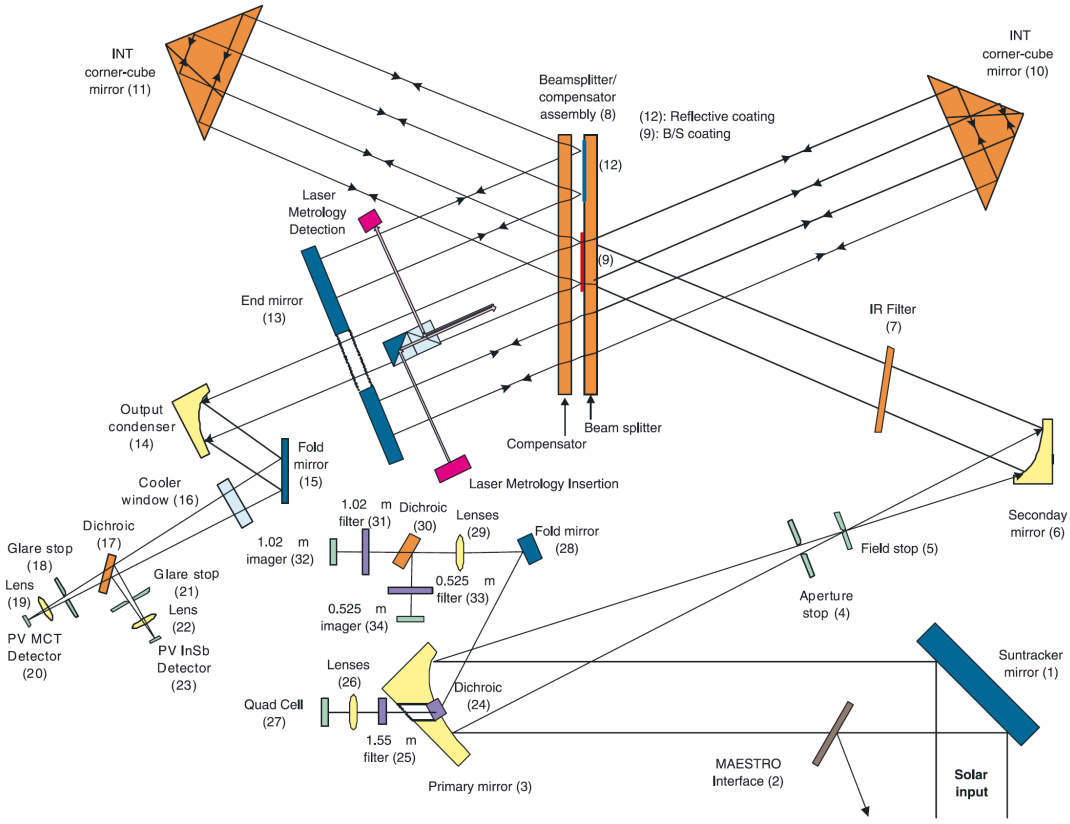

Figure 3.4: Optical design of ACE-FTS. Incoming solar light is passed through/reflected from a beamsplitter to two corner-cube mirrors, reflected back through the beamsplitter assembly to an end mirror, and returned along their paths to the detectors. The corner-cube mirrors are mounted on pendulum arms that rotate to create a difference between the lengths of the optical paths for the two corner-cube mirrors. From *Bernath et al.* (2005).

or after an occultation. The deep space spectrum is subtracted from occultation spectra and calibration spectra. Occultation intensity spectra are divided by an un-occulted sun-viewing calibration intensity spectrum to obtain transmission spectra. Transmission spectra have amplitudes between 0, signifying total absorption at that wavenumber, and 1, signifying total transmission at that wavenumber. Regions of the spectra outside the wavenumber range of the two detectors are discarded and spectra from the InSb and MCT detectors are combined by taking the weighted mean over their overlapping spectral region (*Dutil et al.*, 2002).

Interferogram acquisition takes 2 seconds. How many interferograms are acquired during an occultation, and the altitude spacing between them, depends on the β angle (between the orbit plane and the vector from the Sun to the Earth). With ACE-FTS, β angles between $\pm 20^\circ$ result in a mean tangent altitude spacing between measurements of 5.5 to 6 km above 20 km during an occultation.

3.3.1 Differences between ACE-FTS and MATMOS

While the optical layout and interferometer remain largely unchanged between ACE-FTS and MATMOS, mission requirements for Mars necessitated changes to the detectors and electronics. There were minor changes, such as a new mechanism for locking the interferometer in place during launch and a new cryo-cooler developed to a smaller form factor.

The solar imager would be upgraded with four channels to improve tracking of the centre of the solar disk, and to image and identify dust and cloud layers. This is still included in the current TGO configuration. The ability to transmit data from the spacecraft to Earth will be significantly reduced at Mars, so the onboard electronics will have a much larger role in data processing. Interferograms would be Fourier transformed by MATMOS and only transmission spectra, which are much shorter data records, would be routinely transmitted to Earth.

ACE-FTS interferograms are AC recorded, or high-pass filtered such that they have amplitudes centred at zero. In order to correct for the effects of dust, low amplitude signals will need to be maintained (see Chapter 5) and MATMOS will record DC-coupled interferograms. To enable this, sigma-delta ADCs with a higher dynamic range would be used[1], which also alleviate the need to maintain two ADC channels and have a different gain for the ZPD region. However, sigma-delta ADCs can only sample at a fixed time interval, and cannot be triggered by a metrology laser at accurate OPD spacing. They

[1]Suitable space-qualified hardware was unavailable at the time of ACE-FTS' construction.

would be operated at a much higher sampling rate and re-sampled using the metrology system.

3.4 Solar occultation Fourier transform spectroscopy

The spectral resolution, $\Delta\tilde{\nu}$, of an FTS is determined by the maximum OPD, L[2]:

$$\Delta\tilde{\nu} = \frac{1}{2L}. \tag{3.1}$$

This is the distance between statistically independent samples in the spectrum (*Brault*, 1985). Other definitions of spectral resolution, such as the Rayleigh criterion, depend on the instrument's response to monochromatic radiation and describe the separation between two independent spectral lines required for both to be resolved. The wavenumber range of a discretely sampled FTS system is from zero to the Nyquist frequency, which is half the sampling rate:

$$\tilde{\nu}_{Nyq} = \frac{1}{2}\frac{N}{2L}, \tag{3.2}$$

where N is the number of samples taken, and is generally a power of 2 or the product of small primes to improve the computational performance of the FFT. Interferograms from the MCT detector have 323560 samples and a Nyquist frequency of 3235.6 cm^{-1}, which necessarily corresponds to $2L$ divided by the metrology laser's wavelength. To achieve a spectral range up to 4320 cm^{-1}, the InSb detector samples twice as fast to obtain a Nyquist frequency of 6471.2 cm^{-1}.

The discrete Fourier transform applied to an interferogram $I(x)$ is:

$$\hat{I}(k\Delta\tilde{\nu}) = \sum_{j=0}^{N-1} I(jL/N)e^{-2\pi ijk/N} \quad k = 0, \ldots N-1, \tag{3.3}$$

where OPD, x, is expressed as discrete steps of width L/N, and the indices j and k define the discrete range of the interferogram and spectrum, respectively. The inverse Fourier transform applied to a spectrum $\hat{I}(\tilde{\nu})$ is:

$$I(jL/N) = \frac{1}{N}\sum_{k=0}^{N-1} \hat{I}(k\Delta\tilde{\nu})e^{2\pi ijk/N} \quad j = 0, \ldots N-1. \tag{3.4}$$

Information about a spectrum's baseline is contained in the high amplitude centreburst

[2]For MATMOS and ACE-FTS L is 25 cm and $\Delta\tilde{\nu}$ is 0.02 cm^{-1}.

of an interferogram at ZPD, while information about photon absorption at discrete wavenumbers is contained elsewhere. Absorption lines obtained by a real FTS are affected by changes in the frequency of incoming radiation, an instrument line shape reflecting practical limitations, and errors made while recording the interferogram.

The line shape function commonly used in atmospheric Fourier transform spectroscopy is the Voigt line shape. Transmission or absorption of a photon by an energetic molecule results from the change of its quantum state. An absorption line from a vibration-rotation band of a molecule would therefore be a delta function. However, several processes cause the shape of an absorption line in the atmosphere to broaden. The two dominant mechanisms are pressure, or Lorentz, broadening and Doppler broadening. Pressure broadening is caused by collisions between molecules, and is characterized by a broad Lorentz profile. When an emitting molecule collides with another molecule, energy gained or lost alters the radiating harmonic wave train, causing a shift in the wavelength of the absorbed or emitted photon. A Lorentz broadening profile is (e.g. *Liou*, 2002; *Notholt et al.*, 2006):

$$f_L(\tilde{\nu} - \tilde{\nu}_\circ) = \frac{1}{\pi} \frac{\alpha_L}{(\tilde{\nu} - \tilde{\nu}_\circ - \delta_L)^2 + \alpha_L^2}, \tag{3.5}$$

where $\tilde{\nu}_\circ$ is the central wavenumber of the line, $\delta_L = \delta_\circ P$ is a shift of the line centre frequency, and α_L is the half-width of the line at half-maximum and given by:

$$\alpha_L = \alpha_\circ \left(\frac{P}{P_\circ}\right) \left(\frac{T_\circ}{T}\right)^{n_L}. \tag{3.6}$$

$P_\circ$ and $T_\circ$ are 1013.25 hPa and 296 K, respectively. $\alpha_\circ$ is the pressure broadening coefficient at normal pressure and temperature. $\alpha_\circ$, $\delta_\circ$, and the exponent n_L for a transition with central wavenumber $\tilde{\nu}_\circ$ are provided by the (HIgh Resolution TRANsmission) linelist (*Rothman et al.*, 2013) .

Doppler broadening is due to small changes in the frequency of the absorbed or emitted photon caused by thermal motion of the radiating molecule via the Doppler effect. The Doppler profile is Gaussian and narrower in the centre than the Lorentz profile, with wings that fall off more rapidly. A Doppler broadening profile is (e.g. *Liou*, 2002; *Notholt et al.*, 2006):

$$f_D(\tilde{\nu} - \tilde{\nu}_\circ) = \frac{1}{\alpha_D \sqrt{\pi}} \exp\left(-\left(\frac{\tilde{\nu} - \tilde{\nu}_\circ}{\alpha_D}\right)^2\right), \tag{3.7}$$

where $\alpha_D\sqrt{\ln 2}$ is the half-width at half-maximum and α_D is given by:

$$\alpha_D = \frac{\tilde{\nu}_\circ}{c}\sqrt{\frac{2kT}{m}}. \tag{3.8}$$

where c is the speed of light, k is the Boltzmann constant, m is the molecular mass.

The significance of Lorentz broadening depends on pressure and it is dominant in Earth's troposphere, becoming less important as pressure decreases with altitude. Doppler broadening depends on temperature, which governs the rate of thermal motion, and is significant throughout the atmosphere, becoming weak in the lower troposphere where pressure causes the mean free path of molecules to become small enough to limit thermal motion. The Voigt line shape is a convolution of the Lorentz and Doppler line shapes and depends on both temperature and pressure:

$$f_V(\tilde{\nu} - \tilde{\nu}_\circ) = (f_D * f_L)(\tilde{\nu} - \tilde{\nu}_\circ) \tag{3.9}$$

$$(f_D * f_L)(\tilde{\nu} - \tilde{\nu}_\circ) \equiv \int_{-\infty}^{\infty} f_D(\tilde{\nu}') f_L(\tilde{\nu} - \tilde{\nu}_\circ - \tilde{\nu}') d\tilde{\nu}' \tag{3.10}$$

$$f_V(\tilde{\nu} - \tilde{\nu}_\circ) = \frac{1}{\pi^{3/2}}\frac{\alpha_L}{\alpha_D}\int_{-\infty}^{\infty} \frac{1}{(\tilde{\nu} - \tilde{\nu}_\circ - \tilde{\nu}')^2 + \alpha_L^2} \exp\left[\left(\frac{-\tilde{\nu}'}{\alpha_D}\right)^2\right] d\tilde{\nu}'. \tag{3.11}$$

Other approximations to the line shape can be used, but improvements over the Voigt line shape cannot be resolved at ACE-FTS resolution.

A third broadening mechanism is natural line broadening and can be described by a Lorentz profile, as in Equation 3.5, with a natural broadening parameter given in the HITRAN line list. Natural line broadening reflects the inherent uncertainty of a molecule's energy level when undergoing spontaneous emission (or absorption) after occupying an excited state for a finite time. In Earth's atmosphere, the width of natural line broadening is insignificant compared to those of pressure broadening and Doppler broadening. However, due to the lower pressure and temperature of the Mars atmosphere, natural line broadening may play a larger role.

Limitations of an FTS are that it has a finite OPD and finite field-of-view. Finite OPD causes spectral lines to exhibit "ringing". In theory, the operation of an FTS assumes an infinite spectral range and infinitely long interferogram. In practice, the finite length of the interferogram is as if it were multiplied by a boxcar function. The Fourier transform of a boxcar function is a sinc ($\sin(x)/x$) function which is observed as ringing in the spectra (*Brault*, 1985). The lobes of each absorption line interfere with those nearby and must be properly modelled and accounted for. The sinc function is the ideal instrument line shape (ILS) and defines the FTS' response to monochromatic radiation. The finite

field-of-view broadens the ILS and may shift it to a lower wavenumber.

Phase errors occur while interferograms are recorded, resulting in asymmetry about ZPD. These errors result in no loss of information because the interferogram can be symmetrized by two methods which effectively correct the phase errors. A phase correction operator can be measured from the centreburst at ZPD, making the precise recording of a full double-sided interferogram unnecessary. There are, however, two advantages to recording the double-sided interferogram: OPDs are sampled symmetrically about the same mean time resulting in more accurate profiles when the source intensity varies, such as when the air mass changes rapidly in solar occultation mode, and the sensitivity of line positions to the accuracy of the phase correction is reduced (*Brault*, 1985).

For the complex spectrum $\hat{I}(\tilde{\nu}) = \hat{I}_R(\tilde{\nu}) + i\hat{I}_I(\tilde{\nu})$ the phase angle, $\phi(\tilde{\nu})$, can be calculated as:

$$\phi(\tilde{\nu}) = \arctan\left(\frac{\hat{I}_I(\tilde{\nu})}{\hat{I}_R(\tilde{\nu})}\right). \tag{3.12}$$

A phase correction in wavenumber space can be applied by multiplying the complex spectrum by $\exp(-i\phi(\tilde{\nu}))$, and is known as the Mertz method (*Mertz*, 1967). The mathematically equivalent Forman method can be done in the OPD domain (*Forman et al.*, 1966). A properly phase-corrected interferogram will be perfectly symmetric about ZPD and its Fourier transform will result in a purely real spectrum; the complex components arise from an asymmetric interferogram. ACE-FTS performs phase error corrections in wavenumber space (*Dutil et al.*, 2002).

Retrieving trace gas abundances from solar occultation spectra is done by fitting a computed spectrum to the measured data. A single occultation sequence generates a set of spectra at different tangent altitudes, and all are fit simultaneously. Achieving a good fit requires properly modelling the shape of each line (using physical and spectroscopic parameters), accounting for background and interfering components, and having the correct line depth. The depth is determined by the amount of the absorber, but includes contributions from multiple altitudes.

The retrieval strategy commonly used is to determine and fix as many parameters as possible prior to fitting the spectra, since the system may be underdetermined if insufficient *a priori* information is provided to ensure a unique solution. Pre-determining parameters is further advantageous since gas absorption coefficients depend on temperature and pressure. However, T, P and altitude are inter-dependent and must be restricted by the equation of hydrostatic equilibrium. The MATMOS team selected the GGG software suite (*Goldman et al.*, 1999), maintained at JPL, for performing retrievals. GGG was developed for the ATMOS Space Shuttle mission (*Norton and Rinsland*, 1991) and is

used by TCCON (*Wunch et al.*, 2011) and the MkIV balloon program (*Toon*, 1991). The ACE-FTS retrieval software, described in Sec. 4.1, relies on a combination of assumptions, *a priori* knowledge and data from models. Operating at another planet, these *a priori* profiles are unknown and models of the Mars atmosphere have not been developed to a suitable level for this purpose.

The main component of GGG is the GFIT subroutine which computes a spectrum over a small wavenumber window and compares it to the measured spectrum. Up to six gases can be varied simultaneously to obtain a best fit. A spectrum is calculated by determining the appropriate line strength of a vibration-rotation transition, convolving it with line shape functions, and then summing the contributions from all relevant transitions over the wavenumber range. Each absorption feature being fitted is a function of line strength, VMR, temperature, pressure and optical path, but only VMRs are varied during fitting.

The line strength of an absorption line with central frequency $\tilde{\nu}$ is determined from its line strength at a reference temperature ($T_\circ = 296$ K):

$$S(\tilde{\nu}, T) = S(\tilde{\nu}, T_\circ)\frac{Q(T_\circ)}{Q(T)}\frac{1 - e^{-hc\tilde{\nu}/kT}}{1 - e^{-hc\tilde{\nu}/kT_\circ}}\frac{e^{hcE''/kT_\circ}}{e^{hcE''/kT}}, \tag{3.13}$$

where the lower energy state of the transition, E'', is expressed in cm^{-1}, and $Q(T)$ is the total partition function (e.g., *Rothman et al.*, 1998). Line strengths at the reference temperature and broadening parameters are taken from the HITRAN linelist (*Rothman et al.*, 2013) with additional updates and corrections made by JPL (*Wunch et al.*, 2011).

The variables in GGG's state vector are ratios of the total slant column of a target gas deduced from the measurement to the *a priori* total slant column of that target gas. These are the VSFs, and are defined for a gas, G, as:

$$\mathrm{Column}_G = \mathrm{VSF}_G \int_l \chi'_G n ds \tag{3.14}$$

where the integral is taken over the slant path, s is the path variable, l is the optical path length, and n and χ'_G are the total number density and *a priori* VMR, respectively, which both vary along the slant path. In solar occultation geometry, once fitting has been performed, and if the altitude, pressure, and temperature are correct, then the slant paths of the actual column and the *a priori* column are the same. Therefore, the VSF can be treated as simply the ratio between *a priori* and true VMRs averaged over the ray path.

Equation 3.14 implies that only one VSF value is returned for all layers along the optical path, and this is a result of the current control flow of GGG. In past versions, GFIT

was applied using an onion-peeling[3] method (*Abrams et al.*, 1996), and a global-fitting method (*López-Puertas et al.*, 1992; *Rinsland et al.*, 1992). Currently, when applied to occultation spectra, GGG is run over a single spectral window at a time, and the results from each window used for a target gas are combined to compute average VMRs and then the vertical profile after fitting. For a given window, GFIT pre-computes the necessary absorption coefficients, then analyzes each spectrum separately using an optimal estimation method described in *Wunch et al.* (2011). Therefore, each spectral window in each spectrum is used to estimate a single and unique VSF which is then used to scale the entire *a priori* VMR vertical profile. When GGG is applied to a single spectrum (e.g., as for TCCON), a retrieved VMR vertical profile will have the same shape as the *a priori*. For occultation measurements (e.g., ACE-FTS and MkIV), the shape of the retrieved vertical profile is changed by using spectra recorded at multiple altitudes. A future version of GFIT, known as GFIT2, will implement a full optimal estimation scheme as described in *Rodgers* (2000) that will allow the retrieval of VSFs for each altitude from a single spectrum.

[3]An onion-peeling retrieval scheme is used to analyze each atmospheric layer individually and propagates results from the highest observed layer downward. Errors made during a layer's retrieval contribute to the retrievals from layers below.

Chapter 4

Temperature and pressure retrieval algorithms

In contrast to Earth-observing instruments, which can rely on accurate meteorological models, *a priori* information, and spacecraft position, Mars retrievals require a method with minimal reliance on such data. Accurate temperature and pressure are of critical importance to a MATMOS-like mission since the depth of solar absorption lines depends on these parameters. *A priori* temperature and pressure up to 40 km for TCCON, and for ACE-FTS analysis with GGG, are derived from the National Centers for Environmental Prediction (NCEP) reanalysis data. Above 40 km, the US standard atmosphere (*Committee on Extension of the U.S. Standard Atmosphere (COESTA)*, 1976) is used, which can deviate strongly from the true state of the atmosphere, especially at polar latitudes. Figure 4.1 shows a spectral fit to the CO_2 ν_3 vibration-rotation band by GFIT at high-altitude, where the *a priori* temperature differs from the ACE-FTS retrieved temperature by over 10 K. Because the best-fit spectrum was computed with an error in temperature, there are systematic errors in absorption line depth throughout the ν_3 band. GFIT underestimates line depths in the wings, and overestimates line depths in the band centre.

When used for trace gas VMR retrievals, the ACE-FTS and GGG methods perform spectral fitting over micro-windows encompassing only a few absorption lines. Performing fitting over a micro-window will result in matched absorption line depth between the measured and computed spectra, and the errors seen in Figure 4.1 will impact the retrieved VMR which is adjusted to compensate.

While the temperature and pressure on Mars have been monitored by instruments such as MCS for over ten Earth years, the accuracy, vertical resolution ($\sim$5 km), and spatial coverage are not suitable to provide *a priori* meteorological data for a MATMOS-

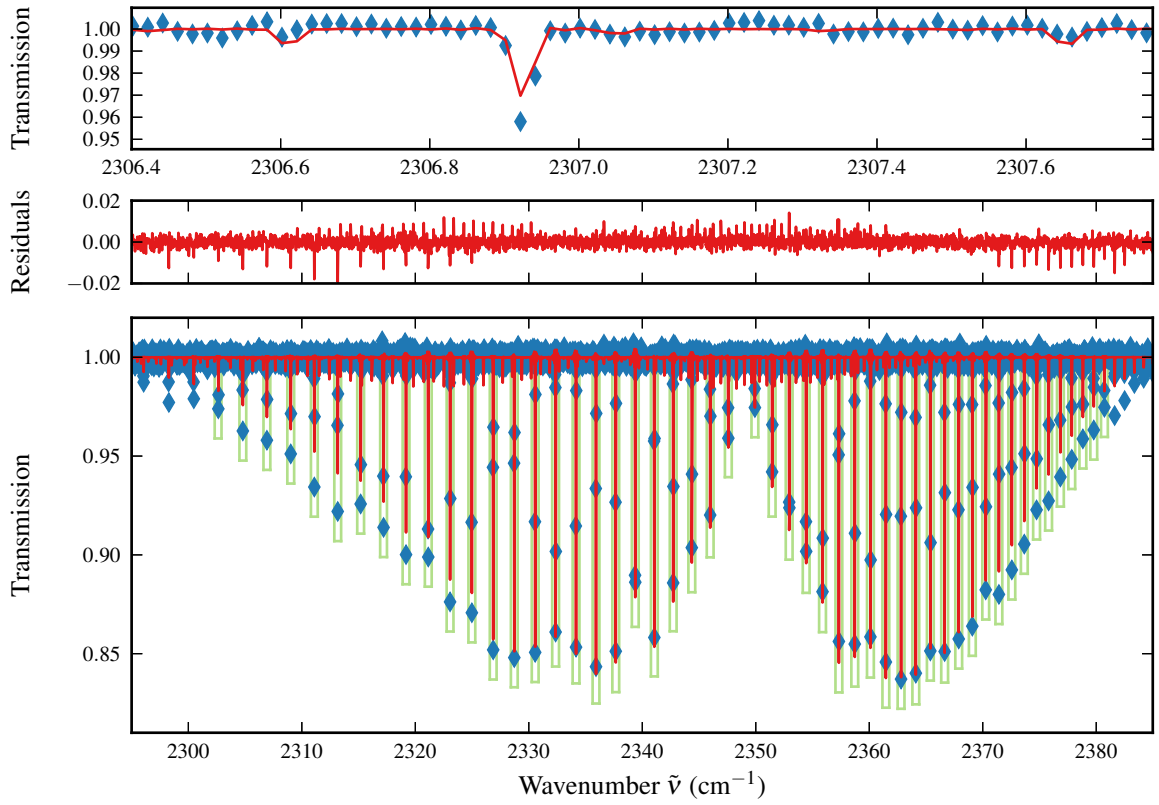

Figure 4.1: The CO_2 ν_3 spectrum from ACE-FTS occultation ss16000, from August 2^{nd}, 2006, over the Middle East, has been fitted with GGG at 115 km, where the *a priori* temperature values are not representative of the true state of the atmosphere (bottom panel). The middle panel shows the spectral residuals (measured − fitted). The blue diamonds are the measured data points and the red line is the fitted spectrum calculated by GFIT. The green boxes indicate the micro-windows used to fit individual lines for temperature and pressure retrievals. Atmospheric absorption lines have been broadened as described in Section 3.4 to the extent that an absorption line encompasses several spectral points, as shown in the top panel for a single line near 2307 cm^{-1}. Note that positive residuals centred near 2325 and 2350 cm^{-1} are due to another CO_2 vibration-rotation band ($01^11 \leftarrow 01^10$) that is not properly accounted for at this temperature and altitude.

like mission. The source of *a priori* temperature and pressure for a MATMOS-like mission would be a GCM for the atmosphere of Mars. Current Mars GCMs are not as well developed as those for Earth and do not have enough incoming input measurements to constrain their forward models for accurate real-time forecasting. For a MATMOS-like mission, the temperature and pressure of the atmosphere at the tangent points of the solar occultation line-of-sight will be retrieved from measured spectra to obtain the highest accuracy trace gas VMR vertical profiles possible. ACE-FTS retrieves temperature and pressure for terrestrial observations as well.

The algorithm employed by ACE-FTS to retrieve temperature and pressure relies on low-altitude meteorological data, precise knowledge of the vertical profile of the CO_2 VMR, and empirical and model-derived input parameters. My objective is to develop algorithms and software with minimal reliance on *a priori* data. Practical advantages of developing a new method are that it will be integrated into GGG, which has been adapted for Mars, while the ACE method is highly specific to Earth observations and the ACE-FTS instrument and may be challenging to adapt without key personnel on the ACE team. Section 4.1 describes the ACE-FTS retrieval method, Section 4.2.2 describes the new GGG temperature retrieval, and Section 4.2.3 describes the new GGG pressure retrieval algorithm.

This method exploits the temperature-dependence of individual absorption lines in vibration-rotation bands of CO_2. Spectral fitting is done over micro-windows containing CO_2 absorption lines with different ground state energies by varying the CO_2 VMR. This method requires *a priori* CO_2 VMRs, T and P, and its sensitivity to those *a priori* is discussed in Section 4.5.1. The fitting results for all windows encompassing a band are analyzed to deduce temperature and pressure. This technique is based on early ATMOS retrievals (*Stiller et al.*, 1995), but benefits from the broader simultaneously measured spectral range of ACE-FTS and MATMOS (allowing us to use more CO_2 bands and retrieve over the full altitude range) and advancements made to GGG (e.g., updated spectral parameters, line lists, and line shapes, but especially the ability to fit multiple gases in a window simultaneously, and no longer relying on onion-peeling method). I use a different mathematical treatment, a new scheme for determining a pressure profile, and a new restriction for maintaining hydrostatic equilibrium.

A set of 129 occultations recorded by ACE-FTS, representing different latitudes and seasons, were analyzed; they are discussed in Section 4.3 and results are shown in Section 4.4.1. COSMIC uses GPS radio occultation to obtain high-precision vertical profiles of temperature (*Anthes et al.*, 2008). Many of the ACE-FTS occultations presented in Section 4.3 were chosen to be coincident with COSMIC GPS occultations, using tight

coincidence criteria of 1 hour and 150 km. I use the COSMIC data product to independently validate my analysis, and an intercomparison is shown in Section 4.4.2.

4.1 ACE-FTS pressure and temperature retrievals

ACE-FTS retrievals are described in *Boone et al.* (2005) for version 2.2 (v2.2) and *Boone et al.* (2013) for version 3.0 (v3.0). Validation of ACE-FTS v2.2 temperature by *Sica et al.* (2008) revealed three issues with retrieved temperature profiles: unphysical oscillations in the mesosphere for some occultations, a systematic bias near 23 km related to an empirical function used to impose smooth behaviour in retrieved pressures below 23 km in v2.2, and a warm bias of around 3–6 K in the mesosphere. ACE-FTS v3.0 addresses the above issues with temperature. In October 2010, a change in the format of the outputs from the Canadian Meteorological Centre's (CMC's) analysis model introduced errors into the *a priori* pressure and temperature data used by the ACE-FTS retrievals, which impacted v2.2 and v3.0 results from that date onward. In ACE-FTS version 3.5 (v3.5), occultations since September 2010 have been reprocessed with the correct *a priori* pressure and temperature. Pointing information from SCISAT-1 is subject to systematic errors in timing, which necessitates determination of the measurement geometry from analysis of the ACE-FTS spectra. Comparisons presented here use ACE-FTS v3.5.

ACE-FTS P/T retrievals are divided near 50 km into a high-altitude regime, up to 120 km, and a low-altitude regime, down to 15 km. The retrieval proceeds in two stages, beginning with the determination of a crossover pressure near 50 km that serves as the boundary between the high- and low-altitude regions. The high-altitude retrieval is performed first, and includes the tangent pressure at the crossover level as a fitting parameter. The low-altitude retrieval follows with the crossover pressure fixed. The crossover pressure is refined, and P/T retrievals are repeated. The ACE-FTS retrieval follows these steps:

1. Calculate high-altitude tangent altitudes from satellite position.
2. Estimate low-altitude tangent altitudes from N_2 continuum.
3. Perform high-altitude P/T retrieval with the crossover pressure as a fitting parameter.
4. Refine low-altitude tangent altitude spacing using the equation of hydrostatic equilibrium.
5. Perform low-altitude P/T retrieval.

6. Refine the crossover pressure.
7. Repeat high-altitude P/T retrieval with the crossover pressure fixed.
8. Repeat low-altitude P/T retrieval.
9. Shift tangent altitudes to make P agree with low-altitude (15–25 km) meteorological data.

The high- and low-altitude retrievals both determine the temperature profile by fitting a set of spectral windows containing CO_2 lines with $1/T$ as a free parameter. They differ in how they determine pressure, tangent altitude, and the CO_2 VMR.

Prior to the retrieval, the crossover level between the high- and low-altitude retrievals is chosen. During the first pass of the high-altitude retrieval, pressure at the crossover level is fitted along with temperature. During the first pass of the low-altitude retrieval, a refined value for the crossover pressure is determined that yields the closest match to expectations for the highest calculated tangent altitude.

The high-altitude retrieval pre-determines tangent altitudes, pressures, and a portion of the CO_2 VMR profile. In the absence of conditions that would impact the alignment of the suntracker on the solar disk, such as clouds or significant refraction, relative pointing information can be accurately determined from knowledge of the satellite's orbital data, which is used to directly calculate tangent altitudes. Knowing the measurement geometry, the change in tangent pressure from one measurement to the next can be calculated by integrating the equation for hydrostatic equilibrium, taking into account the decrease in acceleration due to gravity with altitude and the changing average mean molecular mass. The altitude dependence of the mean molecular mass is determined from the outputs of the US Naval Research Laboratory (NRL) Mass Spectrometer and Incoherent Scatter (MSIS) radar model (NRL-MSISE-00) (*Picone et al.*, 2002). Beginning around 60 to 90 km, depending on the geolocation and season, CO_2 concentrations fall off with increasing altitude, making the *a priori* CO_2 VMRs less reliable. The CO_2 VMR is fixed to the *a priori* between the crossover pressure level and ∼70 km. Spectral fitting is then performed to determine the temperature profile with $1/T$, the crossover pressure, and CO_2 VMR above 70 km as parameters. An empirical function is used to describe the fitted CO_2 VMR profile above ∼70 km in order to force the results to exhibit smooth behaviour.

At low altitudes, *a priori* knowledge of the CO_2 VMR profile is relatively accurate, so it is fixed. A first guess of the tangent altitudes is made using the baseline ratio in the N_2 continuum level. Tangent altitudes below the crossover pressure level are determined

by integrating the hydrostatic equation downward from that altitude using the results of the high-altitude retrieval. Spectral fitting over a set of micro-windows containing CO_2 lines is done with both pressure and temperature ($1/T$) as parameters.

4.2 Retrieval technique

4.2.1 Tangent altitudes

As described in Section 4.1, the geometry at high altitudes is directly calculated from knowledge of the satellite's orbit, while the tangent altitudes at low altitudes are determined during the P/T retrieval through integration of the equation for hydrostatic equilibrium. This process yields good relative pointing information, but to obtain absolute pointing information, an altitude registration step is required. In v3.5, at the end of the P/T retrieval, all tangent altitudes are shifted by a common amount in order to have the retrieved pressures between 15 and 25 km match the *a priori* pressures from the CMC. Below 15 km, P and T are fixed to the *a priori* data from the CMC, and tangent altitudes in this altitude region are fitted using a set of $^{18}O^{12}C^{16}O$ spectral lines (*Boone et al.*, 2013).

Ideally, future iterations of an ACE-like FTS will have more reliable pointing information, allowing tangent altitudes to be determined independently of T, P, and gas VMRs. One method used by the MkIV balloon missions determines tangent altitudes from CO_2 lines (*Goldman et al.*, 1999). In GGG, tangent altitudes are computed geometrically from the solar zenith angle, and account for effects such as refraction. Corrections to tangent altitude in GGG are made by iteratively adding pointing offsets to the solar zenith angles until the retrieved CO_2 VMR profile matches the *a priori*.

The MkIV method works by fitting a set of strong CO_2 absorption features, and then estimating the fractional change in air mass that would occur for a 1° change in pointing angle. The result is the pointing offset required to return a CO_2 VMR that preserves the proper air mass along the optical path. Initially, retrievals from ACE-FTS spectra were done using these retrieved tangent altitudes. A known problem is that at low altitudes, where refraction is strong and optically thick clouds may be present, the retrieved tangent altitudes oscillate. Smoothing was done below 20 km using a polynomial fit to the tangent altitude time series to correct these oscillations. Figure 4.2 shows tangent altitudes for an ACE-FTS occultation computed from satellite ephemeris data by GGG, tangent altitudes retrieved using the MkIV software, and the smoothed retrieved tangent altitudes. There is a difference of around 5 km between the computed and retrieved tangent altitudes.

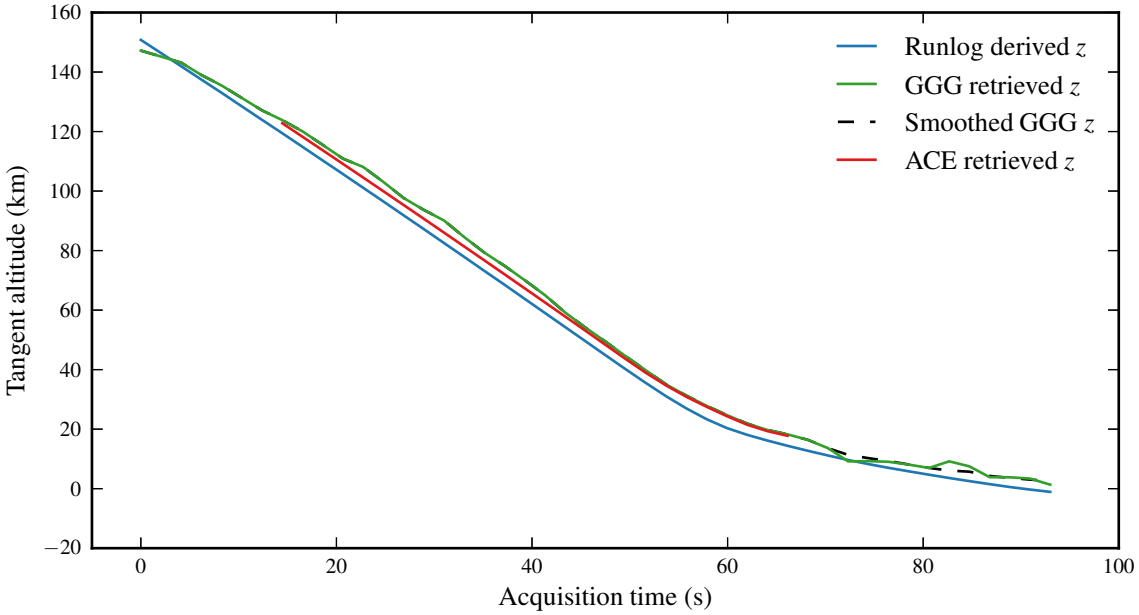

Figure 4.2: Tangent altitudes for ACE-FTS occultation ss16000 with mean altitude spacing of 4.3 km (interferograms recorded every 2 seconds). Initial tangent altitudes are computed by GGG using information in the ACE-FTS runlogs, these are shown in blue. Tangent altitudes retrieved using the MkIV method are shown in green. The low-altitude region oscillates and is smoothed, shown dashed black. The ACE-FTS retrieved tangent altitudes are shown in red and do not extend into the smoothed low-altitude region for this occultation.

Also shown in Figure 4.2 are the tangent altitudes retrieved by ACE-FTS, which agree very well with the MkIV/GGG retrievals between 20 and 60 km. At high altitudes, the MkIV retrievals are affected by weakening CO_2 absorption features, and the fall off of the CO_2 VMR which may not match the *a priori*. The observed low-altitude oscillations in the retrieved tangent altitudes may be real, a result of the suntracker attempting to locate the centre of the solar disk distorted by strong refraction, or partially obscured by clouds or the Earth's surface. Note that the ACE-FTS retrieval does not extend below 20 km, indicating difficulties in fitting, which may be due to total absorption of solar radiation in the fitting micro-windows, or interference from clouds.

For my application, I encountered two problems: (*i*) the MkIV method requires very accurate *a priori* CO_2, T and P; (*ii*) I are using the same data to first obtain tangent altitude, then T and P, which can iteratively be used to re-determine z, and so on. An iterative approach does not reduce uncertainties, can introduce unphysical oscillations, and is estimating too many unknown parameters from the same data.

These retrievals are very sensitive to altitude (since variations in altitude are effectively variations in T and P), and the MkIV method tended to yield a 0.5–1.5 km bias when compared to ACE-FTS retrievals. To avoid biases caused by altitude errors, I use ACE-FTS retrieved tangent altitudes instead. Ideally, a MATMOS-like mission would have better pointing information available, and a more accurate altitude determination scheme. MATMOS pointing information would have come from the absolute satellite pointing determined from star trackers, rather than movements in the suntracker mirror, MATMOS would hopefully not suffer from errors in time-keeping, and MATMOS would use an improved, four-channel solar imager. This provides a more direct comparison of temperatures retrieved here and by ACE-FTS, and I can be certain I are comparing temperatures estimated from a single spectrum at a given altitude, which becomes difficult when tangent altitude spacing is of the same order as tangent altitude uncertainty. A minimization scheme is used to determine the pointing offset that returns the ACE-FTS altitudes in GGG.

4.2.2 Determining temperatures

Rather than using T and P as fitting parameters, I developed a method to estimate T and P by analyzing the results of spectral fitting using CO_2 VMR as the adjusted parameter. A similar technique was first demonstrated by *Stiller et al.* (1995), and was used to determine temperature profiles from the ATMOS solar occultation FTS, deployed on the Space Shuttle for four missions (*Gunson et al.*, 1996; *Irion et al.*, 2002). I start by fitting

Table 4.1: List of CO_2 vibration-rotation bands used in P/T analysis. Each band's central wavenumber is given by *Rothman et al.* (1992) and the range is of the micro-windows used, which are predominantly between 0.2 and 0.32 cm^{-1}. Interfering species are gases with absorption lines occupying the micro-windows, but are also fitted by GGG. The effective altitude range is that over which absorption lines are strong enough relative to noise to be fitted, but not so strong that absorption is total over the range of the micro-window, and where the micro-window is not dominated by strong absorption by interfering species.

Transition	Central Wavenumber (cm^{-1})	Band Range (cm^{-1})	Windows Used	Primary Interfering Species	Effective Altitude Range (km)
$00^01 \leftarrow 10^00^a$	961.0	920.6–984.6	38	O_3, CCl_2F_2	12–62
$00^01 \leftarrow 02^00$	1063.7	1016.5–1095.0	49	O_3, H_2O	50–65
$03^10 \leftarrow 00^00^a$	1932.5	1888.7–1977.0	69	H_2O, O_3	22–70
$11^10 \leftarrow 00^00^a$	2076.9	2002.3–2127.6	89	O_3, H_2O, CO	25–86
$00^01 \leftarrow 00^00^{a,b}$	2349.1	2303.2–2382.8	53		60–140
$10^01 \leftarrow 02^00^a$	2429.4	2396.8–2457.8	41	N_2O, CH_4	30–50
$15^10 \leftarrow 00^00^a$	3181.5	3152.7–3221.7	32	O_3, CH_4, H_2O	10–35
$13^10 \leftarrow 00^00^a$	3339.4	3298.0–3381.9	50	N_2O, H_2O	12–60
$02^01 \leftarrow 00^00$	3612.8	3494.5–3646.4	94	H_2O, N_2O, O_3	45–109
$10^01 \leftarrow 00^00$	3714.8	3674.3–3743.7	45	H_2O	50–109

[a] Lines from this band were used by *Stiller et al.* (1995).
[b] CO_2 ν_3.

individual spectral lines in a CO_2 vibration-rotation band. I then exploit the temperature dependence of the absorption lines by looking at systematic variations in retrieved VMR as a function of the lower energy state of each line's transition in a band. Spectral fitting is performed for all altitudes and windows first, then followed by the analysis of retrieved VMR and energy states to derive a vertical profile of T. The following steps are taken to retrieve vertical profiles of temperature and pressure, and are explained in the following sections:

1. Spectral fitting of CO_2 lines is performed for ten CO_2 vibration-rotation bands with around 40 lines each.
2. Data quality criteria are imposed on resulting VMR scale factors (VSFs).
3. Temperature and pressure are computed for each band at each altitude.
4. Weighted means of T and P are calculated for each altitude to produce vertical profiles of T and P.
5. The altitude with the highest quality pressure retrieval is estimated.
6. The vertical profile of temperature is integrated above and below the altitude with the highest quality pressure retrieval.
7. A vertical profile of pressure is computed using the equation of hydrostatic equilibrium.

When GGG fits a computed spectrum to a measured spectrum over a spectral window, it varies the VMR of the target gases until a best fit is achieved. The result is the VSF for each target gas at each altitude, defined for some target gas, by the equation:

$$\text{Column} = \text{VSF} \int \chi' n_a ds, \tag{4.1}$$

where the left-hand side is the total column of the target gas along the slant path through the atmosphere, between the sun and the instrument, taking into account bending due to refraction. χ' is the VMR of the target gas, the prime notation indicates that it is an a priori quantity, n_a is the total number density, and s is the path variable. VSF is therefore the ratio between the true total column of gas, and that calculated by GGG. In solar occultation geometry, once fitting has been performed, and if the altitude, pressure, and temperature are correct, then the slant paths of the actual column and the a priori column are the same. GGG divides the atmosphere into homogeneous layers, calculates

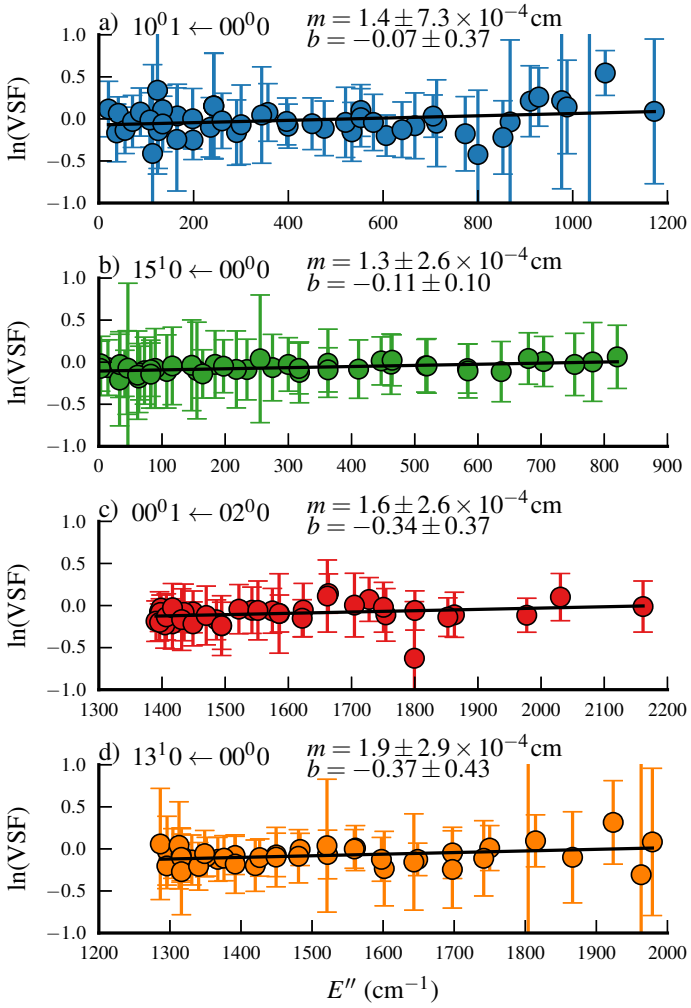

Figure 4.3: Example of ln(VSF) vs. E'' relationships for CO_2 bands that passed all quality criteria and were used to retrieve T. The four transitions are a) $10^01 \leftarrow 00^00$, b) $15^10 \leftarrow 00^00$, c) $00^01 \leftarrow 02^00$, and d) $13^10 \leftarrow 00^00$. These are from ACE-FTS occultation ss5211 on July 31st, 2004, over the Middle East, at an altitude of 38.1 km. Labelled for each band are the transition, slope m and y-intercept b of the best fit line.

the optical path for an observation, and accounts for the contributions from each layer. Therefore, the VSF is the ratio between a priori and true gas amounts averaged over the slant path, and we express the retrieved VMR as VSFχ'.

For transmission spectra, I can describe the depth of an absorption feature with the Beer-Lambert law:

$$I(\tilde{\nu}) = I_\circ(\tilde{\nu}) \exp\left[\sum_i -S(T_i) f(T_i, P_i, \tilde{\nu}) \chi_i (P_i/kT_i) l_i\right], \tag{4.2}$$

where the sum is of contributions from each layer of the atmosphere the solar ray passes through, i is an atmospheric layer, $I(\tilde{\nu})$ is the transmitted intensity at wavenumber $\tilde{\nu}$, $I_\circ(\tilde{\nu})$ is the incident intensity, $S(T_i)$ is the temperature-dependent line strength defined in *Rothman et al.* (1998), $f(T_i, P_i, \tilde{\nu})$ is the line shape function, k is the Boltzmann constant, and l_i is the optical path length. After fitting, I assume that the measured transmittance, $I(\tilde{\nu})/I_\circ(\tilde{\nu})$, is equal to the calculated transmittance, $I'(\tilde{\nu})/I'_\circ(\tilde{\nu})$, computed by GGG using a priori quantities and the VSF. I also assume that the line shape function, optical path length, and incident intensity for $I(\tilde{\nu})$ and $I'(\tilde{\nu})$ are equivalent ($f_i \equiv f'_i$, $l_i \equiv l'_i$, $I_\circ(\tilde{\nu}) \equiv I'_\circ(\tilde{\nu})$). I further simplify the expression for $I(\tilde{\nu}) = I'(\tilde{\nu})$ by assuming GGG has already accounted for the contributions from each layer i and obtain an expression for the retrieved VMR, VSFχ', at the altitude of the observation:

$$\text{VSF}_j \chi'_j = \frac{S(T_j)}{S(T'_j)} \chi_j \frac{P_j}{P'_j} \frac{T'_j}{T_j}, \tag{4.3}$$

where j represents the altitude of the tangent point of the optical path for an observation.

The ratio of line strengths is:

$$\frac{S(T)}{S(T')} = \frac{Q_R(T')}{Q_R(T)} \frac{Q_V(T')}{Q_V(T)} \frac{1 - e^{-\frac{hc\tilde{\nu}}{kT}}}{1 - e^{-\frac{hc\tilde{\nu}}{kT'}}} \frac{e^{hcE''/kT'}}{e^{hcE''/kT}}, \tag{4.4}$$

where the lower energy state of the transition, E'', is expressed in cm^{-1}, and $Q_R(T)$ and $Q_V(T)$ are the rotational and vibrational partition functions. The ratio of rotational partition functions can be expressed as simply T'/T for CO_2 and I argue that ratio of vibrational partition functions and the ratio of spontaneous emission terms ($1 - e^{-\frac{hc\nu}{kT}}$) are approximately equal to 1 for the differences between T and T' that I expect (on the order of 1 to 10 K). GGG uses an empirical model developed for TCCON to calculate the telluric *a priori* CO_2 profile as described in *Wunch et al.* (2011). I rely on the quality of the *a priori* CO_2 VMR profiles to remove the dependence on the true CO_2 VMR, χ,

from these equations by assuming $\chi/\chi' \approx 1$. The *a priori* VMR vertical profiles for other molecules were provided by TCCON, while *a priori* T, P and specific humidity vertical profiles up to 40 km were derived from NCEP reanalysis data (*Kalnay et al.*, 1996) (the US standard atmosphere was used above 40 km). With these assumptions, combining Equations 4.3 and 4.4 yields:

$$\ln(\text{VSF}) = \ln\left(\frac{\chi}{\chi'}\left(\frac{T'}{T}\right)^2 \frac{P}{P'}\right) + \frac{hcE''}{k}\left(\frac{1}{T'} - \frac{1}{T}\right). \tag{4.5}$$

The result is a linear relationship between ln(VSF) and E''. A set of spectral microwindows targets individual CO_2 absorption lines in a CO_2 vibration-rotation band. Each line is fitted at each observation altitude to determine the VSF and the linear relationship in Equation 4.5 is fitted using E'' values reported by *Rothman et al.* (2013). From the slope of the best fit line, I derive T, and from the y-intercept, I derive P.

In this study, 10 strong CO_2 bands were studied. Each band has its own effective altitude range, below which absorption may be total and above which absorption may be negligible. In some cases, interference from other molecules may hamper the CO_2 line fits. The bands used, and their effective altitude ranges and interfering molecules, are listed in Table 4.1. Because at certain altitudes, lines in some bands may be too weak to fit reliably, each band is analyzed separately. Least squares estimation is used, with each data point weighted using the propagated uncertainties returned from spectral fitting. I rely on these uncertainties to flag bad fits to VSF, and, thus, which bands are unsuitable for retrieving temperature at each altitude. At a given altitude, temperature, T, pressure, P, and their uncertainties, δT and δP, are computed for each band and then a data quality filter is applied to T values from each band to determine which results to use in a weighted mean. This is followed by a data quality filter on pressure. For temperature, I require $0 < \delta T/T < a$ and $|T - T'| < 25$, and pressure additionally requires $0 < \delta P/P < b$, with a and b determined empirically and subject to change, but usually < 1. Figure 4.3 shows typical ln(VSF) vs. E'' relationships for an altitude where four bands passed the data quality filter and were used to estimate T, with transitions, fitting results and uncertainties labelled. Error bars are the variance of the weighted mean.

After a vertical profile for T and P has been found, the method can be applied iteratively, using the retrieved vertical profiles as refined *a priori*. This was originally done by *Stiller et al.* (1995) for ATMOS. While there can be convergence issues with an iterative approach, as noted in Section 4.2.1, it may be used for a MATMOS-like mission. The ACE-FTS retrievals presented here were not done iteratively because of the high-

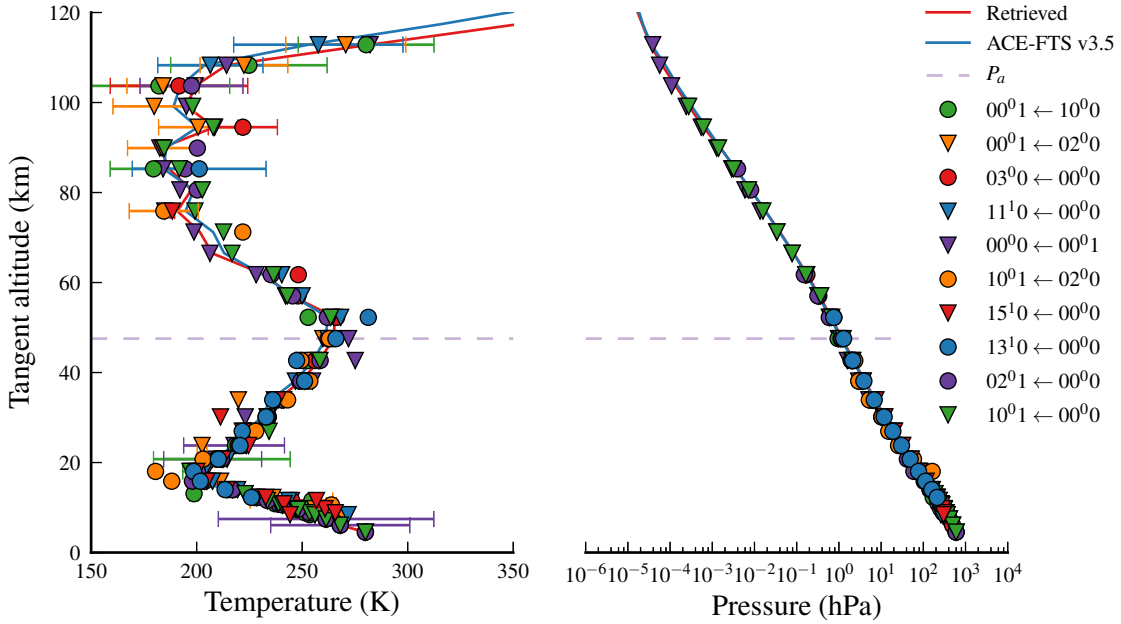

Figure 4.4: Retrieved T and P using all CO_2 bands at all tangent altitudes for ACE-FTS occultation ss5211. Each marker indicates a band that passed data quality criteria; no bands contribute at every altitude. The retrieved pressure profile (red line) is that computed from Equation 4.6 by integrating the retrieved temperature profile above and below P_a. The horizontal dashed line indicates the P_a level.

quality of the *a priori*. Iterating the retrieval too many times for ACE-FTS tended to introduce oscillations in the temperature profile, especially above 70 km, where our assumptions break down. For Mars, where the *a priori* will be less accurate, iterating the temperature retrieval may be beneficial.

After processing all 129 occultations, I assessed any biases between CO_2 bands, incorporated corrections into our software, and compared results of reprocessing with my original results. I investigated slope, intercept, retrieved T, and VSF, and their relationships with altitude, season, and retrieved and *a priori* temperatures for each band at every altitude and occultation. Any bias between bands is very small, and obscured by the spread of data, and insignificant compared to seasonal variations. For VSF, slope, and T, I computed the exponentially weighted mean at every altitude for all the fitting data and for each band. The ratio of each band's mean to the total mean was found and interpolated onto a 1 km grid to be used as a bias correction. The VSF ratios for each band were between 0.8 and 1.2 and tended to diverge at higher altitudes, while those for temperature were between 0.95 and 1.05. Means of slope were on the order of 10^{-3} leading to unstable ratios. The effect of incorporating a bias correction was negligible.

Using several CO_2 bands and a statistical approach to data quality control provides a robust retrieval method capable of retrieving T at all observation altitudes and for a variety of atmospheric conditions without extensive rewriting of retrieval software, nor highly specific retrieval procedures for a set of scenarios. Figure 4.4 shows vertical profiles of T and P retrieved using GGG compared to ACE-FTS v3.5 and the individual values retrieved from each band. This illustrates the spread of estimated T and P derived from different bands at each observation, the varying altitude range of the bands, and the effectiveness of the retrieval algorithm.

4.2.3 Determining pressures

Retrieving a vertical profile of pressure using Equation 4.5 can give unrealistic results and large discrepancies between CO_2 bands. One problem is that small errors in tangent altitude lead to large errors in pressure due to the exponential relationship between the two. Another is that varying T, P and z independently violates the assumption of hydrostatic equilibrium, which must constrain simultaneous retrievals of T and P.

A vertical profile of pressure is retrieved by first determining the pressure level with the highest retrieval quality, P_a, then integrating the retrieved T profile above and below this observation level and computing pressure from the equation of hydrostatic equilibrium:

$$P(h) = P_a \exp\left(-\frac{gM}{R}\int_a^h \frac{1}{T(z)}dz\right), \tag{4.6}$$

which is used to determine P at a given altitude, h, from P_a at altitude a. The acceleration due to gravity, g, and the mean molar mass of air, M, are left constant to keep the retrieval algorithm general and adaptable to other planets. R is the gas constant. P_a is restricted to altitudes between 18 and 52 km where T was retrieved. It is the level with the minimum standard deviations and fractional uncertainties of retrieved T and P.

Integration in Equation 4.6 is done by dividing the retrieved T profile into four layers (troposphere, stratosphere, mesosphere, thermosphere) at each inversion point and fitting a fifth order polynomial to $1/T(z)$ in each layer. The integrals are then evaluated exactly using the fitting coefficients. This method is used because spacing in z is non-uniform, there may be very large gaps in z between measurements, there may be discontinuities in T, or the domain of z may not be ordered. The latter can occur physically at low altitudes when tracking the centre of the solar disk is complicated by refraction affecting its shape, or by the horizon partially obscuring it. It can also occur at any altitude if the altitude spacing is tight and there are errors in retrieved altitude. This method

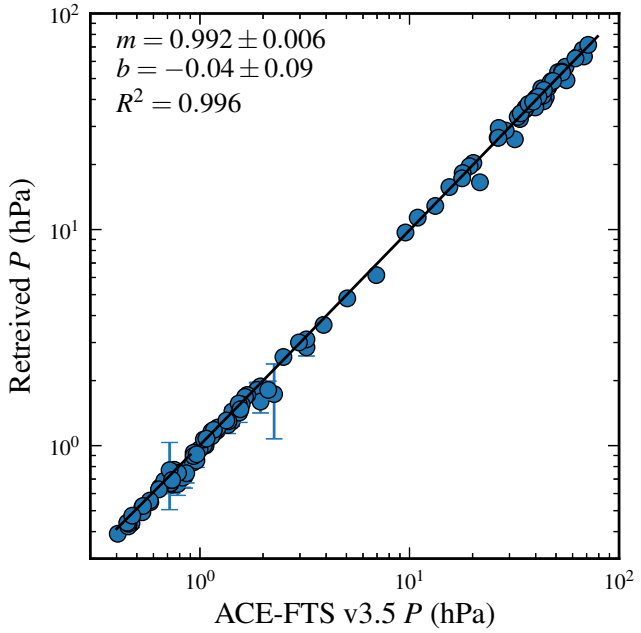

Figure 4.5: Correlation between retrieved pressure at the P_a level between this work (y-axis) and ACE-FTS v3.5 (x-axis) for 129 ACE-FTS occultations. The range of P values corresponds to the range of altitudes chosen by the retrieval algorithm to be the P_a level. Error bars are uncertainty in retrieved P_a.

also relaxes the restriction that the integrated function pass through every data point by weighting them according to uncertainty.

Since P is computed from the equation of hydrostatic equilibrium, as it is at higher altitudes in the ACE-FTS retrievals, there are only three factors that introduce deviations from ACE-FTS P, which is registered against meteorological data at low altitudes (*Boone et al.*, 2013): pressure at the P_a level, the T profile, and using constant M and g. Figure 4.5 shows the correlation between the retrieved P_a and the P used by ACE-FTS v3.5 at the same observation level for all 129 occultations in Section 4.3. The slope and intercept are 0.991 ± 0.007 and -0.01 ± 0.04, respectively, and the correlation coefficient, R^2, is 0.996. After retrieving P profiles, I investigated registration of tangent altitudes using ACE-FTS P profiles below 15 km and found that adjusting tangent altitudes to align pressure levels resulted in changes of < 0.1 km, so retrievals were left on the ACE-FTS altitude grid.

4.3 ACE-FTS data sets

The ACE-FTS v2.2 temperature product was thoroughly validated by *Sica et al.* (2008), which included a preliminary discussion about ACE-FTS v3.0 temperature. Comparisons were made against data from three lidar locations, 31 radiosonde locations, the SPectromètre Infra Rouge pour l'étude de l'Atmosphère par diodes Laser Embarquées (SPIRALE) balloon-borne spectrometer, and three satellite instruments: the Sounding of the Atmosphere using Broadband Emission Radiometry (SABER), the Michelson Interferometer for Passive Atmospheric Sounding (MIPAS), and the Halogen Occultation Experiment (HALOE). ACE-FTS v2.2 temperatures agreed with other sensors within 2 K in the stratosphere and upper troposphere, but exhibited a warm bias of 3–6 K in the mesosphere. A previous comparison with the Microwave Limb Sounder (MLS) found a larger bias of 5–7 K in the mesosphere (*Schwartz et al.*, 2008). An agreement between ACE-FTS v2.2, SABER, and MLS within 5 K in the tropopause and lower stratopause was confirmed while studying the Arctic winters by *Manney et al.* (2008), while differences of ±2 K were found between ACE-FTS v1.0 and sondes and lidar during the Arctic ACE validation campaign in 2004 (*Kerzenmacher et al.*, 2005). *Nowlan et al.* (2013) performed a temperature and pressure retrieval using measurements of the O_2 *A*- and *B*-bands made by the ACE-MAESTRO instrument on SCISAT-1 and compared their results to ACE-FTS v2.2 and sondes. The sondes matched ACE-FTS within 2–4 K, and ACE-MAESTRO and ACE-FTS had a mean difference of 5 K. *Mamun et al.* (2013) evaluated GEM by comparing simulated temperature and water vapour to ACE-FTS v2.2 and MLS and found an agreement of < 2 K in the troposphere and < 5 K in the stratosphere, but noted that GEM tended to agree more closely with MLS than ACE-FTS about the height of the tropopause and stratopause.

Validation of High Resolution Dynamics Limb Sounder (HIRDLS) temperature retrievals included a comparison with sondes, COSMIC and ACE-FTS v2.2 (*Gille et al.*, 2008). HIRDLS was found to be warmer than the sondes by 1–2 K and warmer than COSMIC by about 1 K between 15 and 40 km. HIRDLS tended to be warmer than ACE-FTS in the lower portion of that altitude range, and cooler higher, with differences of ±3 K. MIPAS temperature validation used ACE-FTS v3.0, but only found five coincident measurements during their measurement campaign (*Stiller et al.*, 2012). Temperature differences vary up to ±3 K, with maxima in the middle stratosphere, and there continued to be a bias at 23 km. A separate study examining MIPAS kinetic temperatures above 45 km observed ACE-FTS v2.2 to be consistently warmer than MIPAS above 50 km, with increasing magnitude to ∼10 K near 80 km (*García-Comas et al.*, 2012). An

Table 4.2: List of ACE-FTS occultation sets analyzed by GGG, showing the number of occultations each contains, their zonal coverage, season, and altitude spacing.

Set name	Set size	Longitude range	Latitude range	Mean z spacing	σ of z spacing	Time frame
Arctic 2010	30	unrestricted	62°–78°N	5.6 km	1.2 km	March 2010–Nov. 2010
Middle East	24	49°–87° E	28°–35° N	3.8 km	0.9 km	July 2004–Aug. 2010
Arctic Fall	16	unrestricted	62°–84°N	4.9 km	1.1 km	Sept.–Nov.; 2009–2010
Arctic Winter	23	unrestricted	56°–79°N	4.4 km	2.2 km	Jan.–Feb.; 2009–2012
Antarctic Spring	29	unrestricted	58°–84°S	4.3 km	1.3 km	March–May; 2009–2011
Low-Latitudes	7	unrestricted	34°S–27°N	3.2 km	1.1 km	April 2009–Feb. 2012

updated version of MIPAS temperature data was compared to ACE-FTS v3.0 by *García-Comas et al.* (2014), as well as SABER, MLS, the Optical Spectrograph and InfraRed Imaging System (OSIRIS), and the Solar Occultation For Ice Experiment (SOFIE). The new version generally exhibits 1–2 K better agreement with the other instruments below 80 km. MIPAS and ACE-FTS agree within 2 K below 80 km, except in summer, when differences are between −15 K and 3 K. They note that in the summer, between 40 and 60 km, MIPAS is 3 K warmer than ACE-FTS v3.0 than when they compared to ACE-FTS v2.2 in *García-Comas et al.* (2012). Though that study used an older version of the MIPAS data, they note that the difference is likely due to the changes between the two ACE-FTS versions since differences between the two MIPAS versions were smaller than the observed bias.

OSIRIS retrieved temperature profiles were compared to SABER, SOFIE, ACE-FTS v2.2, and ACE-FTS v3.0 (*Sheese et al.*, 2012). Comparison with ACE-FTS v2.2 and v3.0 found that ACE-FTS was 9 K warmer at 48 km, but less than 3 K warmer between 60 and 80 km. The region in the ACE-FTS v2.2 data noted to have a warm bias, 50–80 km shows an improvement of 0–2 K in the v3.0 data set. Validation of SOFIE was done using SABER, MLS, ACE-FTS v2.2 (*Marshall et al.*, 2011) and ACE-FTS v3.0 (*Stevens et al.*, 2012). SOFIE and ACE-FTS v2.2 agree within 2 K through the troposphere and stratosphere, SOFIE being warmer at the stratopause (3–5 K), and cooler through the mesosphere (4 K in summer). ACE-FTS v3.0 comparisons were done for the Arctic in July, and for the Antarctic between December and January. They exhibited the same trend as against ACE-FTS v2.2, but with differences of only ∼1 K. In general, ACE-FTS agrees with other instruments within 2–5 K, with v2.2 exhibiting a warm bias in the mesosphere of 3–6 K, and reduced to only 2 K in v3.0.

Six sets of ACE-FTS data were analyzed to provide different seasonal and zonal coverage. Details about the sets are provided in Table 4.2 and a complete list of ACE-FTS occultations used can be found in Appendix A. Five of the sets feature occultations selected in coincidence with COSMIC observations. The sixth set is of 24 occultations measured between 2005 and 2008 over the Middle East. The Middle East occultations generally have low β angles and have a mean altitude spacing of 3.8 km. They are all between 49 and 87° E longitude and 28 and 35°N latitude. The Arctic 2010 set consists of 30 occultations restricted to latitudes above 62°N measured in 2010, and 13 occultations are coincident with COSMIC measurements within 3 hours and 400 km.

The remaining four sets are composed of ACE-FTS occultations for which there are COSMIC coincidences within less than 150 km and 1 hour. Three of these sets also satisfy a seasonal and zonal restriction, while the fourth is composed of measurements over the tropics with no restriction on time of year. Occultations in this set, denoted Low-Latitudes, were chosen for their very high β angles and small vertical spacing (mean of 3.2 km) in order to examine whether tight altitude spacing strongly affected the quality of retrievals.

The Arctic Fall and Antarctic Spring sets were originally chosen to also examine the effect of altitude spacing. Arctic Fall occultations were measured during the months September, October or November in 2009 and 2010, and are above 62°N. Antarctic Spring occultations were measured during the months March, April or May, between the years 2009 to 2012, and are below 58°S. Arctic Fall originally consisted of 14 occultations with a mean z spacing of 3.2 km and standard deviation of 1 km, and Antarctic Spring originally consisted of 10 occultations with a mean z spacing of 5.5 km and standard deviation of 0.2 km. Smaller z spacing provides more information for interpolation to a 1 km grid, which is where comparisons to ACE-FTS are made, while large z spacing means the observation is made over a wide altitude range with varying temperature and pressure from the start of each spectral acquisition to its end. With these sets, however, no improvement to retrieval quality (large deviations from *a priori* or ACE-FTS retrievals) was found with tight z spacing. Quality issues were mostly the result of errors in tangent altitude and interpolation, which were later resolved. To improve the statistics of mean difference temperature profiles, I increased the size of these sets without a restriction in z spacing and also added the Arctic Winter set. Arctic Winter occultations are above 56°N, measured in the months of January or February between 2009 and 2012.

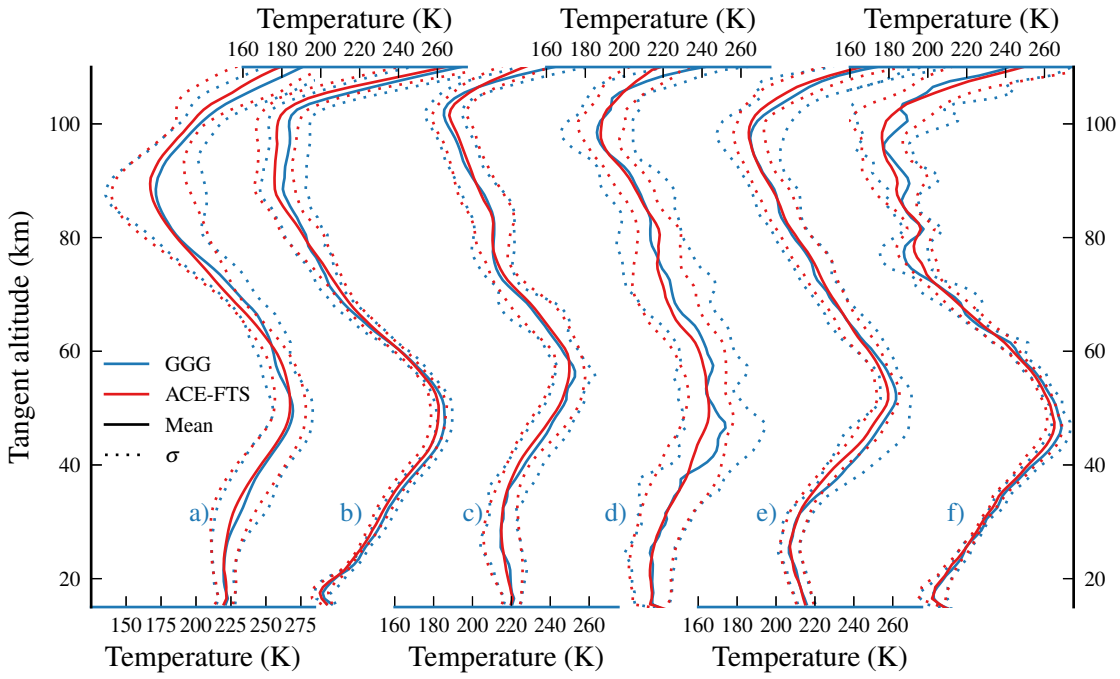

Figure 4.6: Mean T profiles for each set of occultations in Table 4.2: a) Arctic 2010, b) Middle East, c) Arctic Fall, d) Arctic Winter, e) Antarctic Spring, f) Low-Latitudes. Solid lines are mean T profiles for each set, and dashed lines are $\pm$ their respective standard deviations. The blue lines represent retrieved T profiles from GGG and the red lines represent ACE-FTS v3.5 retrievals. Means are computed on the 1 km interpolated grid, see Table 4.2 for the number of occultations in each set.

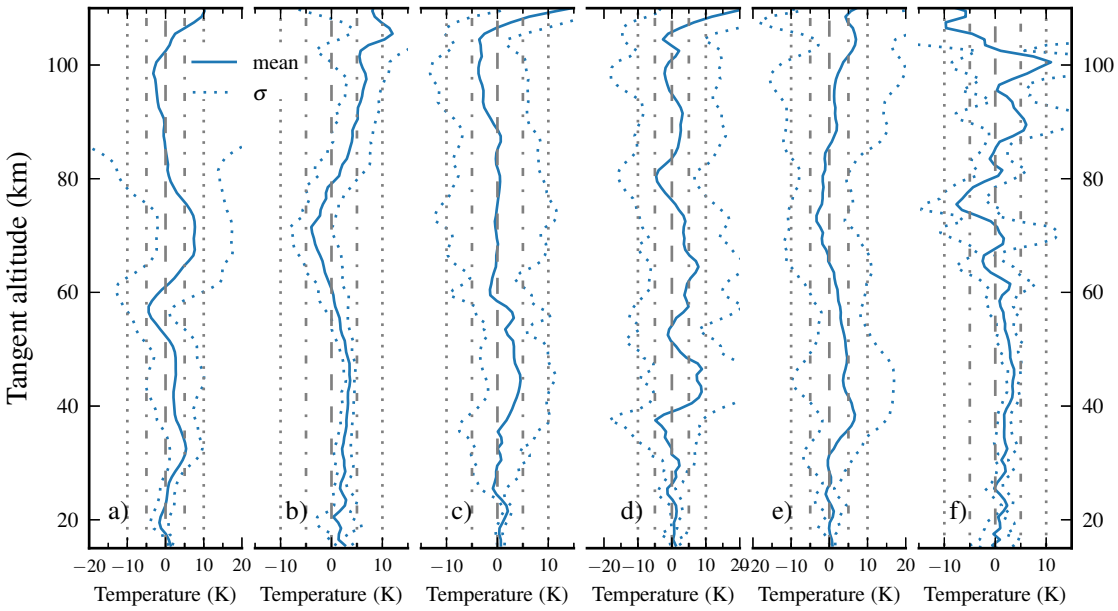

Figure 4.7: The mean of the differences between temperature profiles retrieved by GGG and ACE-FTS v3.5 (GGG − ACE) for each set of occultations in Table 4.2: a) Arctic 2010, b) Middle East, c) Arctic Fall, d) Arctic Winter, e) Antarctic Spring, f) Low-Latitudes. Standard deviations are shown as dashed lines ($\pm 1\sigma$).

4.4 Results

4.4.1 Retrieved T profiles and ACE-FTS comparison

Vertical profiles of T are interpolated onto an altitude grid with 1 km spacing for comparison, using a three-point, piecewise quadratic scheme. Over each set, I compute the mean and standard deviation at each altitude on the 1 km grid, at altitudes where ACE-FTS T retrievals were successful. The means and standard deviations of each set, for both ACE-FTS and GGG retrievals, are shown in Figure 4.6.

There are two sets comprised of warm, low-latitude occultations (Figures 4.6b and 4.6f): Middle East and Low-Latitudes. These are characterized by a sharper and lower-altitude tropopause, a lower stratopause, and small variability between occultations, as demonstrated by the small standard deviations in both ACE-FTS and GGG retrievals. The Low-Latitudes set exhibits the most structure at higher altitudes, 75–100 km, with the retrievals presented here having larger mean T variations with altitude than ACE-FTS, but with similar variability.

The Arctic 2010 set, Figure 4.6a, is not restricted to a single season, and thus has the largest variability. The Arctic Winter, Figure 4.6d, set is seasonally restricted, but also features large variability, especially at low altitudes. These profiles were all recorded in January or February, without any longitudinal restriction. They are mostly around 65°N, and all are over land. Four occultations are in the high Arctic, at latitudes between 73 and 79°N, and have tropopause temperatures of 200 K, whereas five occultations were recorded below 60°N and have tropopause temperatures of 220 K (although for these data sets the altitude of the tropopause is not clearly defined). Note the similar standard deviations from both ACE-FTS and GGG retrievals for the Arctic Winter set. A common feature of these profiles, occurring in 70% of them, is temperature oscillations above the tropopause, which is seen in the *a priori*, my retrievals, and the ACE-FTS retrievals. In the Arctic Winter set, the *a priori* T profiles have larger deviations from the ACE-FTS retrievals than in any other set, over 30 K near 50 km in some cases, which strongly affects my ability to reproduce the ACE-FTS retrievals due to the dependence in Equation 4.5. This is clearly visible in Figures 4.6d and 4.7d. The retrievals tend to have more T oscillations than ACE-FTS, and this can be seen in the mean profiles.

The Arctic Fall set, Figure 4.6c, has moderate variability, and the mean T profiles exhibit the best agreement between ACE-FTS and this work. The structure between 70 and 100 km is reproduced by both retrievals, while below 35 km, the ACE-FTS mean is smoother.

The Antarctic Spring set, Figure 4.6e, has polar measurements with large β angles,

and tight altitude spacing, which should improve retrievals due to the increased density of measurements. Deviations from the *a priori* or ACE-FTS retrievals tend to be less frequent and smaller, and those introduced by interpolation to the 1 km grid are eliminated. Small-scale structure is also better captured, which is especially important if there is uncertainty in tangent altitudes. These retrieved profiles exhibit more variability than those from ACE-FTS, and they tend to be colder in the mesosphere.

Figure 4.7 shows the mean of the differences between this work and ACE-FTS retrievals for each set, which are generally within ±3 K except at peaks in the mid-stratosphere and mid-mesosphere. Figures 4.7b and 4.7c have the smallest mean differences (GGG − ACE), less than ±5 K, followed by Figure 4.7e, which exceeds −5 K near 35 km, and Fig. 4.7f, which exceeds 5 K near 75 km. Figures 4.7a and 4.7d have the largest differences of around ±7.5 K at several altitudes. A similar structure appears in all six panels: the GGG profiles match ACE-FTS very closely in the troposphere, are consistently warmer in the mid-stratosphere, have zero crossings near 60 km in Figures 4.7a–f (which corresponds to the stratopause, 45–55 km, in Figures 4.6a–f), and are cooler in the mesosphere. The mid-stratospheric differences are around −4 K (except for Arctic Winter) and indicate a bias in my retrievals, since no bias in ACE-FTS retrievals at these altitudes has been indicated by other comparisons. In the mesosphere, I find GGG can be 3–5 K cooler than ACE-FTS, but not uniformly so. In this altitude range, there is a known warm bias observed in ACE-FTS v2.2 by *Sica et al.* (2008) and seen persisting in ACE-FTS v3.0 by *Sheese et al.* (2012) and *Stevens et al.* (2012), but reduced to only ∼2 K.

Figure 4.8 shows the mean of the differences for all 129 occultations, and has a shape as described above. Below 100 km, the mean (GGG − ACE) is between +5 K (in the mid-stratosphere) and −0.7 K (in the mesosphere) with standard deviations on the order of ∼10 K. The mean tends towards zero near 50 km, corresponding to the stratopause in Figure 4.6, but remains above zero, except at 80 km. Thus I confirm a warm bias in the GGG retrievals, stronger in the stratosphere. This bias was initially attributed to errors in altitude determination, as it appeared that the profiles were very similar, but that GGG temperatures were at lower altitudes than those of ACE-FTS. As detailed in Section 4.2.1, I attempted to mitigate altitude errors, but this did not fully resolve the bias. If these altitudes are correct, then the bias could be due to errors in my *a priori* T, P, or gas VMRs, which are chosen for each spectrum from the tangent altitude. The same *a priori* VMRs were used for all occultations, but CO_2 is constant below 80 km and only a few well-known molecules interfere in the windows used. The *a priori* T and P are unique for each occultation and would more likely produce random errors. When

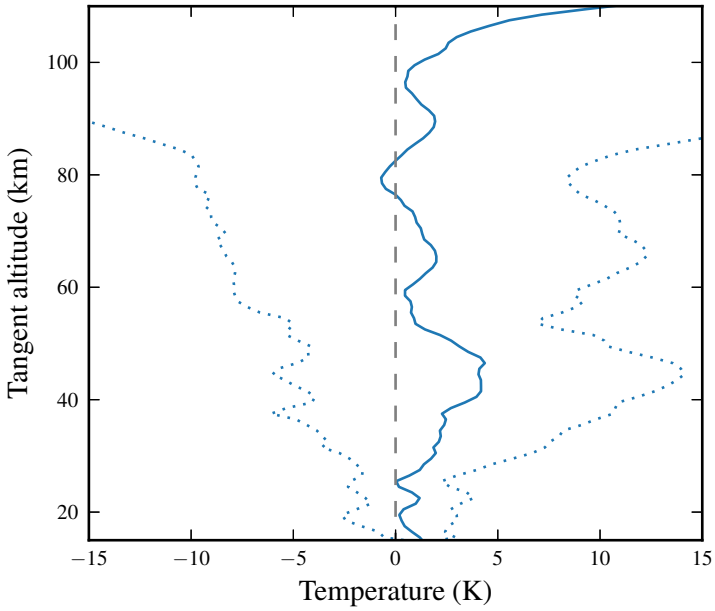

Figure 4.8: Mean and standard deviation of the differences in retrieved temperature between GGG and ACE-FTS v3.5 retrievals (GGG − ACE) for all 129 occultations in Figure 4.7. The largest difference occurs near 40 km and is mostly attributed to the Arctic Winter set, Figure 4.7d. The dotted line shows one standard deviation.

compared to the *a priori* used by GGG, ACE-FTS is predominantly 0.5 K cooler, except near 90 km, where ACE-FTS is 1 K warmer. It should be noted that 50 km is the altitude of the crossover pressure in the ACE-FTS retrievals, where a different retrieval scheme is used above and below. However, if the bias were in the ACE-FTS data, this would have been identified when performing P/T validation as in *Sica et al.* (2008).

4.4.2 COSMIC comparison

GPS signals passing through the atmosphere experience refraction, which causes a phase delay before being received by a COSMIC satellite. Vertical profiles of bending angle are obtained from the phase data, and are used to compute refractivity, which depends on T, P, water vapour, and electron density. The primary data products are high-resolution ($\sim$1 km) vertical profiles of T and water vapour pressure up to 40 km. The precision of the technique was verified by intercomparison after launch, while the six COSMIC satellites were in close proximity to each other (*Schreiner et al.*, 2007). COSMIC has been extensively compared to other data sets and is in close agreement with them, as summarized below, with only small biases.

COSMIC results have been compared to other GPS radio occultation satellites, the CHAllenging Minisatellite Payload for geoscientific research (CHAMP) and the Gravity Recovery and Climate Experiment (GRACE-A), and found to have consistent climatologies within 0.05% (*Foelsche et al.*, 2011). Over Antarctica, *Wang et al.* (2013) found COSMIC to be consistent with sondes, but to have a warm bias of 1 K when compared to satellite measurements made by the Advanced InfraRed Sounder (AIRS), the Infrared Atmospheric Sounding Interferometer (IASI), the Advanced TIROS Operational Vertical Sounder (ATOVS), and the Microwave Integrated Retrieval System (MIRS). Previous comparisons with sondes over Antarctica showed a 1–2 K cold bias (*Wang and Lin*, 2007), which was also seen in CHAMP. A comparison between CHAMP and COSMIC over Australia found only a 0.4 K mean temperature difference (*Zhang et al.*, 2011). Another sonde campaign with near global coverage also found that COSMIC had a cold bias (*Sun et al.*, 2010), but it was less than 1 K and consistent with *Wang et al.* (2013). COSMIC T validation has recently been reported by *Das and Pan* (2014) against SABER and MLS. COSMIC was found to be 3–4 K colder than SABER at low altitudes (10–20 km), but increasing steadily to more than 5 K warmer above 40 km. MLS and COSMIC agreed within 3 K, and no bias towards season or latitude was shown for either MLS or SABER. *Gille et al.* (2008) compared HIRDLS to COSMIC and ACE-FTS v2.2 and also found COSMIC to be about 1 K colder than both instruments (see Section 4.3). COSMIC has

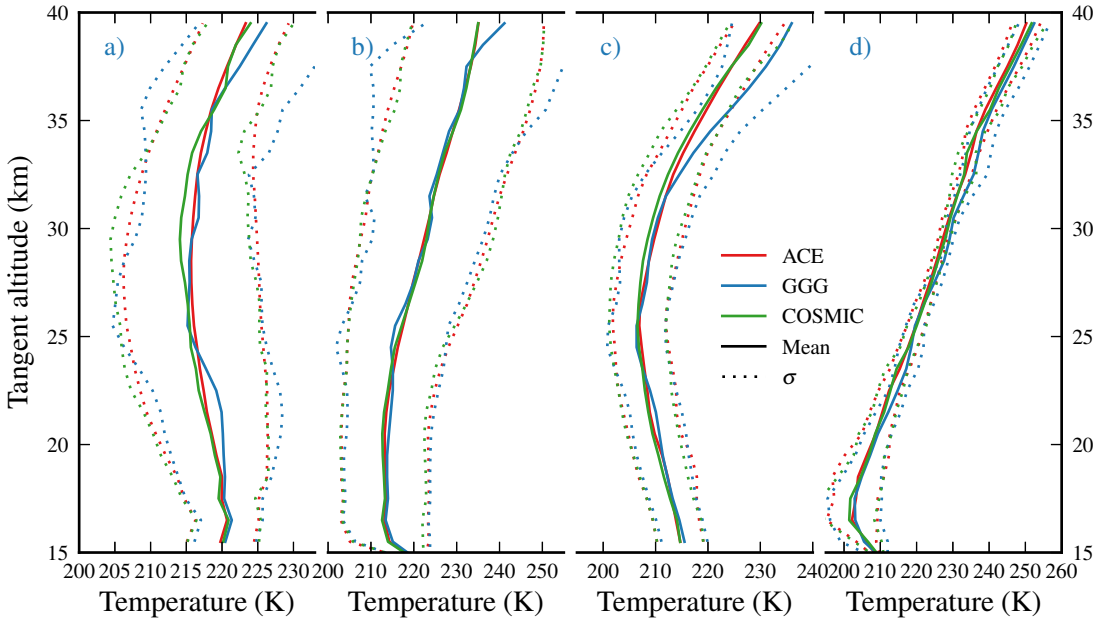

Figure 4.9: Mean temperature profiles and standard deviations retrieved by ACE-FTS v3.5 (red), GGG (blue), and COSMIC (green) for sets: a) Arctic Fall, b) Arctic Winter, c) Antarctic Spring, and d) Low-Latitudes. Means are solid lines, and standard deviations are dashed. 40 km is the maximum altitude of the COSMIC data set.

also been compared to several data assimilation products which revealed a 2 K temperature bias, but warm in the northern hemisphere, and cold in the southern hemisphere (*Kishore et al.*, 2009). COSMIC has been shown to agree closely with sondes and satellite instruments within less than 1–3 K, but the differences are consistently with COSMIC colder.

Vertical profiles of mean temperature for all COSMIC radio occultations coincident with ACE-FTS solar occultations are shown in Figure 4.9, divided seasonally and zonally as in Table 4.2, alongside ACE-FTS v3.5 and profiles retrieved from ACE-FTS by GGG. Comparing GGG to ACE-FTS v3.5, I see that GGG is warmer than ACE-FTS except around 25 km, the altitude of a known feature in the ACE-FTS v2.2 data product caused by the empirical function used to determine pressure in this region. It is discussed in *Sica et al.* (2008) and seen in other comparisons (e.g., *Gille et al.*, 2008) with v2.2 data. This effect has been reduced in the v3.0 and v3.5 data products(*Boone et al.*, 2013), but was still noted by *Stiller et al.* (2012). In Figure 4.9 there is no discernible feature in the ACE-FTS v3.5 profiles, while the GGG profiles are seen to oscillate about the ACE-FTS and COSMIC profiles in all four panels.

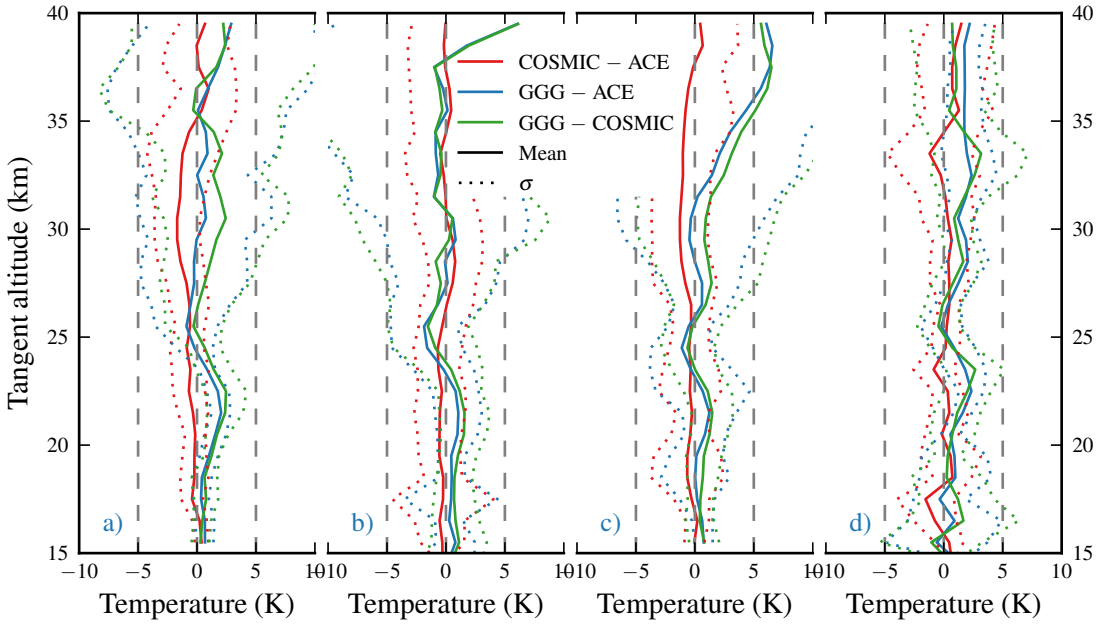

Figure 4.10: The mean of the differences between temperature profiles and standard deviations retrieved by GGG, ACE-FTS v3.5, and COSMIC for sets: a) Arctic Fall, b) Arctic Winter, c) Antarctic Spring, and d) Low-Latitudes. Shown are COSMIC − ACE (red), GGG − ACE (blue), and GGG − COSMIC (green). Means are solid lines, and standard deviations are dashed.

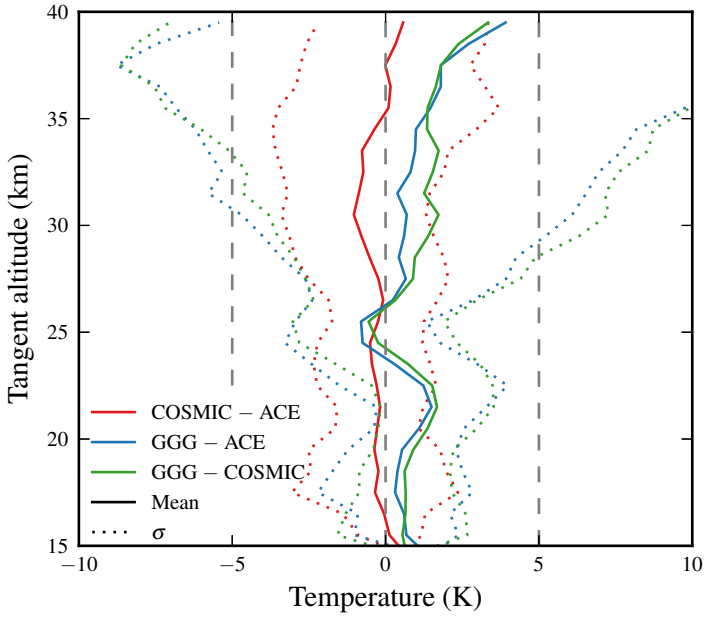

Figure 4.11: Mean and standard deviations of the differences in retrieved temperature between temperature profiles retrieved by GGG, ACE-FTS v3.5, and COSMIC for all 74 occultations in Figure 4.10. Shown are COSMIC − ACE (red), GGG − ACE (blue), and GGG − COSMIC (green). Means are solid lines, and standard deviations are dashed.

In the lower stratosphere and upper troposphere, the shapes of mean T profiles in the four zonally and seasonally restricted data sets are very different, featuring different tropopause heights and lapse rates. The mean differences between these retrievals with GGG and the COSMIC and ACE-FTS v3.5 data products share a consistent shape, shown in Figure 4.10. There are no significant dependencies on latitude or season in these T differences. I see that GGG is warmer than COSMIC by < 2 K below 24 km, where COSMIC is known to be cold, GGG is consistently cooler than COSMIC between 24 km and 30 km by 1–4 K, and GGG is again warmer than COSMIC by 3–5 K between 30 and 40 km. The closest agreement with COSMIC is seen in the Low-Latitudes set, Figure 4.10b, where the differences are between -1.7 to 0.9 K, while the largest differences are seen in the Antarctic Spring set, Figure 4.10c, with maxima of -6.5 and 3.5 K.

Considering all 72 occultations in these four data sets without restriction, shown in Figure 4.11, I find the ACE-FTS v3.5 and the COSMIC data products agree with each other within -0.9 to 0.5 ± 0.3 K, with COSMIC predominantly exhibiting a < 0.5 K cold bias. This agrees with previous results in which ACE-FTS and COSMIC both show close agreement with sondes within a few K, but with COSMIC generally having a small

cold bias relative to other data products, as discussed above. The difference between the GGG retrievals and those from COSMIC reflects that where GGG deviates from ACE-FTS v3.5, GGG also deviates from COSMIC. However, below 30 km GGG has the best agreement with ACE-FTS, where mean differences are within −2 to 3 K.

4.5 Discussion

4.5.1 Retrieval sensitivity

The motivation behind the method for retrieving P/T vertical profiles presented here was to reduce the reliance on high-quality *a priori* quantities and model input that the ACE-FTS retrievals use. Spectral fitting requires *a priori* vertical profiles of temperature, pressure and trace gas VMRs to compute a first-guess spectrum. When used for spectra recorded from the surface, such as for TCCON, GFIT scales the VMR vertical profiles, so errors in their shape lead to errors in the retrieved profile (*Wunch et al.*, 2011). For solar occultation applications, the shape of the VMR vertical profile below the highest observation altitude will be allowed to change since measurements are made at all altitudes and trace gas retrievals should not be sensitive to the *a priori* VMRs (*Boone et al.*, 2005). *A priori* profiles closer to the true state of the atmosphere can reduce errors in retrieved gas VMR, however, by increasing the speed of convergence, especially when spectral lines from interfering species overlap. The quality of fit, and therefore the trace gas retrieval, is more sensitive to the spectral micro-windows used than to the *a priori* VMR profiles.

The methods presented here for P/T retrievals specifically rely on the *a priori* vertical profiles of CO_2 VMR, T and P. Retrievals are done by fitting CO_2 lines using an existing profile. As with other trace gas retrievals, fitting results should not be sensitive to the CO_2 *a priori*, if the fits are good, and assuming the VSF for CO_2 is not unity. CO_2 in the Martian atmosphere is well mixed and its vertical profile is nearly constant up to 80-100 km, similar to on Earth (e.g., *Forget et al.*, 1999). Its VMR is around 95%, making it ideally suited for use in P/T retrievals, since it will have strong absorption features and minimal interference from other gases. It has also been closely monitored by multiple spacecraft for over a decade. ExoMars TGO was to include an updated version of Mars Reconnaissance Orbiter's Mars Climate Sounder, called EMCS, to continue these measurements. EMCS would have used a different viewing geometry than MATMOS and would not make co-located measurements of the same air mass, and therefore could not provide *a priori* temperature and pressure data. *A priori* profiles for the MATMOS

mission were to have been provided by the CMC's Global Environmental Multiscale Model (GEM), which would be continuously constrained by new observations.

Accurate T and P *a priori* profiles have a higher impact on retrieval quality than CO_2 VMR since T is directly computed from the *a priori* T in Equation 4.5. The sensitivity of the retrievals to the *a priori* temperature was tested using Earth-observing spectra by perturbing the *a priori* temperature profile by ± 5, ± 10, and ± 20 K (with random noise added within 3 K of the perturbation). Systematic errors in the *a priori* T of around ± 5 K had little effect on the retrieval T, except at altitudes greater than 80 km, where oscillations were increased or amplified. Systematic errors in the *a priori* T greater than 10 K reduced the stability of the retrieval and led to unphysical oscillations at all altitudes. Fewer CO_2 vibration-rotation bands passed quality criteria at each altitude as well. Aside from the dependence on *a priori* temperature in Equation 4.5, the spectral fits also depend on temperature. Spectra computed at the wrong temperature have incorrect line strengths and cause a fit to result in an incorrect VSF. At Earth, a priori errors on the order of 10 K are expected to occur only at very high altitudes, above 70 km. At such altitudes, the retrieval algorithm presented is impacted by weaker absorption by CO_2 as density decreases, loss of accuracy in the a priori CO_2 VMR as it falls off, and the departure from local thermodynamic equilibrium.

Application of this method to a mission to Mars will strive to provide the highest quality *a priori* temperature possible from observations and models, and this method is intended to improve those *a priori* for use in trace gas retrievals. The method's dependence on pressure is less severe since pressure is constrained by the equation of hydrostatic equilibrium. Pressure does not vary strongly diurnally, unlike temperature, and though it varies seasonally, this retrieval scheme is independent of surface pressure.

The initial objective of a MATMOS-like mission would be trace gas detection, which would be initially achieved using spectral absorption features and fitting, followed by an estimation of their abundances, and then vertical profiles. Throughout the duration of the mission, the retrievals would continue to be developed and improved, including updating the *a priori* and spectral windows. Deducing the vertical distribution of target gases will be the most challenging aspect of a MATMOS-like mission, especially at higher altitudes where P/T retrievals become more difficult. The low pressure and density of the Martian atmosphere and low expected VMRs of target gases will result in very weak absorption features, while the assumptions of hydrostatic equilibrium and local thermal equilibrium also become less valid at higher altitudes. The vertical range through which each of the ten CO_2 bands used is effective is chosen automatically by the P/T retrieval algorithm based on fitting uncertainties. Once a MATMOS-like mission is underway, a

qualitative examination of the effective altitude range of each band could be performed, and fitting could be restricted to those altitudes to improve retrieval stability and speed.

4.5.2 Future work

The software developed for this work and GGG are far from finished products. ACE-FTS is still releasing updated data products after over ten years of development and TCCON releases new versions of GGG regularly. Routine developments include window selection, data quality monitoring, and finding and fixing systematic problems as data is processed. By the time a MATMOS-like mission reaches Mars, GGG will have an updated line list, improved spectroscopy, including updated line shape parameters and line shape modelling (e.g., incorporating line mixing), and numerous bug fixes and performance improvements. GCMs will be more advanced, featuring more complex physics and incorporating results from the ExoMars mission in its current form. Regarding temperature and pressure retrievals, I have identified three aspects that should be addressed in the lead up to a future MATMOS-like mission that could improve accuracy.

The modelling of dust in GGG is based on laboratory spectroscopy done in the mid 1990's. Since then, several orbiting and landing spacecraft have visited Mars, learning a great deal about the size distribution and composition of airborne dust. The dust absorption model in GGG can be updated to reflect new observations, and new laboratory spectra can be obtained prior to a mission. Longer-term goals would be to write new software for modelling the dust that is separate from gas absorption line modelling, such that the dust model is more realistic and includes parameters, such as single scattering albedo, particle size distribution, or composition, which may then be retrieved.

A major benefit of this work compared to that done with ATMOS by *Stiller et al.* (1995) is the spectral ranges of ACE-FTS and MATMOS, which allow one to use ten CO_2 vibration-rotation bands in their entirety. In each band, a spectral line can only be resolved well enough at certain altitudes to be used for T and P retrievals. An absorption line may otherwise be too weak, obscured by an interfering gas, or the absorption may be total, as is the case terrestrially for the ν_3 band below 60 km. The algorithm presented here uses the fitting uncertainty to estimate whether a line was well enough resolved. A more prudent approach would be to set altitude ranges for each CO_2 absorption line micro-window[1] to be fit and used for T and P retrievals. Currently, the GGG software flow, the way GFIT is executed and input files are used, prevents this from easily being accomplished. A front-end program, written in Python or as a set of Bash scripts, could

[1]Not each CO_2 band, but each line in the bands, since weaker lines in the wings disappear at a lower altitude than those in the branch centres.

accomplish this by using a log table of absorption line altitude ranges and the GGG input files that include spectrum names and retrieved tangent altitudes. It would need to re-write the window list and runlog for each absorption line, which caries a risk of data loss since those files are stored with the GGG source code rather than with retrieval outputs. Determining the line altitude ranges for ACE-FTS has little application to a mission for Mars due to differences in pressure and gas abundance. This is best done as a software update after spectra are recorded at Mars, and may need to depend on the dust level.

The data quality criteria applied during the retrieval may be optimized for atmospheric conditions and altitude. For temperature, I require $0 < \delta T/T < a$ & $|T - T'| < 25$, and pressure additionally requires $0 < \delta P/P < b$, with a and b determined empirically and usually < 1. This would require a much larger sample of occultations than used in this study, and should be done when the software is being used for production and include spectra recorded at Mars.

4.6 Conclusions

A new technique to retrieve vertical profiles of temperature and pressure from high-resolution infrared solar occultation spectra has been developed, with the intention that it finds application on a future Mars mission. I have demonstrated the technique's success and evaluated the quality of the retrievals by comparing with two satellite data products: COSMIC and ACE-FTS v3.5. Pressure is constrained by the equation of hydrostatic equilibrium and retrieved values are closely correlated to those from ACE-FTS v3.5.

I find that GGG temperature retrievals are predominantly warmer than ACE-FTS by 2 K in the troposphere, up to 5 K in the stratosphere, and between -3 and 1 K in the mesosphere. The largest deviations occur at the tropopause and stratopause, which can occur at different altitudes. No seasonal or zonal biases are found. I find very good agreement between ACE-FTS v3.5 and COSMIC, with mean differences of < 1 K below 40 km. COSMIC has been found to have a cold bias, consistent with other profile comparisons. When GGG is compared to COSMIC, mean differences are within -2 and 3 K below 35 km. GGG is warmer than COSMIC at all altitudes except near 25 km.

The objective was to develop a technique with minimal reliance on high-quality *a priori*, model input, or empirical functions. With suitable refinement to the application of Martian solar occultation, this technique will be capable of retrieving accurate temperature and pressure profiles, enabling definitive detection of several trace gases in the atmosphere of Mars.

Chapter 5

Mitigating the effects of dust

Solar absorption spectroscopy is affected by airborne aerosols, which absorb and scatter incoming solar radiation. These often take the form of thin clouds, water vapour, pollution, and smog. In the case of ground-based observations, these conditions may change during the day, and lead to biases in retrieved VMRs that may vary between measurements. While making remote sensing observations from orbit, the optical path observed by the instrument changes during acquisition, and if the line-of-sight passes through atmospheric layers with varying aerosol loading, the aerosol optical depth may also change during acquisition.

A challenge of applying the ACE-FTS technique to the Martian atmosphere is the presence of suspended dust particles. Dust storms occur frequently on Mars, can be global in scale, and can elevate dust to altitudes above 50 km (*McCleese et al.*, 2010; *Guzewich et al.*, 2013a). With ACE-FTS, the treatment of interference from aerosols involves the use of retrievals from altitudes with clear skies, or specific studies of cloud properties (e.g., *Eremenko et al.*, 2005; *Dodion et al.*, 2007) or dust events (e.g., *Sioris et al.*, 2010; *Doeringer et al.*, 2012). However, on Mars, the extent of the dust layers can be too large to discount, while the duration of dust events can last the majority of a proposed mission length (*Cantor et al.*, 2010; *Korablev et al.*, 2014), so retrieval algorithms for an ACE-FTS-like instrument at Mars must be able to derive trace gas VMR vertical profiles from a dusty atmosphere.

Keppel-Aleks et al. (2007) proposed a now-widely-used technique to mitigate the effects of source intensity variations (SIV) for TCCON. The Greenhouse gases Observing SATellite (GOSAT) Thermal And Near infrared Sensor for carbon Observation (TANSO) FTS uses a similar technique (*Kuze et al.*, 2012). Both techniques Fourier transform a raw interferogram, apply a high-pass filter, perform an inverse Fourier transform, and divide the raw interferogram by the filtered interferogram. This requires knowledge of

the DC signal level and cannot be applied to AC-coupled interferograms, which are commonly recorded due the requirements of specific ADCs used on the ground (e.g., *Warneke et al.*, 2010; *Petri et al.*, 2012) and from orbit (e.g., *Bernath et al.*, 2005; *Kleinert et al.*, 2007). If operating an ACE-FTS-like instrument at Mars, DC coupling will be a necessary requirement to measure and mitigate changes in the incoming solar signal.

On Mars, the amount of dust along the optical path can vary significantly over the altitude range tracked during a single interferogram acquisition (1–6 km, depending on β angle), especially at the boundary of a dust layer. I generated synthetic spectra to simulate Mars atmospheric conditions, transformed these spectra into interferograms, and added DC signals. To simulate continuous acquisition, each interferogram was perturbed using the interferograms and DC levels of the measurements from the previous and next tangent height. I then investigated three methods to recover transmission spectra and compared them to the original synthetic spectra.

Section 5.1 provides a brief overview of measurements made related to suspended dust. In Section 5.2, I describe the creation of synthetic spectra for the Mars atmosphere, their transformation into interferograms, and the SIV perturbation applied. In Section 5.3, I present the SIV mitigation strategies that were investigated, and in Sections 5.4 and 5.5 I discuss comparisons of spectra and gas retrievals between the original synthetic spectra and those influenced by SIVs.

5.1 Mars atmospheric dust

Early observations of the optical properties of dust on Mars came from the Viking landers (*Pollack et al.*, 1977). *Toon et al.* (1977) and *Pollack et al.* (1979) developed models for Mie scattering by non-spherical particles to interpret the observations and estimated the dust particle size distribution during global dust storms. They found that the number of parameters in the scattering model could be reduced by assuming the dust's composition. In preparation for incoming data from the MGS mission, new models were proposed. *Clancy et al.* (1995) used spectroscopic measurements of samples of palagonite to estimate the new mean effective radius and distribution of dust observed by the Viking landers. *Pollack et al.* (1995) introduced a new model that assumed no mineralogy. The model was generalized to be wavenumber-dependent (*Ockert-Bell et al.*, 1997) and to include radiative transfer calculations (*Forget*, 1998), and was applied to several data sets collected by the Viking and Mariner missions to estimate the particle size distribution, shape, single scattering albedo, and complex indices of refraction. These models were applied to new data with the arrival of Mars Pathfinder (*Tomasko et al.*,

1999; *Markiewicz et al.*, 1999).

When MGS arrived, the TES instrument emission phase function measurements in the infrared were used to deduce the complex optical constants without Earth-analog materials, and to derive dust extinction optical depth and effective particle size. The size of the MGS TES data set allowed trends in both parameters to be observed (*Clancy et al.*, 2003; *Wolff and Clancy*, 2003; *Korablev et al.*, 2005). Further refinements of dust properties were made by combining upward-viewing Mini-TES observations with those from MGS TES (*Wolff et al.*, 2006). Instruments on MEX continued to be used to retrieve the effective radius of dust, its distribution (*Montmessin et al.*, 2006; *Rannou et al.*, 2006), and its single scattering albedo (*Vincendon et al.*, 2008; *Määttänen et al.*, 2009b), and finally to measure the vertical distribution of dust. MCS on MRO used parameters derived by MGS TES and Mini-TES to measure vertical profiles of dust opacity (*Kleinböhl et al.*, 2009).

Armed with a plethora of data about the properties and distribution of atmospheric dust, both vertical and spatial, current research has focused on its impact on climate. *Lefèvre et al.* (2008) modelled the interaction between chemical species transported by dust lifted from the surface and their impact as aerosol nucleation sites. By introducing heterogeneous chemistry into a GCM, they found much better agreement with ozone observations, which are affected by the increased H_2O_2 loading. *Madeleine et al.* (2011) refined modelling of dust distribution and radiative properties to improve GCM-predicted temperatures. *Guzewich et al.* (2013b) showed that introducing high-altitude detached dust layers impacted the meridional circulation by strengthening high-altitude, westerly winds, increasing temperatures near the poles, and impeding the diurnal tide.

5.2 Simulated spectra

Synthetic transmission spectra, with a range of 850 to 4320 cm^{-1} and resolution of 0.02 cm^{-1} were generated using GGG, divided into two channels representing an MCT detector between 850 and 2000 cm^{-1}, and an InSb detector between 1900 and 4320 cm^{-1}. The synthetic spectra were computed by GFIT in GGG by providing *a priori* vertical profiles of temperature, pressure, trace gas VMRs, and dust loading. The *a priori* vertical profiles of temperature, pressure, and CO_2 VMR that were used are shown in Figure 5.1. The *a priori* vertical profiles of other major atmospheric constituents, CO, H_2O, NO, O_3, H_2O_2, and CH_4, are shown in Figure 5.2.

The radiative transfer code in GGG is made general, so to adapt it for Mars, besides providing new *a priori* for the physical state of the atmosphere (T, P, humidity, VMRs),

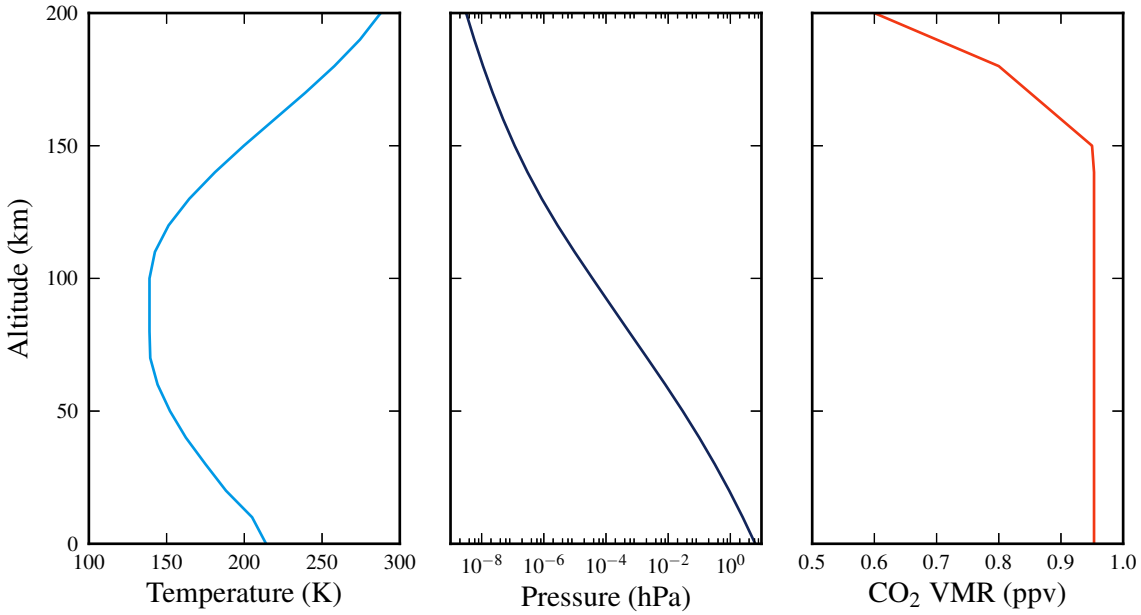

Figure 5.1: The *a priori* vertical profiles of temperature, pressure, and CO_2 VMR that represent the Martian atmosphere and were used to compute synthetic spectra with GGG. *A priori* profiles provided by JPL.

we needed only to change the mean radius, mean molecular mass, and gravitational acceleration at the surface. The shape of Mars is assumed to be an oblate spheroid (unchanged from Earth-application) with mean equatorial radius of 3389.5 km. The mean molecular mass and surface gravity used are 44.43×10^{-3} kg/mol and 3.73 m/s^2, and are constant with altitude in the current software version.

A priori dust profiles were developed at JPL, based on Viking mission results (*Izakov*, 1978; *Lindal et al.*, 1979), and hypothesized trace gas quantities and vertical distributions, and include two cases for dust loading (prior to a MATMOS-like mission, these would likely be updated and incorporate Mars GCM output). The vertical profiles of the mole fraction of atmospheric dust used to generate the synthetic spectra are shown in Figure 5.3 for the high- and low-dust scenarios. Near the surface, the high-dust case contains around six times more dust particles, and the area most susceptible to SIVs, where the rate of change of dust loading with altitude is greatest, occurs near 60 km, compared to 20 km for the low-dust scenario. Other dust profiles were created to make stronger SIVs and are shown in Figure 5.3. Two such profiles feature strong vertical stratification and a high-altitude detached layer, and are based on observations made by MCS on MRO (*McCleese et al.*, 2010; *Heavens et al.*, 2011) and by TES on MGS (*Guzewich et al.*,

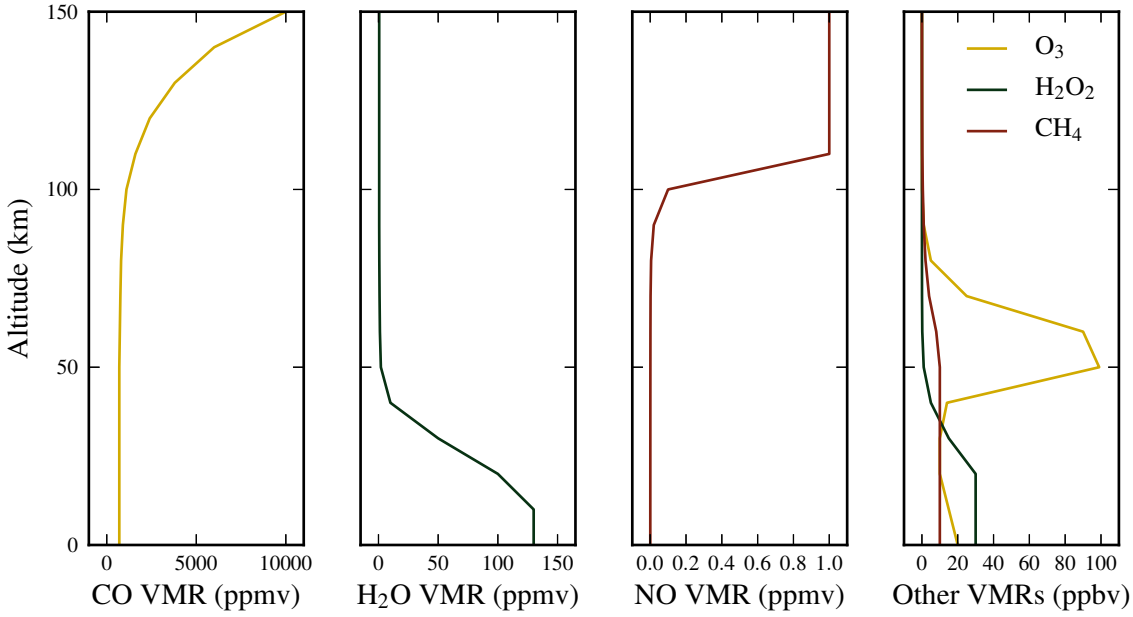

Figure 5.2: The *a priori* vertical profiles of trace gas VMRs that were used to compute synthetic spectra with GGG that represent the Martian atmosphere. Trace gas VMR vertical profiles shown are CO, H_2O, NO, O_3, H_2O, and CH_4. *A priori* provided by JPL.

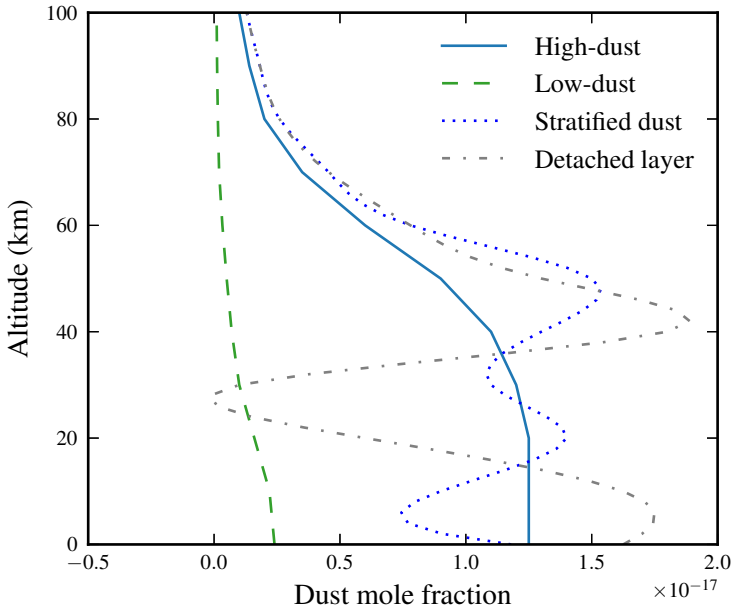

Figure 5.3: Vertical profiles of the dust mole fraction used to generate synthetic spectra for the Martian atmosphere for high-dust (blue) and low-dust (green dashed) conditions. The maximum rate of change of dust quantity with altitude occurs near 20 km in the low-dust case and near 60 km in the high-dust case. Also shown are scenarios that attempt to enhance the SIVs featuring strong stratification in the dust profile (grey dotted), or detached layers of dust (grey dash-dotted).

2013a). These profiles greatly increase the rate of change of dust mole fraction with altitude, but results from their use do not differ strongly from the high-dust scenario as discussed in Section 5.5.

Enhanced dust produces broad spectral features characterized by a non-unity spectral baseline that varies with wavenumber. GGG uses a pseudo-line approach (*Toon et al.*, 2006) to calculate the wavenumber-dependent attenuation due to dust from a set of laboratory-measured line strength parameters. Figure 5.4 shows synthetic spectra simulating Martian atmospheric conditions for high-dust and low-dust conditions at an altitude where the rate of change of dust mole fraction is significant in both scenarios. In the high-dust case, three consecutive altitudes are shown, which illustrate the inherent problem of a real interferometer's scan beginning in the lower layer and ending in the upper layer. Also shown is a terrestrial spectrum from ACE-FTS at a similar pressure level.

These synthetic spectra are converted from transmission spectra to absorption spectra by: multiplication by the solar Planck function, addition of a Mars Planck function,

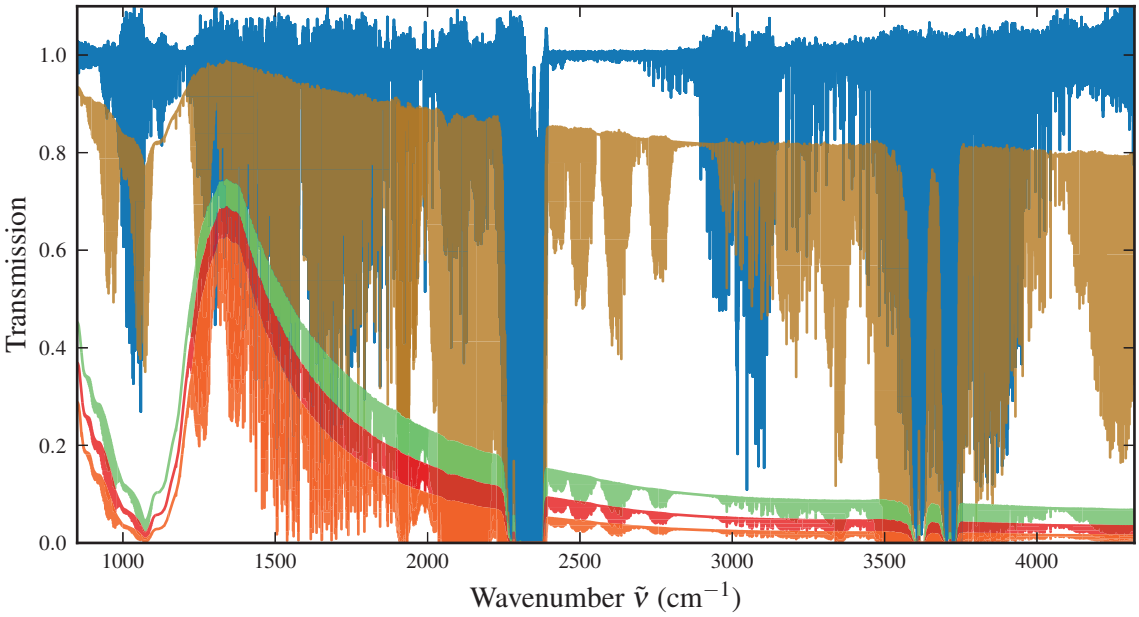

Figure 5.4: Example spectra from an ACE-FTS-like instrument. Shown are a terrestrial spectrum recorded by ACE-FTS (ss16000) at 47 km (blue); a simulated Mars spectrum in low-dust conditions at 34 km (brown); a simulated Mars spectrum in high-dust conditions at 34 km (red); and the two spectra from altitudes immediately above and below the high-dust spectrum (green and orange). The altitudes shown for Earth and Mars share a similar pressure of $\sim 7.9 \times 10^{-4}$ mbar.

and conversion of units to photons (using the field-of-view, aperture radius, throughput efficiency, integration time and spectral resolution). The spectra are multiplied by an instrument function and an efficiency function to simulate the active spectral range of the MCT and InSb detectors. Both functions were determined at JPL and based on the MkIV interferometer. The resulting spectra are then zero-filled from 0 cm^{-1} to the Nyquist frequency (3235.6 cm^{-1} for MCT and 6471.2 cm^{-1} for InSb). Each spectrum is inverse Fourier transformed to obtain AC interferograms from which the centreburst amplitude can be measured. A DC level, I_{DC}, is computed using the maximum and minimum of the interferogram, I_{max} and I_{min}, and the modulation efficiency, ME:

$$\mathrm{ME} = \frac{I_{max} - I_{min}}{2I_{DC}}. \tag{5.1}$$

I use an ME of 80%, a realistic value obtained using the MATMOS EDU. The 0 cm^{-1} values in the spectra are replaced by I_{DC}, and can now be inverse Fourier transformed into DC interferograms.

The inclusion of dust in the spectra affects the centreburst amplitude proportionally to the amount of extinction produced, since the centreburst carries information about a spectrum's baseline level. At high altitudes, where dust levels fall off, the simulated DC interferograms all have the same centreburst amplitudes and DC levels, while at the lower altitudes centreburst amplitudes are reduced by up to 90%. Figure 5.5a shows simulated interferograms for the low-dust conditions at three tangent altitudes centred at 16.5 km where the variability of dust quantity is greatest, showing the differences in centreburst amplitudes and DC levels.

To simulate SIVs, two aspects are taken into account: the DC level of the spectrometer input must vary continuously, and the intensity should change with altitude smoothly, as quantities of gas and dust vary. The interferograms created assume that the atmosphere and optical path have remained constant, and are perfectly symmetric. In reality, the optical path changes continuously as the instrument tracks the solar disk, so I must convolve each interferogram with those recorded at the tangent altitudes above, z_{i+1}, and below, z_{i-1}, it. Fixing ZPD to the I_{DC} for each occultation yields a continuous, time-varying function of intensity for the entire occultation. This function, interpolated to sample points, x, and denoted $V(x)$, is used to weight the interferograms at z_{i+1} and z_{i-1} as:

$$wt(x, z_{i+j}) = \begin{cases} \dfrac{(I_{DC}(z_i) - V(x))}{(V(x) - I_{DC}(z_{i+j}))}, & \text{if } x < 0 \text{ and } j = -1 \\ & \text{if } x > 0 \text{ and } j = +1 \\ 0, & \text{otherwise} \end{cases} \tag{5.2}$$

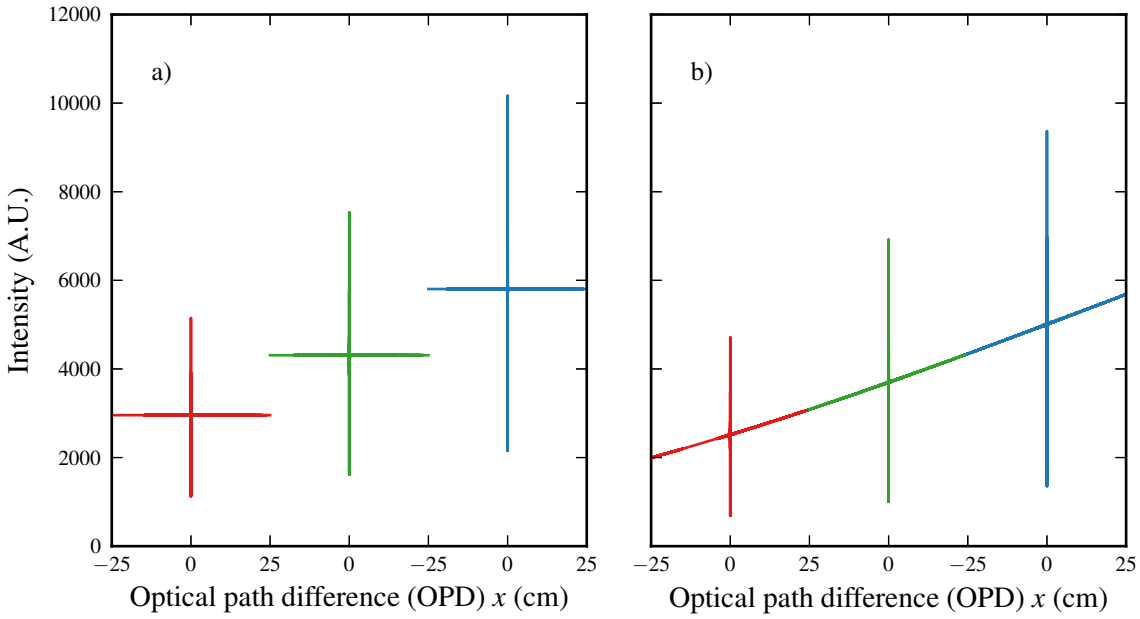

Figure 5.5: Three consecutive simulated interferograms showing the effects of decreasing dust levels during acquisition for low-dust conditions, at altitudes of 13.6, 16.5 and 19.4 km. In a), the interferograms have different centreburst amplitudes depending on the strength of the dust absorption, responsible for the baseline level in Figure 5.4, and DC levels computed from Equation 5.1. In b), the maximum OPD regions have been perturbed with the symmetric interferograms from altitudes above and below, and the DC level has been forced to vary continuously.

where x is OPD and $j = \pm 1$ depending on whether the weighting function will be applied to the measurement above or below. The resulting interferogram, perturbed with an SIV, is thus the weighted average of the three interferograms:

$$I_{SIV}(x, z_i) = \frac{wt(x, z_{i-1})I(x, z_{i-1}) + I(x, z_i) + wt(x, z_{i+1})I(x, z_{i+1})}{wt(x, z_{i-1}) + 1 + wt(x, z_{i+1})}. \tag{5.3}$$

This gives approximately even weights between the current layer and those above or below at maximum OPD, while leaving ZPD unaffected. Figure 5.5b shows the interferograms from Figure 5.5a now perturbed with an SIV.

5.3 Mitigation

The strategy to mitigate SIVs, originally suggested by *Brault* (1985), is to obtain a smooth function with which to re-weight the interferogram as:

$$I_{corr}(x) = \frac{I_{SIV}(x)}{I_{smooth}(x)}. \tag{5.4}$$

The resulting $I_{corr}(x)$ will have a constant DC level of 1, preserving spectral information in the centreburst and high-OPD wings, but requiring re-normalization. I examined three methods to obtain $I_{smooth}(x)$:

(i) using the known $V(x)$ as $I_{smooth}(x)$,

(ii) obtaining $I_{smooth}(x)$ by high-pass filtering $I_{SIV}(x)$ in the wavenumber domain as in *Keppel-Aleks et al.* (2007),

(iii) applying a convolution operator to $I_{SIV}(x)$ to obtain $I_{smooth}(x)$.

item i simply removes the known DC level without taking into account perturbations caused by mixing the interferogram with adjacent altitudes. This is used as the baseline case, representing no correction.

item ii refers to the following filter suggested by *Keppel-Aleks et al.* (2007):

$$f(\tilde{\nu}) = \begin{cases} \left(\dfrac{1 + \cos \pi\tilde{\nu}/s}{2}\right)^N, & \text{if } \tilde{\nu} < s \\ 0, & \text{if } \tilde{\nu} > s, \end{cases} \tag{5.5}$$

where $s = 300$ cm^{-1} is the wavenumber cutoff, and $N = 8$ controls the cutoff steepness. The interferograms in Figure 5.5b cannot be usefully Fourier transformed without any

treatment since the slope of the baseline results in a spectrum containing the transform of a linear function. This is not confined to low-wavenumbers, but interferes throughout the entire wavenumber range. Thus, high-pass filtering $\hat{I}_{SIV}(\tilde{\nu})$ to obtain $I_{smooth}(x)$ insufficiently mitigates SIVs (where $\hat{I}(\tilde{\nu})$ represents the Fourier transform of $I(x)$). The resulting $I_{smooth}(x)$ has large perturbations at maximum OPD that must undergo an additional step constraining the endpoints to $V(x)$ in the OPD domain to obtain a corrected spectrum.

The convolution operator in item iii is that by used the slice-ipp software, a fast Fourier transform algorithm developed at JPL and used by TCCON. It is meant to be the OPD-domain equivalent to the high-pass filter presented in *Keppel-Aleks et al.* (2007), and the result of that work. To perform a high-pass filter in the OPD domain, the OPD-domain interferogram is convolved with the inverse Fourier transform of an appropriate wavenumber-domain filter function. In slice-ipp, the function convolved with an interferogram is given by:

$$F(x) = \frac{\sin(2sx\pi)}{2sx\pi} + \frac{1}{2}\left(\frac{\sin(2sx\pi+\pi)}{2sx\pi+\pi} + \frac{\sin(2sx\pi-\pi)}{2sx\pi-\pi}\right), \tag{5.6}$$

and $I_{smooth}(x) = I_{SIV}(x) * F(x)$. The wavenumber cutoff, s, is higher in the slice-ipp method, close to the lower bound of the wavenumber range of the detector, and the cutoff steepness is less sharp than the original high-pass filter of *Keppel-Aleks et al.* (2007). Near zero OPD, where the centreburst amplitude is largest, $I_{smooth}(x)$ requires an additional smoothing step to reduce its amplitude. Practical advantages of applying the filter in the OPD domain, are computational simplicity and efficiency, since it can be done with shorter operators and does not require calling a fast Fourier transform subroutine.

Other methods of smoothing $I_{SIV}(x)$, such as using a moving average, an exponential filter (*Hamming*, 1983), and a Savitzky-Golay filter (*Savitzky and Golay*, 1964), were investigated. These either left artifacts at maximum OPD that lead to interference in the detector wavenumber range, or leave too much low-amplitude structure from $I_{SIV}(x)$ in $I_{smooth}(x)$, resulting in changes to absorption line relative depths. Other forms of a high-pass filter in the wavenumber domain suffer from the same inherent problem with the simulated SIVs described above.

Renormalization is done by multiplying the DC interferogram, $I_{corr}(x)$, by the ZPD level of the smoothed function, $I_{smooth}(x)$. The interferograms are then Fourier transformed, phase corrected in the wavenumber domain using the Mertz method (*Mertz*, 1967), and the reverse of the steps in Section 5.2 are performed to obtain transmission spectra.

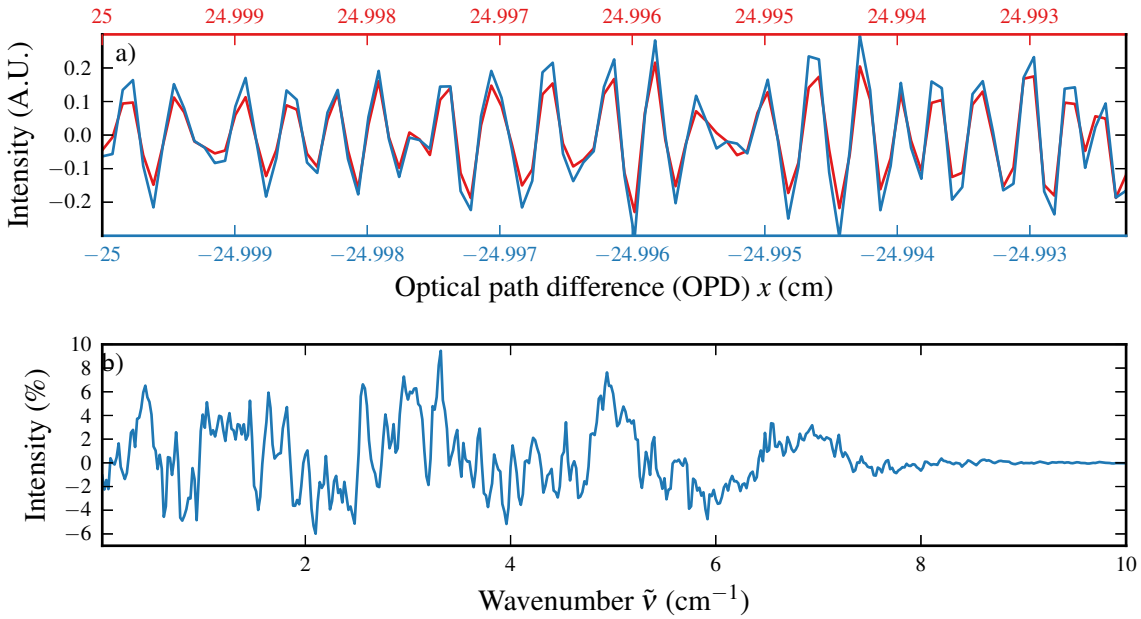

Figure 5.6: The effects of simulated SIVs in the a) OPD domain and b) wavenumber domain. a) shows an SIV-perturbed interferogram that has had its DC level removed using $V(x)$, such that the regions of maximum OPD (-25 cm and $+25$ cm) have the same DC level, but are no longer symmetric, containing spectral information from different altitudes. b) shows the low-wavenumber region of the Fourier transform of the same interferogram expressed as a percent of the mean peak amplitude. This region was zero-padded prior to simulating SIVs and can be high-pass filtered to obtain $I_{smooth}(x)$. Interferogram and spectrum are shown for low-dust conditions at 19.4 km.

5.4 Results

5.4.1 Spectra

The effects of the SIV perturbation are shown in Figure 5.6. The top panel shows the maximum OPD regions of an interferogram with the +25 cm^{-1} region's x-axis reversed. This interferogram has been corrected using only the known $V(x)$, such that the -25 cm^{-1} region and the +25 cm^{-1} have the same DC level. This illustrates the magnitude of the asymmetry caused by perturbing the interferograms with those from altitudes above and below, simulating interferogram acquisition beginning in a different optical layer than it ends in, with different gas and dust quantities. The bottom panel shows the low-wavenumber region of the resulting spectrum. Prior to simulating an SIV, this region of the spectrum was zero-filled; all the structure has been caused by the SIV simulation. The filter presented in *Keppel-Aleks et al.* (2007) would leave only the signal in this region to produce $I_{smooth}(x)$. The interferogram and corresponding spectrum shown are from 19.4 km in low-dust conditions, the same conditions as in Figure 5.5.

A sequence of 64 spectra from 2 to 167 km were created for low- and high-dust conditions, and each one was transformed into an interferogram and had the SIV perturbation applied. Each of the mitigation strategies were applied to produce three sets of transmission spectra over the wavenumber range of the MCT and InSb detectors.

Figure 5.7 shows mean percent residuals comparing the SIV-perturbed spectra to the original synthetic spectra for each mitigation strategy. Means are taken between 20 and 75 km. Above 75 km, the residuals fall to zero, as there is little gas absorption, and are omitted from the mean to avoid biasing the amplitude. Below 20 km, many absorption lines reach zero transmission, leading to zero division in the fractional residuals. This is a larger problem in the high-dust scenario where the transmission baseline is reduced to below 1% in the high-wavenumber region. Figures 5.7e and 5.7f use only spectra above 25 km and 30 km, respectively. At 30 km, orange in Figure 5.4, the baseline level is below 0.002 near 4000 cm^{-1}, and the small relative line depths in that region increase the percent residual. Mean percent residuals extending to 20 km are shown in grey for Figures 5.7e and 5.7f and extend to -19% and -14%, respectively (note that this is the result of division by a small number, the residuals remain small).

In Figure 5.7, the upper panels show the low-dust scenario, while the lower panels show the high-dust scenario. The light blue dashed lines in the lower panel indicate the y-axis limits of the upper panels, showing that when dust loading increases, the percent residuals are larger for all wavenumbers and for each mitigation strategy. In general, the residuals are very small, less than 0.25%, except for when absorption lines

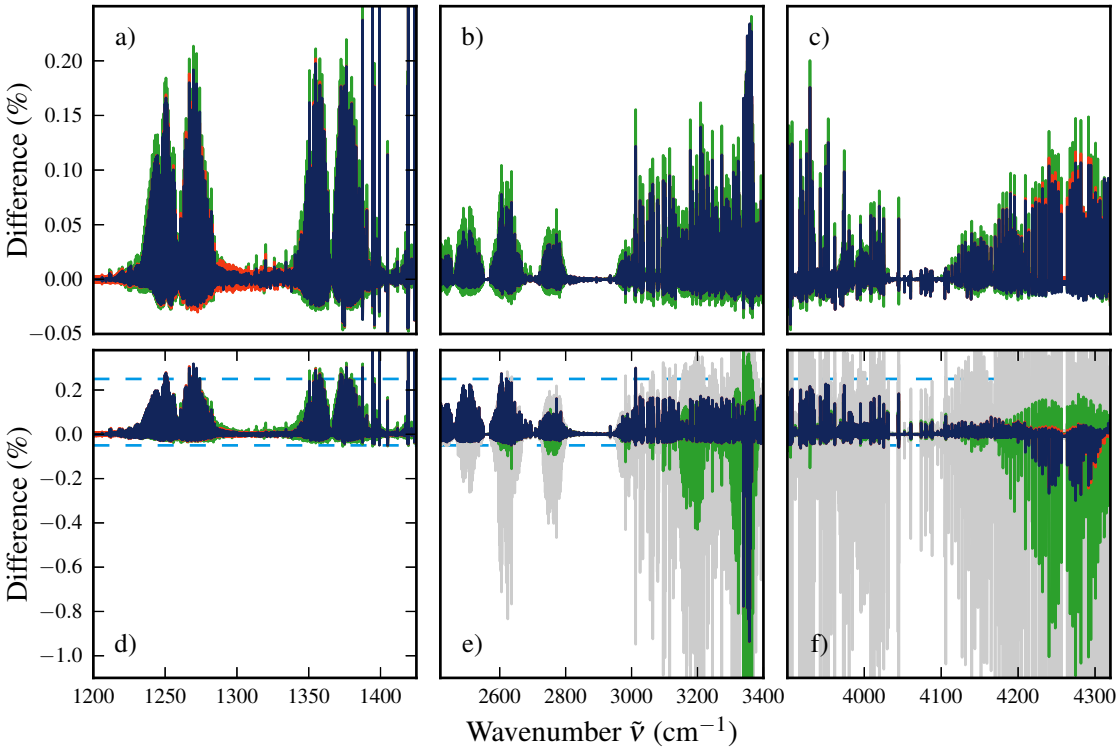

Figure 5.7: Mean residuals between the SIV-perturbed spectra and the original synthetic spectra, $I_{corr}(\tilde{\nu}) - I(\tilde{\nu})$, after applying each mitigation technique. Residuals are expressed as a percentage of the original synthetic spectra, and shown are spectral regions where transmission does not approach zero: a) and d) are 1200 - 1425 cm^{-1} in the MCT detector, b) and e) are 2420 - 3400 cm^{-1} in the InSb detector, and c) and f) are 3900 - 4320 cm^{-1} in the InSb detector. The upper panels, a), b) and c), are for low-dust conditions and the lower panels, d), e) and f) are for high-dust conditions. The dashed line (light blue) indicates the y-axis range of the low-dust panels. Means are taken over spectra between 20 and 75 km (20 spectra). Mitigation techniques use $I_{smooth}(x)$ obtained by: item i, using known $V(x)$ (green); item ii, high-pass filtering in the wavenumber domain, as in *Keppel-Aleks et al.* (2007), (red); and item iii, high-pass filtering in the OPD domain with a convolution operation (dark blue). In high-dust conditions, the baseline of the high-wavenumber spectral region rapidly approaches zero with decreasing altitude, so the minimum altitudes used in panel e) and f) are 25 km (16 spectra) and 30 km (18 spectra), respectively. The grey lines in panels e) and f) are of the mean residuals extending to 20 km when $I_{smooth}(x)$ is obtained from $V(x)$.

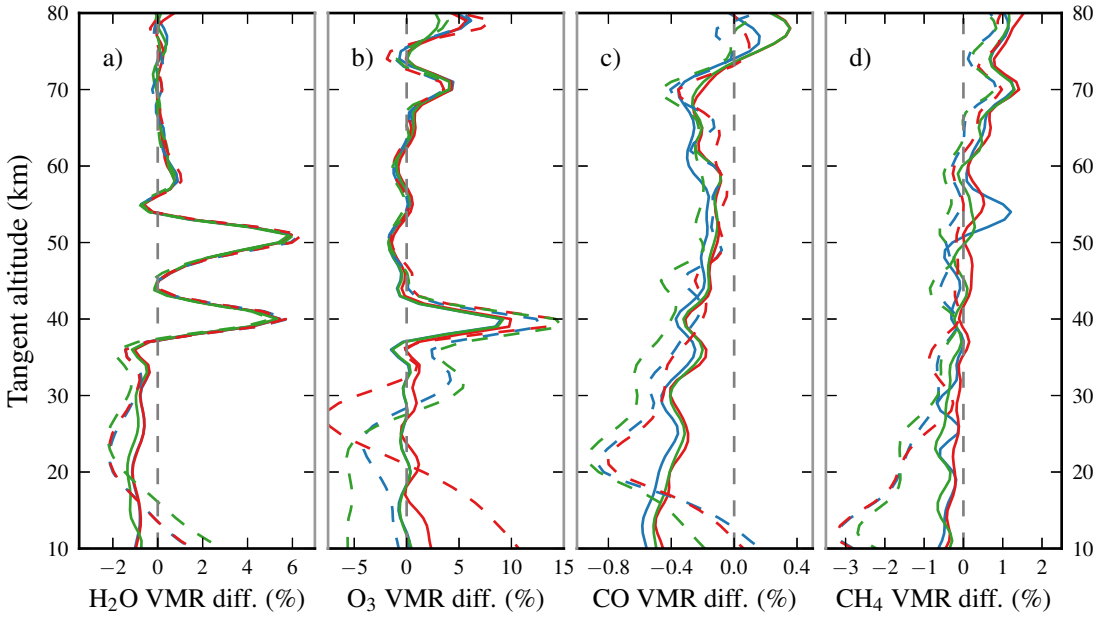

Figure 5.8: Differences between trace gas retrievals performed using SIV-perturbed and original synthetic spectra, $\mathrm{VMR}_{corr} - \mathrm{VMR}_{orig}$, expressed as a percentage of VMR_{orig}: a) H_2O, b) O_3, c) CO, d) CH_4. SIV perturbations are mitigated with $I_{smooth}(x)$ obtained by: item i, using known $V(x)$ (green); item ii, high-pass filtering in the wavenumber domain, as in *Keppel-Aleks et al.* (2007), (red); and item iii, high-pass filtering in the OPD domain with a convolution operation (dark blue). Low-dust conditions are solid lines, High-dust conditions are dashed lines.

approach zero, due either to strong absorption, or to strong dust attenuation (e.g., Figure 5.4). Residuals tend to be larger when the relative depth of absorption lines is greatest, peaking near 30 km. Higher in the atmosphere, gas absorption weakens, while lower in the atmosphere, dust attenuates the baseline. Because dust attenuation is weakest in the MCT detector wavenumber region, residuals remain large below 30 km. Residuals at all altitudes averaged in Figures 5.7a and 5.7d are less than 1%, except near 1350 cm^{-1}, which differs by up to 3% at lower altitudes.

The best performance is observed when $I_{smooth}(x)$ is obtained from item iii, by convolving $I_{SIV}(x)$ with Equation 5.6 in the OPD domain, as in the slice-ipp software (dark blue in Figure 5.7). The performance when $I_{smooth}(x)$ is obtained by high-pass filtering in the wavenumber domain, item ii (red in Figure 5.7), is very similar, and the two methods were designed to be equivalent. When only the interferogram baseline is removed using the known $V(x)$, item i (green in Figure 5.7), the poorest performance is seen, especially in the high-dust scenario at lower altitudes (Figures 5.7e and 5.7f).

5.4.2 VMR vertical profiles

The SNR of ACE-FTS is typically between 100 and 400 (*Boone et al.*, 2005). Noise levels in the spectra in regions without strong absorption lines are typically around 0.6%. The magnitude of the residuals between the SIV-perturbed spectra and the noise-free synthetic spectra presented here is generally smaller than typical noise levels of a real FTS. MATMOS was intended to have an SNR > 250 throughout its spectral range, which is comparable to that of ACE-FTS.

Differences in the spectra on the order of 1%, or less, can have an effect on trace gas retrievals. Trace gas retrievals were performed on all three sets of SIV-perturbed spectra, and the original synthetic spectra using GGG. I applied MkIV microwindows and used the same *a priori* temperature, pressure, and gas VMR vertical profiles that I used to generate the synthetic spectra. Figure 5.8 presents VMR vertical profile percent differences between retrievals from each of the SIV-perturbed spectra sets and the original synthetic spectra. Shown are H_2O, O_3, CO, and CH_4. Differences between the high- and low-dust scenarios increase as altitude decreases and dust levels increase. There are two large spikes in the H_2O VMR difference vertical profile and one in the O_3 VMR difference vertical profile in the altitude range where spectral residuals are largest. These occur at inflection points in the *a priori* VMR vertical profiles for those gases where the change in VMR between tangent altitudes is largest.

The closest agreement between SIV-perturbed spectra and the original spectra is for CO, which has the largest VMR among the gases presented. Retrievals from the high-dust spectra deviate below 30 km, and their percent difference is double those from the low-dust spectra, but remains below 1%. CH_4 retrievals also have very small VMR differences, and show large deviations between high- and low-dust scenarios below 30 km, but have a higher magnitude, with VMR differences for the high-dust scenario reaching 3% near 20 km. Low-dust scenario VMR differences remain below 1%. Between the two dust scenarios and three SIV mitigation techniques, obtaining $I_{smooth}(x)$ following *Keppel-Aleks et al.* (2007) (item ii) often has the smallest VMR differences, while using the known $V(x)$ to obtain $I_{smooth}(x)$ (item i) tends to result in the largest VMR differences. However, differences between methods are small, and no method is consistently better or worse at all altitudes.

The H_2O and O_3 VMR differences in the low-dust scenario are similar, below 2%, except where there are spikes. The high-dust scenario deviates strongly below 30 km for all SIV mitigation strategies, where the VMRs of H_2O and O_3 are large. VMR differences from mitigation using item iii, are similar to those obtained by using item ii for H_2O, and item i for O_3.

Noise was added to the spectra to test the retrieval sensitivity. Two noise sources were applied: extracting noise from spectra recorded by ACE-FTS, and generating random noise based on ACE-FTS spectra. The typical noise in an ACE-FTS spectrum can be measured using spectra recorded at the start or end of an occultation, where there can be no discernible gas absorption at high altitudes, or no solar transmission near the ground, or from spectra recorded while observing deep space. ACE-FTS noise spectra can be added directly to synthetic spectra, or I can assume the noise follows a Gaussian distribution, measure Gaussian parameters from the spectra, and generate random noise to add to synthetic spectra. The noise observed in ACE-FTS spectra is not normally distributed, however, and the amplitude varies with wavenumber (*Boone et al.*, 2005), so using noise recorded by ACE-FTS is preferred.

The magnitude of the VMR differences in Figure 5.8 is much smaller than for differences between retrievals from the original synthetic spectra and those spectra with noise added; these differences oscillate between ±5%, but can be larger than 10% at some altitudes. VMR differences for noisy spectra are also much larger at high altitudes, where absorption line depth is reduced to the same magnitude as the noise level.

5.5 Discussion

Keppel-Aleks et al. (2007) distinguish between grey (absorbed equally at all wavelengths) and non-grey SIVs, correctly identifying the limitation of item ii when the SIV strength is wavenumber-dependent. They applied and evaluated their filter on non-grey SIVs measured by a ground-based interferometer, then simulated low-amplitude grey SIVs that may be encountered by a ground-based FTS on Earth. They found that the correction was less effective for the grey dataset than non-grey, but still within the tolerance set by TCCON. The SIVs presented here are much stronger, and intended to investigate the limits of the TCCON correction method presented in *Keppel-Aleks et al.* (2007) for application to the dusty Martian atmosphere. These SIVs differ by the inclusion of dust, increased optical path length, reduced spectral resolution, and larger relative DC levels of consecutive spectra.

The SIVs I have simulated result in a sloped DC level in the interferograms that must be removed before a Fourier transform is performed, otherwise distortions will appear in the target spectral region. The method presented by *Keppel-Aleks et al.* (2007) cannot correct for these SIVs by high-pass filtering the spectra. However, the technique currently applied by TCCON, which smooths the interferogram in the OPD domain, effectively corrects these strong, grey SIVs. The quality of the correction depends on the type of

smoothing algorithm used, which may not effectively remove the centreburst amplitude, or affect the spectral information at high OPD.

Ridder et al. (2011) identified an issue with the *Keppel-Aleks et al.* (2007) method in the mid-infrared range where an MCT detector is used, as on ACE-FTS and future ACE-FTS-like instruments. The ADCs used by MCT detectors apply an unknown voltage offset to the signal which adds to the DC level of the interferogram. *Ridder et al.* (2011) present two methods to measure and remove the unknown offset, and evaluate their effectiveness using ground-based FTSs on Earth. In one case, they measured the offset by recording two consecutive interferograms using an MCT detector, and determined the offset by equating their modulation efficiencies, as in Equation 5.1 with the offset added to the denominator. In the other case, the modulation efficiency was measured using an InSb detector and assumed to be equal for both detectors. Since an ACE-FTS-like instrument will use MCT and InSb detectors, and interferograms will be acquired continuously, both methods will be applicable, while the modulation efficiency can be characterized and monitored. Furthermore, the offset can be measured directly when interferograms of deep space are recorded between occultations.

Stronger SIVs were created by altering the *a priori* dust mole fraction vertical profiles used to generate synthetic spectra for the high-dust scenario (Figure 5.3). When comparing different mitigation techniques, results are similar to the original high- and low-dust scenarios, where Methods (ii) and (iii) achieve close to the same performance, and item i performs slightly worse. The effects of the simulation on spectra are also similar to the high-dust simulation, and can be seen in the spectral residuals shown in Figure 5.9, which is the same as Figure 5.7d, but compares the four dust scenarios rather than mitigation techniques. Figure 5.9 shows mean spectral residuals for synthetic spectra before and after mitigation using item iii in the MCT region for the following dust scenarios: a detached layer of dust, high-dust, high-dust with stratification, and low-dust. Relative to spectral residuals from the high-dust scenario, a strong detached layer decreases the similarity of perturbed spectra to the original spectra, while introducing stratification produces results similar to the low-dust scenario. This is partially due to the density of observations, which can reduce the amount dust can change over a single observation. The rates of change of pressure and density with altitude produce a more dominant effect, however. When one introduces stratification, and decrease or increase the dust loading at a given altitude relative to the high-dust scenario, the dust extinction along the optical path still varies monotonically because the change in the total column of dust along the line-of-sight is greater than the change in dust mole fraction. Furthermore, when computing synthetic spectra, GGG does not distinguish local dust clouds,

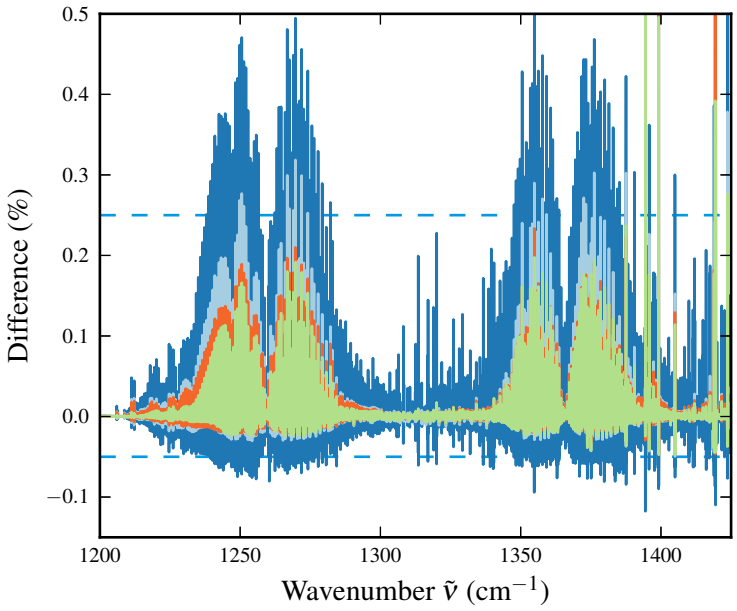

Figure 5.9: Comparison of the mean spectral residuals caused by varying the *a priori* dust profile used to generate synthetic spectra. Each residual is the mean of the difference between the original synthetic spectra and the dust-perturbed spectra mitigated using $I_{smooth}(x)$ obtained from item iii. Means are taken over an altitude range of 20 to 75 km (20 spectra) and the wavenumber region shown is 1200 - 1425 cm^{-1} in the MCT detector, as in Figures 5.7a and 5.7d. Dust scenarios are: a detached layer (blue), high-dust (light blue), stratified dust (orange), and low-dust (green).

so layers of increased dust loading are global, and every observation at lower altitudes passes through those layers. With respect to Figure 5.7, the effect of introducing stratification is to reduce the percent differences, as I have reduced the total dust, moving the simulation closer to the low-dust scenario. The effect of a detached layer is greater, as it causes the strongest vertical gradient of dust loading, and produces the largest mean spectral differences throughout the wavenumber region of the MCT and InSb detectors. The detached layer simulated here, however, contains a higher dust content than observations of the Martian atmosphere support (e.g., *Heavens et al.*, 2011; *Guzewich et al.*, 2013a).

5.6 Conclusions

A solar occultation FTS similar to the Earth-observing ACE-FTS is ideally suited to detecting unknown trace gases in the Martian atmosphere and retrieving their VMR vertical profiles. Dust storms elevate the dust content of the Martian atmosphere, scattering and absorbing transmitted solar radiation. A problem faced by an ACE-FTS-like mission to Mars is that the dust level through the optical path can vary strongly during the acquisition of each interferogram. I simulated transmission spectra and interferograms for the Martian atmosphere, and perturbed them with SIVs to evaluate whether these perturbations can be effectively mitigated.

Mean residuals between the original synthetic spectra and those perturbed with, and corrected for, an SIV with each of the three methods are below 0.25% between 20 and 75 km for both high- and low-dust conditions at most wavenumbers, except above 3000 cm^{-1} and below 30 km in the high-dust scenario. The residual magnitudes are smaller than the typical noise levels of ACE-FTS, which are around 0.6% for an SNR of 100 to 400. Such small differences in the spectra do affect trace gas retrievals, and I investigated H_2O, O_3, CO and CH_4 in this study. The percent differences in VMR vertical profiles retrieved from each set of perturbed spectra and the original spectra was largest for H_2O and O_3, peaking at 6% and 10%, at inflection points in their vertical profiles where there are large changes in VMR between layers. Otherwise, differences remain below 2%. The CO VMR differences are below 0.5% and the CH_4 VMR differences are below 1%. The high-dust scenario most strongly affects the lower altitudes (below 40 km), as there is very little suspended dust or gas above 60 km in either scenario, and the high-dust VMR vertical profiles diverge from the low-dust profiles with decreasing altitude. The spectral differences caused by simulating, then mitigating, SIVs affect VMR vertical profile retrievals less significantly than adding noise to the spectra.

While all three SIV mitigation methods perform well, as seen in Figures 5.7 and 5.8, it should be stressed that only the item iii used by slice-ipp is applicable to a future ACE-FTS-like mission. The high-pass filter described in *Keppel-Aleks et al.* (2007) cannot effectively mitigate the SIVs simulated here, because the perturbation affects the entire wavenumber range. The results shown in Figure 5.7 and 5.8 required additional processing steps that required knowledge of how the SIV perturbation was created. item i, where a fit to known $V(x)$ is used to remove the interferogram baseline is also not applicable to future missions since it requires accurately measuring $V(x)$ at the centreburst location and assumes the SIV is smooth throughout acquisition. SIV mitigation using item iii, where $I_{smooth}(x)$ is obtained by a high-pass filter in OPD space through a convolution operation, currently applied by the slice-ipp software, will be suitable for performing trace gas retrievals at Mars using an ACE-FTS-like instrument on a future mission.

Chapter 6

Conclusions

Sending an ACE-FTS-like instrument to Mars is an exciting prospect, but faces serious challenges in data analysis. The solar occultation technique has a long optical path length, increasing absorption by trace gases along the line-of-sight, and strong input signal, resulting in a high SNR ratio. The main drawback of solar occultation is its low temporal and spatial coverage. The interferometer design of ACE-FTS and MATMOS has an optical path difference of ± 25 cm resulting in a spectral resolution (data point spacing) of 0.02 cm^{-1}. This is sufficient to resolve individual absorption lines and distinguish isotopologues. The spectral range of an FTS is suitably broad enough to target a suite of trace gases, enabling the study of several photochemical cycles by simultaneously detecting related trace gas species.

The goals of the ExoMars TGO are to detect a broad suite of atmospheric trace gases and isotopologues, to map the distribution of trace gases and isotopic ratios geographically and seasonally, and to characterize the state of the atmosphere by monitoring temperatures, aerosols, water vapour, and ozone. These address key objectives of both NASA and ESA, set out, respectively, in the Decadal Survey on Planetary Science and the Cosmic Vision, which are to understand the origin of life and habitability in the Solar System, and to better understand the processes of planetary formation and evolution.

The ExoMars mission will hopefully continue without MATMOS, and is currently scheduled for a March 2016 launch. The ACS and NOMAD spectrometers will feature improvements over contemporary instruments, but lack the spectral range and resolution of MATMOS. Their results will improve our knowledge and understanding of the Martian atmosphere, but their improvements may not be sufficient for determining the source of atmospheric methane or detecting new trace gas species.

Solar occultation Fourier transform spectroscopy in the Martian atmosphere benefits from analysis techniques developed for Earth, but presents a unique set of challenges.

Atmospheric temperatures are generally very cold, far from the reference temperature at which absorption line strengths are computed, and outside the typical range of laboratory spectroscopy performed in support of terrestrial missions. The diurnal variation in temperature can be over 80–90 K at the Mars surface, and the surface pressure has seasonal changes of around 25% due to the CO_2 condensation cycles. Dust is prevalent in the atmosphere and may distort the shapes of absorption lines, as well as attenuate the input signal. The atmosphere is much thinner, so even with a long path length through the atmospheric limb, absorption lines will be very weak, and we lack the meteorological infrastructure to provide accurate *a priori* vertical profiles of temperature, pressure, and major gas abundances, such as CO_2 and water vapour.

The work presented in this thesis directly addresses some of the problems faced at Mars: detectability and sources of methane, determining the temperature and pressure of the atmosphere, and estimating the impact of dust on high-resolution solar occultation spectra.

For MMM, I calculated the rate of dispersion of a methane source on Mars using surface conditions, including winds, of the landing site of Curiosity, and basing the source strength on observations. I found that the width of a methane plume in the presence of wind on Mars would be only ∼10–30 m wide after travelling 500 m, depending on wind speed. Therefore, the likelihood of a point source detector identifying a methane plume source is unlikely.

I adapted the GGG software suite to retrieve VMR vertical profiles from ACE-FTS in preparation for MATMOS. I developed a new algorithm, based on early ATMOS work, and new software to retrieve vertical profiles of temperature and pressure from high-resolution solar occultation spectra. The software's ability to estimate the temperature and pressure of the atmosphere was demonstrated in a variety of conditions by processing 129 sets of spectra from ACE-FTS and comparing my results with the ACE-FTS v3.5 data product and results from COSMIC. I found no biases related to season, location, or β angle, but see that on average my retrievals are warmer than those from ACE-FTS. The mean temperature difference is 1.5 K below 100 km when compared with ACE-FTS, with a maximum occurring near 45 km. Results are similar when comparing my results to COSMIC, my retrievals tend to be warmer and the mean temperature difference is 1.2 K. COSMIC exhibits a small cold bias compared to ACE-FTS, which is noted in other comparisons, but both data sets are very close and differences are less that 1 K.

Dealing with high levels of atmospheric dust has also been identified as a critical component of preparations for MATMOS. I created data sets of synthetic spectra representing solar occultations from a Mars-orbiting ACE-FTS-like instrument. To simulate the effects

of dust, I transformed the spectra into DC interferograms and perturbed the interferograms by forcing the DC level to vary continuously over time and by adding information from observation levels above and below each interferogram to the high-OPD regions, simulating time-varying altitude changes during each acquisition. SIV were corrected in the OPD domain and wavenumber domain and the corrected spectra were compared with the original synthetic spectra. Spectral differences are below 0.25% between 20 and 75 km for both high- and low-dust conditions, similar to the SNR of ACE-FTS. These spectral differences lead to VMR vertical profile differences on the order of 1%.

6.1 Summary of results

6.1.1 Mars Methane Analogue Mission

During the course of my thesis research, through MATMOS collaborators, I became involved in the CSA's MMM micro-rover mission to deploy the Kapvik rover (and a Pioneer rover) at Mars analogue sites in Québec. The theme of the mission was to study the source of methane in the Martian atmosphere and my role was as an atmospheric science specialist. I went on two MMM field deployments to the Jeffrey and Norbestos mines and collected water and gas samples. At Jeffrey Mine, we found methane seeps in drainage boreholes in the mine walls most likely of biological origin, despite being at a site where large-scale serpentinization has taken place and been exposed at the surface.

On the second deployment, at Norbestos Mine, the team released methane from gas bottles along the rover path so see whether it could follow a source and determine the methane's origin from the isotopic ratio of carbon in methane isotopologues. Because of winds and rapid dispersion, the samples collected did not have the same isotopic ratio as the bottled gas. To understand these processes on Mars, I created a dispersion model to probe the metre-scale strength of gas dispersion on Mars, using published observations to estimate source strengths, and included surface winds. I estimated that the natural methane source at Jeffrey Mine had a strength of 5.3×10^{-10} kg s^{-1} and found that a source this weak cannot produce measurable enhancements close to the borehole of 0.5 to 3.1 ppmv above background levels (1.6 ppmv) when wind is present. To detect a highly localized methane source on Mars, a rover collecting *in situ* gas samples would need to be within metres of the plume axis.

6.1.2 Temperature and pressure retrievals

Having accurate temperature and pressure at the tangent point along the optical path in the limb of the atmosphere has been identified as a critically important aspect of retrieval software preparation for MATMOS. Characterizing trace gases and studying photochemical cycles and trace gas interactions would require accurate volume mixing ratios. While trace gases will be able to be identified and discovered from their spectral lines, retrieving their VMR vertical profiles will require accurate temperatures, which affect the calculated spectral line depths.

I have developed new algorithms and software to retrieve the vertical profiles of temperature and pressure from high-resolution absorption spectra with a spectral range encompassing strong CO_2 vibration-rotation bands. The technique exploits a relationship between the lower energy state of an absorption line's transition and the ratio of VMR scale factor estimated by GFIT to match the measured and calculated spectra. At each observation in an occultation, the temperature and pressure are estimated from ten CO_2 bands and the results are averaged to obtain vertical profiles. Pressure, temperature and altitude cannot be varied independently, and they are all retrieved quantities, so we identify the altitude with the best estimate of pressure and then integrate the equation of hydrostatic equilibrium to each observation tangent altitude to constrain pressure retrievals. This method is therefore independent of surface pressure, but even the temperature and pressure retrievals require *a priori* estimates to be close to the true state of the atmosphere, e.g., *a priori* temperatures greater than 10 K lead to retrieval instability.

The software has been applied to terrestrial spectra recorded by ACE-FTS and compared to their well-validated data product, and that of COSMIC. COSMIC was chosen primarily because its six satellites provide unrivalled spatial coverage, allowing for very tight coincidences with ACE-FTS, and secondarily because of the reputed accuracy of its temperature data product. My pressure retrievals are closely correlated with those of ACE-FTS, and mean temperature differences between my retrievals and ACE-FTS v3.5 are less than 5 K throughout the atmosphere, with the highest discrepancies occurring in the upper stratosphere and above, where the atmosphere may not be in local thermal equilibrium, CO_2 absorption becomes weak, and the CO_2 VMR falls off. A warm bias is exhibited in our retrievals relative to ACE-FTS, but no seasonal or zonal biases were found.

COSMIC and ACE-FTS v3.5 have mean temperature differences of < 1 K within the limited altitude range of COSMIC's temperature data product. Other COSMIC comparisons have seen a cold bias in the COSMIC temperature data product, which is also present here. Other than the continuing ACE-FTS validation, this work is the first

reported ACE-FTS v3.5 temperature validation, and as a result COSMIC's temperature and water vapour have become new members of the ACE-FTS validation effort. When comparing our retrievals to ACE-FTS I find mean temperature differences of around ±2 K, except near the tropopause.

6.1.3 Effects of dust on interferogram acquisition

While we expect that GGG will be able to fit the broad absorption features caused by atmospheric dust well enough to accurately retrieve the VMRs of trace gases, we expect that the 2 second acquisition time and a moving line-of-sight will distort absorption line shapes and relative line depths. I used GGG to compute synthetic spectra for the atmosphere of Mars, transformed these into interferograms, then applied perturbations to simulate continuous acquisition, but with changes in air mass along the line-of-sight over time.

Each interferogram was given a DC offset using the modulation efficiency of the MATMOS EDU and the centreburst amplitude of the inverse Fourier transformed spectrum. A continuous DC baseline was measured using all of the interferograms from an occultation, and amplitudes of the interferograms over acquisition time (and OPD) were perturbed with those from the altitudes above and below to create variations in the signal caused by changing trace gas absorption over time.

I found that the variations in the DC baseline were strong enough to necessitate removal prior to a Fourier transformation. Otherwise spectra are multiplied with the Fourier transform of a linear function which leaves systematic errors throughout a spectrum. I examined three methods of removing the DC level, one by fitting and subtracting the baseline, two by filtering the interferogram. Once the DC level is removed and a phase correction is applied, the resulting spectra closely return the line depths of the original synthetic spectra.

Comparing the original and SIV-corrected synthetic spectra, I found mean spectral residuals of less than 0.25%, except at low altitudes in the presence of dust, which is comparable to the noise levels measured in ACE-FTS spectra (SNR 100-400). I performed trace gas retrievals on the synthetic spectra to determine the extent to which the spectral differences affect the retrieved VMR. Trace gases studied were methane, water vapour, ozone, and CO. The largest differences observed were at inflection points in the VMR vertical profiles of water vapour and ozone (6% and 10%, respectively). Differences were less than 2% for water vapour and ozone, otherwise, less than 1% for methane, and less than 0.5% for CO.

6.2 Recommendations for future work

ACE-FTS and TCCON retrievals have undergone continuous development and have been improving over time. The software used in both experiments has roots in the ATMOS Space Shuttle missions. A MATMOS-like mission would be a continuation of their legacy and will also undergo development from the framework laid out in this thesis.

Minor improvements will come from iterations of GGG, with updates to the physical computation models and spectroscopic parameters. A major improvement that has been identified at this stage is to tune or train the data quality criteria, e.g., such that we find the best parameters which return the closest temperature profiles to ACE-FTS. The current software uses the fits of all CO_2 absorption lines at all altitudes, and relies on the data quality criteria to reduce the impact of fits made when there is no absorption, total absorption, or the presence of a strong interfering species. A future version may pre-select the altitude range for each line to be used, which should improve the stability and precision of retrievals.

Further improvements will come from further evaluation of the retrieval software against real measurements. The MkIV FTS is balloon-borne, has a higher spectral resolution that ACE-FTS, and trace gas profiles are already retrieved using GGG. The Portable Atmospheric Research Interferometric Spectrometer (PARIS) is a portable high-resolution interferometer sharing the design of ACE-FTS and MATMOS and is being used on balloon campaigns. PARIS, MkIV and ACE-FTS offer three distinct platforms for further evaluation of temperature and pressure retrievals.

The way the current version of GGG models dust absorption should be updated prior to Mars deployment. It relies on laboratory experiments that pre-date several of the most significant Mars missions with dust sensing instruments. A poorly modelled dust absorption baseline will directly impact the computed depths of absorption lines, leading to errors in trace gas VMR retrievals. New measurements from Mars have constrained the composition and scattering parameters of atmospheric dust, which can be used to develop more accurate and more physically realistic scattering models for solar occultation absorption spectra.

The simulations of source intensity variations presented here attempt to reproduce measurements at Mars by smoothly varying the DC level of the interferograms and perturbing the interferogram's symmetry. Both aspects aim to simulate a solar occultation instrument's line-of-sight vertically tracking through the atmosphere. I found that correcting for these perturbations using the methods proposed by TCCON returned spectra with line depth differences on the same order or less than the noise in ACE-FTS spec-

tra. These simulations may not suitably represent the Martian atmosphere and can be validated prior to a Mars deployment with either laboratory spectra in which dust is injected into a gas cell during acquisition, or through further atmospheric observations which record DC interferograms, such as with TCCON.

Bibliography

Abrajano, T. A., N. C. Sturchio, J. K. Bohlke, G. L. Lyon, R. J. Poreda, and C. M. Stevens (1988), Origins of Methane in the Earth Methane-hydrogen gas seeps, Zambales Ophiolite, Philippines: Deep or shallow origin?, *Chem. Geol.*, *71*(1), 211–222, doi:10.1016/0009-2541(88)90116-7.

Abrams, M. C., M. R. Gunson, L. L. Lowes, C. P. Rinsland, and R. Zander (1996), Pressure sounding of the middle atmosphere from ATMOS solar occultation measurements of atmospheric CO_2 absorption lines, *Appl. Opt.*, *35*, 2810–2820, doi: 10.1364/AO.35.002810.

Anthes, R. A., P. A. Bernhardt, Y. Chen, L. Cucurull, K. F. Dymond, D. Ector, S. B. Healy, S.-P. Ho, D. C. Hunt, Y.-H. Kuo, H. Liu, K. Manning, C. McCormick, T. K. Meehan, W. J. Randel, C. Rocken, W. S. Schreiner, S. V. Sokolovskiy, S. Syndergaard, D. C. Thompson, K. E. Trenberth, T.-K. Wee, N. L. Yen, and Z. Zeng (2008), The COSMIC/FORMOSAT-3 Mission: Early Results, *B. Am. Meteorol. Soc.*, *89*, 313, doi: 10.1175/BAMS-89-3-313.

Aoki, S., M. Giuranna, Y. Kasaba, H. Nakagawa, G. Sindoni, A. Geminale, and V. Formisano (2015a), Search for hydrogen peroxide in the Martian atmosphere by the Planetary Fourier Spectrometer onboard Mars Express, *Icarus*, *245*, 177–183, doi: 10.1016/j.icarus.2014.09.034.

Aoki, S., H. Nakagawa, H. Sagawa, M. Giuranna, G. Sindoni, A. Aronica, and Y. Kasaba (2015b), Seasonal variation of the HDO/H_2O ratio in the atmosphere of Mars at the middle of northern spring and beginning of northern summer, *Icarus*, *260*, 7–22, doi: 10.1016/j.icarus.2015.06.021.

Arvidson, R. E., S. W. Squyres, J. F. Bell, J. G. Catalano, B. C. Clark, L. S. Crumpler, P. A. de Souza, A. G. Fairén, W. H. Farrand, V. K. Fox, R. Gellert, A. Ghosh, M. P. Golombek, J. P. Grotzinger, E. A. Guinness, K. E. Herkenhoff, B. L. Jolliff, A. H.

Knoll, R. Li, S. M. McLennan, D. W. Ming, D. W. Mittlefehldt, J. M. Moore, R. V. Morris, S. L. Murchie, T. J. Parker, G. Paulsen, J. W. Rice, S. W. Ruff, M. D. Smith, and M. J. Wolff (2014), Ancient Aqueous Environments at Endeavour Crater, Mars, *Science*, *343*(6169), 1248097, doi:10.1126/science.1248097.

Atreya, S. K., A.-S. Wong, N. O. Renno, W. M. Farrell, G. T. Delory, D. D. Sentman, S. A. Cummer, J. R. Marshall, S. C. R. Rafkin, and D. C. Catling (2006), Oxidant Enhancement in Martian Dust Devils and Storms: Implications for Life and Habitability, *Astrobiology*, *6*, 439–450, doi:10.1089/ast.2006.6.439.

Atreya, S. K., P. R. Mahaffy, and A.-S. Wong (2007), Methane and related trace species on Mars: Origin, loss, implications for life, and habitability, *Planet and Space Sci.*, *55*, 358–369, doi:10.1016/j.pss.2006.02.005.

Atreya, S. K., M. G. Trainer, H. B. Franz, M. H. Wong, H. L. K. Manning, C. A. Malespin, P. R. Mahaffy, P. G. Conrad, A. E. Brunner, L. A. Leshin, J. H. Jones, C. R. Webster, T. C. Owen, R. O. Pepin, and R. Navarro-González (2013), Primordial argon isotope fractionation in the atmosphere of Mars measured by the SAM instrument on Curiosity and implications for atmospheric loss, *Geophys. Res. Lett.*, *40*, 5605–5609, doi:10.1002/2013GL057763.

Barth, C. A., A. I. F. Stewart, S. W. Bougher, D. M. Hunten, S. J. Bauer, and A. F. Nagy (1992), Aeronomy of the current Martian atmosphere, in *Mars*, edited by H. H. Kieffer, B. M. Jakosky, C. W. Snyder, and M. S. Matthews, pp. 1054–1089, University of Arizona Press, Tuscon.

Basu, S., M. I. Richardson, and R. J. Wilson (2004), Simulation of the Martian dust cycle with the GFDL Mars GCM, *J. Geophys. Res.*, *109*(E18), E11006, doi:10.1029/2004JE002243.

Bernath, P. F., C. T. McElroy, M. C. Abrams, C. D. Boone, M. Butler, C. Camy-Peyret, M. Carleer, C. Clerbaux, P.-F. Coheur, R. Colin, P. DeCola, M. DeMazière, J. R. Drummond, D. Dufour, W. F. J. Evans, H. Fast, D. Fussen, K. Gilbert, D. E. Jennings, E. J. Llewellyn, R. P. Lowe, E. Mahieu, J. C. McConnell, M. McHugh, S. D. McLeod, R. Michaud, C. Midwinter, R. Nassar, F. Nichitiu, C. Nowlan, C. P. Rinsland, Y. J. Rochon, N. Rowlands, K. Semeniuk, P. Simon, R. Skelton, J. J. Sloan, M.-A. Soucy, K. Strong, P. Tremblay, D. Turnbull, K. A. Walker, I. Walkty, D. A. Wardle, V. Wehrle, R. Zander, and J. Zou (2005), Atmospheric Chemistry Experiment (ACE): Mission overview, *Geophys. Res. Lett.*, *32*, L15S01, doi:10.1029/2005GL022386.

Bertaux, J.-L., F. Leblanc, S. Perrier, E. Quemerais, O. Korablev, E. Dimarellis, A. Reberac, F. Forget, P. C. Simon, S. A. Stern, and B. Sandel (2005a), Nightglow in the Upper Atmosphere of Mars and Implications for Atmospheric Transport, *Science*, *307*, 566–569, doi:10.1126/science.1106957.

Bertaux, J.-L., F. Leblanc, O. Witasse, E. Quemerais, J. Lilensten, S. A. Stern, B. Sandel, and O. Korablev (2005b), Discovery of an aurora on Mars, *Nature*, *435*, 790–794, doi:10.1038/nature03603.

Bertaux, J.-L., D. Nevejans, O. Korablev, E. Villard, E. Quémerais, E. Neefs, F. Montmessin, F. Leblanc, J. P. Dubois, E. Dimarellis, A. Hauchecorne, F. Lefèvre, P. Rannou, J. Y. Chaufray, M. Cabane, G. Cernogora, G. Souchon, F. Semelin, A. Reberac, E. Van Ransbeek, S. Berkenbosch, R. Clairquin, C. Muller, F. Forget, F. Hourdin, O. Talagrand, A. Rodin, A. Fedorova, A. Stepanov, I. Vinogradov, A. Kiselev, Y. Kalinnikov, G. Durry, B. Sandel, A. Stern, and J. C. Gérard (2007), SPICAV on Venus Express: Three spectrometers to study the global structure and composition of the Venus atmosphere, *Planet and Space Sci.*, *55*, 1673–1700, doi:10.1016/j.pss.2007.01.016.

Bertaux, J. L., B. Gondet, F. Lefèvre, J. P. Bibring, and F. Montmessin (2012), First detection of O_2 1.27 μm nightglow emission at Mars with OMEGA/MEX and comparison with general circulation model predictions, *J. Geophys. Res.*, *117*, E00J04, doi:10.1029/2011JE003890.

Bignami, G., P. Cargill, C. Schutz, and C. Turon (2005), *Cosmic Vision: Space Science for Europe 2015-2025*, BR-247, European Space Agency Publication Division, Noordwijk, Netherlands.

Bockelée-Morvan, D., J. Crovisier, M. J. Mumma, and H. A. Weaver (2004), The composition of cometary volatiles, in *Comets II*, edited by M. C. Festou, H. U. Keller, and H. A. Weaver, pp. 391–423, University of Arizona Press, Tuscon.

Boivin, A., P. Lai, C. Samson, E. Cloutis, S. Holladay, and F. A. Monteiro Santos (2013), Electromagnetic induction sounding and 3D laser imaging in support of a Mars methane analogue mission, *Planet and Space Sci.*, *82*, 27–33, doi:10.1016/j.pss.2013.03.005.

Bonnet, R.-M., and J.-P. Swings (2004), *The Aurora Programme*, BR-214, European Space Agency Publication Division, Noordwijk, Netherlands.

Boone, C. D., R. Nassar, K. A. Walker, Y. Rochon, S. D. McLeod, C. P. Rinsland, and P. F. Bernath (2005), Retrievals for the atmospheric chemistry experiment Fourier-transform spectrometer, *Appl. Opt.*, *44*, 7218–7231, doi:10.1364/AO.44.007218.

Boone, C. D., K. A. Walker, and P. F. Bernath (2013), Version 3 Retrievals for the Atmospheric Chemistry Experiment Fourier Transform Spectrometer (ACE-FTS), in *ACE at 10: Solar Occultation Anthology*, edited by P. F. Bernath, pp. 103–127, A. Deepak Publishing, Hampton, Virg.

Boynton, W. V., D. W. Ming, S. P. Kounaves, S. M. M. Young, R. E. Arvidson, M. H. Hecht, J. Hoffman, P. B. Niles, D. K. Hamara, R. C. Quinn, P. H. Smith, B. Sutter, D. C. Catling, and R. V. Morris (2009), Evidence for Calcium Carbonate at the Mars Phoenix Landing Site, *Science*, *325*, 61–64, doi:10.1126/science.1172768.

Brault, J. W. (1985), Fourier Transform Spectroscopy, in *High Resolution in Astronomy*, edited by A. O. Benz, M. Huber, and M. Mayor, pp. 3–61, Swiss Society of Astronomy and Astrophysics, Sauverny, Switzerland.

Bridges, N. T., P. E. Geissler, A. S. McEwen, B. J. Thomson, F. C. Chuang, K. E. Herkenhoff, L. P. Keszthelyi, and S. Martínez-Alonso (2007), Windy Mars: A dynamic planet as seen by the HiRISE camera, *Geophys. Res. Lett.*, *34*, L23205, doi:10.1029/2007GL031445.

Cantor, B. A., P. B. James, and W. M. Calvin (2010), MARCI and MOC observations of the atmosphere and surface cap in the north polar region of Mars, *Icarus*, *208*, 61–81, doi:10.1016/j.icarus.2010.01.032.

Carter, J., F. Poulet, J.-P. Bibring, N. Mangold, and S. Murchie (2013), Hydrous minerals on Mars as seen by the CRISM and OMEGA imaging spectrometers: Updated global view, *J. Geophys. Res.*, *118*, 831–858, doi:10.1029/2012JE004145.

Catalfamo, C., D. Bruno, G. Colonna, A. Laricchiuta, and M. Capitelli (2009), High temperature Mars atmosphere. Part II: transport properties, *Eur. Phys. J. D*, *54*, 613–621, doi:10.1140/epjd/e2009-00193-6.

Chapman, S., and T. Cowling (1970), *The Mathematical Theory of Nonuniform Gases*, Cambridge Univ. Press, New York.

Chassefière, E., and F. Leblanc (2011), Constraining methane release due to serpentinization by the observed D/H ratio on Mars, *Earth Planet. Sci. Lett.*, *310*, 262–271, doi:10.1016/j.epsl.2011.08.013.

Chassefière, E., B. Langlais, Y. Quesnel, and F. Leblanc (2013), The fate of early Mars' lost water: The role of serpentinization, *J. Geophys. Res.*, *118*, 1123–1134, doi:10.1002/jgre.20089.

Christensen, P. R. (2003), Formation of recent martian gullies through melting of extensive water-rich snow deposits, *Nature*, *422*, 45–48.

Christensen, P. R., J. L. Bandfield, M. D. Smith, V. E. Hamilton, and R. N. Clark (2000), Identification of a basaltic component on the Martian surface from Thermal Emission Spectrometer data, *J. Geophys. Res.*, *105*, 9609–9621, doi:10.1029/1999JE001127.

Christensen, P. R., M. B. Wyatt, T. D. Glotch, A. D. Rogers, S. Anwar, R. E. Arvidson, J. L. Bandfield, D. L. Blaney, C. Budney, W. M. Calvin, A. Fallacaro, R. L. Fergason, N. Gorelick, T. G. Graff, V. E. Hamilton, A. G. Hayes, J. R. Johnson, A. T. Knudson, H. Y. McSween, G. L. Mehall, L. K. Mehall, J. E. Moersch, R. V. Morris, M. D. Smith, S. W. Squyres, S. W. Ruff, and M. J. Wolff (2004), Mineralogy at Meridiani Planum from the Mini-TES Experiment on the Opportunity Rover, *Science*, *306*, 1733–1739, doi:10.1126/science.1104909.

Clancy, R. T., S. W. Lee, G. R. Gladstone, W. W. McMillan, and T. Rousch (1995), A new model for Mars atmospheric dust based upon analysis of ultraviolet through infrared observations from Mariner 9, Viking, and PHOBOS, *J. Geophys. Res.*, *100*, 5251–5263, doi:10.1029/94JE01885.

Clancy, R. T., B. J. Sandor, M. J. Wolff, P. R. Christensen, M. D. Smith, J. C. Pearl, B. J. Conrath, and R. J. Wilson (2000), An intercomparison of ground-based millimeter, MGS TES, and Viking atmospheric temperature measurements: Seasonal and interannual variability of temperatures and dust loading in the global Mars atmosphere, *J. Geophys. Res.*, *105*, 9553–9572, doi:10.1029/1999JE001089.

Clancy, R. T., M. J. Wolff, and P. R. Christensen (2003), Mars aerosol studies with the MGS TES emission phase function observations: Optical depths, particle sizes, and ice cloud types versus latitude and solar longitude, *J. Geophys. Res.*, *108*(E9), 5098, doi:10.1029/2003JE002058.

Clancy, R. T., B. J. Sandor, and G. H. Moriarty-Schieven (2004), A measurement of the 362 GHz absorption line of Mars atmospheric H_2O_2, *Icarus*, *168*, 116–121, doi:10.1016/j.icarus.2003.12.003.

Clancy, R. T., B. J. Sandor, M. J. Wolff, M. D. Smith, F. Lefèvre, J.-B. Madeleine, F. Forget, S. L. Murchie, F. P. Seelos, K. D. Seelos, H. A. Nair, A. D. Toigo, D. Humm, D. M. Kass, A. Kleinböhl, and N. Heavens (2012), Extensive MRO CRISM observations of 1.27 μm O_2 airglow in Mars polar night and their comparison to MRO MCS temperature profiles and LMD GCM simulations, *J. Geophys. Res.*, *117*, E00J10, doi: 10.1029/2011JE004018.

Clancy, R. T., B. J. Sandor, A. García-Muñoz, F. Lefèvre, M. D. Smith, M. J. Wolff, F. Montmessin, S. L. Murchie, and H. Nair (2013), First detection of Mars atmospheric hydroxyl: CRISM Near-IR measurement versus LMD GCM simulation of OH Meinel band emission in the Mars polar winter atmosphere, *Icarus*, *226*, 272–281, doi:10.1016/ j.icarus.2013.05.035.

Clark, B. C., A. J. Castro, C. D. Rowe, A. K. Baird, P. H. Evans, H. J. Rose, Jr., P. Toulmin III, K. Keil, and W. C. Kelliher (1976), Inorganic analyses of Martian surface samples at the Viking landing sites, *Science*, *194*, 1283–1288, doi:10.1126/ science.194.4271.1283.

Cloutis, E. A., L. Whyte, A. Qadi, J. F. Bell, G. Berard, A. Boivin, A. Ellery, E. Haddad, W. Jamroz, R. Kruzelecky, P. Mann, K. Olsen, M. Perrot, D. Popa, T. Rhind, C. Samson, R. Sharma, J. Stromberg, K. Strong, A. Tremblay, R. Wilhelm, B. Wing, and B. Wong (2012), The Mars Methane Analogue Mission (M3): Results of the 2011 Field Deployment, in *Lunar Planet. Sci. Conf.*, vol. 43, p. 1569.

Cloutis, E. A., L. Whyte, A. Qadi, L. Anderson-Trocme, J. F. Bell, G. Berard, A. Boivin, A. Ellery, R. Greenberger, E. Haddad, W. Jamroz, W. Kruzelecky, P. Mann, J. F. Mustard, K. Olsen, M. Perrot, D. Popa, M. Ralchenko, T. Rhind, C. Samson, R. Sharma, J. Stromberg, K. Strong, A. Tremblay, and B. Wing (2013), The Mars Methane Analogue Mission (M^3): Results of the 2012 Field Deployment, in *Lunar Planet. Sci. Conf.*, vol. 44, p. 1579.

Committee on Extension of the U.S. Standard Atmosphere (COESTA) (1976), *U.S. Standard Atmosphere 1976*, Govt. Print. Off., Washington, D. C.

Conrath, B. J. (1975), Thermal structure of the Martian atmosphere during the dissipation of the dust storm of 1971, *Icarus*, *24*, 36–46, doi:10.1016/0019-1035(75)90156-6.

Cowie, M., and H. Watts (1971), Diffusion of Methane and Chloromethanes in Air, *Can. J. Chem.*, *49*, 74–77.

Das, U., and C. J. Pan (2014), Validation of FORMOSAT-3/COSMIC level 2 atmPrf global temperature data in the stratosphere, *Atmos. Meas. Tech.*, *7*, 731–742, doi: 10.5194/amt-7-731-2014.

Dickinson, C., J. A. Whiteway, L. Komguem, J. E. Moores, and M. T. Lemmon (2010), Lidar measurements of clouds in the planetary boundary layer on Mars, *Geophys. Res. Lett.*, *37*, L18203, doi:10.1029/2010GL044317.

Dodion, J., D. Fussen, F. Vanhellemont, C. Bingen, N. Mateshvili, K. Gilbert, R. Skelton, D. Turnbull, S. D. McLeod, C. D. Boone, K. A. Walker, and P. F. Bernath (2007), Cloud detection in the upper troposphere-lower stratosphere region via ACE imagers: A qualitative study, *J. Geophys. Res.*, *112*, D03208, doi:10.1029/2006JD007160.

Doeringer, D., A. Eldering, C. D. Boone, G. González Abad, and P. F. Bernath (2012), Observation of sulfate aerosols and SO_2 from the Sarychev volcanic eruption using data from the Atmospheric Chemistry Experiment (ACE), *J. Geophys. Res.*, *117*, D03203, doi:10.1029/2011JD016556.

Drummond, R., A.-C. Vandaele, F. Daerden, D. Fussen, A. Mahieux, L. Neary, E. Neefs, S. Robert, Y. Willame, and V. Wilquet (2011), Studying methane and other trace species in the Mars atmosphere using a SOIR instrument, *Planet and Space Sci.*, *59*, 292–298, doi:10.1016/j.pss.2010.05.009.

Dutil, Y., S. Lantagne, S. Dube, and R. H. Poulin (2002), ACE-FTS level 0 to 1 data processing, *Proc. SPIE*, *4814*, 102–110, doi:10.1117/12.451779.

Ehlmann, B. L., J. F. Mustard, C. I. Fassett, S. C. Schon, J. W. Head III, D. J. Des Marais, J. A. Grant, and S. L. Murchie (2008), Clay minerals in delta deposits and organic preservation potential on Mars, *Nat. Geosci.*, *1*, 355–358, doi:10.1038/ngeo207.

Ehlmann, B. L., J. F. Mustard, G. A. Swayze, R. N. Clark, J. L. Bishop, F. Poulet, D. J. Des Marais, L. H. Roach, R. E. Milliken, J. J. Wray, O. Barnouin-Jha, and S. L. Murchie (2009), Identification of hydrated silicate minerals on Mars using MRO-CRISM: Geologic context near Nili Fossae and implications for aqueous alteration, *J. Geophys. Res.*, *114*, E00D08, doi:10.1029/2009JE003339.

Ehlmann, B. L., J. F. Mustard, and S. L. Murchie (2010), Geologic setting of serpentine deposits on Mars, *Geophys. Res. Lett.*, *37*, L06201, doi:10.1029/2010GL042596.

Ellehoj, M. D., H. P. Gunnlaugsson, P. A. Taylor, H. Kahanpää, K. M. Bean, B. A. Cantor, B. T. Gheynani, L. Drube, D. Fisher, A.-M. Harri, C. Holstein-Rathlou,

M. T. Lemmon, M. B. Madsen, M. C. Malin, J. Polkko, P. H. Smith, L. K. Tamppari, W. Weng, and J. Whiteway (2010), Convective vortices and dust devils at the Phoenix Mars mission landing site, *J. Geophys. Res.*, *115*, E00E16, doi:10.1029/2009JE003413.

Encrenaz, T. (2001), The Atmosphere of Mars as Constrained by Remote Sensing, *Space Sci. Rev.*, *96*, 411–424, doi:10.1023/A:1011922011532.

Encrenaz, T., T. K. Greathouse, M. J. Richter, J. H. Lacy, T. Fouchet, B. Bézard, F. Lefèvre, F. Forget, and S. K. Atreya (2011), A stringent upper limit to SO_2 in the Martian atmosphere, *Astron. Astrophys.*, *530*, A37, doi:10.1051/0004-6361/201116820.

Encrenaz, T., T. K. Greathouse, F. Lefèvre, and S. K. Atreya (2012), Hydrogen peroxide on Mars: Observations, interpretation and future plans, *Planet and Space Sci.*, *68*, 3–17, doi:10.1016/j.pss.2011.03.019.

Eremenko, M. N., A. Y. Zasetsky, C. D. Boone, and J. J. Sloan (2005), Properties of high-altitude tropical cirrus clouds determined from ACE FTS observations, *Geophys. Res. Lett.*, *32*, L15S07, doi:10.1029/2005GL022428.

Etiope, G., and B. Sherwood Lollar (2013), Abiotic Methane on Earth, *Rev. Geophys.*, *51*, 276–299, doi:10.1002/rog.20011.

Etiope, G., M. Schoell, and H. Hosgörmez (2011), Abiotic methane flux from the Chimaera seep and Tekirova ophiolites (Turkey): Understanding gas exhalation from low temperature serpentinization and implications for Mars, *Earth Planet. Sci. Lett.*, *310*, 96–104, doi:10.1016/j.epsl.2011.08.001.

Etiope, G., B. L. Ehlmann, and M. Schoell (2013), Low temperature production and exhalation of methane from serpentinized rocks on Earth: A potential analog for methane production on Mars, *Icarus*, *224*, 276–285, doi:10.1016/j.icarus.2012.05.009.

Farrand, W. H., T. D. Glotch, J. W. Rice, J. A. Hurowitz, and G. A. Swayze (2009), Discovery of jarosite within the Mawrth Vallis region of Mars: Implications for the geologic history of the region, *Icarus*, *204*, 478–488, doi:10.1016/j.icarus.2009.07.014.

Fedorova, A., O. Korablev, J.-L. Bertaux, A. Rodin, A. Kiselev, and S. Perrier (2006), Mars water vapor abundance from SPICAM IR spectrometer: Seasonal and geographic distributions, *J. Geophys. Res.*, *111*, E09S08, doi:10.1029/2006JE002695.

Fedorova, A. A., O. I. Korablev, J.-L. Bertaux, A. V. Rodin, F. Montmessin, D. A. Belyaev, and A. Reberac (2009), Solar infrared occultation observations by SPICAM

experiment on Mars-Express: Simultaneous measurements of the vertical distributions of H_2O, CO_2 and aerosol, *Icarus*, *200*, 96–117, doi:10.1016/j.icarus.2008.11.006.

Foelsche, U., B. Scherllin-Pirscher, F. Ladstädter, A. K. Steiner, and G. Kirchengast (2011), Refractivity and temperature climate records from multiple radio occultation satellites consistent within 0.05%, *Atmos. Meas. Tech.*, *4*, 2007–2018, doi:10.5194/amt-4-2007-2011.

Fonti, S., and G. A. Marzo (2010), Mapping the methane on Mars, *Astron. Astrophys.*, *512*, A51, doi:10.1051/0004-6361/200913178.

Forget, F. (1998), Improved optical properties of the Martian atmospheric dust for radiative transfer calculations in the infrared, *Geophys. Res. Lett.*, *25*, 1105–1108, doi:10.1029/98GL50653.

Forget, F., F. Hourdin, R. Fournier, C. Hourdin, O. Talagrand, M. Collins, S. R. Lewis, P. L. Read, and J.-P. Huot (1999), Improved general circulation models of the Martian atmosphere from the surface to above 80 km, *J. Geophys. Res.*, *104*, 24,155–24,176, doi:10.1029/1999JE001025.

Forget, F., F. Montmessin, J.-L. Bertaux, F. González-Galindo, S. Lebonnois, E. Quémerais, A. Reberac, E. Dimarellis, and M. A. López-Valverde (2009), Density and temperatures of the upper Martian atmosphere measured by stellar occultations with Mars Express SPICAM, *J. Geophys. Res.*, *114*, E01004, doi:10.1029/2008JE003086.

Forman, M. L., W. H. Steel, and G. A. Vanasse (1966), Correction of Asymmetric Interferograms Obtained in Fourier Spectroscopy, *J. Opt. Soc. Am.*, *56*, 59–63.

Formisano, V., S. Atreya, T. Encrenaz, N. Ignatiev, and M. Giuranna (2004), Detection of Methane in the Atmosphere of Mars, *Science*, *306*, 1758–1761, doi:10.1126/science.1101732.

Fouchet, T., E. Lellouch, N. I. Ignatiev, F. Forget, D. V. Titov, M. Tschimmel, F. Montmessin, V. Formisano, M. Giuranna, A. Maturilli, and T. Encrenaz (2007), Martian water vapor: Mars Express PFS/LW observations, *Icarus*, *190*, 32–49, doi:10.1016/j.icarus.2007.03.003.

Franz, H. B., M. G. Trainer, M. H. Wong, P. R. Mahaffy, S. K. Atreya, H. L. K. Manning, and J. C. Stern (2015), Reevaluated martian atmospheric mixing ratios from the mass

spectrometer on the Curiosity rover, *Planet and Space Sci.*, *109*, 154–158, doi:10.1016/j.pss.2015.02.014.

Frigo, M., and S. G. Johnson (2005), The design and implementation of FFTW3, *Proc. IEEE*, *93*(2), 216–231, special issue on "Program Generation, Optimization, and Platform Adaptation".

Gagné, M.-E., J.-L. Bertaux, F. González-Galindo, S. M. L. Melo, F. Montmessin, and K. Strong (2013), New nitric oxide (NO) nightglow measurements with SPICAM/MEx as a tracer of Mars upper atmosphere circulation and comparison with LMD-MGCM model prediction: Evidence for asymmetric hemispheres, *J. Geophys. Res.*, *118*, 2172–2179, doi:10.1002/jgre.20165.

García-Comas, M., B. Funke, M. López-Puertas, D. Bermejo-Pantaleón, N. Glatthor, T. von Clarmann, G. Stiller, U. Grabowski, C. D. Boone, W. J. R. French, T. Leblanc, M. J. López-González, and M. J. Schwartz (2012), On the quality of MIPAS kinetic temperature in the middle atmosphere, *Atmos. Chem. Phys.*, *12*, 6009–6039, doi:10.5194/acp-12-6009-2012.

García-Comas, M., B. Funke, A. Gardini, M. López-Puertas, A. Jurado-Navarro, T. von Clarmann, G. Stiller, M. Kiefer, C. D. Boone, T. Leblanc, B. T. Marshall, M. J. Schwartz, and P. E. Sheese (2014), MIPAS temperature from the stratosphere to the lower thermosphere: Comparison of vM21 with ACE-FTS, MLS, OSIRIS, SABER, SOFIE and lidar measurements, *Atmos. Meas. Tech.*, *7*, 3633–3651, doi:10.5194/amt-7-3633-2014.

Geminale, A., V. Formisano, and G. Sindoni (2011), Mapping methane in Martian atmosphere with PFS-MEX data, *Planet and Space Sci.*, *59*, 137–148, doi:10.1016/j.pss.2010.07.011.

Gendrin, A., N. Mangold, J.-P. Bibring, Y. Langevin, B. Gondet, F. Poulet, G. Bonello, C. Quantin, J. Mustard, R. Arvidson, and S. Le Mouélic (2005), Sulfates in Martian Layered Terrains: The OMEGA/Mars Express View, *Science*, *307*, 1587–1591, doi:10.1126/science.1109087.

Gille, J., J. Barnett, P. Arter, M. Barker, P. Bernath, C. Boone, C. Cavanaugh, J. Chow, M. Coffey, J. Craft, C. Craig, M. Dials, V. Dean, T. Eden, D. P. Edwards, G. Francis, C. Halvorson, L. Harvey, C. Hepplewhite, R. Khosravi, D. Kinnison, C. Krinsky, A. Lambert, H. Lee, L. Lyjak, J. Loh, W. Mankin, S. Massie, J. McInerney,

J. Moorhouse, B. Nardi, D. Packman, C. Randall, J. Reburn, W. Rudolf, M. Schwartz, J. Serafin, K. Stone, B. Torpy, K. Walker, A. Waterfall, R. Watkins, J. Whitney, D. Woodard, and G. Young (2008), High Resolution Dynamics Limb Sounder: Experiment overview, recovery, and validation of initial temperature data, *J. Geophys. Res.*, *113*(D12), D16S43, doi:10.1029/2007JD008824.

Glavin, D. P., C. Freissinet, K. E. Miller, J. L. Eigenbrode, A. E. Brunner, A. Buch, B. Sutter, P. D. Archer, S. K. Atreya, W. B. Brinckerhoff, M. Cabane, P. Coll, P. G. Conrad, D. Coscia, J. P. Dworkin, H. B. Franz, J. P. Grotzinger, L. A. Leshin, M. G. Martin, C. McKay, D. W. Ming, R. Navarro-González, A. Pavlov, A. Steele, R. E. Summons, C. Szopa, S. Teinturier, and P. R. Mahaffy (2013), Evidence for perchlorates and the origin of chlorinated hydrocarbons detected by SAM at the Rocknest aeolian deposit in Gale Crater, *J. Geophys. Res.*, *118*, 1955–1973, doi:10.1002/jgre.20144.

Glotch, T. D., and P. R. Christensen (2005), Geologic and mineralogic mapping of Aram Chaos: Evidence for a water-rich history, *J. Geophys. Res.*, *110*, E09006, doi:10.1029/2004JE002389.

Goldman, A., C. Paton-Walsh, W. Bell, G. C. Toon, J.-F. Blavier, B. Sen, M. T. Coffey, J. W. Hannigan, and W. G. Mankin (1999), Network for the Detection of Stratospheric Change Fourier transform infrared intercomparison at Table Mountain Facility, November 1996, *J. Geophys. Res.*, *104*(D23), 30,481–30,503, doi:10.1029/1999JD900879.

Gough, R. V., M. A. Tolbert, C. P. McKay, and O. B. Toon (2010), Methane adsorption on a Martian soil analog: An abiogenic explanation for methane variability in the Martian atmosphere, *Icarus*, *207*, 165–174, doi:10.1016/j.icarus.2009.11.030.

Greeley, R., P. L. Whelley, R. E. Arvidson, N. A. Cabrol, D. J. Foley, B. J. Franklin, P. G. Geissler, M. P. Golombek, R. O. Kuzmin, G. A. Landis, M. T. Lemmon, L. D. V. Neakrase, S. W. Squyres, and S. D. Thompson (2006a), Active dust devils in Gusev crater, Mars: Observations from the Mars Exploration Rover Spirit, *J. Geophys. Res.*, *111*(E10), E12S09, doi:10.1029/2006JE002743.

Greeley, R., R. E. Arvidson, P. W. Barlett, D. Blaney, N. A. Cabrol, P. R. Christensen, R. L. Fergason, M. P. Golombek, G. A. Landis, M. T. Lemmon, S. M. McLennan, J. N. Maki, T. Michaels, J. E. Moersch, L. D. V. Neakrase, S. C. R. Rafkin, L. Richter, S. W. Squyres, P. A. de Souza, R. J. Sullivan, S. D. Thompson, and P. L. Whelley (2006b), Gusev crater: Wind-related features and processes observed by the Mars Exploration Rover Spirit, *J. Geophys. Res.*, *111*, E02S09, doi:10.1029/2005JE002491.

Grotzinger, J. P., R. E. Arvidson, J. F. Bell, W. Calvin, B. C. Clark, D. A. Fike, M. Golombek, R. Greeley, A. Haldemann, K. E. Herkenhoff, B. L. Jolliff, A. H. Knoll, M. Malin, S. M. McLennan, T. Parker, L. Soderblom, J. N. Sohl-Dickstein, S. W. Squyres, N. J. Tosca, and W. A. Watters (2005), Stratigraphy and sedimentology of a dry to wet eolian depositional system, Burns formation, Meridiani Planum, Mars, *Earth Planet. Sci. Lett.*, *240*, 11–72, doi:10.1016/j.epsl.2005.09.039.

Grotzinger, J. P., D. Y. Sumner, L. C. Kah, K. Stack, S. Gupta, L. Edgar, D. Rubin, K. Lewis, J. Schieber, N. Mangold, and et al. (2014), A Habitable Fluvio-Lacustrine Environment at Yellowknife Bay, Gale Crater, Mars, *Science*, *343*(6169), 1242777, doi:10.1126/science.1242777.

Gunson, M. R., M. M. Abbas, M. C. Abrams, M. Allen, L. R. Brown, T. L. Brown, A. Y. Chang, A. Goldman, F. W. Irion, L. L. Lowes, E. Mahieu, G. L. Manney, H. A. Michelsen, M. J. Newchurch, C. P. Rinsland, R. J. Salawitch, G. P. Stiller, G. C. Toon, Y. L. Yung, and R. Zander (1996), The Atmospheric Trace Molecule Spectroscopy (ATMOS) Experiment: Deployment on the ATLAS space shuttle missions, *Geophys. Res. Lett.*, *23*, 2333–2336, doi:10.1029/96GL01569.

Guzewich, S. D., E. R. Talaat, and D. W. Waugh (2012), Observations of planetary waves and nonmigrating tides by the Mars Climate Sounder, *J. Geophys. Res.*, *117*, E03010, doi:10.1029/2011JE003924.

Guzewich, S. D., E. R. Talaat, A. D. Toigo, D. W. Waugh, and T. H. McConnochie (2013a), High-altitude dust layers on Mars: Observations with the Thermal Emission Spectrometer, *J. Geophys. Res.*, *118*, 1177–1194, doi:10.1002/jgre.20076.

Guzewich, S. D., A. D. Toigo, M. I. Richardson, C. E. Newman, E. R. Talaat, D. W. Waugh, and T. H. McConnochie (2013b), The impact of a realistic vertical dust distribution on the simulation of the Martian General Circulation, *J. Geophys. Res.*, *118*, 980–993, doi:10.1002/jgre.20084.

Guzewich, S. D., M. D. Smith, and M. J. Wolff (2014), The vertical distribution of Martian aerosol particle size, *J. Geophys. Res.*, *119*, 2694–2708, doi:10.1002/2014JE004704.

Haberle, R. M., M. M. Joshi, J. R. Murphy, J. R. Barnes, J. T. Schofield, G. Wilson, M. Lopez-Valverde, J. L. Hollingsworth, A. F. C. Bridger, and J. Schaeffer (1999), General circulation model simulations of the Mars Pathfinder atmospheric structure investigation/meteorology data, *J. Geophys. Res.*, *104*, 8957–8974, doi:10.1029/1998JE900040.

Haberle, R. M., J. Gómez-Elvira, M. Torre Juárez, A.-M. Harri, J. L. Hollingsworth, H. Kahanpää, M. A. Kahre, M. Lemmon, F. J. Martín-Torres, M. Mischna, J. E. Moores, C. Newman, S. C. R. Rafkin, N. Rennó, M. I. Richardson, J. A. Rodríguez-Manfredi, A. R. Vasavada, and M.-P. Zorzano-Mier (2014), Preliminary interpretation of the REMS pressure data from the first 100 sols of the MSL mission, *J. Geophys. Res.*, *119*, 440–453, doi:10.1002/2013JE004488.

Hamilton, V. E., A. R. Vasavada, E. Sebastián, M. Torre Juárez, M. Ramos, C. Armiens, R. E. Arvidson, I. Carrasco, P. R. Christensen, M. A. De Pablo, W. Goetz, J. Gómez-Elvira, M. T. Lemmon, M. B. Madsen, F. J. Martín-Torres, J. Martínez-Frías, A. Molina, M. C. Palucis, S. C. R. Rafkin, M. I. Richardson, R. A. Yingst, and M.-P. Zorzano (2014), Observations and preliminary science results from the first 100 sols of MSL Rover Environmental Monitoring Station ground temperature sensor measurements at Gale Crater, *J. Geophys. Res.*, *119*, 745–770, doi:10.1002/2013JE004520.

Hamming, R. W. (1983), *Digital Filters*, 2^{nd} ed., Prentice-Hall, New Jersey.

Hanna, S. R., G. A. Briggs, and R. P. Hosker Jr. (1982), *Handbook on Atmospheric Diffusion*, Technical Information Center, U.S. Department of Energy, Springfield, Technical Report DOE/TIC-11223.

Hansen, C. J., M. Bourke, N. T. Bridges, S. Byrne, C. Colon, S. Diniega, C. Dundas, K. Herkenhoff, A. McEwen, M. Mellon, G. Portyankina, and N. Thomas (2011), Seasonal Erosion and Restoration of Mars' Northern Polar Dunes, *Science*, *331*, 575–578, doi:10.1126/science.1197636.

Harri, A.-M., M. Genzer, O. Kemppinen, J. Gomez-Elvira, R. Haberle, J. Polkko, H. Savijärvi, N. Rennó, J. A. Rodriguez-Manfredi, W. Schmidt, M. Richardson, T. Siili, M. Paton, M. D. L. Torre-Juarez, T. Mäkinen, C. Newman, S. Rafkin, M. Mischna, S. Merikallio, H. Haukka, J. Martín-Torres, M. Komu, M.-P. Zorzano, V. Peinado, L. Vazquez, and R. Urqui (2014), Mars Science Laboratory relative humidity observations: Initial results, *J. Geophys. Res.*, *119*, 2132–2147, doi:10.1002/2013JE004514.

Hartogh, P., M. I. Błecka, C. Jarchow, H. Sagawa, E. Lellouch, M. de Val-Borro, M. Rengel, A. S. Medvedev, B. M. Swinyard, R. Moreno, T. Cavalié, D. C. Lis, M. Banaszkiewicz, D. Bockelée-Morvan, J. Crovisier, T. Encrenaz, M. Küppers, L.-M. Lara, S. Szutowicz, B. Vandenbussche, F. Bensch, E. A. Bergin, F. Billebaud, N. Biver, G. A. Blake, J. A. D. L. Blommaert, J. Cernicharo, L. Decin, P. Encrenaz, H. Feuchtgruber,

T. Fulton, T. de Graauw, E. Jehin, M. Kidger, R. Lorente, D. A. Naylor, G. Portyankina, M. Sánchez-Portal, R. Schieder, S. Sidher, N. Thomas, E. Verdugo, C. Waelkens, A. Lorenzani, G. Tofani, E. Natale, J. Pearson, T. Klein, C. Leinz, R. Güsten, and C. Kramer (2010a), First results on Martian carbon monoxide from Herschel/HIFI observations, *Astron. Astrophys.*, *521*, L48, doi:10.1051/0004-6361/201015159.

Hartogh, P., C. Jarchow, E. Lellouch, M. de Val-Borro, M. Rengel, R. Moreno, A. S. Medvedev, H. Sagawa, B. M. Swinyard, T. Cavalié, D. C. Lis, M. I. Błęcka, M. Banaszkiewicz, D. Bockelée-Morvan, J. Crovisier, T. Encrenaz, M. Küppers, L.-M. Lara, S. Szutowicz, B. Vandenbussche, F. Bensch, E. A. Bergin, F. Billebaud, N. Biver, G. A. Blake, J. A. D. L. Blommaert, J. Cernicharo, L. Decin, P. Encrenaz, H. Feuchtgruber, T. Fulton, T. de Graauw, E. Jehin, M. Kidger, R. Lorente, D. A. Naylor, G. Portyankina, M. Sánchez-Portal, R. Schieder, S. Sidher, N. Thomas, E. Verdugo, C. Waelkens, N. Whyborn, D. Teyssier, F. Helmich, P. Roelfsema, J. Stutzki, H. G. Leduc, and J. A. Stern (2010b), Herschel/HIFI observations of Mars: First detection of O_2 at submillimetre wavelengths and upper limits on HCl and H_2O_2, *Astron. Astrophys.*, *521*, L49, doi:10.1051/0004-6361/201015160.

Hayne, P. O., D. A. Paige, J. T. Schofield, D. M. Kass, A. Kleinböhl, N. G. Heavens, and D. J. McCleese (2012), Carbon dioxide snow clouds on Mars: South polar winter observations by the Mars Climate Sounder, *J. Geophys. Res.*, *117*, E08014, doi:10.1029/2011JE004040.

Hayne, P. O., D. A. Paige, and N. G. Heavens (2014), The role of snowfall in forming the seasonal ice caps of Mars: Models and constraints from the Mars Climate Sounder, *Icarus*, *231*, 122–130, doi:10.1016/j.icarus.2013.10.020.

Heavens, N. G., J. L. Benson, D. M. Kass, A. Kleinböhl, W. A. Abdou, D. J. McCleese, M. I. Richardson, J. T. Schofield, J. H. Shirley, and P. M. Wolkenberg (2010), Water ice clouds over the Martian tropics during northern summer, *Geophys. Res. Lett.*, *37*, L18202, doi:10.1029/2010GL044610.

Heavens, N. G., M. I. Richardson, A. Kleinböhl, D. M. Kass, D. J. McCleese, W. Abdou, J. L. Benson, J. T. Schofield, J. H. Shirley, and P. M. Wolkenberg (2011), The vertical distribution of dust in the Martian atmosphere during northern spring and summer: Observations by the Mars Climate Sounder and analysis of zonal average vertical dust profiles, *J. Geophys. Res.*, *116*, E04003, doi:10.1029/2010JE003691.

Heavens, N. G., M. S. Johnson, W. A. Abdou, D. M. Kass, A. Kleinböhl, D. J. McCleese, J. H. Shirley, and R. J. Wilson (2014), Seasonal and diurnal variability of detached dust layers in the tropical Martian atmosphere, *J. Geophys. Res.*, *119*, 1748–1774, doi:10.1002/2014JE004619.

Hecht, M. H., S. P. Kounaves, R. C. Quinn, S. J. West, S. M. M. Young, D. W. Ming, D. C. Catling, B. C. Clark, W. V. Boynton, J. Hoffman, L. P. DeFlores, K. Gospodinova, J. Kapit, and P. H. Smith (2009), Detection of Perchlorate and the Soluble Chemistry of Martian Soil at the Phoenix Lander Site, *Science*, *325*, 64–67, doi:10.1126/science.1172466.

Hinson, D. P., M. D. Smith, and B. J. Conrath (2004), Comparison of atmospheric temperatures obtained through infrared sounding and radio occultation by Mars Global Surveyor, *J. Geophys. Res.*, *109*(E18), E12002, doi:10.1029/2004JE002344.

Hipkin, V., G. Dubreuil-Laniel, Y. Gonthier, T. Haltigin, R. Léveillé, E. Martin, and A. Monarque (2013), Canadian Space Agency Analogue Missions – Approach to Evaluation and Lessons Learned, in *Lunar Planet. Sci. Conf.*, vol. 44, p. 2952.

Hipkin, V. J., P. O. Wennberg, J. R. Drummond, G. C. Toon, M. Allen, J.-F. Blavier, L. R. Brown, A. Kleinböhl, J. P. D. Abbatt, B. Sherwood Lollar, K. Strong, K. A. Walker, P. F. Bernath, R. T. Clancy, E. A. Cloutis, D. J. Desmarais, J. M. Eiler, Y. Yung, T. Encrenaz, and J. C. McConnell (2011), The Mars atmospheric Trace Molecule Occultation Spectrometer: Science Objectives, in *Mars Atmosphere: Modelling and observation*, edited by F. Forget and E. Millour, pp. 482–483.

Holstein-Rathlou, C., H. P. Gunnlaugsson, J. P. Merrison, K. M. Bean, B. A. Cantor, J. A. Davis, R. Davy, N. B. Drake, M. D. Ellehoj, W. Goetz, S. F. Hviid, C. F. Lange, S. E. Larsen, M. T. Lemmon, M. B. Madsen, M. Malin, J. E. Moores, P. Nørnberg, P. Smith, L. K. Tamppari, and P. A. Taylor (2010), Winds at the Phoenix landing site, *J. Geophys. Res.*, *115*, E00E18, doi:10.1029/2009JE003411.

Holt, J. W., A. Safaeinili, J. J. Plaut, J. W. Head, R. J. Phillips, R. Seu, S. D. Kempf, P. Choudhary, D. A. Young, N. E. Putzig, D. Biccari, and Y. Gim (2008), Radar Sounding Evidence for Buried Glaciers in the Southern Mid-Latitudes of Mars, *Science*, *322*, 1235–1238, doi:10.1126/science.1164246.

Horita, J., and M. E. Berndt (1999), Abiogenic methane formation and isotopic fractionation under hydrothermal conditions, *Science*, *285*(5430), 1055–1057, doi:10.1126/science.285.5430.1055.

Hudson, T. L., and O. Aharonson (2008), Diffusion barriers at Mars surface conditions: Salt crusts, particle size mixtures, and dust, *J. Geophys. Res.*, *113*(E12), E09008, doi:10.1029/2007JE003026.

Hudson, T. L., O. Aharonson, N. Schorghofer, C. B. Farmer, M. H. Hecht, and N. T. Bridges (2007), Water vapor diffusion in Mars subsurface environments, *J. Geophys. Res.*, *112*(E11), E05016, doi:10.1029/2006JE002815.

Irion, F. W., M. R. Gunson, G. C. Toon, A. Y. Chang, A. Eldering, E. Mahieu, G. L. Manney, H. A. Michelsen, E. J. Moyer, M. J. Newchurch, G. B. Osterman, C. P. Rinsland, R. J. Salawitch, B. Sen, Y. L. Yung, and R. Zander (2002), Atmospheric Trace Molecule Spectroscopy (ATMOS) Experiment Version 3 data retrievals, *Appl. Opt.*, *41*, 6968–6979, doi:10.1364/AO.41.006968.

Izakov, M. N. (1978), The Martian upper atmosphere structure from the Viking spacecraft experiments, *Icarus*, *36*, 189–197, doi:10.1016/0019-1035(78)90103-3.

Kahre, M. A., J. R. Murphy, and R. M. Haberle (2006), Modeling the Martian dust cycle and surface dust reservoirs with the NASA Ames general circulation model, *J. Geophys. Res.*, *111*, E06008, doi:10.1029/2005JE002588.

Kalnay, E., M. Kanamitsu, R. Kistler, W. Collins, D. Deaven, L. Gandin, M. Iredell, S. Saha, G. White, J. Woollen, Y. Zhu, A. Leetmaa, B. Reynolds, M. Chelliah, W. Ebisuzaki, W. Higgins, J. Janowiak, K. C. Mo, C. Ropelewski, J. Wang, R. Jenne, and D. Joseph (1996), The NCEP/NCAR 40-Year Reanalysis Project., *Bull. Am. Astron. Soc.*, *77*, 437–472, doi:10.1175/1520-0477(1996)077⟨0437:TNYRP⟩2.0.CO;2.

Keller, J. M., W. V. Boynton, S. Karunatillake, V. R. Baker, J. M. Dohm, L. G. Evans, M. J. Finch, B. C. Hahn, D. K. Hamara, D. M. Janes, K. E. Kerry, H. E. Newsom, R. C. Reedy, A. L. Sprague, S. W. Squyres, R. D. Starr, G. J. Taylor, and R. M. S. Williams (2006), Equatorial and midlatitude distribution of chlorine measured by Mars Odyssey GRS, *J. Geophys. Res.*, *111*(E3), E03S08, doi:10.1029/2006JE002679.

Kelley, D. S., J. A. Karson, G. L. Früh-Green, D. R. Yoerger, T. M. Shank, D. A. Butterfield, J. M. Hayes, M. O. Schrenk, E. J. Olson, G. Proskurowski, M. Jakuba, A. Bradley, B. Larson, K. Ludwig, D. Glickson, K. Buckman, A. S. Bradley, W. J. Brazelton, K. Roe, M. J. Elend, A. Delacour, S. M. Bernasconi, M. D. Lilley, J. A. Baross, R. E. Summons, and S. P. Sylva (2005), A Serpentinite-Hosted Ecosystem: The Lost City Hydrothermal Field, *Science*, *307*, 1428–1434, doi:10.1126/science.1102556.

Kelly, N. J., W. V. Boynton, K. Kerry, D. Hamara, D. Janes, R. C. Reedy, K. J. Kim, and R. M. Haberle (2006), Seasonal polar carbon dioxide frost on Mars: CO_2 mass and columnar thickness distribution, *J. Geophys. Res.*, *111*(E3), E03S07, doi: 10.1029/2006JE002678.

Keppel-Aleks, G., G. C. Toon, P. O. Wennberg, and N. M. Deutscher (2007), Reducing the impact of source brightness fluctuations on spectra obtained by Fourier-transform spectrometry, *Appl. Opt.*, *46*, 4774–4779, doi:10.1364/AO.46.004774.

Kerzenmacher, T. E., K. A. Walker, K. Strong, R. Berman, P. F. Bernath, C. D. Boone, J. R. Drummond, H. Fast, A. Fraser, K. MacQuarrie, C. Midwinter, K. Sung, C. T. McElroy, R. L. Mittermeier, J. Walker, and H. Wu (2005), Measurements of O_3, NO_2 and Temperature during the 2004 Canadian Arctic ACE Validation Campaign, *Geophys. Res. Lett.*, *32*(16), L16S07, doi:10.1029/2005GL023032.

Kishore, P., S. P. Namboothiri, J. H. Jiang, V. Sivakumar, and K. Igarashi (2009), Global temperature estimates in the troposphere and stratosphere: a validation study of COSMIC/FORMOSAT-3 measurements, *Atmos. Chem. Phys.*, *9*, 897–908.

Kleinböhl, A., J. T. Schofield, D. M. Kass, W. A. Abdou, C. R. Backus, B. Sen, J. H. Shirley, W. G. Lawson, M. I. Richardson, F. W. Taylor, N. A. Teanby, and D. J. McCleese (2009), Mars Climate Sounder limb profile retrieval of atmospheric temperature, pressure, and dust and water ice opacity, *J. Geophys. Res.*, *114*(E13), E10,006, doi:10.1029/2009JE003358.

Kleinert, A., G. Aubertin, G. Perron, M. Birk, G. Wagner, F. Hase, H. Nett, and R. Poulin (2007), MIPAS Level 1B algorithms overview: operational processing and characterization, *Atmos. Chem. Phys.*, *7*, 1395–1406, doi:10.5194/acp-7-1395-2007.

Klingelhöfer, G., R. V. Morris, B. Bernhardt, C. Schröder, D. S. Rodionov, P. A. de Souza, A. Yen, R. Gellert, E. N. Evlanov, B. Zubkov, J. Foh, U. Bonnes, E. Kankeleit, P. Gütlich, D. W. Ming, F. Renz, T. Wdowiak, S. W. Squyres, and R. E. Arvidson (2004), Jarosite and Hematite at Meridiani Planum from Opportunity's Mössbauer Spectrometer, *Science*, *306*, 1740–1745, doi:10.1126/science.1104653.

Komguem, L., J. A. Whiteway, C. Dickinson, M. Daly, and M. T. Lemmon (2013), Phoenix LIDAR measurements of Mars atmospheric dust, *Icarus*, *223*, 649–653, doi: 10.1016/j.icarus.2013.01.020.

Korablev, O., V. I. Moroz, E. V. Petrova, and A. V. Rodin (2005), Optical properties of dust and the opacity of the Martian atmosphere, *Adv. Space Res.*, *35*, 21–30, doi:10.1016/j.asr.2003.04.061.

Korablev, O., A. Trokhimovsky, A. V. Grigoriev, A. Shakun, Y. S. Ivanov, B. Moshkin, K. Anufreychik, D. Timonin, I. Dziuban, Y. K. Kalinnikov, and F. Montmessin (2014), Three infrared spectrometers, an atmospheric chemistry suite for the ExoMars 2016 trace gas orbiter, *J. Appl. Remote Sens.*, *8*, 084983, doi:10.1117/1.JRS.8.084983.

Kounaves, S. P., M. H. Hecht, J. Kapit, R. C. Quinn, D. C. Catling, B. C. Clark, D. W. Ming, K. Gospodinova, P. Hredzak, K. McElhoney, and J. Shusterman (2010), Soluble sulfate in the martian soil at the Phoenix landing site, *Geophys. Res. Lett.*, *37*, L09201, doi:10.1029/2010GL042613.

Krasnopolsky, V. A. (2007), Long-term spectroscopic observations of Mars using IRTF/CSHELL: Mapping of O_2 dayglow, CO, and search for CH_4, *Icarus*, *190*, 93–102, doi:10.1016/j.icarus.2007.02.014.

Krasnopolsky, V. A. (2010), Solar activity variations of thermospheric temperatures on Mars and a problem of CO in the lower atmosphere, *Icarus*, *207*, 638–647, doi:10.1016/j.icarus.2009.12.036.

Krasnopolsky, V. A. (2011), Atmospheric chemistry on Venus, Earth, and Mars: Main features and comparison, *Planet and Space Sci.*, *59*, 952–964, doi:10.1016/j.pss.2010.02.011.

Krasnopolsky, V. A. (2012), Search for methane and upper limits to ethane and SO_2 on Mars, *Icarus*, *217*, 144–152, doi:10.1016/j.icarus.2011.10.019.

Krasnopolsky, V. A. (2015), Variations of the HDO/H_2O ratio in the martian atmosphere and loss of water from Mars, *Icarus*, *257*, 377–386, doi:10.1016/j.icarus.2015.05.021.

Krasnopolsky, V. A., and P. D. Feldman (2001), Detection of Molecular Hydrogen in the Atmosphere of Mars, *Science*, *294*, 1914–1917, doi:10.1126/science.1065569.

Krasnopolsky, V. A., and F. Lefèvre (2013), Chemistry of the Atmospheres of Mars, Venus, and Titan, in *Comparative Climatology of Terrestrial Planets*, edited by S. J. Mackwell, A. A. Simon-Miller, J. W. Harder, and M. A. Bullock, pp. 231–275, University of Arizona Press, Tuscon, doi:10.2458/azu_uapress_9780816530595-ch11.

Krasnopolsky, V. A., G. L. Bjoraker, M. J. Mumma, and D. E. Jennings (1997), High-resolution spectroscopy of Mars at 3.7 and 8 μm: A sensitive search of H_2O_2, H_2CO, HCl, and CH_4, and detection of HDO, *J. Geophys. Res.*, *102*, 6525–6534, doi:10.1029/96JE03766.

Krasnopolsky, V. A., J. P. Maillard, and T. C. Owen (2004), Detection of methane in the Martian atmosphere: evidence for life?, *Icarus*, *172*, 537–547, doi:10.1016/j.icarus.2004.07.004.

Kuze, A., H. Suto, K. Shiomi, T. Urabe, M. Nakajima, J. Yoshida, T. Kawashima, Y. Yamamoto, F. Kataoka, and H. Buijs (2012), Level 1 algorithms for TANSO on GOSAT: processing and on-orbit calibrations, *Atmos. Meas. Tech.*, *5*, 2447–2467, doi:10.5194/amt-5-2447-2012.

Langevin, Y., F. Poulet, J.-P. Bibring, and B. Gondet (2005), Sulfates in the North Polar Region of Mars Detected by OMEGA/Mars Express, *Science*, *307*, 1584–1586, doi:10.1126/science.1109091.

Laurent, A., and Y. Hébert (1979), Paragenesis of serpentine assemblages in harzburgite tectonite and dunite cumulate from the Québec Appalachians, *Can. Mineral.*, *17*, 857–869.

Lebonnois, S., E. Quémerais, F. Montmessin, F. Lefèvre, S. Perrier, J.-L. Bertaux, and F. Forget (2006), Vertical distribution of ozone on Mars as measured by SPICAM/Mars Express using stellar occultations, *J. Geophys. Res.*, *111*, E09S05, doi:10.1029/2005JE002643.

Lee, C., W. G. Lawson, M. I. Richardson, N. G. Heavens, A. Kleinböhl, D. Banfield, D. J. McCleese, R. Zurek, D. Kass, J. T. Schofield, C. B. Leovy, F. W. Taylor, and A. D. Toigo (2009), Thermal tides in the Martian middle atmosphere as seen by the Mars Climate Sounder, *J. Geophys. Res.*, *114*, E03005, doi:10.1029/2008JE003285.

Lefèvre, F., and F. Forget (2009), Observed variations of methane on Mars unexplained by known atmospheric chemistry and physics, *Nature*, *460*, 720–723, doi:10.1038/nature08228.

Lefèvre, F., J.-L. Bertaux, R. T. Clancy, T. Encrenaz, K. Fast, F. Forget, S. Lebonnois, F. Montmessin, and S. Perrier (2008), Heterogeneous chemistry in the atmosphere of Mars, *Nature*, *454*, 971–975, doi:10.1038/nature07116.

Lemmon, M. T., M. J. Wolff, M. D. Smith, R. T. Clancy, D. Banfield, G. A. Landis, A. Ghosh, P. H. Smith, N. Spanovich, B. Whitney, P. Whelley, R. Greeley, S. Thompson, J. F. Bell, and S. W. Squyres (2004), Atmospheric Imaging Results from the Mars Exploration Rovers: Spirit and Opportunity, *Science*, *306*, 1753–1756, doi:10.1126/science.1104474.

Lemmon, M. T., M. J. Wolff, J. F. Bell III, M. D. Smith, B. A. Cantor, and P. H. Smith (2015), Dust aerosol, clouds, and the atmospheric optical depth record over 5 Mars years of the Mars Exploration Rover mission, *Icarus*, *251*, 96–111, doi:10.1016/j.icarus.2014.03.029.

Leovy, C., and Y. Mintz (1969), Numerical Simulation of the Atmospheric Circulation and Climate of Mars., *J. Atmos. Sci.*, *26*, 1167–1190, doi:10.1175/1520-0469(1969)026⟨1167:NSOTAC⟩2.0.CO;2.

Lindal, G. F., H. B. Hotz, D. N. Sweetnam, Z. Shippony, J. P. Brenkle, G. V. Hartsell, and R. T. Spear (1979), Viking radio occultation measurements of the atmosphere and topography of Mars - Data acquired during 1 Martian year of tracking, *J. Geophys. Res.*, *84*, 8443–8456, doi:10.1029/JB084iB14p08443.

Liou, K. N. (2002), *An Introduction to Atmospheric Radiation*, Academic Press, San Diego.

López-Puertas, M., M. A. López-Valverde, C. P. Rinsland, and M. R. Gunson (1992), Analysis of the upper atmosphere $CO_2(nu_2)$ vibrational temperatures retrieved from ATMOS/Spacelab 3 observations, *J. Geophys. Res.*, *97*, 20,469–20,478, doi:10.1029/92JD02026.

Lundin, R., S. Barabash, H. Andersson, M. Holmström, A. Grigoriev, M. Yamauchi, J.-A. Sauvaud, A. Fedorov, E. Budnik, J.-J. Thocaven, D. Winningham, R. Frahm, J. Scherrer, J. Sharber, K. Asamura, H. Hayakawa, A. Coates, D. R. Linder, C. Curtis, K. C. Hsieh, B. R. Sandel, M. Grande, M. Carter, D. H. Reading, H. Koskinen, E. Kallio, P. Riihela, W. Schmidt, T. Säles, J. Kozyra, N. Krupp, J. Woch, J. Luhmann, S. McKenna-Lawler, R. Cerulli-Irelli, S. Orsini, M. Maggi, A. Mura, A. Milillo, E. Roelof, D. Williams, S. Livi, P. Brandt, P. Wurz, and P. Bochsler (2004), Solar Wind-Induced Atmospheric Erosion at Mars: First Results from ASPERA-3 on Mars Express, *Science*, *305*, 1933–1936, doi:10.1126/science.1101860.

Määttänen, A., T. Fouchet, O. Forni, F. Forget, H. Savijärvi, B. Gondet, R. Melchiorri, Y. Langevin, V. Formisano, M. Giuranna, and J.-P. Bibring (2009a), A study of the

properties of a local dust storm with Mars Express OMEGA and PFS data, *Icarus*, *201*, 504–516.

Määttänen, A., T. Fouchet, O. Forni, F. Forget, H. Savijärvi, B. Gondet, R. Melchiorri, Y. Langevin, V. Formisano, M. Giuranna, and J.-P. Bibring (2009b), A study of the properties of a local dust storm with Mars Express OMEGA and PFS data, *Icarus*, *201*, 504–516, doi:10.1016/j.icarus.2009.01.024.

Madeleine, J.-B., F. Forget, E. Millour, L. Montabone, and M. J. Wolff (2011), Revisiting the radiative impact of dust on Mars using the LMD Global Climate Model, *J. Geophys. Res.*, *116*(E15), E11,010.

Maguire, W. C. (1977), Martian isotopic ratios and upper limits for possible minor constituents as derived from Mariner 9 infrared spectrometer data, *Icarus*, *32*, 85–97, doi:10.1016/0019-1035(77)90051-3.

Mahaffy, P. R., C. R. Webster, S. K. Atreya, H. Franz, M. Wong, P. G. Conrad, D. Harpold, J. J. Jones, L. A. Leshin, H. Manning, T. Owen, R. O. Pepin, S. Squyres, M. Trainer, and the MSL Science Team (2013), Abundance and Isotopic Composition of Gases in the Martian Atmosphere from the Curiosity Rover, *Science*, *341*, 263–266, doi:10.1126/science.1237966.

Mahaffy, P. R., C. R. Webster, J. C. Stern, A. E. Brunner, S. K. Atreya, P. G. Conrad, S. Domagal-Goldman, J. L. Eigenbrode, G. J. Flesch, L. E. Christensen, H. B. Franz, C. Freissinet, D. P. Glavin, J. P. Grotzinger, J. H. Jones, L. A. Leshin, C. Malespin, A. C. McAdam, D. W. Ming, R. Navarro-González, P. B. Niles, T. Owen, A. A. Pavlov, A. Steele, M. G. Trainer, K. H. Williford, J. J. Wray, and the MSL Science Team (2015), The imprint of atmospheric evolution in the D/H of Hesperian clay minerals on Mars, *Science*, *347*, 412–414, doi:10.1126/science.1260291.

Maltagliati, L., F. Montmessin, A. Fedorova, O. Korablev, F. Forget, and J.-L. Bertaux (2011), Evidence of Water Vapor in Excess of Saturation in the Atmosphere of Mars, *Science*, *333*, 1868–1871, doi:10.1126/science.1207957.

Maltagliati, L., F. Montmessin, O. Korablev, A. Fedorova, F. Forget, A. Määttänen, F. Lefèvre, and J.-L. Bertaux (2013), Annual survey of water vapor vertical distribution and water-aerosol coupling in the martian atmosphere observed by SPICAM/MEx solar occultations, *Icarus*, *223*, 942–962.

Mamun, A., J. Kaminski, A. Lupu, K. Semeniuk, and J. C. McConnell (2013), Evaluation of Stratospheric Temperature and Water Vapor from GEM using ACE-FTS and MLS Measurements, in *ACE at 10: Solar Occultation Anthology*, edited by P. F. Bernath, pp. 295–302, A. Deepak Publishing, Hampton, Virg.

Mancinelli, R. L., and A. Banin (2003), Where is the nitrogen on Mars?, *Int. J. Astrobiol.*, *2*, 217–225, doi:10.1017/S1473550403001599.

Mangold, N., C. Quantin, V. Ansan, C. Delacourt, and P. Allemand (2004), Evidence for Precipitation on Mars from Dendritic Valleys in the Valles Marineris Area, *Science*, *305*, 78–81, doi:10.1126/science.1097549.

Manney, G. L., W. H. Daffer, K. B. Strawbridge, K. A. Walker, C. D. Boone, P. F. Bernath, T. Kerzenmacher, M. J. Schwartz, K. Strong, R. J. Sica, K. Krüger, H. C. Pumphrey, A. Lambert, M. L. Santee, N. J. Livesey, E. E. Remsberg, M. G. Mlynczak, and J. R. Russell III (2008), The high Arctic in extreme winters: vortex, temperature, and MLS and ACE-FTS trace gas evolution, *Atmos. Chem. Phys.*, *8*, 505–522.

Markiewicz, W. J., R. M. Sablotny, H. U. Keller, N. Thomas, D. Titov, and P. H. Smith (1999), Optical properties of the Martian aerosols as derived from Imager for Mars Pathfinder midday sky brightness data, *J. Geophys. Res.*, *104*, 9009–9018, doi: 10.1029/1998JE900033.

Marshall, B. T., L. E. Deaver, R. E. Thompson, L. L. Gordley, M. J. McHugh, M. E. Hervig, and J. M. Russell III (2011), Retrieval of temperature and pressure using broadband solar occultation: SOFIE approach and results, *Atmos. Meas. Tech.*, *4*, 893–907, doi:10.5194/amt-4-893-2011.

Mau, S., D. L. Valentine, J. F. Clark, J. Reed, R. Camilli, and L. Washburn (2007), Dissolved methane distributions and air-sea flux in the plume of a massive seep field, Coal Oil Point, California, *J. Geophys. Res.*, *34*, L22603, doi:10.1029/2007GL031344.

McCleese, D. J., N. G. Heavens, J. T. Schofield, W. A. Abdou, J. L. Bandfield, S. B. Calcutt, P. G. J. Irwin, D. M. Kass, A. Kleinböhl, S. R. Lewis, D. A. Paige, P. L. Read, M. I. Richardson, J. H. Shirley, F. W. Taylor, N. Teanby, and R. W. Zurek (2010), Structure and dynamics of the Martian lower and middle atmosphere as observed by the Mars Climate Sounder: Seasonal variations in zonal mean temperature, dust, and water ice aerosols, *J. Geophys. Res.*, *115*(E14), E12016, doi:10.1029/2010JE003677.

McEwen, A. S., L. Ojha, C. M. Dundas, S. S. Mattson, S. Byrne, J. J. Wray, S. C. Cull, S. L. Murchie, N. Thomas, and V. C. Gulick (2011), Seasonal Flows on Warm Martian Slopes, *Science*, *333*, 740–743, doi:10.1126/science.1204816.

Mertz, L. (1967), Auxiliary computation for fourier spectrometry, *Infrared Phys.*, *7*(1), 17–23, doi:10.1016/0020-0891(67)90026-7.

Ming, D. W., P. D. Archer, D. P. Glavin, J. L. Eigenbrode, H. B. Franz, B. Sutter, A. E. Brunner, J. C. Stern, C. Freissinet, A. C. McAdam, and et al. (2014), Volatile and Organic Compositions of Sedimentary Rocks in Yellowknife Bay, Gale Crater, Mars, *Science*, *343*(6169), 1245267, doi:10.1126/science.1245267.

Mischna, M. A., M. Allen, M. I. Richardson, C. E. Newman, and A. D. Toigo (2011), Atmospheric modeling of Mars methane surface releases, *Planet and Space Sci.*, *59*, 227–237, doi:10.1016/j.pss.2010.07.005.

Montabone, L., F. Forget, E. Millour, R. J. Wilson, S. R. Lewis, B. Cantor, D. Kass, A. Kleinböhl, M. T. Lemmon, M. D. Smith, and M. J. Wolff (2015), Eight-year climatology of dust optical depth on Mars, *Icarus*, *251*, 65–95, doi:10.1016/j.icarus.2014.12.034.

Montmessin, F., and F. Lefèvre (2013), Transport-driven formation of a polar ozone layer on Mars, *Nat. Geosci.*, *6*, 930–933, doi:10.1038/ngeo1957.

Montmessin, F., E. Quémerais, J. L. Bertaux, O. Korablev, P. Rannou, and S. Lebonnois (2006), Stellar occultations at UV wavelengths by the SPICAM instrument: Retrieval and analysis of Martian haze profiles, *Journal of Geophysical Research (Planets)*, *111*, E09S09, doi:10.1029/2005JE002662.

Montmessin, F., B. Gondet, J.-P. Bibring, Y. Langevin, P. Drossart, F. Forget, and T. Fouchet (2007), Hyperspectral imaging of convective CO_2 ice clouds in the equatorial mesosphere of Mars, *J. Geophys. Res.*, *112*(E11), E11S90, doi:10.1029/2007JE002944.

Moores, J. E., M. T. Lemmon, P. H. Smith, L. Komguem, and J. A. Whiteway (2010), Atmospheric dynamics at the Phoenix landing site as seen by the Surface Stereo Imager, *J. Geophys. Res.*, *115*, E00E08, doi:10.1029/2009JE003409.

Mouginot, J., A. Pommerol, P. Beck, W. Kofman, and S. M. Clifford (2012), Dielectric map of the Martian northern hemisphere and the nature of plain filling materials, *Geophys. Res. Lett.*, *39*, L02202, doi:10.1029/2011GL050286.

Mumma, M. J., G. L. Villanueva, R. E. Novak, T. Hewagama, B. P. Bonev, M. A. DiSanti, A. M. Mandell, and M. D. Smith (2009), Strong Release of Methane on Mars in Northern Summer 2003, *Science*, *323*, 1041–1045, doi:10.1126/science.1165243.

Murchie, S. L., J. F. Mustard, B. L. Ehlmann, R. E. Milliken, J. L. Bishop, N. K. McKeown, E. Z. Noe Dobrea, F. P. Seelos, D. L. Buczkowski, S. M. Wiseman, R. E. Arvidson, J. J. Wray, G. Swayze, R. N. Clark, D. J. Des Marais, A. S. McEwen, and J.-P. Bibring (2009), A synthesis of Martian aqueous mineralogy after 1 Mars year of observations from the Mars Reconnaissance Orbiter, *J. Geophys. Res.*, *114*, E00D06, doi:10.1029/2009JE003342.

Mustard, J. F., S. L. Murchie, S. M. Pelkey, B. L. Ehlmann, R. E. Milliken, J. A. Grant, J.-P. Bibring, F. Poulet, J. Bishop, E. N. Dobrea, L. Roach, F. Seelos, R. E. Arvidson, S. Wiseman, R. Green, C. Hash, D. Humm, E. Malaret, J. A. McGovern, K. Seelos, T. Clancy, R. Clark, D. D. Marais, N. Izenberg, A. Knudson, Y. Langevin, T. Martin, P. McGuire, R. Morris, M. Robinson, T. Roush, M. Smith, G. Swayze, H. Taylor, T. Titus, and M. Wolff (2008), Hydrated silicate minerals on Mars observed by the Mars Reconnaissance Orbiter CRISM instrument, *Nature*, *454*, 305–309, doi:10.1038/nature07097.

NASA (2013), FY 2014 President's budget request summary, `www.nasa.gov/content/fy-2014-budget-proposal/`, retrieved 8 Oct. 2015.

NASA (2015), FY 2016 President's budget request summary, `www.nasa.gov/news/budget/index.html`, retrieved 8 Oct. 2015.

NASA/JPL/Goddard/ASU/Cornell (2004), A Full Profile on Mars Temperature, `www.jpl.nasa.gov/missions/mer/images.cfm?id=1078`, retrieved 8 Oct. 2015.

Navarro, T., F. Forget, E. Millour, and S. J. Greybush (2014), Detection of detached dust layers in the Martian atmosphere from their thermal signature using assimilation, *Geophys. Res. Lett.*, *41*, 6620–6626, doi:10.1002/2014GL061377.

Neary, L., and F. Daerden (2014), The GEM-Mars GCM: Current Status and Evaluation, in *Mars Atmosphere: Modelling and observation*, edited by F. Forget and M. Millour, p. 1207.

Neubeck, A., N. Duc, D. Bastviken, P. Crill, and N. Holm (2011), Formation of H_2 and CH_4 by weathering of olivine at temperatures between 30 and 70°C, *Geochem. Trans.*, *12*, doi:10.1186/1467-4866-12-6.

Nier, A. O., and M. B. McElroy (1976), Structure of the neutral upper atmosphere of Mars - Results from Viking 1 and Viking 2, *Science*, *194*, 1298–1300, doi:10.1126/science.194.4271.1298.

Niles, P. B., W. V. Boynton, J. H. Hoffman, D. W. Ming, and D. Hamara (2010), Stable Isotope Measurements of Martian Atmospheric CO_2 at the Phoenix Landing Site, *Science*, *329*, 1334–1337, doi:10.1126/science.1192863.

Norton, R. H., and C. P. Rinsland (1991), ATMOS data processing and science analysis methods, *Appl. Opt.*, *30*, 389–400, doi:10.1364/AO.30.000389.

Notholt, J., G. Toon, N. Jones, D. Griffith, and T. Warneke (2006), Spectral line finding program for atmospheric remote sensing using full radiation transfer, *J. Quant. Spectrosc. Radiat. Transfer*, *97*, 112–125, doi:10.1016/j.jqsrt.2004.12.025.

Nowlan, C. R., J. R. Drummond, C. T. McElroy, and D. V. Barton (2013), Solar Occultation Measurements of Atmospheric Pressure and Temperature from the A- and B-bands of Molecular Oxygen, in *ACE at 10: Solar Occultation Anthology*, edited by P. F. Bernath, pp. 261–270, A. Deepak Publishing, Hampton, Virg.

Ockert-Bell, M. E., J. F. Bell, J. B. Pollack, C. P. McKay, and F. Forget (1997), Absorption and scattering properties of the Martian dust in the solar wavelengths, *J. Geophys. Res.*, *102*, 9039–9050, doi:10.1029/96JE03991.

Ojha, L., M. B. Wilhelm, S. L. Murchie, A. S. McEwen, J. J. Wray, J. Hanley, M. Massé, and M. Chojnacki (2015), Spectral evidence for hydrated salts in recurring slope lineae on Mars, *Nat. Geosci.*, *8*, 829–832, doi:10.1038/ngeo2546.

Olsen, K. S., E. Cloutis, and K. Strong (2012), Small-scale methane dispersion modelling for possible plume sources on the surface of Mars, *Geophys. Res. Lett.*, *39*, L19201, doi:10.1029/2012GL052922.

Olsen, K. S., G. C. Toon, C. D. Boone, and K. Strong (2015a), New temperature and pressure retrieval algorithm for high-resolution infrared solar occultation spectrometry: analysis and validation against ACE-FTS and COSMIC, *Atmos. Meas. Tech. Disc.*, *8*, 10,823–10,873, doi:10.5194/amtd-8-10823-2015.

Olsen, K. S., G. C. Toon, and K. Strong (2015b), Simulation of source intensity variations from atmospheric dust for solar occultation Fourier transform infrared spectroscopy, *J. Mol. Spectrosc.*, doi:10.1016/j.jms.2015.11.008, accepted manuscript in press.

Owen, T. (1992), The composition and early history of the atmosphere of Mars, in *Mars*, edited by M. George, pp. 818–834.

Owen, T., K. Biemann, J. E. Biller, A. L. Lafleur, D. R. Rushneck, and D. W. Howarth (1977), The composition of the atmosphere at the surface of Mars, *J. Geophys. Res.*, *82*, 4635–4639, doi:10.1029/JS082i028p04635.

Oze, C., and M. Sharma (2005), Have olivine, will gas: Serpentinization and the abiogenic production of methane on Mars, *Geophys. Res. Lett.*, *32*, L10,203, doi: 10.1029/2005GL022691.

Pankine, A. A., L. K. Tamppari, and M. D. Smith (2009), Water vapor variability in the north polar region of Mars from Viking MAWD and MGS TES datasets, *Icarus*, *204*, 87–102, doi:10.1016/j.icarus.2009.06.009.

Petri, C., T. Warneke, N. Jones, T. Ridder, J. Messerschmidt, T. Weinzierl, M. Geibel, and J. Notholt (2012), Remote sensing of CO_2 and CH_4 using solar absorption spectrometry with a low resolution spectrometer, *Atmos. Meas. Tech.*, *5*, 1627–1635, doi: 10.5194/amt-5-1627-2012.

Phillips, R. J., M. T. Zuber, S. E. Smrekar, M. T. Mellon, J. W. Head, K. L. Tanaka, N. E. Putzig, S. M. Milkovich, B. A. Campbell, J. J. Plaut, A. Safaeinili, R. Seu, D. Biccari, L. M. Carter, G. Picardi, R. Orosei, P. S. Mohit, E. Heggy, R. W. Zurek, A. F. Egan, E. Giacomoni, F. Russo, M. Cutigni, E. Pettinelli, J. W. Holt, C. J. Leuschen, and L. Marinangeli (2008), Mars North Polar Deposits: Stratigraphy, Age, and Geodynamical Response, *Science*, *320*, 1182–1185, doi:10.1126/science.1157546.

Picone, J. M., A. E. Hedin, D. P. Drob, and A. C. Aikin (2002), NRLMSISE-00 empirical model of the atmosphere: Statistical comparisons and scientific issues, *J. Geophys. Res.*, *107*(A12), 1486, doi:10.1029/2002JA009430.

Pinet, N., and A. Tremblay (1995), Tectonic evolution of the Quebec-Maine Appalachians; from oceanic spreading to obduction and collision in the Northern Appalachians, *Am. J. Sci.*, *295*, 173–200, doi:10.2475/ajs.295.2.173.

Plaut, J. J., G. Picardi, A. Safaeinili, A. B. Ivanov, S. M. Milkovich, A. Cicchetti, W. Kofman, J. Mouginot, W. M. Farrell, R. J. Phillips, S. M. Clifford, A. Frigeri, R. Orosei, C. Federico, I. P. Williams, D. A. Gurnett, E. Nielsen, T. Hagfors, E. Heggy, E. R. Stofan, D. Plettemeier, T. R. Watters, C. J. Leuschen, and P. Edenhofer (2007),

Subsurface Radar Sounding of the South Polar Layered Deposits of Mars, *Science*, *316*, 92–95, doi:10.1126/science.1139672.

Pollack, J. B., D. Colburn, R. Kahn, J. Hunter, W. van Camp, C. E. Carlston, and M. R. Wolf (1977), Properties of aerosols in the Martian atmosphere, as inferred from Viking Lander imaging data, *J. Geophys. Res.*, *82*, 4479–4496, doi:10.1029/JS082i028p04479.

Pollack, J. B., D. S. Colburn, F. M. Flasar, R. Kahn, C. E. Carlston, and D. G. Pidek (1979), Properties and effects of dust particles suspended in the Martian atmosphere, *J. Geophys. Res.*, *84*, 2929–2945, doi:10.1029/JB084iB06p02929.

Pollack, J. B., M. E. Ockert-Bell, and M. K. Shepard (1995), Viking Lander image analysis of Martian atmospheric dust, *J. Geophys. Res.*, *100*, 5235–5250, doi:10.1029/94JE02640.

Poulet, F., J.-P. Bibring, J. F. Mustard, A. Gendrin, N. Mangold, Y. Langevin, R. E. Arvidson, B. Gondet, and C. Gomez (2005), Phyllosilicates on Mars and implications for early Martian climate, *Nature*, *438*, 623–627, doi:10.1038/nature04274.

Putzig, N. E., R. J. Phillips, B. A. Campbell, J. W. Holt, J. J. Plaut, L. M. Carter, A. F. Egan, F. Bernardini, A. Safaeinili, and R. Seu (2009), Subsurface structure of Planum Boreum from Mars Reconnaissance Orbiter Shallow Radar soundings, *Icarus*, *204*, 443–457, doi:10.1016/j.icarus.2009.07.034.

Qadi, A., E. Cloutis, C. Samson, L. Whyte, A. Ellery, J. F. Bell, G. Berard, A. Boivin, E. Haddad, J. Lavoie, W. Jamroz, R. Kruzelecky, A. Mack, P. Mann, K. Olsen, M. Perrot, D. Popa, T. Rhind, R. Sharma, J. Stromberg, K. Strong, A. Tremblay, R. Wilhelm, B. Wing, and B. Wong (2015), Mars methane analogue mission: Mission simulation and rover operations at Jeffrey Mine and Norbestos Mine Quebec, Canada, *Adv. Space Res.*, *55*, 2414–2426, doi:10.1016/j.asr.2014.12.008.

Quesnel, Y., C. Sotin, B. Langlais, S. Costin, M. Mandea, M. Gottschalk, and J. Dyment (2009), Serpentinization of the martian crust during Noachian, *Earth Planet. Sci. Lett.*, *277*, 184–193, doi:10.1016/j.epsl.2008.10.012.

Rafkin, S. C. R., R. M. Haberle, and T. I. Michaels (2001), The Mars Regional Atmospheric Modeling System: Model Description and Selected Simulations, *Icarus*, *151*, 228–256, doi:10.1006/icar.2001.6605.

Rafkin, S. C. R., J. L. Hollingsworth, M. A. Mischna, C. E. Newman, and M. I. Richardson (2013), Mars: Atmosphere and Climate Overview, in *Comparative Climatology of Terrestrial Planets*, edited by S. J. Mackwell, A. A. Simon-Miller, J. W. Harder, and M. A. Bullock, pp. 55–89, University of Arizona Press, Tuscon, doi: 10.2458/azu_uapress_9780816530595-ch003.

Rannou, P., S. Perrier, J.-L. Bertaux, F. Montmessin, O. Korablev, and A. Rébérac (2006), Dust and cloud detection at the Mars limb with UV scattered sunlight with SPICAM, *J. Geophys. Res.*, *111*(E10), E09S10, doi:10.1029/2006JE002693.

Reid, R. C., J. M. Prausnitz, and B. E. Poling (1987), *The Properties of Liquids and Gases*, 4^{th} ed., McGraw-Hill, New York.

Richardson, M. I., A. D. Toigo, and C. E. Newman (2007), PlanetWRF: A general purpose, local to global numerical model for planetary atmospheric and climate dynamics, *J. Geophys. Res.*, *112*, E09,001, doi:10.1029/2006JE002825.

Ridder, T., T. Warneke, and J. Notholt (2011), Source brightness fluctuation correction of solar absorption fourier transform mid infrared spectra, *Atmos. Meas. Tech.*, *4*, 1045–1051, doi:10.5194/amt-4-1045-2011.

Rinsland, C. P., M. R. Gunson, R. Zander, and M. López-Puertas (1992), Middle and upper atmosphere pressure-temperature profiles and the abundances of CO_2 and CO in the upper atmosphere from ATMOS/Spacelab 3 observations, *J. Geophys. Res.*, *97*, 20,479–20,495, doi:10.1029/92JD01622.

Rodgers, C. D. (2000), *Inverse Methods For Atmospheric Sounding*, World Scientific, Singapore.

Rodrigo, R., E. Garcia-Alvarez, M. J. López-González, and M. A. Lopez-Valerde (1990), Estimates of eddy diffusiona coefficient in the Mars' atmosphere, *Atmósfera*, *3*, 31–43.

Rothman, L. S., R. L. Hawkins, R. B. Wattson, and R. R. Gamache (1992), Energy levels, intensities, and linewidths of atmospheric carbon dioxide bands, *J. Quant. Spectrosc. Radiat. Transfer*, *48*, 537–566, doi:10.1016/0022-4073(92)90119-O.

Rothman, L. S., C. P. Rinsland, A. Goldman, S. T. Massie, D. P. Edwards, J.-M. Flaud, A. Perrin, C. Camy-Peyret, V. Dana, J.-Y. Mandin, J. Schroeder, A. Mccann, R. R. Gamache, R. B. Wattson, K. Yoshino, K. V. Chance, K. W. Jucks, L. R. Brown, V. Namtchinov, and P. Varanasi (1998), The HITRAN molecular spectroscopic

database and HAWKS (HITRAN atmospheric workstation): 1996 edition, *J. Quant. Spectrosc. Radiat. Transfer*, *60*(5), 665–710, doi:10.1016/S0022-4073(98)00078-8.

Rothman, L. S., I. E. Gordon, Y. Babikov, A. Barbe, D. Chris Benner, P. F. Bernath, M. Birk, L. Bizzocchi, V. Boudon, L. R. Brown, A. Campargue, K. Chance, E. A. Cohen, L. H. Coudert, V. M. Devi, B. J. Drouin, A. Fayt, J.-M. Flaud, R. R. Gamache, J. J. Harrison, J.-M. Hartmann, C. Hill, J. T. Hodges, D. Jacquemart, A. Jolly, J. Lamouroux, R. J. Le Roy, G. Li, D. A. Long, O. M. Lyulin, C. J. Mackie, S. T. Massie, S. Mikhailenko, H. S. P. Müller, O. V. Naumenko, A. V. Nikitin, J. Orphal, V. Perevalov, A. Perrin, E. R. Polovtseva, C. Richard, M. A. H. Smith, E. Starikova, K. Sung, S. Tashkun, J. Tennyson, G. C. Toon, V. G. Tyuterev, and G. Wagner (2013), The HITRAN2012 molecular spectroscopic database, *J. Quant. Spectrosc. Radiat. Transfer*, *130*, 4–50, doi:10.1016/j.jqsrt.2013.07.002.

Russell, P., N. Thomas, S. Byrne, K. Herkenhoff, K. Fishbaugh, N. Bridges, C. Okubo, M. Milazzo, I. Daubar, C. Hansen, and A. McEwen (2008), Seasonally active frost-dust avalanches on a north polar scarp of Mars captured by HiRISE, *Geophys. Res. Lett.*, *35*, L23204, doi:10.1029/2008GL035790.

Savitzky, A., and M. J. E. Golay (1964), Smoothing and differentiation of data by simplified least squares procedures., *Anal. Chem.*, *36*(8), 1627–1639, doi:10.1021/ac60214a047.

Schofield, J. T., J. R. Barnes, D. Crisp, R. M. Haberle, S. Larsen, J. A. Magalhaes, J. R. Murphy, A. Seiff, and G. Wilson (1997), The Mars Pathfinder Atmospheric Structure Investigation/Meteorology, *Science*, *278*, 1752–1757, doi:10.1126/science.278.5344.1752.

Schreiner, W., C. Rocken, S. Sokolovskiy, S. Syndergaard, and D. Hunt (2007), Estimates of the precision of GPS radio occultations from the COSMIC/FORMOSAT-3 mission, *Geophys. Res. Lett.*, *34*, L04808, doi:10.1029/2006GL027557.

Schwartz, M. J., A. Lambert, G. L. Manney, W. G. Read, N. J. Livesey, L. Froidevaux, C. O. Ao, P. F. Bernath, C. D. Boone, R. E. Cofield, W. H. Daffer, B. J. Drouin, E. J. Fetzer, R. A. Fuller, R. F. Jarnot, J. H. Jiang, Y. B. Jiang, B. W. Knosp, K. Krüger, J.-L. F. Li, M. G. Mlynczak, S. Pawson, J. M. Russell, M. L. Santee, W. V. Snyder, P. C. Stek, R. P. Thurstans, A. M. Tompkins, P. A. Wagner, K. A. Walker, J. W. Waters, and D. L. Wu (2008), Validation of the Aura Microwave Limb Sounder temperature

and geopotential height measurements, *J. Geophys. Res.*, *113*(D12), D15S11, doi:10.1029/2007JD008783.

Sheese, P. E., K. Strong, E. J. Llewellyn, R. L. Gattinger, J. M. Russell III, C. D. Boone, M. E. Hervig, R. J. Sica, and J. Bandoro (2012), Assessment of the quality of OSIRIS mesospheric temperatures using satellite and ground-based measurements, *Atmos. Meas. Tech.*, *5*, 2993–3006, doi:10.5194/amt-5-2993-2012.

Sherwood Lollar, B., G. Lacrampe-Couloume, K. Voglesonger, T. C. Onstott, L. M. Pratt, and G. F. Slater (2008), Isotopic signatures of CH_4 and higher hydrocarbon gases from Precambrian Shield sites: A model for abiogenic polymerization of hydrocarbons, *Geochim. Cosmochim. Acta*, *72*, 4778–4795, doi:10.1016/j.gca.2008.07.004.

Shirley, J. H., T. H. McConnochie, D. M. Kass, A. Kleinböhl, J. T. Schofield, N. G. Heavens, D. J. McCleese, J. Benson, D. P. Hinson, and J. L. Bandfield (2015), Temperatures and aerosol opacities of the Mars atmosphere at aphelion: Validation and inter-comparison of limb sounding profiles from MRO/MCS and MGS/TES, *Icarus*, *251*, 26–49, doi:10.1016/j.icarus.2014.05.011.

Sica, R. J., M. R. M. Izawa, K. A. Walker, C. Boone, S. V. Petelina, P. S. Argall, P. Bernath, G. B. Burns, V. Catoire, R. L. Collins, W. H. Daffer, C. de Clercq, Z. Y. Fan, B. J. Firanski, W. J. R. French, P. Gerard, M. Gerding, J. Granville, J. L. Innis, P. Keckhut, T. Kerzenmacher, A. R. Klekociuk, E. Kyrö, J. C. Lambert, E. J. Llewellyn, G. L. Manney, I. S. McDermid, K. Mizutani, Y. Murayama, C. Piccolo, P. Raspollini, M. Ridolfi, C. Robert, W. Steinbrecht, K. B. Strawbridge, K. Strong, R. Stübi, and B. Thurairajah (2008), Validation of the Atmospheric Chemistry Experiment (ACE) version 2.2 temperature using ground-based and space-borne measurements, *Atmos. Chem. Phys.*, *8*, 35–62.

Sindoni, G., V. Formisano, and A. Geminale (2011), Observations of water vapour and carbon monoxide in the Martian atmosphere with the SWC of PFS/MEX, *Planet and Space Sci.*, *59*, 149–162, doi:10.1016/j.pss.2010.12.006.

Sioris, C. E., C. D. Boone, P. F. Bernath, J. Zou, C. T. McElroy, and C. A. McLinden (2010), Atmospheric Chemistry Experiment (ACE) observations of aerosol in the upper troposphere and lower stratosphere from the Kasatochi volcanic eruption, *J. Geophys. Res.*, *115*, D00L14, doi:10.1029/2009JD013469.

Sleep, N. H., A. Meibom, T. Fridriksson, R. G. Coleman, and D. K. Bird (2004), H_2-rich

fluids from serpentinization: Geochemical and biotic implications, *Proc. Natl. Acad. Sci.*, *101*, 12,818–12,823, doi:10.1073/pnas.0405289101.

Smith, D., G. Neumann, P. Ford, R. E. Arvidson, E. A. Guinness, and S. Slavney (1999), Mars Global Surveyor Laser Altimeter Precision Experiment Data Record, *Tech. rep.*, NASA Planetary Data System, MGS-M-MOLA-3-PEDR-L1A-V1.0.

Smith, M. D. (2002), The annual cycle of water vapor on Mars as observed by the Thermal Emission Spectrometer, *J. Geophys. Res.*, *107*, 5115, doi:10.1029/2001JE001522.

Smith, M. D. (2004), Interannual variability in TES atmospheric observations of Mars during 1999-2003, *Icarus*, *167*, 148–165, doi:10.1016/j.icarus.2003.09.010.

Smith, M. D. (2009), THEMIS observations of Mars aerosol optical depth from 2002-2008, *Icarus*, *202*, 444–452, doi:10.1016/j.icarus.2009.03.027.

Smith, M. D., J. C. Pearl, B. J. Conrath, and P. R. Christensen (2000), Mars Global Surveyor Thermal Emission Spectrometer (TES) observations of dust opacity during aerobraking and science phasing, *J. Geophys. Res.*, *105*, 9539–9552, doi:10.1029/1999JE001097.

Smith, M. D., J. L. Bandfield, P. R. Christensen, and M. I. Richardson (2003), Thermal Emission Imaging System (THEMIS) infrared observations of atmospheric dust and water ice cloud optical depth, *J. Geophys. Res.*, *108*, 5115, doi:10.1029/2003JE002115.

Smith, M. D., M. J. Wolff, M. T. Lemmon, N. Spanovich, D. Banfield, C. J. Budney, R. T. Clancy, A. Ghosh, G. A. Landis, P. H. Smith, B. Whitney, P. R. Christensen, and S. W. Squyres (2004), First Atmospheric Science Results from the Mars Exploration Rovers Mini-TES, *Science*, *306*, 1750–1753, doi:10.1126/science.1104257.

Smith, M. D., M. J. Wolff, N. Spanovich, A. Ghosh, D. Banfield, P. R. Christensen, G. A. Landis, and S. W. Squyres (2006), One Martian year of atmospheric observations using MER Mini-TES, *J. Geophys. Res.*, *111*(E10), E12S13, doi:10.1029/2006JE002770.

Smith, M. D., M. J. Wolff, R. T. Clancy, and S. L. Murchie (2009a), Compact Reconnaissance Imaging Spectrometer observations of water vapor and carbon monoxide, *J. Geophys. Res.*, *114*, E00D03, doi:10.1029/2008JE003288.

Smith, M. D., M. J. Wolff, R. T. Clancy, A. Kleinböhl, and S. L. Murchie (2013), Vertical distribution of dust and water ice aerosols from CRISM limb-geometry observations, *J. Geophys. Res.*, *118*, 321–334, doi:10.1002/jgre.20047.

Smith, P. H., J. F. Bell III, N. T. Bridges, D. T. Britt, L. Gaddis, R. Greeley, H. U. Keller, K. E. Herkenhoff, R. Jaumann, J. R. Johnson, R. L. Kirk, M. Lemmon, J. N. Maki, M. C. Malin, S. L. Murchie, J. Oberst, T. J. Parker, R. J. Reid, R. Sablotny, L. A. Soderblom, C. Stoker, R. Sullivan, N. Thomas, M. G. Tomasko, W. Ward, and E. Wegryn (1997), Results from the Mars Pathfinder Camera, *Science*, *278*, 1758, doi:10.1126/science.278.5344.1758.

Smith, P. H., L. K. Tamppari, R. E. Arvidson, D. Bass, D. Blaney, W. V. Boynton, A. Carswell, D. C. Catling, B. C. Clark, T. Duck, E. DeJong, D. Fisher, W. Goetz, H. P. Gunnlaugsson, M. H. Hecht, V. Hipkin, J. Hoffman, S. F. Hviid, H. U. Keller, S. P. Kounaves, C. F. Lange, M. T. Lemmon, M. B. Madsen, W. J. Markiewicz, J. Marshall, C. P. McKay, M. T. Mellon, D. W. Ming, R. V. Morris, W. T. Pike, N. Renno, U. Staufer, C. Stoker, P. Taylor, J. A. Whiteway, and A. P. Zent (2009b), H_2O at the Phoenix Landing Site, *Science*, *325*, 58–61, doi:10.1126/science.1172339.

Sprague, A. L., W. V. Boynton, K. E. Kerry, D. M. Janes, D. M. Hunten, K. J. Kim, R. C. Reedy, and A. E. Metzger (2004), Mars' South Polar Ar Enhancement: A Tracer for South Polar Seasonal Meridional Mixing, *Science*, *306*(5700), 1364–1367, doi:10.1126/science.1098496.

Sprague, A. L., W. V. Boynton, F. Forget, Y. Lian, M. Richardson, R. Starr, A. E. Metzger, D. Hamara, and T. Economou (2012), Interannual similarity and variation in seasonal circulation of Mars' atmospheric Ar as seen by the Gamma Ray Spectrometer on Mars Odyssey, *J. Geophys. Res.*, *117*, E04005, doi:10.1029/2011JE003873.

Squyres, S. W., J. P. Grotzinger, R. E. Arvidson, J. F. Bell, W. Calvin, P. R. Christensen, B. C. Clark, J. A. Crisp, W. H. Farrand, K. E. Herkenhoff, J. R. Johnson, G. Klingelhöfer, A. H. Knoll, S. M. McLennan, H. Y. McSween, R. V. Morris, J. W. Rice, R. Rieder, and L. A. Soderblom (2004), In Situ Evidence for an Ancient Aqueous Environment at Meridiani Planum, Mars, *Science*, *306*, 1709–1714, doi:10.1126/science.1104559.

Squyres, S. W., R. E. Arvidson, S. Ruff, R. Gellert, R. V. Morris, D. W. Ming, L. Crumpler, J. D. Farmer, D. J. Des Marais, A. Yen, S. M. McLennan, W. Calvin, J. F. Bell, B. C. Clark, A. Wang, T. J. McCoy, M. E. Schmidt, and P. A. de Souza (2008), Detection of Silica-Rich Deposits on Mars, *Science*, *320*, 1063–1067, doi:10.1126/science.1155429.

Squyres, S. W., R. E. Arvidson, J. F. Bell, F. Calef, B. C. Clark, B. A. Cohen, L. A. Crumpler, P. A. de Souza, W. H. Farrand, R. Gellert, J. Grant, K. E. Herkenhoff, J. A. Hurowitz, J. R. Johnson, B. L. Jolliff, A. H. Knoll, R. Li, S. M. McLennan, D. W. Ming, D. W. Mittlefehldt, T. J. Parker, G. Paulsen, M. S. Rice, S. W. Ruff, C. Schröder, A. S. Yen, and K. Zacny (2012), Ancient Impact and Aqueous Processes at Endeavour Crater, Mars, *Science*, *336*, 570–575, doi:10.1126/science.1220476.

Stevens, M. H., L. E. Deaver, M. E. Hervig, J. M. Russell III, D. E. Siskind, P. E. Sheese, E. J. Llewellyn, R. L. Gattinger, J. Höffner, and B. T. Marshall (2012), Validation of upper mesospheric and lower thermospheric temperatures measured by the Solar Occultation for Ice Experiment, *J. Geophys. Res.*, *117*(D16), D16304, doi:10.1029/2012JD017689.

Stiller, G. P., M. R. Gunson, L. L. Lowes, M. C. Abrams, O. F. Raper, C. B. Farmer, R. Zander, and C. P. Rinsland (1995), Stratospheric and mesospheric pressure-temperature profiles from rotational analysis of CO_2 lines in Atmospheric Trace Molecule Spectroscopy/ATLAS 1 infrared solar occultation spectra, *J. Geophys. Res.*, *100*, 3107–3118, doi:10.1029/94JD03105.

Stiller, G. P., M. Kiefer, E. Eckert, T. von Clarmann, S. Kellmann, M. García-Comas, B. Funke, T. Leblanc, E. Fetzer, L. Froidevaux, M. Gomez, E. Hall, D. Hurst, A. Jordan, N. Kämpfer, A. Lambert, I. S. McDermid, T. McGee, L. Miloshevich, G. Nedoluha, W. Read, M. Schneider, M. Schwartz, C. Straub, G. Toon, L. W. Twigg, K. Walker, and D. N. Whiteman (2012), Validation of MIPAS IMK/IAA temperature, water vapor, and ozone profiles with MOHAVE-2009 campaign measurements, *Atmos. Meas. Tech.*, *5*, 289–320, doi:10.5194/amt-5-289-2012.

Sullivan, R., D. Banfield, J. F. Bell, W. Calvin, D. Fike, M. Golombek, R. Greeley, J. Grotzinger, K. Herkenhoff, D. Jerolmack, M. Malin, D. Ming, L. A. Soderblom, S. W. Squyres, S. Thompson, W. A. Watters, C. M. Weitz, and A. Yen (2005), Aeolian processes at the Mars Exploration Rover Meridiani Planum landing site, *Nature*, *436*, 58–61, doi:10.1038/nature03641.

Summers, M. E., B. J. Lieb, E. Chapman, and Y. L. Yung (2002), Atmospheric biomarkers of subsurface life on Mars, *Geophys. Res. Lett.*, *29*, 2171, doi:10.1029/2002GL015377.

Sun, B., A. Reale, D. J. Seidel, and D. C. Hunt (2010), Comparing radiosonde and COSMIC atmospheric profile data to quantify differences among radiosonde types and the

effects of imperfect collocation on comparison statistics, *J. Geophys. Res.*, *115*(D14), D23104, doi:10.1029/2010JD014457.

Tamppari, L. K., M. D. Smith, D. S. Bass, and A. S. Hale (2008), Water-ice clouds and dust in the north polar region of Mars using MGS TES data, *Planet and Space Sci.*, *56*, 227–245, doi:10.1016/j.pss.2007.08.011.

Tamppari, L. K., D. Bass, B. Cantor, I. Daubar, C. Dickinson, D. Fisher, K. Fujii, H. P. Gunnlauggson, T. L. Hudson, D. Kass, A. Kleinböhl, L. Komguem, M. T. Lemmon, M. Mellon, J. Moores, A. Pankine, J. Pathak, M. Searls, F. Seelos, M. D. Smith, S. Smrekar, P. Taylor, C. Holstein-Rathlou, W. Weng, J. Whiteway, and M. Wolff (2010), Phoenix and MRO coordinated atmospheric measurements, *J. Geophys. Res.*, *115*, E00E17, doi:10.1029/2009JE003415.

Taylor, P. A., H. Kahanpää, W. Weng, A. Akingunola, C. Cook, M. Daly, C. Dickinson, A.-M. Harri, D. Hill, V. Hipkin, J. Polkko, and J. Whiteway (2010), On pressure measurement and seasonal pressure variations during the Phoenix mission, *J. Geophys. Res.*, *115*, E00E15, doi:10.1029/2009JE003422.

Telling, J., G. Lacrampe-Couloume, and B. Sherwood Lollar (2013), Carbon and Hydrogen Isotopic Composition of Methane and C_{2+} Alkanes in Electrical Spark Discharge: Implications for Identifying Sources of Hydrocarbons in Terrestrial and Extraterrestrial Settings, *Astrobiology*, *13*, 483–490, doi:10.1089/ast.2012.0915.

Titus, T. N., H. H. Kieffer, and P. R. Christensen (2003), Exposed Water Ice Discovered near the South Pole of Mars, *Science*, *299*, 1048–1051, doi:10.1126/science.299.5609.1048.

Toigo, A. D., and M. I. Richardson (2002), A mesoscale model for the Martian atmosphere, *J. Geophys. Res.*, *107*, 5049, doi:10.1029/2000JE001489.

Tokar, R. L., W. C. Feldman, T. H. Prettyman, K. R. Moore, D. J. Lawrence, R. C. Elphic, M. A. Kreslavsky, J. W. Head, J. F. Mustard, and W. V. Boynton (2002), Ice concentration and distribution near the south pole of Mars: Synthesis of odyssey and global surveyor analyses, *Geophys. Res. Lett.*, *29*, 1904, doi:10.1029/2002GL015691.

Tomasko, M. G., L. R. Doose, M. Lemmon, P. H. Smith, and E. Wegryn (1999), Properties of dust in the Martian atmosphere from the Imager on Mars Pathfinder, *J. Geophys. Res.*, *104*, 8987–9008, doi:10.1029/1998JE900016.

Toon, G. C. (1991), The JPL MkIV interferometer, *Opt. Photonics News*, *2*, 19–21, doi:10.1364/OPN.2.10.000019.

Toon, G. C., B. Sen, and A. Kleinböehl (2006), Derivation of pseudo-lines from laboratory cross-sections, `mark4sun.jpl.nasa.gov/pseudo.html`, retrieved 8 Oct. 2015.

Toon, O. B., J. B. Pollack, and C. Sagan (1977), Physical properties of the particles composing the Martian dust storm of 1971-1972, *Icarus*, *30*, 663–696, doi:10.1016/0019-1035(77)90088-4.

Tschimmel, M., N. I. Ignatiev, D. V. Titov, E. Lellouch, T. Fouchet, M. Giuranna, and V. Formisano (2008), Investigation of water vapor on Mars with PFS/SW of Mars Express, *Icarus*, *195*, 557–575, doi:10.1016/j.icarus.2008.01.018.

Ueno, Y., K. Yamada, N. Yoshida, S. Maruyama, and Y. Isozaki (2006), Evidence from fluid inclusions for microbial methanogenesis in the early Archaean era, *Nature*, *440*, 516–519, doi:10.1038/nature04584.

United States National Research Council (2003), *New Frontiers in the Solar System*, The National Academies Press, Washington, D.C.

University of Colorado and NASA (2014a), IUVS observation of atomic carbon, `lasp.colorado.edu/home/maven/iuvs-observation-of-atomic-carbon/`, retrieved 8 Oct. 2015.

University of Colorado and NASA (2014b), IUVS observation of atomic oxygen, `lasp.colorado.edu/home/maven/iuvs-observation-of-atomic-oxygen/`, retrieved 8 Oct. 2015.

University of Colorado and NASA (2014c), IUVS observation of atomic hydrogen, `lasp.colorado.edu/home/maven/iuvs-observation-of-atomic-hydrogen/`, retrieved 8 Oct. 2015.

University of Colorado, Laboratory for Atmospheric and Space Physics (2014), MAVEN LPW Observes Dust in Mars Upper Atmosphere, `lasp.colorado.edu/home/maven/maven-lpw-observes-dust-in-mars-upper-atmosphere/`, retrieved 8 Oct. 2015.

Vaniman, D. T., D. L. Bish, D. W. Ming, T. F. Bristow, R. V. Morris, D. F. Blake, S. J. Chipera, S. M. Morrison, A. H. Treiman, E. B. Rampe, and et al. (2014), Mineralogy of a Mudstone at Yellowknife Bay, Gale Crater, Mars, *Science*, *343*(6169), 1243480, doi:10.1126/science.1243480.

Villanueva, G. L., M. J. Mumma, R. E. Novak, Y. L. Radeva, H. U. Käufl, A. Smette, A. Tokunaga, A. Khayat, T. Encrenaz, and P. Hartogh (2013), A sensitive search for organics (CH_4, CH_3OH, H_2CO, C_2H_6, C_2H_2, C_2H_4), hydroperoxyl (HO_2), nitrogen compounds (N_2O, NH_3, HCN) and chlorine species (HCl, CH_3Cl) on Mars using ground-based high-resolution infrared spectroscopy, *Icarus*, *223*, 11–27, doi: 10.1016/j.icarus.2012.11.013.

Vincendon, M., Y. Langevin, F. Poulet, J.-P. Bibring, B. Gondet, D. Jouglet, and Omega Team (2008), Dust aerosols above the south polar cap of Mars as seen by OMEGA, *Icarus*, *196*, 488–505, doi:10.1016/j.icarus.2007.11.034.

Wang, J., T. Hock, S. A. Cohn, C. Martin, N. Potts, T. Reale, B. Sun, and F. Tilley (2013), Unprecedented upper-air dropsonde observations over Antarctica from the 2010 Concordiasi Experiment: Validation of satellite-retrieved temperature profiles, *Geophys. Res. Lett.*, *40*, 1231–1236, doi:10.1002/grl.50246.

Wang, K.-Y., and S.-C. Lin (2007), First continuous GPS soundings of temperature structure over Antarctic winter from FORMOSAT-3/COSMIC constellation, *Geophys. Res. Lett.*, *34*, L12805, doi:10.1029/2007GL030159.

Warneke, T., A. K. Petersen, C. Gerbig, A. Jordan, C. Rödenbeck, M. Rothe, R. Macatangay, J. Notholt, and O. Schrems (2010), Co-located column and in situ measurements of CO_2 in the tropics compared with model simulations, *Atmos. Chem. Phys.*, *10*, 5593–5599, doi:10.5194/acp-10-5593-2010.

Webster, C. R., and P. R. Mahaffy (2011), Determining the local abundance of Martian methane and its' $^{13}C/^{12}C$ and D/H isotopic ratios for comparison with related gas and soil analysis on the 2011 Mars Science Laboratory (MSL) mission, *Planet and Space Sci.*, *59*, 271–283, doi:10.1016/j.pss.2010.08.021.

Webster, C. R., P. R. Mahaffy, S. K. Atreya, G. J. Flesch, K. A. Farley, O. Kemppinen, N. Bridges, J. R. Johnson, M. Minitti, D. Cremers, and the MSL Science Team (2013a), Low Upper Limit to Methane Abundance on Mars, *Science*, *342*, 355–357, doi:10.1126/science.1242902.

Webster, C. R., P. R. Mahaffy, G. J. Flesch, P. B. Niles, J. H. Jones, L. A. Leshin, S. K. Atreya, J. C. Stern, L. E. Christensen, T. Owen, H. Franz, R. O. Pepin, A. Steele, and the MSL Science Team (2013b), Isotope Ratios of H, C, and O in CO_2 and H_2O of the Martian Atmosphere, *Science*, *341*, 260–263, doi:10.1126/science.1237961.

Webster, C. R., P. R. Mahaffy, S. K. Atreya, G. J. Flesch, M. A. Mischna, P.-Y. Meslin, K. A. Farley, P. G. Conrad, L. E. Christensen, A. A. Pavlov, J. Martín-Torres, M.-P. Zorzano, T. H. McConnochie, T. Owen, J. L. Eigenbrode, D. P. Glavin, A. Steele, C. A. Malespin, P. D. Archer, B. Sutter, P. Coll, C. Freissinet, C. P. McKay, J. E. Moores, S. P. Schwenzer, J. C. Bridges, R. Navarro-González, R. Gellert, M. T. Lemmon, and the MSL Science Team (2015), Mars methane detection and variability at Gale crater, *Science*, *347*, 415–417, doi:10.1126/science.1261713.

Wennberg, P., and V. Hipkin (2010), Mars atmospheric trace molecule occultation spectrometer, in *ExoMars Trace Gas Orbiter Instruments Program Element, Stand Alone Missions of Opportinity Notice (SALMON)*, California Institute of Technology.

Wennberg, P. O., V. J. Hipkin, J. R. Drummond, U. Dalhousie, G. C. Toon, M. Allen, J.-F. Blavier, L. R. Brown, A. Kleinböhl, J. P. D. Abbatt, B. Sherwood Lollar, K. Strong, K. A. Walker, P. F. Bernath, R. T. Clancy, E. A. Cloutis, D. J. Desmarais, J. M. Eiler, Y. L. Yung, T. Encrenaz, and J. C. McConnell (2011), MATMOS: the Mars atmospheric Trace Molecule Occultation Spectrometer, in *Mars Atmosphere: Modelling and observation*, edited by F. Forget and E. Millour, pp. 480–481.

Whiteway, J. A., L. Komguem, C. Dickinson, C. Cook, M. Illnicki, J. Seabrook, V. Popovici, T. J. Duck, R. Davy, P. A. Taylor, J. Pathak, D. Fisher, A. I. Carswell, M. Daly, V. Hipkin, A. P. Zent, M. H. Hecht, S. E. Wood, L. K. Tamppari, N. Renno, J. E. Moores, M. T. Lemmon, F. Daerden, and P. H. Smith (2009), Mars Water-Ice Clouds and Precipitation, *Science*, *325*, 68–70, doi:10.1126/science.1172344.

Williams, R. M. E., J. P. Grotzinger, W. E. Dietrich, S. Gupta, D. Y. Sumner, R. C. Wiens, N. Mangold, M. C. Malin, K. S. Edgett, S. Maurice, and the MSL Science Team (2013), Martian Fluvial Conglomerates at Gale Crater, *Science*, *340*, 1068–1072, doi:10.1126/science.1237317.

Wolff, M. J., and R. T. Clancy (2003), Constraints on the size of Martian aerosols from Thermal Emission Spectrometer observations, *J. Geophys. Res.*, *108*(E9), 5097, doi:10.1029/2003JE002057.

Wolff, M. J., M. D. Smith, R. T. Clancy, N. Spanovich, B. A. Whitney, M. T. Lemmon, J. L. Bandfield, D. Banfield, A. Ghosh, G. Landis, P. R. Christensen, J. F. Bell, and S. W. Squyres (2006), Constraints on dust aerosols from the Mars Exploration Rovers using MGS overflights and Mini-TES, *J. Geophys. Res.*, *111*(E10), E12S17, doi:10.1029/2006JE002786.

Wolff, M. J., M. D. Smith, R. T. Clancy, R. Arvidson, M. Kahre, F. Seelos, S. Murchie, and H. Savijärvi (2009), Wavelength dependence of dust aerosol single scattering albedo as observed by the Compact Reconnaissance Imaging Spectrometer, *J. Geophys. Res.*, *114*, E00D04, doi:10.1029/2009JE003350.

Wolff, M. J., R. Todd Clancy, J. D. Goguen, M. C. Malin, and B. A. Cantor (2010), Ultraviolet dust aerosol properties as observed by MARCI, *Icarus*, *208*, 143–155, doi:10.1016/j.icarus.2010.01.010.

Wong, A.-S., S. K. Atreya, and T. Encrenaz (2003), Chemical markers of possible hot spots on Mars, *J. Geophys. Res.*, *108*(E4), 5026, doi:10.1029/2002JE002003.

Wong, A.-S., S. K. Atreya, V. Formisano, T. Encrenaz, and N. I. Ignatiev (2004), Atmospheric photochemistry above possible martian hot spots, *Adv. Space Res.*, *33*, 2236–2239, doi:10.1016/S0273-1177(03)00524-6.

Wunch, D., G. C. Toon, J. L. Blavier, R. A. Washenfelder, J. Notholt, B. J. Connor, D. W. T. Griffith, V. Sherlock, and P. O. Wennberg (2011), The Total Carbon Column Observing Network, *Phil. Trans. R. Soc. A*, *369*, 2087–2112, doi:10.1098/rsta.2010.0240.

Zahnle, K., R. S. Freedman, and D. C. Catling (2011), Is there methane on Mars?, *Icarus*, *212*, 493–503, doi:10.1016/j.icarus.2010.11.027.

Zasova, L., V. Formisano, V. Moroz, D. Grassi, N. Ignatiev, M. Giuranna, G. Hansen, M. Blecka, A. Ekonomov, E. Lellouch, S. Fonti, A. Grigoriev, H. Hirsch, I. Khatuntsev, A. Mattana, A. Maturilli, B. Moshkin, D. Patsaev, G. Piccioni, M. Rataj, and B. Saggin (2005), Water clouds and dust aerosols observations with PFS MEX at Mars, *Planet and Space Sci.*, *53*, 1065–1077, doi:10.1016/j.pss.2004.12.010.

Zhang, K., E. Fu, D. Silcock, Y. Wang, and Y. Kuleshov (2011), An investigation of atmospheric temperature profiles in the Australian region using collocated GPS radio occultation and radiosonde data, *Atmos. Meas. Tech.*, *4*, 2087–2092, doi:10.5194/amt-4-2087-2011.

Appendix A

List of ACE-FTS occultations from which temperature and pressure were retrieved

The following is a list of ACE-FTS occultations used in the analysis for Chapter 4 and compared to ACE-FTS v3.5 and COSMIC data products. The list is organized into sets as in Chapter 4. ACE-FTS IDs indicate whether the occultation was at local sunset, measured from the top of the atmosphere downward and marked *ss*, or at local sunrise, marked *sr*, and are sequentially numbered since the start of operation. COSMIC IDs are in the form Cjjj.YYYY.DDD.HH.MM.Gii where jjj and ii are the indices of the COSMIC and GPS satellites, and YYYY.DDD.HH.MM are the year, ordinal date, hour and minute of the occultation. Latitude, longitude, and β angle are of the ACE-FTS vertical profiles at the 30 km tangent altitude. Mean z spacings are calculated from the retrieved ACE-FTS tangent altitudes between 20 and 100 km.

Table A.1: Middle East

ACE ID	Date	Latitude	Longitude	β angle	$\bar{z}$ spacing
ss5195	30 July 2004	34.99°	85.36°	−34.1°	4.5 km
ss5211	31 July 2004	31.37°	52.37°	−36.7°	4.4 km
ss5225	01 Aug. 2004	27.96°	68.53°	−39.0°	4.0 km
sr5616	28 Aug. 2004	29.62°	50.29°	−44.3°	3.7 km
sr10063	25 June 2005	−37.59°	161.36°	62.0°	1.5 km
ss10081	27 June 2005	31.88°	51.38°	58.7°	2.1 km
ss10604	01 Aug. 2005	32.03°	85.72°	−36.4°	4.2 km
ss10605	01 Aug. 2005	31.80°	61.16°	−36.6°	4.6 km
ss10619	02 Aug. 2005	28.39°	77.37°	−38.8°	4.0 km
ss10620	02 Aug. 2005	28.14°	52.82°	−39.0°	4.2 km
sr11009	29 Aug. 2005	29.07°	84.88°	−44.9°	3.7 km
sr11010	29 Aug. 2005	29.38°	60.38°	−44.7°	3.7 km
sr11024	30 Aug. 2005	33.42°	77.42°	−42.6°	3.9 km
sr11025	30 Aug. 2005	33.70°	52.93°	−42.5°	3.9 km
sr15160	06 June 2006	31.28°	63.32°	59.2°	2.0 km
ss15999	02 Aug. 2006	32.02°	81.99°	−36.5°	4.6 km
ss16000	02 Aug. 2006	31.78°	57.43°	−36.7°	4.3 km
ss16015	03 Aug. 2006	28.11°	49.12°	−39.1°	4.1 km
ss21394	03 Aug. 2007	32.10°	85.20°	−36.6°	4.3 km
ss26790	03 Aug. 2008	32.05°	68.94°	−36.9°	4.2 km
ss26804	04 Aug. 2008	28.64°	85.23°	−39.2°	4.1 km
ss26805	04 Aug. 2008	28.39°	60.68°	−39.3°	4.1 km
sr27195	31 Aug. 2008	29.21°	70.17°	−45.3°	3.7 km
sr27209	31 Aug. 2008	33.33°	87.33°	−43.2°	3.8 km

Table A.2: Arctic 2010

ACE ID	Date	Latitude	Longitude	β angle	$\bar{z}$ spacing
ss35483	16 March 2010	77.91°	169.09°	10.0°	5.8 km
ss35533	19 March 2010	74.48°	34.38°	1.0°	5.8 km
ss35542	20 March 2010	73.76°	175.41°	−0.6°	5.9 km
sr36477	22 May 2010	67.81°	139.78°	10.1°	5.8 km
sr36539	26 May 2010	68.76°	39.31°	21.7°	5.3 km
sr36540	26 May 2010	68.74°	14.44°	21.9°	5.3 km
sr36550	27 May 2010	68.48°	125.74°	23.7°	10.8 km
sr36554	27 May 2010	68.34°	26.26°	24.5°	5.3 km
sr36563	28 May 2010	67.96°	162.45°	26.2°	5.1 km
sr36598	30 May 2010	65.44°	12.85°	32.8°	4.7 km
sr36603	31 May 2010	64.95°	−111.25°	33.7°	4.9 km
sr36605	31 May 2010	64.74°	−160.89°	34.1°	4.7 km
ss37209	11 July 2010	66.37°	−100.83°	29.8°	4.8 km
ss37218	11 July 2010	66.97°	35.58°	28.3°	6.8 km
ss37238	13 July 2010	67.92°	−101.52°	24.4°	5.1 km
ss37268	15 July 2010	68.44°	−127.32°	18.8°	5.5 km
ss37280	16 July 2010	68.36°	−65.52°	16.5°	5.5 km
ss37300	17 July 2010	67.90°	157.80°	12.8°	5.6 km
ss37304	17 July 2010	67.76°	58.52°	12.1°	5.8 km
ss37332	19 July 2010	66.42°	84.33°	6.9°	5.8 km
ss37336	19 July 2010	66.17°	−14.73°	6.1°	5.8 km
ss38791	26 Oct. 2010	69.95°	−2.61°	57.7°	2.2 km
ss39009	10 Nov. 2010	67.17°	63.81°	23.3°	5.2 km
ss39045	12 Nov. 2010	66.42°	−95.56°	16.7°	5.6 km
ss39129	18 Nov. 2010	64.59°	13.39°	1.0°	5.8 km
ss39144	19 Nov. 2010	64.24°	7.27°	−1.8°	5.8 km
ss39159	20 Nov. 2010	63.89°	1.19°	−4.6°	5.8 km
ss39160	20 Nov. 2010	63.86°	−23.21°	−4.8°	5.9 km
ss39191	22 Nov. 2010	63.08°	−59.59°	−10.7°	5.7 km
ss39204	23 Nov. 2010	62.74°	−16.71°	−13.2°	5.6 km

Table A.3: Arctic Fall

ACE ID	Date	Latitude	Longitude	β angle	$\bar{z}$ spacing	COSMIC ID
sr32864	19 Sept. 2009	74.57°	−132.61°	1.3°	5.8 km	C003.2009.262.14.38.G08
ss33549	05 Nov. 2009	68.78°	−166.00°	35.0°	4.5 km	C002.2009.309.01.14.G13
ss33562	05 Nov. 2009	68.51°	−123.72°	32.7°	4.7 km	C006.2009.309.23.25.G07
ss33580	07 Nov. 2009	68.15°	156.39°	29.5°	4.9 km	C002.2009.311.05.12.G03
ss33603	08 Nov. 2009	67.66°	−45.58°	25.4°	5.5 km	C002.2009.312.16.43.G15
ss33617	09 Nov. 2009	67.36°	−27.61°	22.9°	5.3 km	C002.2009.313.16.18.G15
ss33643	11 Nov. 2009	66.80°	57.28°	18.1°	5.5 km	C005.2009.315.11.33.G15
ss33665	12 Nov. 2009	66.31°	−120.04°	14.1°	5.7 km	C002.2009.316.21.41.G16
ss33810	22 Nov. 2009	62.79°	−59.25°	−13.2°	5.7 km	C005.2009.326.18.40.G14
ss33827	23 Nov. 2009	62.30°	−113.88°	−16.5°	5.6 km	C002.2009.327.21.49.G25
ss33841	24 Nov. 2009	61.87°	−95.27°	−19.2°	5.4 km	C003.2009.328.22.03.G23
sr38467	04 Oct. 2010	84.27°	−100.62°	37.7°	4.4 km	C001.2010.277.15.59.G27
sr38524	08 Oct. 2010	83.70°	−33.09°	46.9°	3.5 km	C001.2010.281.12.19.G25
sr38634	15 Oct. 2010	80.61°	157.33°	60.6°	1.6 km	C001.2010.289.00.32.G02
ss39000	09 Nov. 2010	67.35°	−76.30°	24.9°	5.2 km	C002.2010.313.20.26.G17
ss39225	25 Nov. 2010	62.15°	−168.89°	−17.2°	5.6 km	C001.2010.329.02.33.G20

Table A.4: Arctic Winter

ACE ID	Date	Latitude	Longitude	β angle	$\bar{z}$ spacing	COSMIC ID
sr29131	09 Jan. 2009	60.13°	−0.32°	−26.9°	5.1 km	C003.2009.009.10.05.G10
sr29551	06 Feb. 2009	67.05°	−180.87°	48.7°	3.3 km	C001.2009.037.21.28.G11
ss29702	17 Feb. 2009	61.45°	−149.60°	61.8°	1.4 km	C005.2009.048.01.46.G13
sr34446	04 Jan. 2010	56.35°	160.98°	−42.1°	3.9 km	C001.2010.004.22.13.G11
sr34474	06 Jan. 2010	58.04°	−160.15°	−36.7°	8.8 km	C003.2010.006.20.23.G15
sr34538	11 Jan. 2010	60.65°	81.09°	−24.5°	5.2 km	C003.2010.011.04.37.G24
sr34581	14 Jan. 2010	61.88°	112.73°	−16.2°	5.6 km	C001.2010.014.00.59.G04
sr34668	19 Jan. 2010	63.81°	149.83°	0.3°	5.8 km	C003.2010.019.23.49.G06
sr34706	22 Jan. 2010	64.52°	−58.01°	7.4°	9.7 km	C001.2010.022.12.36.G04
sr34708	22 Jan. 2010	64.55°	−106.86°	7.8°	5.7 km	C001.2010.022.15.57.G24
ss35082	17 Feb. 2010	55.70°	−124.01°	61.9°	1.4 km	C002.2010.048.01.43.G17
ss35139	20 Feb. 2010	73.71°	−99.45°	61.0°	1.6 km	C002.2010.051.21.57.G12
ss35196	24 Feb. 2010	79.06°	−69.61°	56.1°	2.4 km	C005.2010.055.18.25.G22
sr39838	05 Jan. 2011	56.28°	−106.75°	−42.5°	3.9 km	C001.2011.005.16.07.G09
sr39912	10 Jan. 2011	60.02°	−107.91°	−28.3°	4.9 km	C001.2011.010.15.35.G09
sr39976	15 Jan. 2011	61.98°	132.04°	−16.1°	5.5 km	C001.2011.014.23.54.G08
sr40020	18 Jan. 2011	63.03°	138.69°	−7.7°	5.7 km	C004.2011.017.23.35.G08
sr40139	26 Jan. 2011	65.37°	113.41°	14.6°	5.4 km	C004.2011.026.02.34.G32
sr40193	29 Jan. 2011	66.30°	−125.91°	24.5°	5.2 km	C001.2011.029.17.15.G31
ss40535	21 Feb. 2011	75.14°	−107.45°	61.1°	1.7 km	C006.2011.052.23.09.G22
ss40550	22 Feb. 2011	77.01°	−120.28°	60.1°	1.7 km	C002.2011.053.22.05.G28
sr45403	18 Jan. 2012	62.85°	104.51°	−9.8°	5.6 km	C006.2012.018.03.22.G30
sr45449	21 Jan. 2012	63.88°	62.23°	−1.0°	5.7 km	C006.2012.021.05.23.G13

Table A.5: Antarctic Spring

ACE ID	Date	Latitude	Longitude	β angle	$\bar{z}$ spacing	COSMIC ID
sr30341	01 April 2009	−83.50°	−40.38°	−35.0°	4.5 km	C001.2009.091.11.22.G22
sr30350	02 April 2009	−83.53°	103.16°	−36.5°	4.5 km	C004.2009.092.02.09.G12
sr30475	10 April 2009	−81.47°	−47.62°	−55.1°	2.6 km	C004.2009.100.13.45.G12
sr30480	10 April 2009	−81.32°	−170.19°	−55.7°	2.9 km	C004.2009.100.22.10.G28
ss30628	20 April 2009	−65.39°	−103.32°	−61.7°	1.7 km	C005.2009.110.23.40.G07
ss30664	23 April 2009	−68.41°	89.73°	−59.0°	2.0 km	C005.2009.113.10.34.G25
ss30721	27 April 2009	−69.37°	130.73°	−52.4°	2.9 km	C002.2009.117.07.22.G03
ss30739	28 April 2009	−69.31°	49.76°	−49.9°	3.2 km	C002.2009.118.11.43.G06
ss30754	29 April 2009	−69.19°	42.48°	−47.7°	3.4 km	C004.2009.119.12.06.G18
ss30775	30 April 2009	−68.96°	−111.49°	−44.5°	3.7 km	C006.2009.120.21.27.G28
ss30814	03 May 2009	−68.41°	14.51°	−38.1°	4.3 km	C005.2009.123.14.17.G23
ss30819	03 May 2009	−68.33°	−107.76°	−37.3°	4.4 km	C005.2009.123.22.42.G14
ss30871	07 May 2009	−67.43°	61.02°	−28.4°	5.0 km	C006.2009.127.11.37.G18
ss30945	12 May 2009	−66.03°	52.92°	−15.2°	5.6 km	C006.2009.132.11.04.G18
ss31095	22 May 2009	−62.72°	−9.07°	12.5°	5.7 km	C005.2009.142.16.12.G16
ss31120	24 May 2009	−62.04°	101.09°	17.2°	5.6 km	C002.2009.144.08.46.G27
sr35416	11 March 2010	−60.44°	179.20°	21.9°	5.4 km	C003.2010.070.17.18.G04
sr35691	30 March 2010	−82.42°	−22.81°	−27.2°	5.1 km	C004.2010.089.09.46.G28
sr35774	05 April 2010	−82.93°	137.05°	−41.1°	4.1 km	C002.2010.095.01.30.G15
sr35787	05 April 2010	−82.78°	−177.30°	−43.2°	3.9 km	C001.2010.095.22.50.G27
sr35775	05 April 2010	−82.92°	112.89°	−41.3°	4.5 km	C001.2010.095.02.38.G31
sr35830	08 April 2010	−81.99°	−140.91°	−49.7°	5.2 km	C002.2010.098.20.21.G23
sr35840	09 April 2010	−81.76°	−24.57°	−51.1°	3.1 km	C002.2010.099.13.10.G15
ss36233	06 May 2010	−67.71°	162.96°	−34.0°	4.6 km	C006.2010.126.03.19.G20
ss36308	11 May 2010	−66.44°	129.86°	−20.8°	5.4 km	C005.2010.131.05.25.G03
ss36442	20 May 2010	−63.76°	97.47°	3.7°	5.9 km	C002.2010.140.08.21.G09
ss36472	22 May 2010	−63.06°	85.35°	9.3°	5.8 km	C005.2010.142.08.56.G15
ss36613	31 May 2010	−58.23°	−111.78°	35.7°	4.8 km	C005.2010.151.21.44.G22
ss41959	29 May 2011	−60.25°	24.35°	26.6°	5.9 km	C001.2011.149.14.13.G16

Table A.6: Low-Latitudes

ACE ID	Date	Latitude	Longitude	β angle	$\bar{z}$ spacing	COSMIC ID
sr30660	23 April 2009	−27.84°	43.90°	−59.4°	1.9 km	C004.2009.113.04.19.G18
sr30733	28 April 2009	7.35°	50.15°	−50.7°	3.0 km	C006.2009.118.01.37.G16
ss34863	02 Feb. 2010	−34.24°	−164.73°	35.8°	4.4 km	C004.2010.033.06.04.G02
ss35008	12 Feb. 2010	16.26°	−100.09°	56.8°	2.3 km	C004.2010.043.01.12.G18
ss38637	16 Oct. 2010	22.36°	−164.09°	60.8°	1.7 km	C006.2010.289.05.09.G31
sr38918	04 Nov. 2010	−30.94°	−24.04°	39.2°	4.2 km	C002.2010.308.06.54.G09
ss42994	07 Aug. 2011	27.12°	15.62°	−40.5°	4.1 km	C006.2011.219.18.33.G31